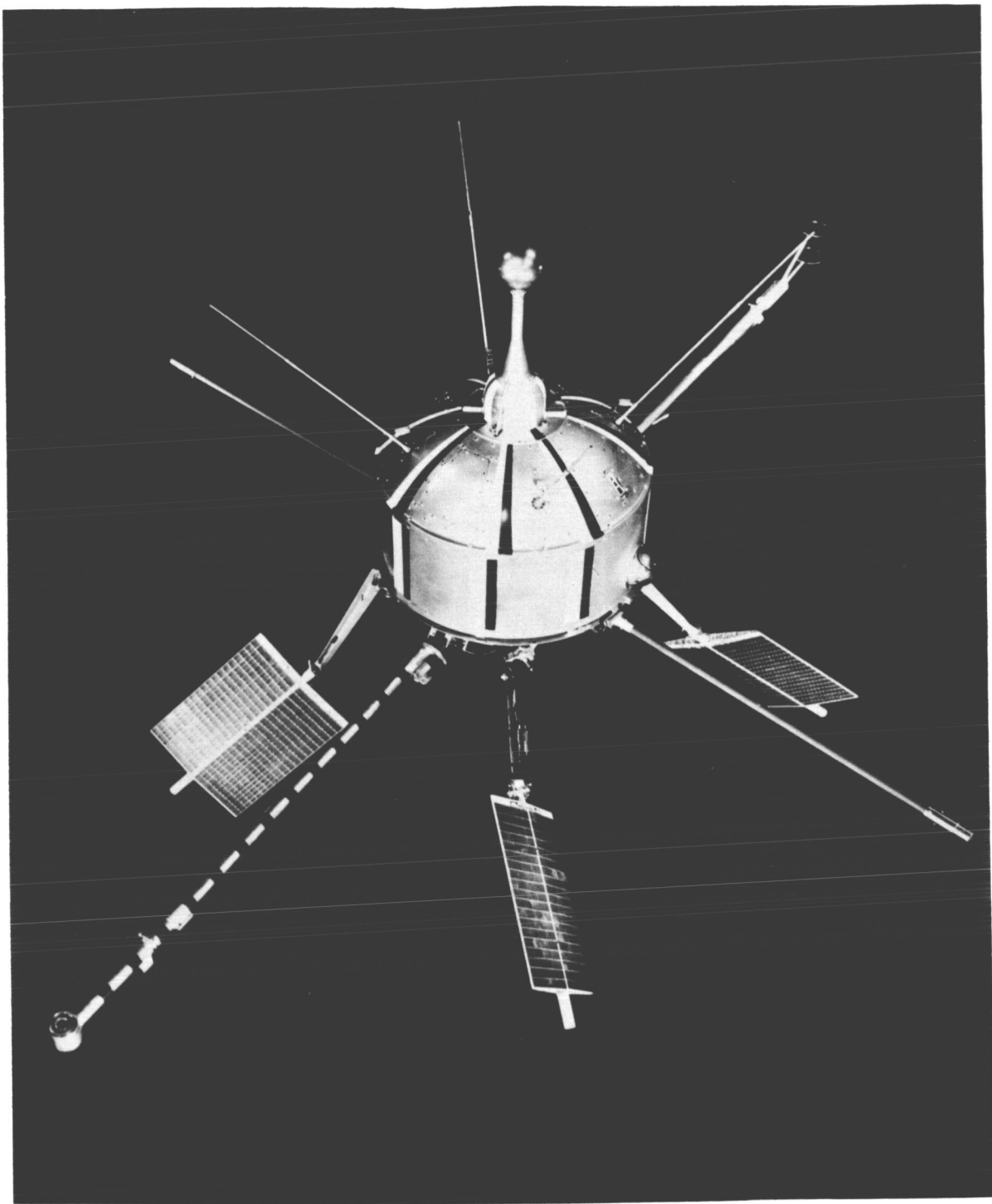
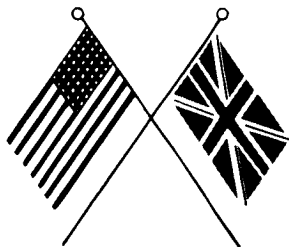


**ARIEL I: THE FIRST INTERNATIONAL SATELLITE
EXPERIMENTAL RESULTS**



Ariel I, the International Ionosphere Satellite, in orbit attitude.



ARIEL I

THE FIRST INTERNATIONAL SATELLITE • Experimental Results

prepared by
GODDARD SPACE FLIGHT CENTER
Greenbelt, Maryland



Scientific and Technical Information Division

NATIONAL AERONAUTICS AND SPACE ADMINISTRATION
Washington, D.C.

1966

For Sale by the Superintendent of Documents, U.S. Government Printing Office, Washington, D. C. 20402 • Price \$1.50

Library of Congress Catalog Card Number 66-60087

FOREWORD

The successful launching and operation of Ariel I, the first international satellite, marked a new era of international cooperation in space research. Although the scientific goals aimed at were ambitious and made severe demands on the scientific, technological and managerial skill of all concerned there is no doubt that, as a pilot project to establish a pattern of international cooperation, Ariel I was an unqualified success.

The scientific payload was chosen to enable an integrated study of the topside ionosphere and related solar behavior to be carried out. Equipment to measure the heavy component of cosmic radiation was also included. Data were collected which have made it possible to study systematically ionospheric parameters such as electron temperature and concentration and ion composition and temperature in relation to geophysical variables. Solar X-ray emission in several wavelength regions was monitored successfully and useful cosmic ray data obtained. Despite the complexity of the payload the project was generally successful both technologically and scientifically, most, if not all, of the scientific goals being realised. The operation of the satellite confirmed the validity of engineering designs which have subsequently become standard for similar spacecraft. At the same time the effectiveness of certain ionospheric measuring techniques for use from a spacecraft was established.

The purpose of this document is to summarize the entire Ariel I project including summary descriptions of experimental results, spacecraft design and performance, tracking, data acquisition, and data reduction. Like the rest of the project it represents a cooperative effort between scientists and engineers of the United States and the United Kingdom. It consists of reports and descriptions contributed by the various persons assigned to the Ariel I project compiled to make up a project results summary.

SIR HARRIE MASSEY, *Chairman of the British National
Committee for Space Research*

CONTENTS

FOREWORD	PAGE v
<i>Chapter 1</i>	
INTRODUCTION	1
Scope	1
Contributors	1
Background	2
Organization and Management	3
Satellite Performance	6
Related Documents	7
<i>Chapter 2</i>	
GENERAL TECHNICAL SUMMARY	9
Background and Purpose	9
Ariel I Configuration	11
Electronic Systems	12
Ariel I Launch Sequence	13
Spacecraft Orbit	14
<i>Chapter 3</i>	
UNITED KINGDOM EXPERIMENTS	15
Energetic Particle Measurements	15
Measurement of the X-Ray Emission from the Sun in the 3 to 12A Band ..	25
Langmuir Probe for Measurement of Electron Temperature and Density ..	30
Spherical Probe for Measurement of Ion Mass Composition and Temperature	42
Measurements of the Spatial Electron Density Distribution by Means of an	
R. F. Electron Density Probe	47
Ionization Produced by a High Altitude Nuclear Explosion	56
Ionization by Corpuscular Radiation at High Magnetic Latitudes	57
Observations During a 'Sudden Commencement'	58
Aspect History and Spin Rate Analysis	59
<i>Chapter 4</i>	
SATELLITE STRUCTURE AND SUBSYSTEMS	67
Structure and Mechanical Design	67
Thermal Design and Coatings	75
Electronic System	80
Encoder	82
Programmer	84
Tape Recorder	86
Telemetry Transmitter	88
Command Receiver	89
One-Year Timer	90
RF Antennas	90
Power System	90
Orbital Injection Programmer	95
<i>Chapter 5</i>	
TRACKING AND DATA ACQUISITION	97
The Launch Window	97

Chapter 6

DATA PROCESSING	101
NASA / GSFC Processing	101
United Kingdom Processing	116
REFERENCES	119
ADDITIONAL BIBLIOGRAPHY	123
Appendix A—PHYSICAL MEASUREMENTS OF ARIEL I	125
Appendix B—SATELLITE PERFORMANCE PROFILE	129

CHAPTER 1

Introduction

The purpose of the Ariel I Project Results Summary Document is to outline the history and document the results of this many faceted project in a single convenient reference. It would, of course, be impractical to include in detail all of the many documents, notes, reports, etc., produced during the course of the project. However, this summary attempts to cover the project in sufficient depth of detail to lead the reader directly to whatever detailed information he may need on a given facet of the program without further research. A comprehensive list of references and a bibliography are included for this purpose.

A previous summary, NASA Special Publication (SP-43),* Ariel I The First International Satellite, outlined the program up to the time of launch, April 26, 1962. Some of the information contained in that document is repeated here for the sake of convenience. However, the emphasis here is on outlining the events that occurred during the period from launch to the end of the useful life of the satellite in November 1964, and on documenting the results of the experiments carried aboard the satellite.

SCOPE

This summary is divided into six major sections of which this introduction is the first. The remainder of this section is devoted to an

overall description of the project, its organization, and a brief summary of the performance of the satellite, its subsystems and experiments. Chapter 2 is a technical summary of the satellite outlining the technical plan and describing its principal physical and functional features. Chapter 3 provides a description and discussion of results of each of the United Kingdom experiments. Chapter 4 describes each of the major sub-systems provided by the GSFC and comments on the performance of each. Chapter 5 is a summary of tracking and data acquisition operations along with an evaluation of these operations. Chapter 6 summarizes the data processing performed by both the U.K. and the GSFC. Those processing functions performed by the U.K. that were peculiar to a given experiment are described in Chapter 3 along with the appropriate U.K. experiments.

CONTRIBUTORS

This document is a collection of descriptions and reports authored prior to and after the launch of Ariel I (April 26, 1962). These contributions have been edited, revised, and updated to produce continuity. The following list includes the authors who have provided major contributions to this summary.

United Kingdom Contributors

Sir Harrie Massey, F. R. S.
Prof. R. L. F. Boyd, University College London
Dr. A. C. Durny, Imperial College London

*For sale by the Superintendent of Documents, U.S. Government Printing Office, Washington, D.C., 20402—Price 70 cents.

Prof. H. Elliot, Imperial College London
 Dr. K. A. Pounds, University of Leicester
 Dr. J. J. Quenby, Imperial College London
 Prof. J. Sayers, University of Birmingham
 Mr. U. Samir, University College London
 Mr. J. Wager, University of Birmingham
 Dr. A. P. Willmore, University College London

BACKGROUND

Ariel I, the first international satellite, was designed to contribute to man's knowledge of the ionosphere and its complex relation to the sun.

This project developed from proposals made in 1959 to NASA by the British National Committee on Space Research. These proposals were in response to a United States offer to the Committee on Space Research (COSPAR) of the International Council of Scientific Unions to launch scientific experiments or complete satellites prepared by scientists of other nations. The content of the program and the division of responsibility between NASA and the British Committee were agreed upon during discussions that took place in late 1959 and early 1960. Subsequently, the NASA Administrator assigned project responsibility for the United States to the Goddard Space Flight Center (GSFC).

This assignment included the design, fabrication, integration, and testing of the spacecraft structure, power supply telemetry, command receiver, thermal control, and data

United States Contributors

(National Aeronautics and Space Administration, Goddard Space Flight Center)

R. C. Baumann	R. G. Martin
R. E. Bourdeau	W. H. Meyer
A. Buige	M. Schach
T. D. Clem	J. C. Schaffert
P. T. Cole	J. T. Shea
C. V. Creveling	L. Slifer
A. G. Ferris	J. K. Steckel
C. F. Fuechsel	C. M. Stout
D. Hepler	E. R. Stroup
W. H. Hord, Jr.	J. M. Turkiewicz
R. E. Kidwell	C. L. Wagner, Jr.
V. L. Krueger	H. D. White, Jr.
T. J. Lynch	F. C. Yagerhofer

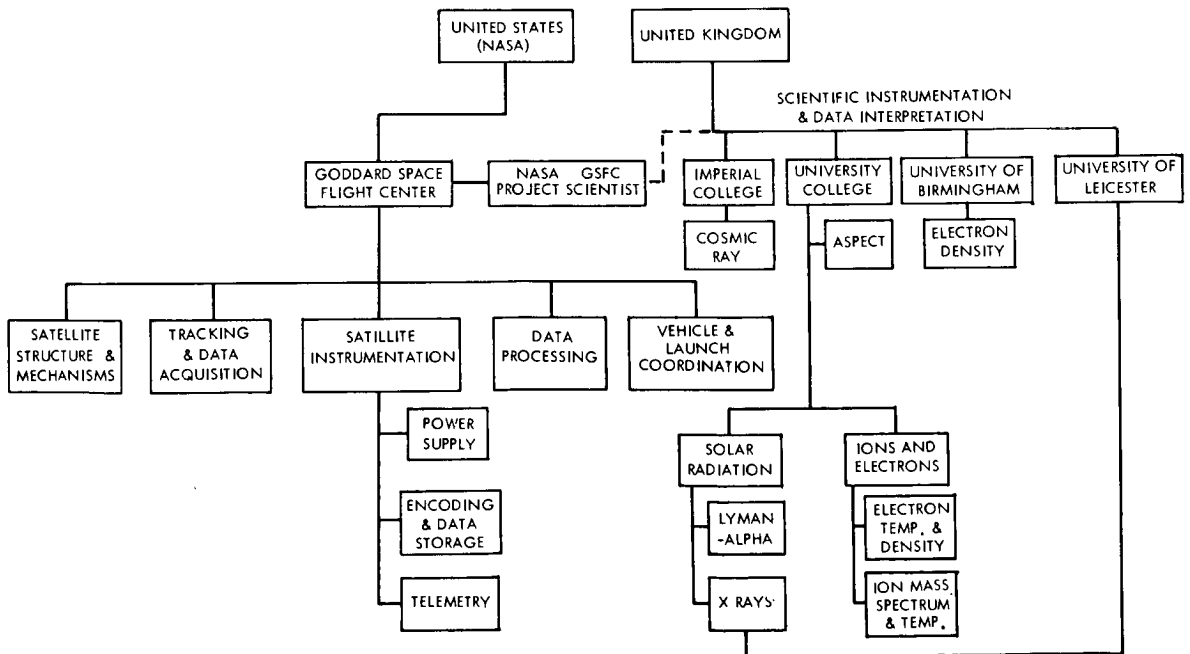


FIGURE 1-1. Ariel I prime responsibilities.

INTRODUCTION

storage. GSFC supplied the vehicle, was responsible for launch, performed data acquisition via the worldwide STADAN (Mini-track) network, and provided a part of the data processing. The United Kingdom (U.K.) had the responsibility for the design, fabrication, and testing of all flight sensors and their associated electronics up to the telemetry encoder input. The U.K. also was responsible for final data reduction, analysis and interpretation. The distribution of responsibilities is outlined in Figure 1-1.

A list of the experiments and electronic subsystems follows. The experiments and subsystems are described in detail in Chapters 3 and 4, respectively.

Experiments

Electron Temperature and Density—University College London
Ion Mass Composition and Temperature—University College London
Solar Lyman-Alpha Emission Measurement—University College London
X-Ray Emission—University College London and University of Leicester
Solar Aspect Measurement—University College London
Cosmic Ray Analyzer—Imperial College London
Ionosphere Electron Density Measurement—University of Birmingham

Electronic Subsystems

Telemetry—Goddard Space Flight Center
Data Encoders—Goddard Space Flight Center
Tape Recorder—Goddard Space Flight Center
Power System—Goddard Space Flight Center
Spacecraft Parameters (Housekeeping) System—Goddard Space Flight Center

Spacecraft and orbital characteristics are detailed in the following list.

Scientific Instrumentation

Electron temperature and density sensors (2)
Ion mass sphere (1)
Solar radiation detectors, Lyman-alpha at 1216A (3)

Solar aspect meter (1)
Electron density sensors (1)
X-ray counters (2)

Spacecraft Characteristics

Size, basic structure—23 inches O.D. by 22 inches high
Weight—136 pounds
Spin rate—36 to 12 rpm throughout life
Lifetime—1 year
Power—p-on-n solar cells and nickel-cadmium batteries
Data Storage—100-minute tape recorder
Antenna—modified crossed dipole
Tracking and data frequency—136.408 Mc nominal

Orbit Parameters

Perigee—390 km (242 statute miles)
Apogee—1214 km (754 statute miles)
Inclination—55 degrees
Period—99 minutes
Eccentricity—0.057

Three complete payloads were constructed: one for prototype testing, a flight model, and a backup in case of malfunction in the first launch attempt. Provision was made for two launching vehicles, including one for backup. Ariel I was launched on April 26, 1962. A cutaway view of the satellite is shown in Figure 1-2.

ORGANIZATION AND MANAGEMENT

The approach of the Ariel I project management utilized a concept of a joint United States-United Kingdom working group with various ad hoc committees named as required. The basic Ariel I working group membership was as follows:

United Kingdom

<i>University of Birmingham</i>	<i>Electron Density</i>
Professor J. Sayers	Project Scientist
<i>Imperial College London</i>	<i>Cosmic Ray</i>
Professor H. Elliot	Project Scientist
Dr. J. J. Quenby	Alternate

ARIEL I: THE FIRST INTERNATIONAL SATELLITE

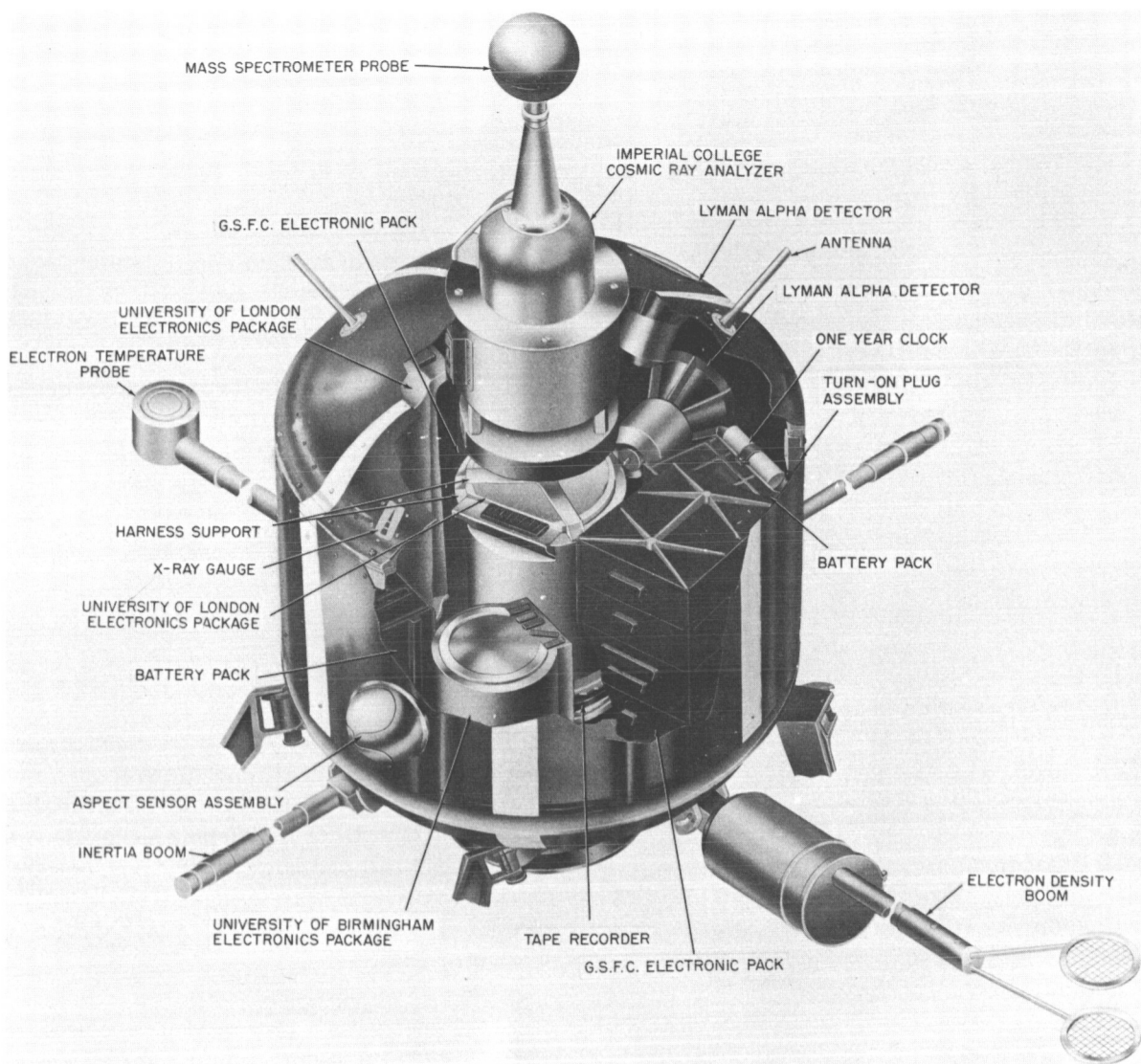


FIGURE 1-2. Cutaway view of Ariel I.

<i>University of Leicester</i>	<i>X-ray</i>	<i>United States</i>	
Dr. K. A. Pounds	Project Scientist	National Aeronautics and Space Administration	
<i>University College London</i>	<i>All</i>	<i>NASA Headquarters:</i>	
Professor R.L.F. Boyd	<i>Other Experiments</i>	Dr. J. E. Naugle	U.S. Project Officer
Dr. A. P. Willmore	Project Scientist	Mr. M. J. Aucre- manne	U.S. Project Chief
Mr. M. O. Robins	Alternate	<i>Goddard Space Flight Center:</i>	
Dr. E. B. Dorling	U.K. Project Man- ager	Mr. R. C. Baumann	U.S. Project Manager
	U.K. Coordinator	Mr. R. E. Bourdeau	Project Scientist

INTRODUCTION

Mr. J. T. Shea	U.S. Coordinator
Mr. H. J. Peake	Telemetry RF
Dr. R. W. Rochelle	Telemetry coding
Mr. J. C. Schaffert	Sequence programming
Mr. P. T. Cole	Data Storage
Mr. C. L. Wagner, Jr.	Mechanical Design
Mr. F. C. Yager-hofer	Power Supply
Mr. M. Schach	Thermal Design
Mr. R. E. Kidwell, Jr.	Thermal Design
Mr. W. H. Hord, Jr.	Environmental Testing
Mr. J. M. Turkiewicz	Electrical Systems Integration
Mr. C. H. Looney	Tracking Systems
Mr. H. E. Carpenter	Tracking Operations
Mr. C. J. Creveling	Data Reduction
Mr. A. Buige	Operations Control
Mr. C. P. Smith	Atlantic Missile Range, Vehicle Coordination
Mr. R. H. Gray	Atlantic Missile Range, Operations and Launch Director

Management responsibility for the Ariel I project was assigned as follows:

Project Management

NASA's Goddard Space Flight Center was assigned project management responsibilities for the Ariel I project.

Each country had an Ariel I Project Manager, Project Coordinator, and Project Scientist. All working decisions were subject to the approval of the Project Managers. Responsibility for the coordination of the many aspects of the overall program was vested in the Project Coordinators. The Project Scientists were responsible for the ultimate compatibility and integration of the various experiments. Overall policy matters were decided by the NASA Administrator for the United States and by the Minister for Science for the U.K. Scientific matters

in the U.K. were decided by the British National Committee for Space Research under the chairmanship of Sir Harrie Massey.

In the case of subsystems, the work (and contract monitoring) was the responsibility of the individual in charge of a given subsystem.

Reports indicating progress in accomplishing scheduled milestones and summarizing the project status were furnished by GSFC to NASA Headquarters on a biweekly basis as required by NASA Management Instruction G-2-3, "Program Management Plans." The U.S. Project Manager submitted to the Director, GSFC, each week a written report that described significant events occurring on the project, highlighted problem areas, and indicated any assistance that was required.

Periodic presentations on the Ariel I project were made to the GSFC Executive Council. This group, chaired by the Director of GSFC, was composed of top management officials. The presentations covered all significant aspects, such as funding, procurement, etc. Emphasis was placed on defining problem areas and applying necessary measures to resolve them.

The U.S. Project Manager made monthly submissions of data for the NASA Administrator's progress report. Such data included the progress made on Ariel I project objectives during the previous month, progress made during current month, and plans for the coming month.

The U.S. Project Manager was responsible for the preparation of semi-annual budget reports on his project.

Experiment Systems Management

Experiment systems management responsibilities were accepted by the U.K. Project Manager and his staff, later to become the Space Research Management Unit, Office of the Minister for Science.

Spacecraft Systems Management

Goddard Space Flight Center was assigned system management responsibilities for the Ariel I spacecraft system.

ARIEL I: THE FIRST INTERNATIONAL SATELLITE

Tracking and Data System Management

Goddard Space Flight Center was assigned system management responsibilities for the Ariel I tracking and data system. Acquired data were sent to the United Kingdom after processing (digitizing), and the U.K. was responsible for data reduction and analysis.

NASA Headquarters Direction

The Director, Office of Space Sciences, NASA Headquarters, was responsible for overall direction and evaluation of the performance of the Goddard Space Flight Center as the Ariel I Project Management Center and as the Systems Management Center for the spacecraft and the tracking and data systems.

The Director, Office of International Programs, NASA Headquarters, was responsible for defining and interpreting international agreements relating to the project and for providing the United States (NASA) coordination with the United Kingdom.

SATELLITE PERFORMANCE

The overall performance of Ariel I was outstanding in the light of several potentially catastrophic events that occurred during its lifetime, the ambitious scope of the project, and the many potential hazards to the success of a highly complex spacecraft. The planned fully integrated attack on designated areas of knowledge of the upper ionosphere was almost realized during the first three months of operation. Events after this period caused considerable degeneration in performance, but the long useful life of the satellite compensated in part for this degeneration.

Launch was originally scheduled for March 1962. This scheduled date was slipped approximately one month because of a minor vehicle failure. Successful launch was accomplished April 26, 1962. At a critical time prior to the original launch date, the volcano on the island of Tristan da Cunha chose to erupt, thereby preventing establishing a temporary telemetry station there to receive signals from the satellite during the early

part of its first passage in orbit. These were especially important because they were designed to provide confirmation of the way the release mechanism for aeriols, booms and solar paddles which should come into play soon after separation from the final stage rocket motor, had operated. The problem was solved through the generous co-operation of the British Admiralty who made available a ship, H.M.S. Protector, in the South Atlantic at the planned launch time. Suitable receiving equipment was fitted and manned. However, the first launch date could not be kept and there was a postponement. The new date was not possible for H.M.S. Protector, which had to return to base, but in a very short time the Admiralty arranged for the frigate H.M.S. Jaguar to be available. Equipment was fitted at Simonstown and the signals from Ariel were successfully recorded.

Data acquired by the H.M.S. Jaguar was of particular significance because the release mechanisms failed to release at the proper time and in proper sequence. In spite of this failure, by sheer good fortune the satellite was injected into its proper orbit at the planned spin rate. A more serious failure during launch was that of the Lyman- α experiment. Since none of the three sensors produced any data during the life of the satellite, it is assumed that a failure occurred in the electronics common to all sensors. Other than these two failures, all satellite systems and experiments were operating satisfactorily after launch.

All experiments and systems that were operative immediately after launch remained so for approximately three months. In July 1963 the Starfish Event (high altitude nuclear explosion) presented a major hazard to further successful operation. The initial effect was to saturate almost all experiment sensors. However, these, for the large part, recovered and continued to operate satisfactorily. A more permanent effect was radiation damage to the solar array, and other components, which resulted in intermittent and erratic satellite operation for the remainder of its useful life. Appendix B pro-

INTRODUCTION

vides a complete mission profile summary of overall satellite operation.

Another significant failure occurred after one year of operation. The one-year cut-off timer failed to operate. This particular failure proved fortuitous in that it enabled useful data to be gathered from the satellite until November 1964. At that time it was judged that performance had become too erratic to provide further useful data.

Other than the minor contretemps previously mentioned, tracking and data acquisition operations went smoothly throughout the program. GSFC data processing fell behind the acquisition rate temporarily, but the situation was remedied by the establish-

ment of a second processing line. The fact that a large quantity of useful data were acquired by experimenters was a tribute to the effectiveness of the data processing functions, both at the U.K. and the GSFC.

RELATED DOCUMENTS

In addition to the specific reports referenced in the text, there are many reports relating to the design, development, and experimental measurements of Ariel I. The reference and bibliography list at the end of this summary report gives the specific reports referenced herein as well as an additional bibliography of related documents.

CHAPTER 2

General Technical Summary

The purpose of this chapter is to establish the technical background of the program, outline the overall technical plan, and provide a frame of reference for the more detailed description of the experiments and spacecraft given in Chapters 3 and 4, respectively.

BACKGROUND AND PURPOSE

In determining the experiments to be carried out by Ariel I, every effort was made not to duplicate experiments already performed or underway by the U.S. and Russia. Simultaneously, experiments were selected to (1) take advantage of techniques developed in the U.K. as part of the Skylark sounding rocket program, and (2) provide an

integrated assault on unknowns connected with the sun-ionosphere relation. Toward this end six specific experiments were designed and installed aboard the spacecraft.

Of the six specific experiments carried on board, five are closely interrelated and provide concurrent measurement of two important types of solar emission and the resulting changing states of the ionosphere. Table 2-1 identifies the various experiments by functional groups.

The three ionospheric experiments measured electron density and temperature as well as the composition and temperature of positive ions. The two solar emission experiments were designed to monitor the intensity

TABLE 2-1.
Experiment Functional Groups

Solar Emission / Ionosphere		Cosmic Ray
Solar Emission	Ionosphere	
Solar Lyman- α Emission- Chromospheric Radiation X-Ray Emission- Corona Radiation	Electron Temperature and Density-Modified Langmuir Probe Ion Mass Composition and Temperature- Mass Spectrometer Electron Density- Plasma Dielectric Constant	Cerenkov Detector- Analysis of Energy Spectrum vs. Magnetic Field

ARIEL I: THE FIRST INTERNATIONAL SATELLITE

of radiation from the sun in the ultraviolet (Lyman-alpha) and x-ray bands of the solar radiation spectrum. Lyman-alpha radiations originate in the sun's chromosphere (solar surface), while x-rays originate farther out in the area around the sun known as the corona. Previous work has shown that

the Lyman-alpha radiation is relatively constant but that x-ray emissions are quite variable with solar conditions. Unfortunately the Lyman-alpha experiment failed at launch and no data were gathered from this experiment.

The sixth experiment measured primary

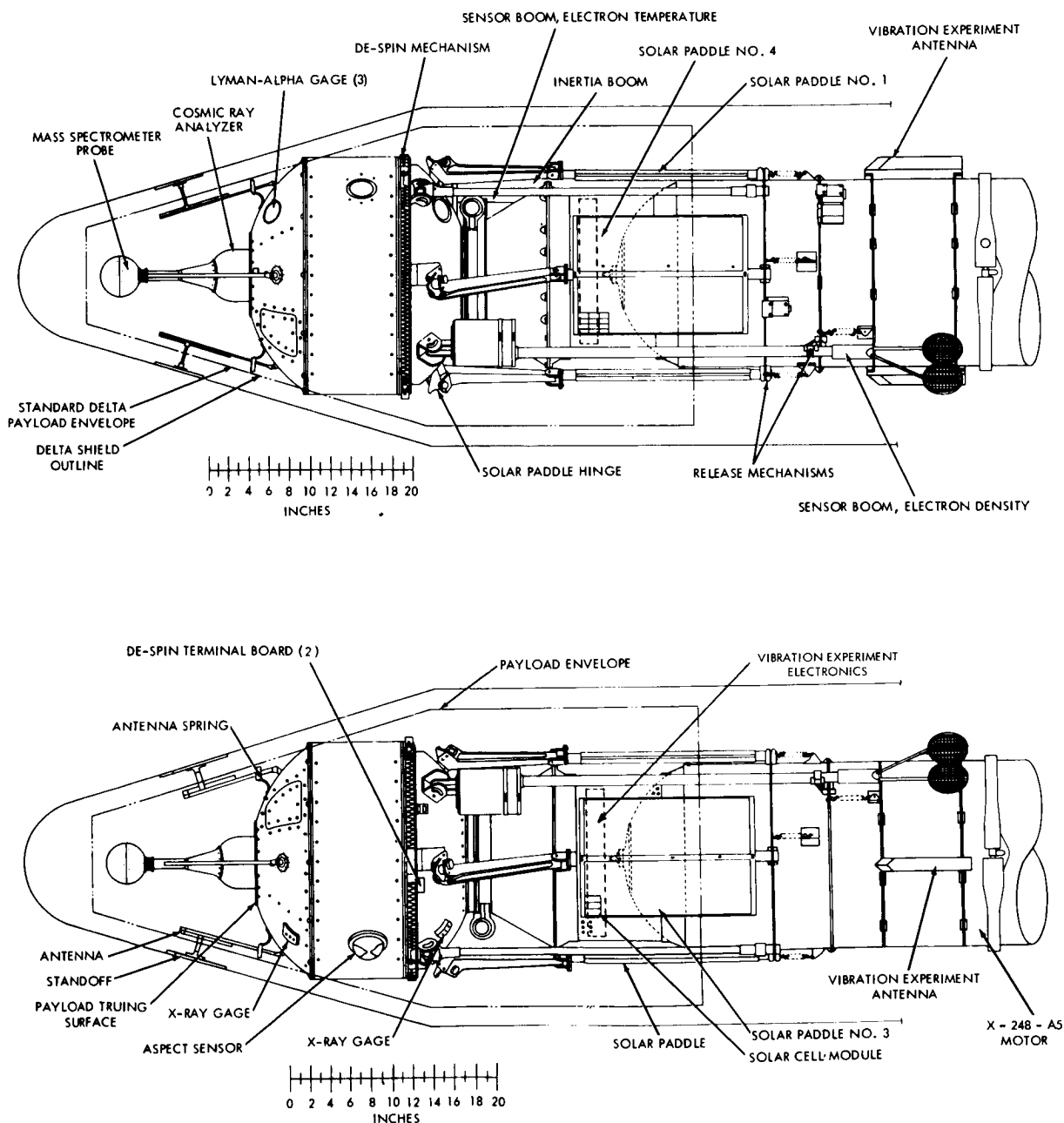


FIGURE 2-1. Ariel I satellite—Delta vehicle compatibility view.

GENERAL TECHNICAL SUMMARY

cosmic rays by means of a Cerenkov detector carried on board the Ariel I. Simultaneously, measurements of secondary cosmic rays were made by means of ground observation and by means of aircraft, balloons, etc.

In addition to the principal experiments listed above, which are essentially scientific, other experiments of an engineering and housekeeping nature were included. The satellite was originally planned to be launched aboard a Scout vehicle, but this was later changed to a Thor-Delta vehicle. This change necessitated an adaptor (the Delta Dutchman) at the spacecraft-vehicle interface which was used to house a solar aspect and spin rate sensor, for sensing these functions prior to separation and a sensor designed to detect contamination of thermal coatings. Also housed in this adaptor was a vibration experiment designed to provide a vibration profile of the vehicle during powered flight.

In addition to the Dutchman experiments, there were housekeeping temperature sensors and an attitude and spin rate sensor in the spacecraft. These may be classified as experiments in that their functional relationship to other spacecraft systems is essentially the same as that of the scientific experiment.

ARIEL I CONFIGURATION

Figures 2-1 and 2-2 provide essential major component outlines and relative positions for Ariel I. Its basic configurations, which had to fit the envelope of the Delta Vehicle's payload compartment, was that of a cylinder $10\frac{11}{16}$ inches long and 23 inches in diameter. The main element of each closure was a spherical section whose large (inboard) terminator circle was $8\frac{7}{16}$ inches in diameter. Each spherical section was $5\frac{1}{4}$ inches long and had an outer surface radius of curvature of $13\frac{1}{2}$ inches. To this basic 22-inch-high configuration were attached the various elements necessary for the support and conduct of the several experiments in the system.

The spin axis of the satellite was the central (z) axis of the cylinder, which—for

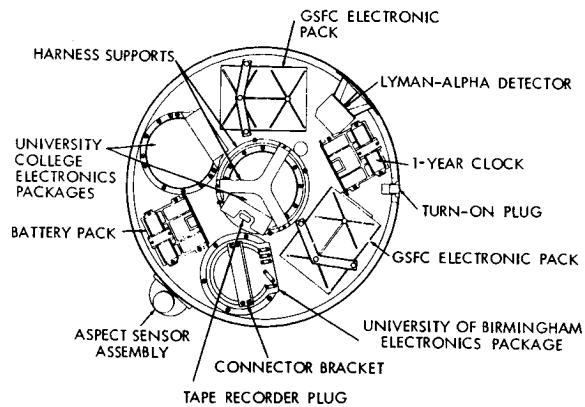


FIGURE 2-2. Ariel I main shell plan view.

purposes of this description—is also considered as the vertical axis. At the bottom of the satellite was a $9\frac{3}{8}$ -inch-diameter fourth-stage separation flange, within which were mounted the electron temperature gage and the tape recorder.

Four solar panels extended horizontally from midway up the lower spherical section, at 90 degree intervals around the satellite circumference.

Offset 45 degrees circumferentially from the solar paddles, opposite and exactly counterbalancing one another, and extending radially in the same horizontal plane are two booms with nominal lengths of four feet. The end of one boom accommodates the two circular capacitor plates of the electron density sensor. Electronics associated with this experiment were housed in a $4\frac{1}{4}$ -inch-diameter by $6\frac{1}{4}$ -inch-long cylinder mounted on the boom close to the main body of the satellite. At the end of the other boom was a second electron temperature gage, whose electronics were located inside the satellite.

In the same horizontal plane as the electron temperature and density boom, two inertia booms were mounted. These were provided to establish a proper spin-to-tumble ratio.

With the exception of a $3\frac{1}{2}$ -inch-diameter hemispherical solar aspect sensor, the central cylindrical section was free of protuberances.

On top of the satellite, in line with the spin axis, was a five-inch-diameter cylinder containing the cosmic ray Cerenkov detector.

Above this, on an eight-inch-long conical and cylindrical section tapering from a three-inch to one-inch diameter was a four-inch-diameter ion mass sphere whose center of mass is located 14 inches above the forward face of the main body.

Four turnstile antennas, spaced circumferentially at 90 degrees and angling up at 45 degrees, were mounted on the top spherical section perpendicular to the sphere at the interfaces.

There were three flush-mounted solar radiation (Lyman-alpha) detectors on the satellite skin: two at 60 degrees (one up and one down) from the equator, and one on the equator. All three were in the same vertical plane and in the same 180-degree sector. There were two proportional x-ray counters

located 45 degrees up and down from the equator and directly opposite the Lyman-alpha gages.

ELECTRONIC SYSTEMS

Relationships among the major electronic subsystems are shown in figure 2-3. In general the probes, conditioning circuits, and subcarrier oscillators were designed and supplied by the U.K., and the remaining circuits were provided by NASA/GSFC. Those circuits shown in figure 2-3 do not include any of those experiments contained in the Dutchman nor the orbital injection programmer. These were omitted because they are not a part of the actual spacecraft, even though they are important parts of the program.

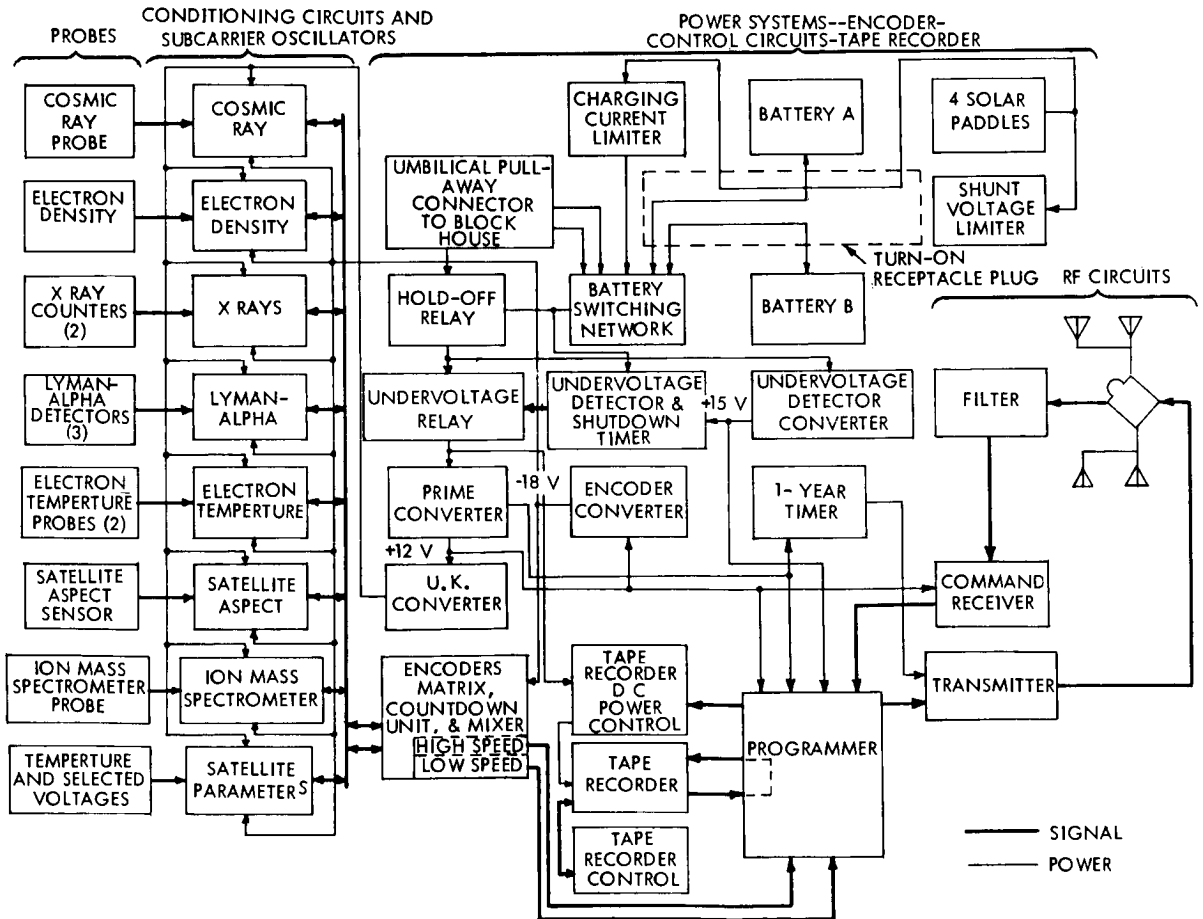


FIGURE 2-3. Electronic systems functional block diagram.

GENERAL TECHNICAL SUMMARY

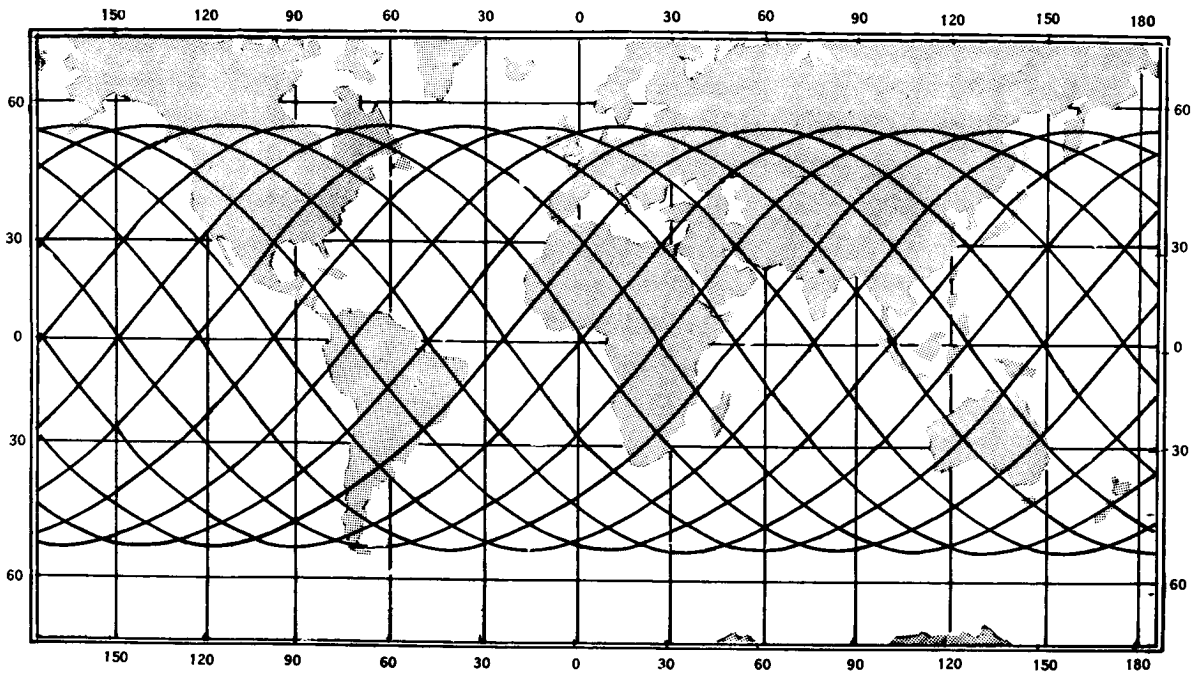


FIGURE 2-4. Orbital coverage vs. world map.

The major path of signal flow through the system starts with the probes which sense the various quantities and produce a proportional analog or digital output. The signal conditioning and subcarrier oscillator circuits convert the probe outputs to analogous FM signals. The signal processing circuits, including the encoder, tape recorder, and programmer, receive the parallel outputs of the SCO's and regiment them into serial word format, storing low-speed data and routing high-speed data to the transmitter for on-line transmission. When a read-out command is received they interrupt the high-speed on-line transmission and play back stored data to the transmitter. The rf circuits consist principally of the transmitter and receiver. These utilize a common antenna system for the transmission of data and the receipt of commands.

ARIEL I LAUNCH SEQUENCE

The planned sequence of events from nose cone ejection to satellite separation was:

1. Nose cone ejection.

2. Second-stage burnout.

3. Second and third-stage coast and yaw until peak of ascent path is reached and vehicle is aligned with its programmed attitude.

4. Third-stage spin-up to approximately 160 rpm and ignition.

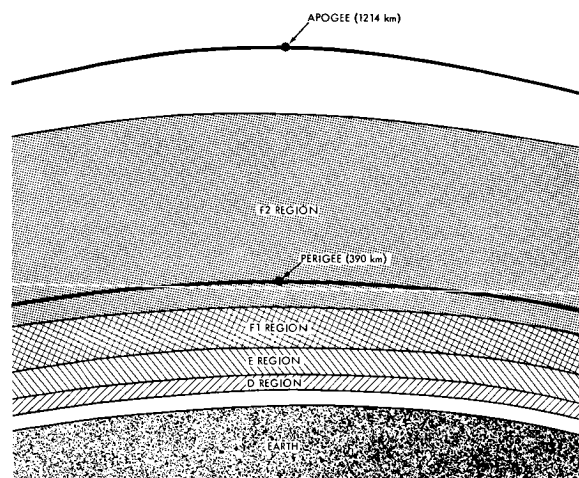


FIGURE 2-5. Orbital coverage vs. cross section of Earth and Ionosphere.

5. Second-stage separation and retro-rockets fired.

6. Burnout of third stage.

7. Coast to allow outgassing (thrust) of the third stage to cease.

8. De-spin of the third-stage—payload combination (first de-spin) to 76.5 rpm, by releasing "stretch yo-yo" de-spin device.

9. Release and erection of experiment booms (second de-spin) and de-spin to 52.4 rpm.

10. Release and erection of the inertia booms and paddles, de-spin (third de-spin) to 36.6 rpm.

11. Separation of the payload from the third stage at a differential velocity of 7 ft/sec.

12. Final rate of spin at the end of 1 year should be less than 12 rpm.

Steps 8, 9 and 10 of this sequence were not accomplished in this order (See Chapter 4), but de-spin was accomplished, and the spacecraft was injected into its planned orbit.

SPACECRAFT ORBIT

Planned orbit parameters are listed in Chapter 1 and a comparison of planned versus actual orbit is given in Chapter 5. Figures 2-4 and 2-5 provide an approximate pictorial presentation of overall orbital coverage. Figure 2-4 shows several orbits plotted against a Mercator projection of the earth. In Figure 2-5 orbits are plotted against a cross section of the earth and ionosphere.

CHAPTER 3

United Kingdom Experiments

This chapter sets forth a summary of the results of each of the United Kingdom experiments carried aboard Ariel I. With the exception of the Lyman α experiment, which failed at launch, considerable experimental data were collected and analyzed for all experiments. Because the scope of this document is limited to a summary of the project, full details of each experiment are not given. However, an extensive list of references and bibliography are included at the end of this document for the benefit of readers who wish to investigate a particular experiment, or facet thereof, in detail.

ENERGETIC PARTICLE MEASUREMENTS

Project Scientists

Professor H. Elliot, Imperial College, London
Dr. J. J. Quenby, Imperial College, London
Dr. R. J. Hynds, Imperial College, London
Dr. A. C. Durney, Imperial College, London

Project Engineer

Mr. D. W. Mayne, McMichael Radio Ltd.,
Slough

The Energy Spectrum of the Heavy Primary Cosmic
Rays

The form of the energy spectrum and the intensity of cosmic rays arriving at the Earth from outside the solar system are controlled by the electromagnetic conditions in interplanetary space, which are in turn a function of solar activity. The configuration of the magnetic fields in and around the solar system is not yet known and the processes where-

by they control the cosmic ray flux are not understood. A limited amount of information on the magnetic fields in the vicinity of the Earth has been acquired by means of the magnetometers carried in the spacecraft Pioneer V and Mariner II. But such space probes can at present only survey a tiny part of the solar system, and we must make full use of the information provided by cosmic-ray studies if we are to establish the large-scale configuration of the interplanetary field and understand its variations with time and with solar activity. Thus, the magnetometer observations and the cosmic ray data are complementary, the former providing detailed information about a very small part of the field and the latter permitting us to sketch its large-scale properties.

In attempting to delineate these large-scale properties and to understand how the cosmic-ray flux is modulated by the interplanetary field, it is important to establish with good accuracy, the energy dependence of the modulation process. In order to do so we need to measure the primary cosmic-ray spectrum in the vicinity of the Earth and to follow the changes in this spectrum over the cycle of solar activity.

Protons are the main constituent of the primary cosmic-ray flux, but measurements of the energy spectrum of these protons is difficult. Complications arise because of the presence of albedo particles generated in the Earth's atmosphere by interaction of the primary particles, the presence of the geomagnetically trapped protons in the Earth's radiation belt, and of energetic protons generated

in the solar atmosphere. Because of these sources of contamination, identification of the genuine cosmic-ray proton is not always possible and becomes progressively more difficult the further we go down the energy spectrum. One solution to this problem is to ignore the protons and to measure instead the energy spectrum of the much less abundant heavy nuclei. The number of heavy nuclei with, say, $Z \geq 6$, is negligible both in the Earth's albedo radiation and in the radiation belt. Furthermore, there is good reason to believe that by using the heavy nuclei as indicators of the spectrum there is better discrimination against contamination by the solar source, since the ratio of such nuclei to protons is smaller for flare-accelerated particles than for the cosmic ray flux generally (Biswas, Fichtel & Guss 1962) (1).

An accurate measurement of the spectrum of heavy primary particles with $Z \geq 6$ in the energy region affected by the solar modulation process was one of the main objectives of the cosmic-ray experiment on board the Ariel I satellite launched on 26 April 1962.

The Experimental Method

In the geomagnetic field it is possible to ascribe to each point in space a minimum rigidity, R_{min} , which a particle coming from infinity must have if it is to reach that point from any specified direction. Thus a heavy particle detector carried in an Earth-orbiting satellite enables us to measure the particle intensity as a function of R_{min} , and we can therefore, in principle, determine the integral number spectrum in terms of either particle rigidity or its corresponding energy.

As a heavy particle selector we used a Cerenkov counter. In such a counter the intensity of Cerenkov light generated by a charged particle in a given range of wavelengths is proportional to $Z^2(1 - 1/\beta^2 n^2)$, where $\beta = v/c$ and n is the refractive index of the radiator. Thus, a particle with $Z = 6$ generates 36 times as much light as a proton with the same velocity and it is a comparatively simple matter to distinguish between the two. The form of counter used is shown in figure 3-1. It consisted of a hollow Perspex sphere with diameter 10 cm and wall

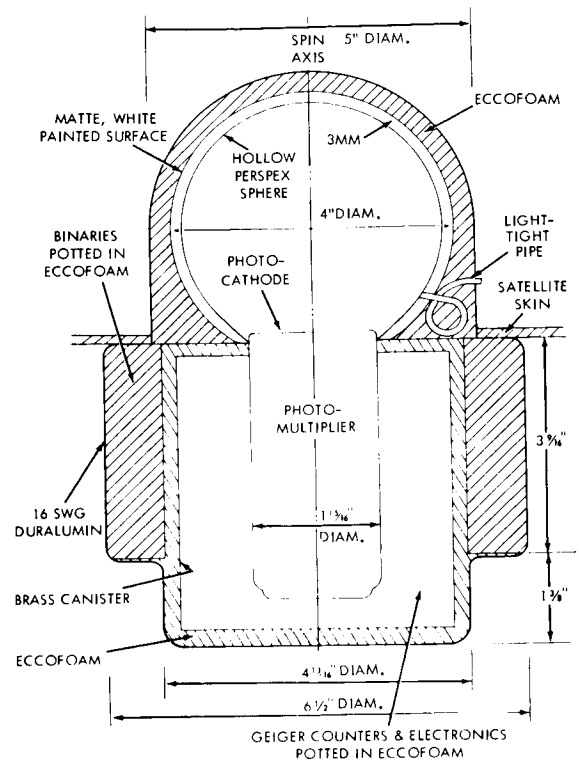


FIGURE 3-1. Cut-away diagram showing the cosmic ray Cerenkov counter and its associated electronics.

thickness 3 mm, viewed by a photomultiplier tube with a 4 cm diameter photocathode. Output pulses from the anode of the photomultiplier were fed through an emitter follower and variable attenuator to a discriminator, as shown in figure 3-2. The discriminator was biased so that it was triggered only by pulses corresponding to the passage of particles through the Perspex sphere with $Z \geq 5$ and had no response to protons. The output of the discriminator was applied, by way of an encoder gate to a data store consisting of eight binary units. The contents of the last six binary units of this store were sampled at intervals of 2.56 seconds by a high-speed encoder and at 30.72 second intervals by a low-speed encoder. The output of the high-speed encoder was fed to the telemetry system providing continuous data transmission, while the output of the low-speed encoder was fed to a tape recorder capable of storing data over a period of 100 minutes (one complete orbit). This

UNITED KINGDOM EXPERIMENTS

ČERENKOV CHANNEL

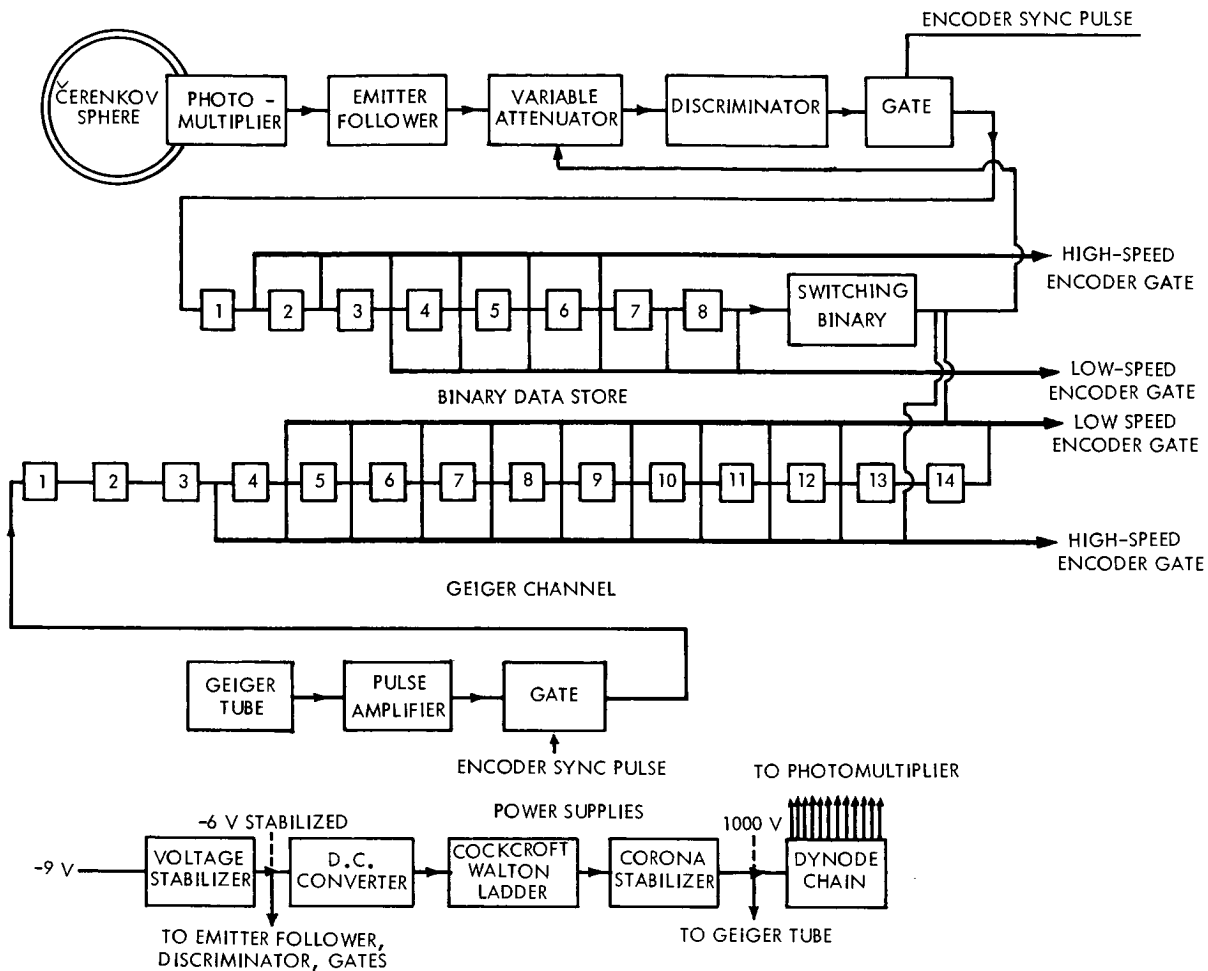


FIGURE 3-2. Block diagram showing the electronics systems for the Čerenkov and G-M counters.

tape recorder read out the previous 100 minutes of data on command from a ground station. The encoder gate ensured that the reading of the binary store did not change during the sampling period.

Because of the possibility of drift in the sensitivity of the phototube, provision was made for an in-flight check by periodically changing the sensitivity of the system by a known factor. This was accomplished by using the variable attenuator shown in the block diagram in figure 3-2. This attenuator had two possible settings determined by the state of the switching binary at the end of the chain. One setting was chosen so that the discriminator responded to particles with $Z \geq 5$, and particles in this category were

counted until 256 of them had passed through the detector. The 256th particle actuated the switching binary which changed the attenuator setting into its alternate position, thereby reducing the phototube output pulse by a factor 1.8 so that the discriminator could then respond only to particles passing through the Perspex sphere with $Z \geq 6$. When 256 particles in this category had been counted the switching binary was again actuated and the system counted alternately 256 particles $Z \geq 5$ and $Z \geq 6$. The state of the switching binary was transmitted by the telemetry system so that the gain setting was known at any particular time. The data could, therefore, be separated into two groups corresponding to the two positions of the attenu-

ator, and if the same spectrum is obtained from the two sets of data we could feel confident that our measurements were not influenced by the sensitivity of the system. This periodic change in gain also enabled us to establish the way in which the counting rate depended on gain, and so permitted a correction to be made for the drop in Cerenkov light output from particles of low magnetic rigidity where β is appreciably less than unity.

The detector was to be carried in a spin-stabilized satellite, and was therefore designed so that it would detect particles incident within as large a solid angle as possible in order to minimize the effects of the continually changing orientation of the satellite relative to the Earth. In this respect the ideal detector would, of course, have been completely omni-directional with a response which was independent of satellite orientation. Such a detector would have been difficult to construct and the design adopted here was necessarily a compromise. This design proved, however, to be entirely adequate and it will be shown that the effects of vehicle orientation were negligible.

There were two consequences of using this type of a detector. In the first place, because of the multitude of different path lengths through the Cerenkov radiator, it was not possible with such a system to produce a sharp resolution of particle charge since a high Z particle with a short path might produce the same amount of light as a low Z particle with a longer path. Consequently, when we speak of selecting particles with $Z \geq 6$ this was a nominal figure only and there was some response to particles of lower Z . This was not important for the determination of the rigidity spectrum, since we could safely assume that the modulation process would be the same for all particles with the same specific charge and the same magnetic rigidity. The validity of this assumption is borne out by the results of the present experiment, which show that the measured spectrum is the same for both sensitivity levels. This was to be expected provided we excluded protons since all the heavier nuclei have specific

charges close to a half. The discriminator levels were chosen so that there was no response to protons in the rigidity range with which we are concerned here.

The value of the geomagnetic threshold rigidity, $R_{min.}$, depends not only on the position of the detector, but also on the direction of arrival of the particles. A second consequence, therefore, of using a detector with a wide angle of acceptance is that we must take a value for $R_{min.}$ which has been obtained by averaging over the appropriate solid angle.

During some parts of the orbit the detector was exposed to the very high electron and proton fluxes in the radiation belt. These fluxes might be many orders of magnitude greater than the particle intensity we wished to measure. Under such extreme conditions there was a strong possibility that the operation of the detector would be affected in some way by these very intense particle fluxes, and in order to guard against the possibility of confusion a Geiger-Müller (G-M) counter was included in the cosmic ray package. A G-M counter has a high sensitivity to the radiation belt particles and gives a clear indication when a satellite is in the radiation belt. The presence of this counter enabled us, therefore, to detect and reject any data from the Cerenkov detector which might have been invalidated through the effects of radiation belt particles. In addition, the G-M counter provided, of course, data about the radiation belt particles themselves and about the total cosmic ray flux.

The counter used was an Anton 302, which had a sensitive area of $\approx 0.5/\text{cm}^2$. This counter and its associated electronics are included in the block diagram in figure 3-2. The output pulses from the counter were fed through an encoder gate and stored in a 14-element binary chain, which like the Cerenkov store, was sampled by both high and low-speed encoders so that the data were available from the continuous telemetry and from the magnetic tape read-out. Because of the length of the telemetry sampling period, the limitation in the size of the binary store, and the requirement that the current through the G-M counter should not overload

the EHT supply, it was necessary to restrict severely the dynamic range of this counter. This was achieved by means of a high series resistance in the G-M counter voltage line, which resulted in a maximum counting rate of about 60 per second. At fluxes greater than ≈ 89 particles $\text{cm}^{-2}\text{s}^{-1}$ the rate of the counter dropped to zero because of voltage reduction by the series resistance. Thus the counter provided either a measure of the particle flux when it was within its dynamic range or an unambiguous statement that the flux was greater than ≈ 89 particles $\text{cm}^{-2}\text{s}^{-1}$ when it was beyond it.

The counter was situated inside the electronics container in the position shown in figure 3-1. It was surrounded by a one mm lead shield and $\approx 2\text{g}/\text{cm}^2$ of aluminium, iron, Fibreglas, potting material, and electronic components. Its presence proved to be extremely useful both for the information it provided about the radiation belt and in enabling us to reject those data from the Cerenkov counter invalidated by a small response in this detector to energetic protons in the inner radiation belt. This response arose in the following way. The glass face of the phototube was a disk of thickness 2.5 mm and diameter 5 cm. Scintillation light was produced in this disk on passage of a charged particle, and when a proton of energy ≈ 100 MeV traversed the glass with a path length of a few centimeters, it could generate a light pulse which exceeded that produced by a relativistic carbon nucleus passing through the Perspex sphere. This effect has been studied by exposing a spare unit in the proton beam of the cyclotron at A.E.R.E. Harwell and it has been shown that the detector responds to protons in the energy range 80 to 140 MeV.

The position of the cosmic ray detector in the satellite is shown in figure 1-2. The Perspex sphere of the Cerenkov detector lay on the spin axis and projected out beyond the front surface in order to reduce the amount of overlying material to a minimum. The University College positive ion probe was mounted on a stem projecting beyond the Cerenkov sphere. The sphere was shielded

by $\approx 0.4\text{ g}/\text{cm}^2$ aluminum and $\approx 0.1\text{ g}/\text{cm}^2$ Eccof foam.

Detector Performance

The cosmic-ray detector worked normally until 18 May when the satellite moved into 100% sunlight. Combination of these circumstances with an unfavorable direction of the spin axis achieved on launch resulted in the thermal balance of the satellite being upset. As a consequence, the temperature of the cosmic-ray sensor rose above the design maximum of 60°C with the result that the phototube suffered an irreversible drop in sensitivity. This in itself was not serious, the only effect being to reduce the statistical accuracy of the measurements. The detector continued to operate in a stable fashion at this lower level of sensitivity until the Starfish nuclear explosion of 9 July 1962. Following this explosion, very high fluxes of fission-product β -particles were encountered by the satellite and on some parts of the orbit the Cerenkov light generated by these electrons in the 1 to 10 MeV range produced sufficient phototube current to overload the EHT supply and drop the voltage below the level at which the tube had enough gain to respond to cosmic rays. Some of the results of the Starfish explosion are discussed later in this chapter. The G-M counter ceased to work at the beginning of September and the Cerenkov counter in mid-December. No command read-out data from the tape recorder were available after mid-August.

A representative command read-out is shown in figure 3-3 where the counting rate of the Cerenkov counter and the G-M counter have been plotted as a function of time for a complete orbit. At the beginning of the read-out, on the left, the satellite was near its northern apex, and as it moved towards the equator and out to apogee both detectors showed the characteristic decrease in cosmic ray intensity with decreasing latitude. This was followed by a corresponding increase after the satellite had crossed the equator and was moving towards its southern apex. The double peak in the G-M counter rate at high southern latitudes was produced as the satel-

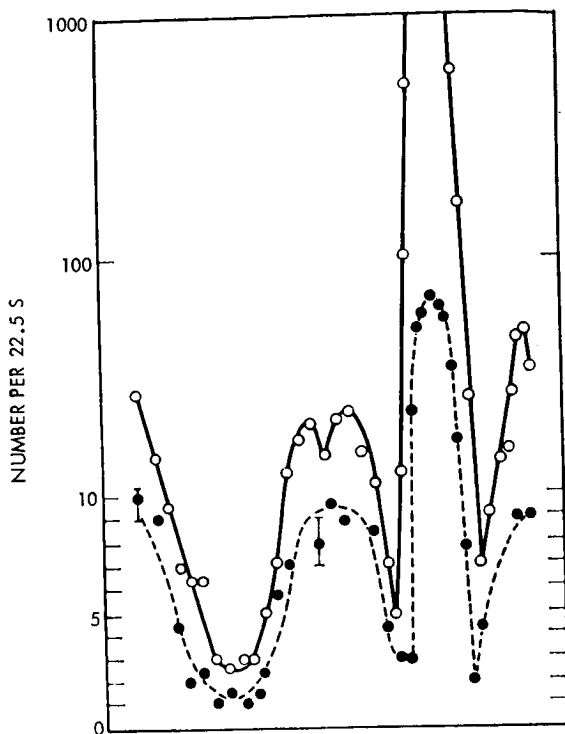


FIGURE 3-3. Typical tape recorder command read-out of Cerenkov (.) and G-M counter (o) rates.

lite crossed the magnetic shells corresponding to maximum intensity in the outer radiation belt. The Cerenkov counter did not respond to these particles and showed the normal behaviour to be expected when it was recording cosmic rays. As the satellite moved once more towards the equator and down to the perigee the rates of both detectors at first fell, but then rose to a large peak in the equatorial region as the satellite entered the inner radiation belt where the lower boundary dips low over the American continent. The G-M counter went into saturation while the Cerenkov counter showed an increase in rate due to ≈ 100 MeV protons detected in the manner already described. On emerging from the radiation belt the rate reverted to that corresponding to the cosmic ray fluxes as the satellite moved towards its northern apex to complete its orbit in a period of ≈ 100 minutes.

Command read-out data of this kind are available for a total of 830 orbits and about half this number have been used in the spectrum determination reported here.

Reduction and Analysis of the Experimental Data

The basic data from the cosmic ray detectors used in the present analysis consist of readings of the last six binaries of the Cerenkov store and of the last eleven binaries of the G-M counter store taken every 30.72 seconds. These readings have been differenced to give the number of counts registered from the two detectors during each of these intervals. The position of the satellite in terms of latitude, longitude and height has been determined at the time corresponding to the center of these intervals from the orbital data. The corresponding value of the threshold rigidity, $R_{min.}$ for cosmic rays arriving vertically at the Earth's surface has been obtained from the table of values prepared by Quenby & Wenk (1962) (2).

These data, taken from approximately 400 orbits and for satellite altitudes lying between 390 and 800 km, were grouped together to obtain the average counting rate for heavy nuclei as a function of threshold rigidity for the two attenuation levels of the detector. In carrying out this analysis the data were divided into two groups corresponding to the intervals preceding and following the change in phototube sensitivity which occurred during the period of high temperature. These intervals were 26 April to 18 May and 4 June to 8 July respectively.

The results of this analysis are shown in figure 3-4. The two attenuation levels have been plotted as a function of threshold rigidity for each of these two time intervals. It will be seen that, fortuitously, the counting rate for the highest attenuation level during the first interval was very nearly the same as that for the lowest attenuation level during the second interval. In order to derive the correct integral spectrum we must make a number of corrections and these will now be discussed in the order of importance.

Variation of Intensity of Cerenkov Light with Particle Velocity. The intensity of Cerenkov light radiated is proportional to $(1 - 1/\beta^2 n^2)$ and we expect, therefore, that the sensitivity of the detector will diminish with diminishing $R_{min.}$ for particles with a given Z . This diminution in light output

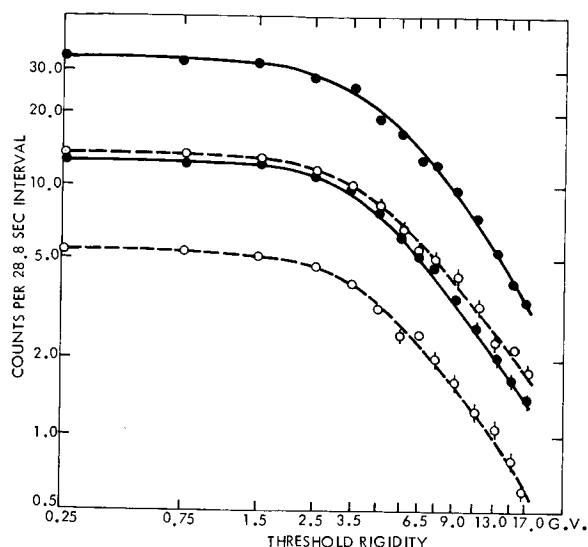


FIGURE 3-4. Counting rate of Cerenkov counter plotted as a function of threshold rigidity for the two attenuation levels before (—) and after (---) the change in gain of the photo-tube.

resulted in an underestimate of the flux of low rigidity primaries. In a hypothetical detector this drop in detector sensitivity could be compensated by making the gain of the phototube a function of the velocity of the particles whose intensity is being measured. In order to achieve compensation the gain would be proportional to $(1 - 1/\beta^2 n^2)^{-1}$ so that the amplitude of the output pulse from the phototube would be independent of particle velocity. We cannot do this in practice, but we can achieve the same result by making use of the *in situ* determination of the counting rate as a function of gain, as illustrated in figure 3-4. These data can be used to construct figure 3-5 which shows the relationship between counting rate and gain for several values of particle rigidity. Using the relation $R = m\beta c^2 / Ze\sqrt{(1 - \beta^2)}$ and the expression $(1 - 1/\beta^2 n^2)^{-1}$ for the gain required for compensation, we can immediately obtain the corrected counting rate for any particular rigidity from figure 3-5. This correction depends only on the known relation between particle velocity and Cerenkov light radiated and on the *in situ* calibration of counting rate against gain of the system.

Threshold Rigidity at Satellite Altitude.

The threshold rigidities which have been used in sorting the data are those applicable at ground level for vertically incident particles, and it is necessary to apply a correction for the altitude of the satellite and for the wide angle of acceptance of our detector. In correcting for the effects of altitude it has simply been assumed that the threshold rigidity at the satellite, R_s , is related to that at ground level by

$$R_s = R_{min} r_e^2 / (r_e + h)^2,$$

where R_{min} is the Quenby-Wenk threshold appropriate to the latitude and longitude of the satellite, r_e is the radius of the Earth, and h is the satellite altitude. Except at low latitudes the threshold rigidity, R_{min} , does not vary widely with direction of incidence, and the value appropriate to the vertically incident particles proves to be a sufficiently good approximation. In the equatorial region a mean value weighted over all directions has been used. This value never differs from that for vertical incidence by more than ≈ 1 GV.

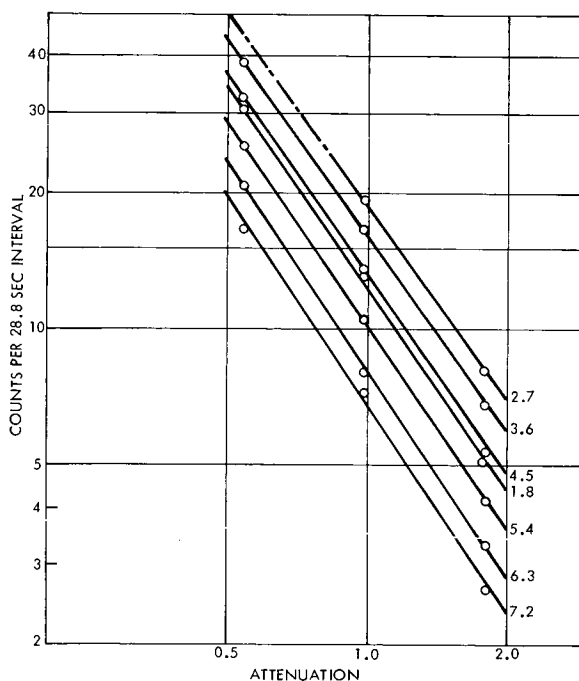


FIGURE 3-5. *In situ* calibration showing the counting rate as a function of attenuation for various particle rigidities. Constructed from curves in figure 3-4.

Variation in Satellite Aspect. The direction of the spin axis of the satellite remains fixed in space so that as the vehicle traces out its orbit the direction of this axis is continually changing relative to the local vertical. Because of this we might expect some 'shadowing' of the detector by absorption of particles in the satellite itself. The direction of the spin axis is known from the sun sensor on board the vehicle (Willmore 1962, private communication) and this effect has been investigated: it turns out to be negligible.

Variation in Altitude of the Satellite. In addition to the variation of threshold rigidity with altitude already discussed, we may expect the vehicle altitude to affect our analysis in another and quite different way. The detector cannot receive particles from the full solid angle to which it is sensitive because of the shadowing effect of the Earth, and as the altitude of the vehicle varies so the solid angle subtended by the Earth will change. This change is of course reflected as a variation in counting rate. Because of the precession of the orbit during the period of observation and the averaging process used, the effective variation in height is only ± 25 km, and here again the correction is negligible.

The Experimental Results

The integral rigidity spectrum obtained after making the corrections described above is shown in figure 3-6 and has a clearly discernible change in slope in the neighborhood 8.5 GV. In the rigidity interval covered by this experiment, the spectrum can be adequately represented by a power law with exponents of ≈ 1.2 below 8.5 GV and ≈ 1.5 above this rigidity. We tentatively interpret the change in slope at ≈ 8.5 as indicative of an upper limit to the long-term solar modulation process at this time.

This spectrum is characteristic of the period May and June 1962, when the neutron intensity at Mount Washington had recovered to a value lying approximately 8 to 10% below the sunspot minimum value. Figure 3-7 shows the neutron intensity measured in London during 1962 and it can be seen from

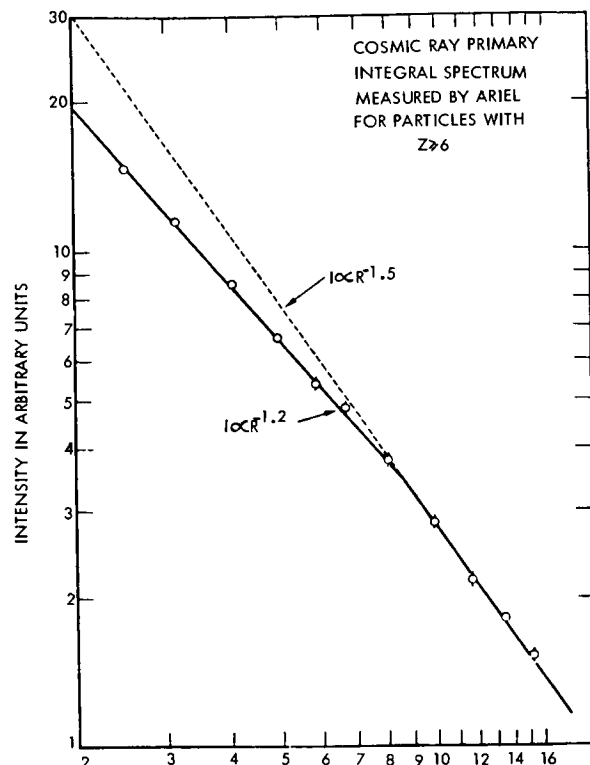


FIGURE 3-6. Integral primary spectrum after applying the various corrections discussed in the text.

this diagram that the satellite measurements were made during a period when the cosmic ray intensity remained rather constant.

In order to determine the dependence of the solar modulation process on rigidity it is necessary to know the form of the unmodulated spectrum. The best approximation to

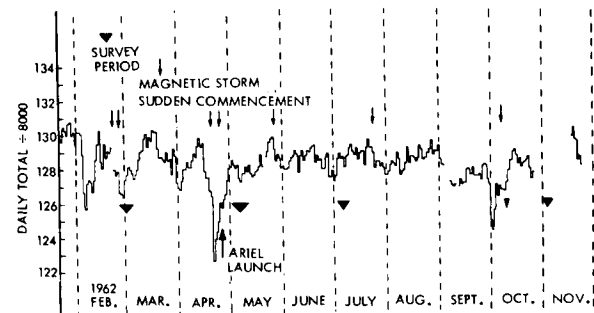


FIGURE 3-7. Neutron intensity recorded in London during 1962. Δ indicates periods during which aircraft latitude surveys were carried out at an atmosphere depth of ≈ 140 gm/cm².

this spectrum that we can expect to obtain at the present time is that observed at solar minimum, when the effects of solar modulation are least. This integral spectrum is not at all well known for the heavy primaries but has an exponent of ≈ 1.5 (Webber 1962) (3). This spectrum, when combined with the present result, would indicate for the period May-June 1962 a rigidity dependence for the solar modulation process in the 2.5 to 8.5 GV region of the form

$$J_E = J_{00} [P/P_0]^{0.3},$$

where J_E is the intensity at the Earth of particles with rigidity greater than P , where P is in GV, J_{00} is the corresponding galactic intensity, and $P_0 \approx 8.5$.

Other determinations of the heavy primary spectrum outside the atmosphere have been made by Ellis, Gottlieb & Van Allen (1954) (4) using rockets, by Pomerantz & Witten (1962) (5) using an ionization chamber carried in Explorer VII, and by Kurnosova, Logachev, Razorenov & Fradkin (1962) (6) using Cerenkov counters carried in the second and third Soviet space vehicles. These measurements were made during 1960 when solar activity was at a higher level than that obtained during the present experiment. Comparison between Explorer VII and Ariel I data shows that the flux of heavy nuclei is dependent on the solar activity cycle in a similar way to the flux of protons in the range of magnetic rigidity covered by these measurements. The implications of these measurements in relation to the structure of the interplanetary magnetic field have been discussed in some detail by Elliot (1963) (7) and by Quenby (1965) (8).

The Artificial Radiation Belt Produced by the Starfish Nuclear Explosion

The material in this section represents a brief summary of some of the main results discussed in detail in the two papers by Durney et al (9).

Both the Anton 302 counter and the Cerenkov detector in the cosmic ray package provided information concerning the artificial radiation belt created by the Starfish

explosion on 9 July 1962, the most directly interpretable data being those from the G-M counter. The shielding of this counter was such that electrons with energies of 7.4 and 10.5 MeV have, respectively, 10 and 50% probabilities of penetration from the direction of minimum shielding. The corresponding energy for protons is 50 ± 5 MeV.

At the moment of the explosion the satellite was at an altitude of 815 km at latitude 52°S and longitude 163°E —a distance of 7400 km from Johnston Island on roughly the same geomagnetic longitude as the explosion point but at a higher L value, namely, $L=4.76$ compared with $L=1.12$.

Delayed Increase in G-M Count Rate

Following the explosion, a sudden increase in counting rate was observed with a delay of 20 ± 5 sec, which drove the G-M counter into saturation (Durney et al. 1962) (9). This radiation burst lasted for about 6 minutes and its cause has not yet been positively identified. It is hard to account for it in terms of either γ rays or neutron-decay electrons. A redistribution of the natural radiation belt population by the hydromagnetic disturbance generated by the explosion would seem to provide a more plausible explanation.

The Johnston Island Shell

Both the G-M counter and the Cerenkov detector revealed the presence of an intense electron flux on the $L=1.12$ shell which passes 400 km above Johnston Island and intersects the Earth's surface in the region of South America (Durney et al. 1962) (9). This high intensity shell was also observed by the TRAAC satellite (Pieper 1963) (10) and was apparently continuously fed by the decay of fission fragments located on the $L=1.12$ shell at the longitude of Johnston Island. This shell could still be distinguished on 12 July, three days after the explosion.

Injection at High L -Values

Although the peak intensity in the long-lived Starfish electron belt occurred in the

neighborhood of $L=1.12$, the Ariel I sensors clearly indicated the presence of some fission electrons as far out as $L=7$ or 8. Figure 3-8 shows a plot of the Anton 302 counting rate as a function of day number. The Starfish explosion took place on day 190. It is clear from the diagram that the lifetime of these electrons was of the order of one day.

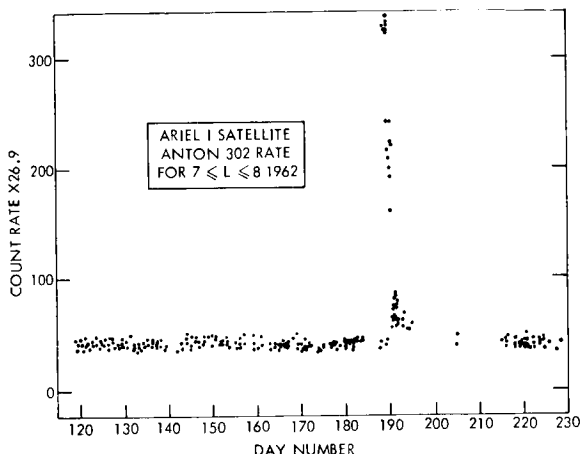


FIGURE 3-8. Plot of the G-M counting rate as a function of day number during 1962 for $7 \leq L \leq 8$. The ordinate gives the number of counts per 26.9 second intervals.

Increased Count Rates Associated with Other Nuclear Explosions

Figure 3-9 shows a plot of the G-M counter rate against day number for the field region $1.0 \leq L \leq 1.1$ prior to Starfish. The large, short-lived spikes in this diagram appear to have been associated with atmospheric explosions in the Dominic series.

Charged Particle Flux in the Equatorial Region Below Radiation Belt

When the satellite is outside the boundaries of the trapped radiation zone the G-M counter provides a measure of the total cosmic ray flux including both protons and heavier nuclei. Also included in this flux are those splash and re-entrant albedo particles generated in the atmosphere by the primary cosmic

rays and having sufficient energy to penetrate the shielding of the counter.

Minimum cosmic ray intensity occurs in the region where the geomagnetic threshold is highest, that is, close to the magnetic equator in the neighborhood of longitude 100°E . Thus we would expect the G-M count-rate to be at a minimum in this region provided the satellite is well below the lower boundary of the radiation belt. Figure 3-10 shows the count-rate plotted as a function of longitude close to the magnetic equator and for a constant altitude of 400km. The sharp increase in counting rate in the neighborhood of 30°W is produced by radiation belt particles where the inner boundary of the belt descends below 400km over the South Atlantic. A second, much smaller, but clearly distinguishable, peak appears in the neighborhood of longitude 130°E close to the position of expected cosmic ray minimum. The dotted line shows, for comparison, the expected cosmic ray count-rate as a function of longitude, and below it are shown the cor-

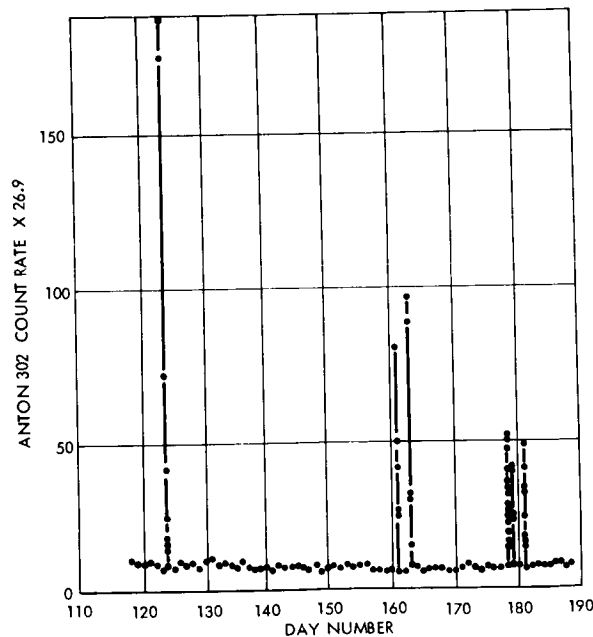


FIGURE 3-9. Plot of the G-M counting rate close to the magnetic equator for $1.0 \leq L \leq 1.1$. The ordinate gives the number of counts per 26.9 second intervals.

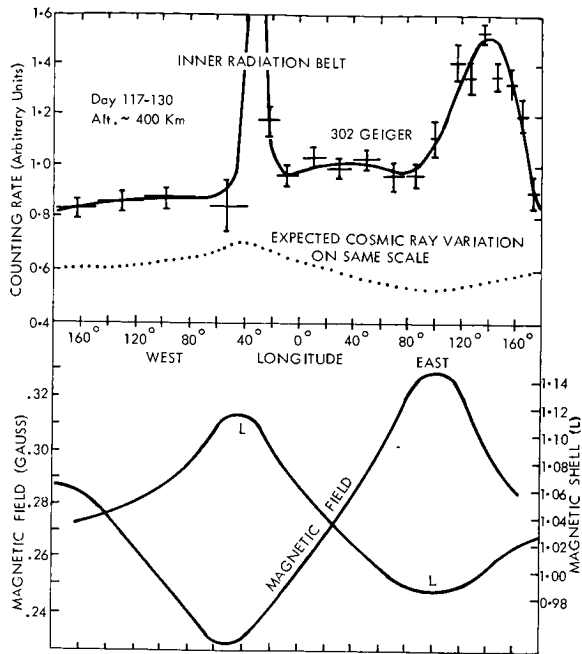


FIGURE 3-10. The G-M count rate close to the magnetic equator or at an altitude of 400 km of longitude. Corresponding values of the McIlwain "L" parameter and the magnetic field strength are also shown epoch being Day 117 to Day 130, 1962.

responding horizontal magnetic field strength and *L*-value.

Similar counting-rate data are shown in figure 3-11 for two altitudes at later times. At an altitude of 800 km the high count-rate due to the radiation belt is, of course, encountered over a much greater range of longitudes, as would be expected. The data for 400 km altitude in this figure, although taken some two months later, show an increase in count-rate in the region of 130°E similar to that shown in figure 3-10. It will be observed that in each case the rate at 400 km altitude is greater than that at 800 km in this region. Figure 3-12 shows a vertical profile of the counting rate in the region of peak intensity. In this figure it can be seen that the counting-rate at first decreases with increasing altitude and then, after passing through a minimum, starts to rise as the satellite enters the lower reaches of the radiation belt.

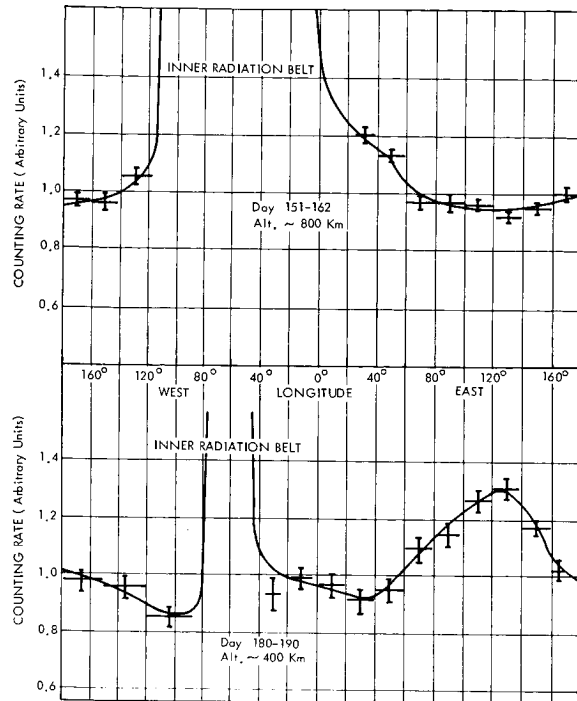


FIGURE 3-11. The G-M count rate close to the magnetic equator at altitudes of 800 km and 400 km plotted as a function of longitude. Epochs are Day 151 to Day 162 and Day 180 to Day 190, 1962 respectively.

The reason for the enhanced counting rate at low altitude has not been established. In view of the minimum that exists between the region of high counting rate and the lower edge of the radiation belt, it seems unlikely that it can be due to loss of particles from the radiation belt into the atmosphere. It may be due to a peculiar distribution of the cosmic ray proton albedo or to induced radioactivity in the satellite resulting from irradiation by protons of the inner radiation belt. Further work is being done to settle this question.

MEASUREMENT OF THE X-RAY EMISSION FROM THE SUN IN THE 3 TO 12 Å BAND

Project Scientists

Dr. R. L. F. Boyd, University College London
 Dr. K. A. Pounds, University of Leicester
 Dr. A. P. Willmore, University College London

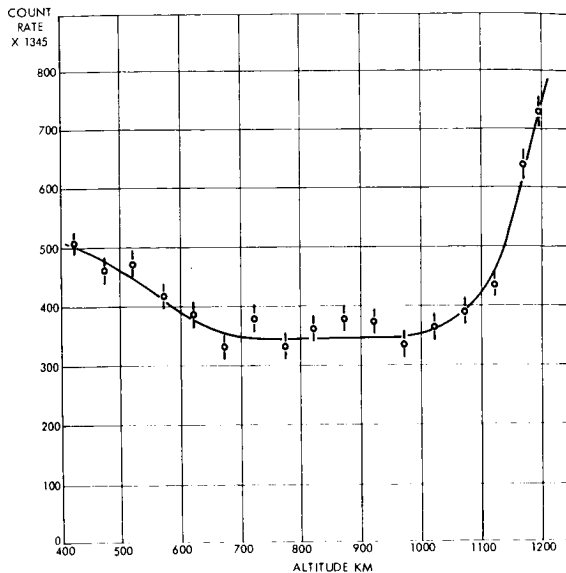


FIGURE 3-12. The G-M count rate plotted as a function of altitude over the region of abnormally high intensity bounded by 0° and 20°N latitude and 100° and 130°E longitude. The estimate gives the number of counts recorded per 1345 seconds.

Project Engineers

Mr. J. Ackroyd, Bristol Aircraft Company
 Dr. P. J. Bowen, University College London
 Mr. P. Walker, Bristol Aircraft Company

The Experiment

The wavelength region selected for this observation was 3 to 12A, in which the solar emission is highly variable and is a sensitive indication of solar conditions. The circuits were designed, for this reason, to have a wide dynamic range. The radiation detectors were proportional counters, filled with argon and methane as a quenching gas, and using 25μ beryllium windows, which have a high quantum efficiency in the 3 to 12A region. Each counter had three windows, each 0.5 millimeter in diameter. The windows were spaced at 30 degree intervals around the circumference, giving the counter a field of view of 90 degrees in the plane normal to its axis, without the radiation angle of incidence exceeding 15 degrees. This condition of nearly normal incidence was necessary because, near the cutoff at 13A, the transmission

of the window varies rapidly with angle of incidence. Two such counters were used, with matched characteristics, mounted at "latitudes" (reckoned as though the spin axis of the satellite were comparable with that of the earth) of ± 45 degrees, so that the whole sky is covered once in each revolution. Each counter is fitted with a mask that restricts the field of view in the longitudinal direction, so that the two counters together have a field of view which is a sector of 30-degree included angle.

A block diagram of the circuit configuration is shown in Figure 3-13. The counter is supplied from an extra high tension (EHT) generator, which was a dc-to-dc converter operating from -6.5 volts and producing 1600 volts; this was stabilized by a corona discharge tube. The counter pulses were fed by a gain-stabilized linear amplifier to a discriminator with a variable bias level. The discriminator output passed through a gate to a 15-stage binary counter capable of counting equally spaced pulses at a one megacycle rate.

The gate circuit is operated by a one-second pulse from the high-speed encoder, so timed that the scaler read-out always occurred in the "off" period of the gate. Closing the gate also operated a staircase generator, which produced a waveform of five equal steps used to obtain the discriminator bias level. Thus, the discriminator automatically moved on at the end of each counting period to the next wavelength interval, until the range from 3 to 12A has been covered in five steps of equal quantum energy interval, after which the process was repeated.

In general, the sun was in the field of view for a time rather shorter than one second, so that the effective counting time was less than one second. The actual time was determined from the spin rate measurement. Moreover, there is only a 1:12 chance that the sun will be in the field of view in any given gate period. Thus, the counters not only observed the sun but also the background radiation from the rest of the sky. On the average, 5×12 —or 60—telemeter periods of 5.12 seconds were required to obtain a complete solar spectrum.

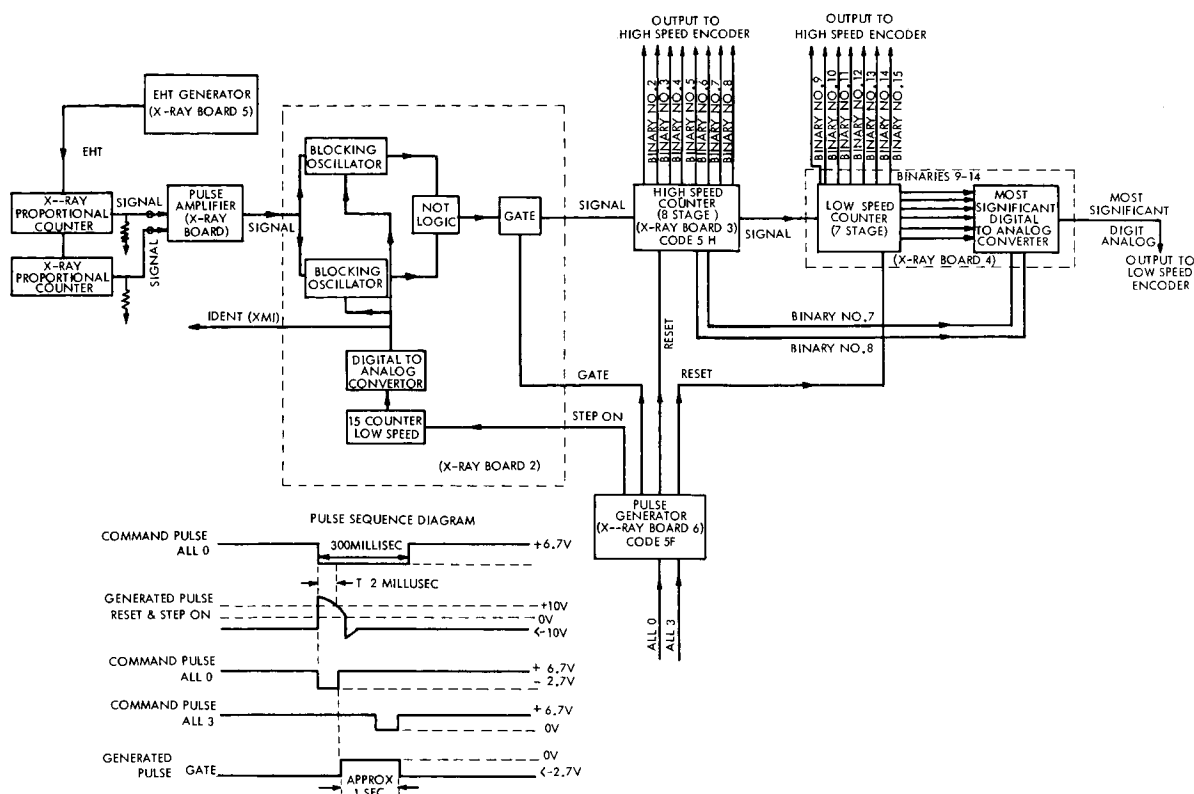


FIGURE 3-13. X-ray spectrometer functional block diagram.

The high-speed encoder was used to sample the binary outputs of all 15 scalars. For the low-speed encoder the necessary information capacity was not available, so the outputs of the central eight scalars were combined to provide an analog voltage representing the logarithm of the stored count to base two, to one significant digit only, within the range covered by the scalars. In addition, the discriminator bias level and an EHT monitor were also terminated with the monitor on the high-speed encoder only.

Experiment Results

Reduction of the high-speed data recorded during the first satellite pass over the Blossom Point Minitrack station showed that the spectrometer was operating correctly in orbit. It continued to function thereafter until 1 November, 1962. Subsequent detailed analysis revealed a small calibration shift in the spectrometer, becoming apparent after 6 May. This shift, which was due to a de-

crease in signal amplification, resulted in movement of the wavelength band, initially 4-14A, toward shorter wavelengths. In principle the flight data can be corrected for this shift, but this has not been done beyond the interval 6-12 May, since, though the wavelength change involved is small, the movement toward a region of lower detector sensitivity, together with the rapid fall of incident flux to shorter wavelengths, result in generally low counting rates. The presence of a fluctuating 'noise' count generated by geomagnetically trapped particles makes evaluation of such data extremely uncertain. The available X-ray data therefore are from the period 26 April to 12 May, 1962, with an average of about four daylight hours of data per day.

The minimum detectable X-ray flux was set by the background counting rate in orbit. This was found to vary between 1 and 1.5 counts per spectrometer channel per second outside the radiation belts, giving X-ray flux

limits of $3 \cdot 10^{-4}$ erg cm^{-2} sec^{-1} below 14A and 10^{-5} erg cm^{-2} sec^{-1} for less than 8A. The solar flux soon after launch was determined to be an order of magnitude above the detection limit. Thereafter it fell by a factor of 5 to the 6th of May and then rose again towards the 12th of May, in general correlation with the plage, coronal green line and 2800 Mc radio flux indices. This is discussed more fully in Reference (11) [See also (12) and (13)], where it is concluded that the major X-ray emission below 20A is derived from local dense regions in the corona. It has also been suggested [(11) and (12)] that these 'condensations' contributing to the short wavelength emission are probably hotter as well, though not all authors agree with this (14).

The marked changes in the solar flux observed concurrently with flares provide the most interesting part of the Ariel I data. The McMath working list of flares for 1962 (15) shows a total of 24 flares and four subflares in the period 26 April to 6 May. X-ray records were obtained from Ariel I during 12 flares and in all but one a significant enhancement in the 4-14A emission was observed. The exception was the importance one flare of 1 May commencing at 1150 U. T.

Neither noise increase nor ionospheric effects have been reported for this flare. The X-ray record extends from 1153 to 1202 U. T., covering the reported Ha maximum at 1159 U. T. The absence of records from sixteen flares in this period results from the satellite being in the Earth's shadow, from radiation belt interference and from periods of no satellite contact with a ground telemetry station.

Detailed study of the X-ray flux changes associated with the 11 observed flares reveal a rather complex pattern. In general the flare X-radiation is 'harder' than the normal spectrum but the degree of enhancement profiles of individual flares vary from those with a gradual and long-enduring increase, measurable over the full period of the flare (See figure 3-14.) to others in which the main X-ray increase occurs as a rapid 'burst' near the flash phase of the flare (See figure 3-15.) In general both the enduring and burst-type enhancements are probably super-imposed in a typical X-ray profile. (See figure 3-16.) In all the cases observed from Ariel I the detailed temporal agreement with the flare microwave increase was remarkable. It has been suggested (reference 16) that with flares such as those of figures 3-15 and 3-16 the long

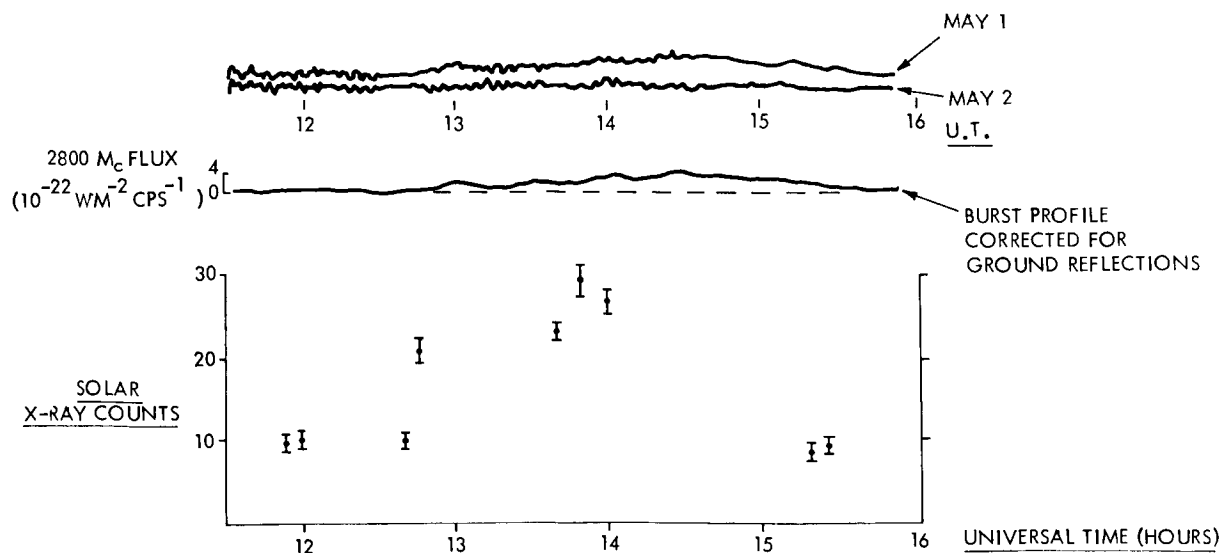


FIGURE 3-14. Solar flare enhancement of 12A X-rays and 2800 Mc flux, importance 1 flare of May 1, 1962 (1241-1252-1400D) and also importance 1 flare (1353-1356-1430D).

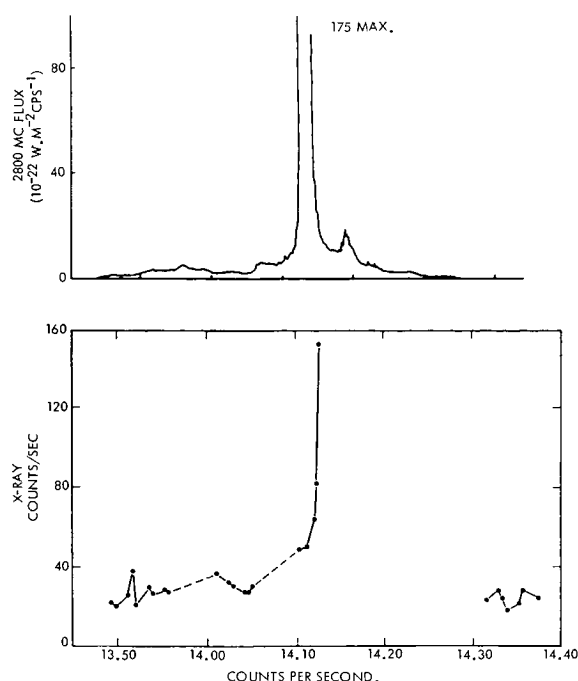


FIGURE 3-15. Solar flare enhancement of X-rays and 2800 Mc flux, importance 2 flare of April 27, 1962 (1346-1413-1440).

enduring components of both microwave and X-ray increases are of thermal nature while the rapid 'bursts' are respectively the synchrotron and impact bremsstrahlung emission from jets of high energy electrons produced in the flash phase of the flare.

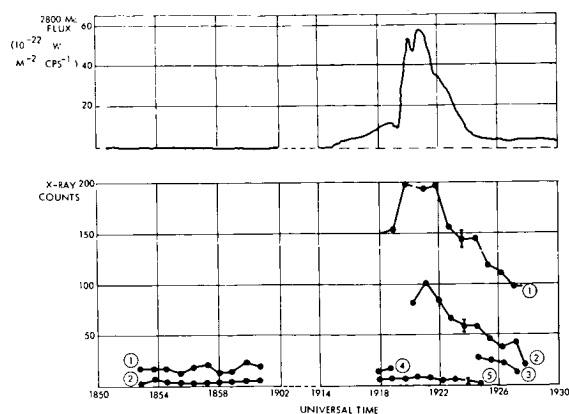


FIGURE 3-16. Solar flare enhancement of X-rays and 2800 Mc flux, importance 1 flare of May 1, 1962 (1915-1924-1940D).

The spectral development of the flare X-radiation lends support to the concept of a dual-mechanism for the X-ray production. For example, the near constant spectral shape observed during the development of the X-ray burst of the 27 April flare (figure 3-15) is contrasted with the gradual hardening observed during the development of a small enduring X-ray increase of a later flare on the same day.

A definitive explanation of flare X-rays probably must await the high resolution spectral studies of individual solar regions, and these should be possible in 3 or 4 years using the stabilized vehicles such as OSO and Advanced OSO. However, it is evident that considerable progress can be made with further development of proven techniques of the Ariel I counter spectrometer type. In this respect the nature of the data from Ariel I has highlighted the desirable improvements in a future experiment and has proved most valuable in development of the sophisticated counter spectrometer being built for OSO-D. Thus:

- (a) The time resolution of 52 seconds in Ariel I, not quite adequate to follow precisely the rapid spectral changes during certain flares, has been improved to 16 seconds.
- (b) The wavelength band covered has been increased from 4-14A to 1.2-70A with resolution into 26 wavelength intervals, thereby providing more complete information for study of the variable solar emission and of its influence on the ionosphere.
- (c) The photon sensitivity for the region below 10A has been increased to allow accurate reading of the weak non-flare emission at those wavelengths.
- (d) A further improvement, made possible by the command system on OSO, provides for in-flight calibration of each individual wavelength interval in the spectrometer.

In conclusion it can be stated that the Ariel I X-ray experiment was a success despite its relatively brief working life. The

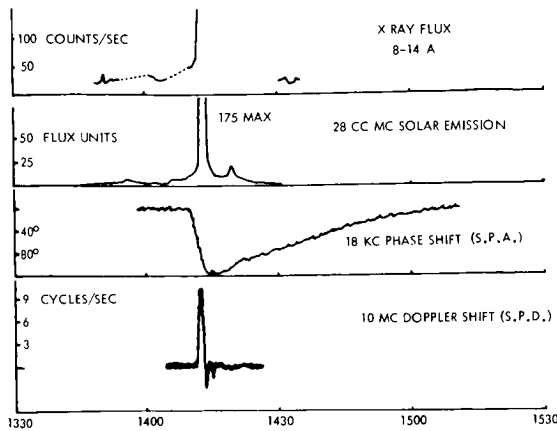


FIGURE 3-17. Events associated with Class 2 flare of April 27, 1962.

most important single result is considered to be the detailed correlation of X-ray and microwave enhancements during solar flares, with the indication thereby of the complex nature of the emission. For the near future it seems that the high sensitivity of such non-

dispersive instruments will provide frequency of spectral scanning and absolute photometry that together will be an ideal complement of the high wavelength resolution crystal and grating spectrometers. The comparison between the flare radiations and two ionospheric indices shown in figure 3-17 illustrate the further power of the low resolution spectrometer for detailed study of the relaxation times and hence the governing electron production and loss processes in the lower ionosphere.

LANGMUIR PROBE FOR MEASUREMENT OF ELECTRON TEMPERATURE AND DENSITY

Project Scientists

Dr. R. L. F. Boyd, University College London
Dr. A. P. Willmore, University College London

Project Engineers

Dr. P. J. Bowen, University College London
Mr. J. Blades, Pye Ltd., Cambridge
Mr. R. Nettalship, Pye Ltd., Cambridge

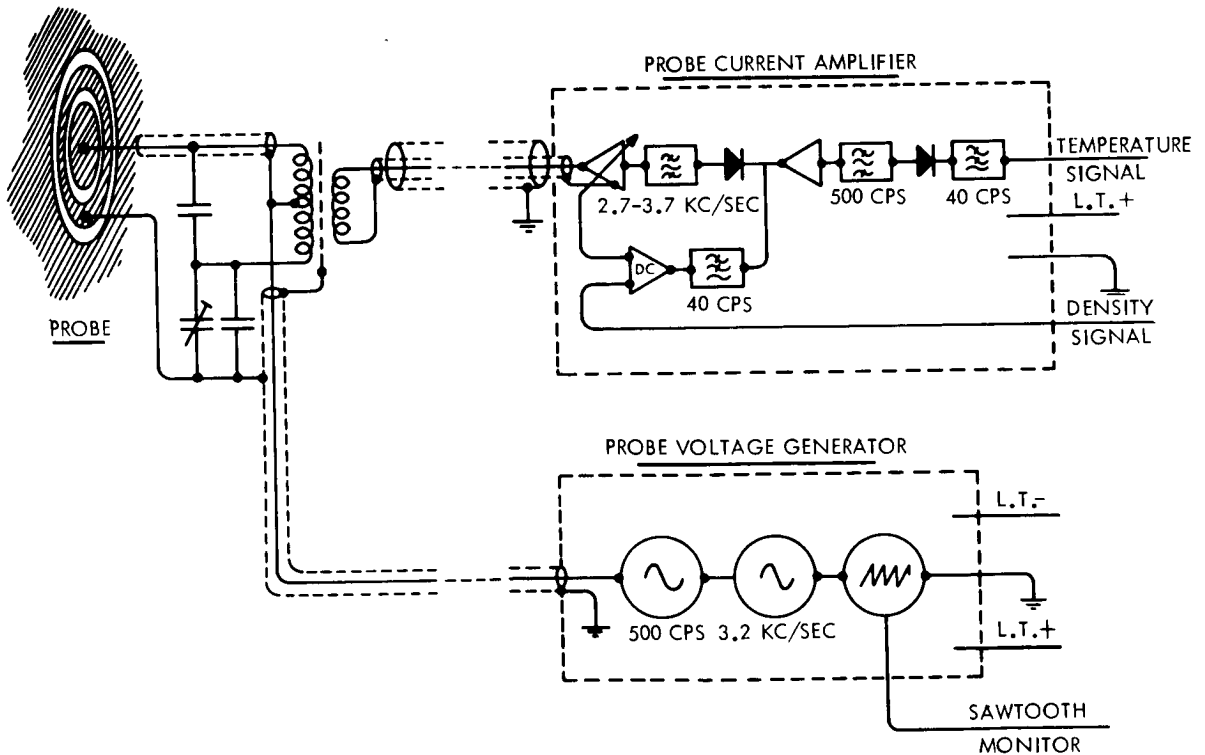


FIGURE 3-18. Electron density and temperature probe, block diagram.

Data Processing Programs

Dr. W. J. Raitt, University College London
Mrs. C. Abbs, University College London

Data Analysis

Mr. C. L. Henderson, University College
London
Mr. U. Samir, University College London
Dr. A. P. Willmore, University College London

The Experiment

This experiment, based on Druyvesteyn's modification of the Langmuir probe, determined the local value of the electron density and temperature near the satellite. Two separate probes were installed in the spacecraft, one nearly flush with the skin and mounted inside the attachment ring to the launching rocket, the other on a boom 1.2m in length. In this way it had been hoped that the charge distribution about the spacecraft could be studied and the validity of the measurements of electron density assured. The results of this investigation are described in Part II of this section.

A block diagram of the circuit is shown in figure 3-18. The probe is a small disk, 2 centimeters in diameter, surrounded by a guard ring. This has the dual purpose of reducing edge effects arising from the fact that the satellite skin is not at probe potential and of reducing the stray capacitance from the probe to ground. The tuned input transformer of the amplifier is mounted behind the probe. The waveform generators and amplifiers are mounted on a 5½-inch card in the interior of the vehicle.

Since the probe was negative with respect to its local ambient atmosphere (potential of which, relative to the vehicle, will be called "space potential"), the density of the electrons was obtained by Boltzmann's relation as:

$$n_c = n_{co} e^{-\frac{eV_p}{kT_e}},$$

where n_{co} is the density for from the vehicle, V_p is the magnitude of the probe potential with respect to space, and T_e is the electron temperature.

Thus, the current collected by the probe is:

$$i_p = i_o e^{-\frac{eV_p}{kT_e}},$$

where $i_o = (2nk/m) T_e n_{co} A$ (A being the probe area).

In order to measure T_e and i_o , from which n_{co} can also be calculated, a composite sweep wave form consisting of (1) a slow sawtooth wave, (2) a 500-cps sine wave whose amplitude is about kT_e/e , and (3) a 3.5-kc sine wave also of amplitude kT_e/e were applied to the probe.

A detailed description of experiment instrumentation is given in NASA report SP-43 (17), and since the experiment functioned exactly as anticipated, no further description is given here.

Computer programs for the reduction of the raw digitized measurements to values of the required ionospheric parameters were written at University College under the supervision of Dr. W. J. Raitt, and large scale data processing operations carried out partly by the S.R.M.U. and partly by Dr. Raitt enabled virtually all the measurements telemetered to the ground, until the cessation of the observations near the end of 1964, to be reduced.

The remainder of this section is divided into two major parts. Part I relates the results of electron temperature and density measurements. One of the conclusions of this work was that the temperature and density measurements by the boom probe suffered little or no disturbance due to the vehicle motion; therefore, Part I is devoted to a discussion of the measurements made by the boom probe. Part II is a discussion of wake effects based on data from the ion probe as well as this experiment.

Part I

Electron Temperature and Density Measurements

The measurements obtained fell into two groups. The first of these was obtained from data stored in the spacecraft tape recorder. This provided a large volume of measurements with an excellent geographical coverage during the period April-July, 1962,

but after this, the intermittent operation of the spacecraft and later the failure of the low speed data system first reduced the flow of measurements and finally brought it to a close. In the period April 27th–July 9th, nearly 51,000 measurements were received from the boom probe, and all the ionospheric studies carried out up to the time of writing (February, 1965) have been based on these.

The second group of measurements was obtained via the high speed telemetry link and therefore was restricted in geographical coverage to the areas surrounding the STADAN stations of NASA and the stations operated by the D.S.I.R. However, the poor geographical coverage was offset by the long period—over $2\frac{1}{2}$ years—covered by the observations. It is planned to use these data for the study of seasonal variations of electron temperature.

Electron Temperature Studies Prior to Ariel I

Observational evidence of the behavior of electron temperature above the altitude of the F_2 maximum was rather scanty. Some important Langmuir probe measurements were made in 1960 by Bordeau and his co-workers (1964) (18) on Explorer VIII; further evidence was obtained through radar back-scatter observations by Bowles et al (1962) (19) and others (Evans, 1962) (20). The greatest amount of data came from studies of the vertical distribution of the ionosphere, the density scale height of which (under certain circumstances) yields the mean of the ion and electron temperatures. For the electron temperature to be deduced it is at least necessary that the ionization be in diffusive equilibrium and, although departures from this condition may become less likely at greater altitudes, it is still not known above what altitude the condition obtains with reasonable accuracy. Moreover, accurate knowledge of the ion composition and temperature is also required, though little information on these was actually available.

The theoretical situation had been investigated by Hanson (1963) (21) and by Delgarne and his co-workers (1963) (22). Hanson suggested that the production of

relatively energetic photo-electrons by sunlight would raise the electron temperature above the gas temperature, since the photo-electron energy would become randomized by electron-electron collisions. The relatively high temperature electron gas would then, by collisions with the heavier particles, communicate the photo-electron energy to the neutral gas so that it finally would be conducted downward to lower altitudes. Hanson predicted that this effect would be most evident in the F_1 region near the level of maximum photo-ionization, where the elevation of the temperature of the electrons above that of the gas might well amount to 1000°K , but that at greater altitudes the electron temperature should fall to the gas temperature as the energy input by photo-ionization became negligible.

The available observations seemed to support this view, as was shown in the review by Bordeau (1963) (23). It followed then that in the altitude region covered by the Ariel I measurements, the electron and gas temperatures should be essentially equal both by day and by night, and the electron temperature should not depend either on latitude or altitude.

The Main Features of the Electron Temperature Distribution

The first analyses of the measurements showed this picture to be incorrect since a strong increase of temperature with latitude was evident, both by day and by night. It is known that a similar behavior is not exhibited by the gas temperature [See, e.g., Groves (1961) (24).] Thus, the electron temperature could not in general be the same as the gas temperature indicating that a heat source was present at altitudes from 400 km to 1200 km both by day and by night. Since this appeared to be more effective at high latitudes, it was at first supposed that particles, presumably electrons, were responsible, a suggestion that was later found to be at least partially incorrect.

Although latitude, altitude and solar time vary simultaneously about one orbit, by using measurements obtained over a time compar-

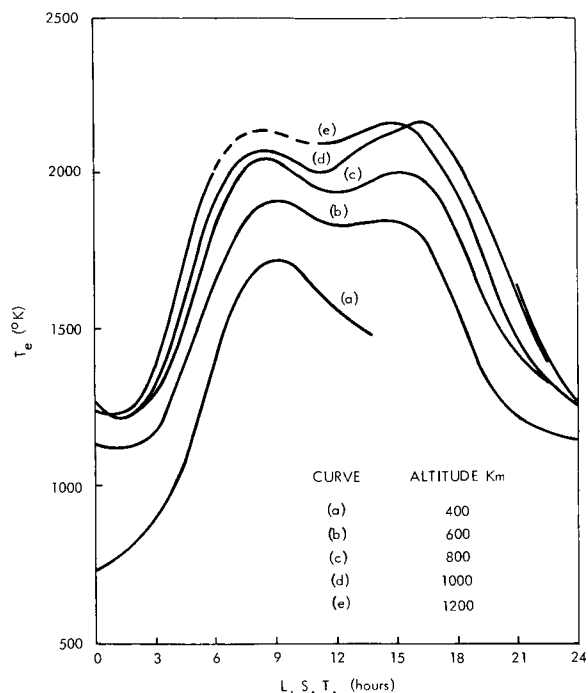


FIGURE 3-19. Diurnal variation of electron temperature at a geomagnetic latitude of 40° at various altitudes.

able with the precession period of the orbit (74 days) or the rotation period of the major

axis (147 days) the variations corresponding to individual variations of these three parameters could be studied. A statistical method was devised for this purpose and applied to the measurements. This confirmed the existence of a latitude increase of temperature and showed also that the temperature increased with increasing altitude; the diurnal, latitude and altitude variations of temperature are shown in figures 3-19, 3-20 and 3-21. Furthermore, it was found that the electron temperature distribution could better be described as a function of geomagnetic than of geographic latitude.

Ionospheric Heating

Since it appeared that the photo-ionization process did not adequately account for the electron temperature distribution, the energy input into the ionosphere required to account for the observed electron temperature was next calculated. The energy exchange rates between the various groups of particles, together with some important relaxation times, had been calculated by Dalgarno, Moffatt and McElroy (1963) (23). They showed that above 400 km the photo-electrons would first randomize their energy. Then the electron gas

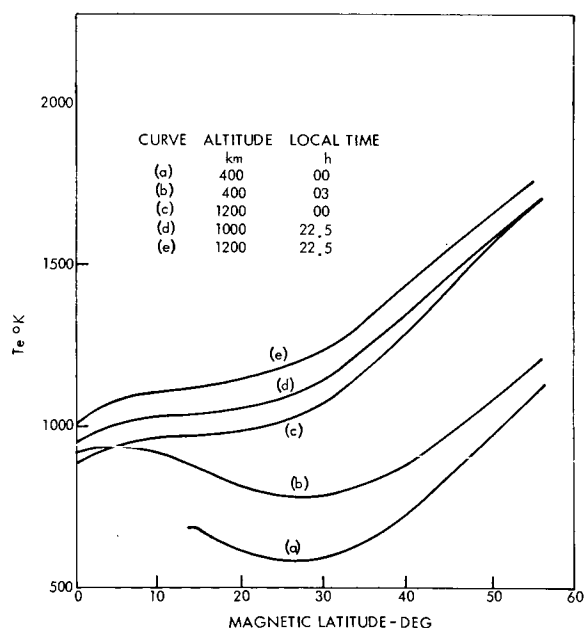
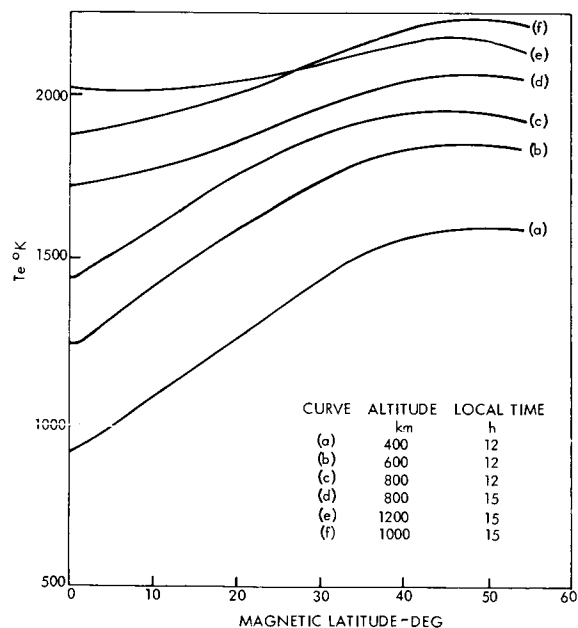


FIGURE 3-20. Variation of electron temperature with geomagnetic latitude near noon and midnight. The curves are for various altitudes and local times.

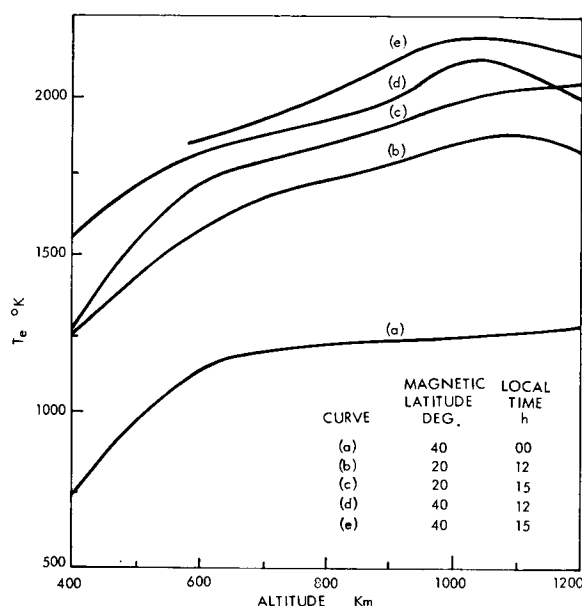


FIGURE 3-21. Altitude variation of electron temperature.

would lose most of this energy by collisions with positive ions, raising the ion temperature, and finally the ions would pass the energy on to the neutral gas. With a suitable model of atmospheric density and composition (Harris and Priester, 1962) (25), the energy required to support a measured electron temperature at a measured electron density can be calculated, and its variation with position, altitude and local time studied. This was done both for the day and for the night hours.

Heat Input in the Daytime. The variation of energy input with altitude near mid-day and near the equator is shown in figure 3-22. It will be seen that at about 600 km, there is an abrupt change in the vertical gradient, suggesting that two processes are occurring. Below 600 km, the energy input Q falls with a scale height close to that of atomic oxygen, thus suggesting that photo-ionization of oxygen is the energy source. Moreover, the latitude variation at 500 km shown in figure 3-23 is consistent with solar radiation as the origin of the energy. The actual magnitude of Q at 400 km altitude and the sub-solar point, about 100 eV/cc sec, is several times

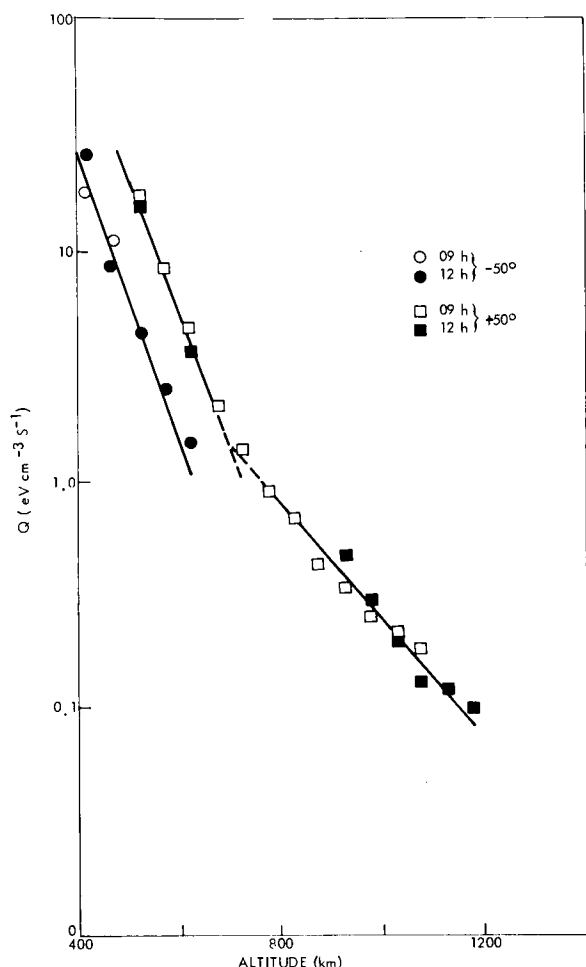


FIGURE 3-22. Variation of Q with altitude near latitudes 50° N and S.

less than was calculated by Dalgarno et al. However, Hanson pointed out that the photo-ionization process will become less efficient above 300 km, since many of those photo-

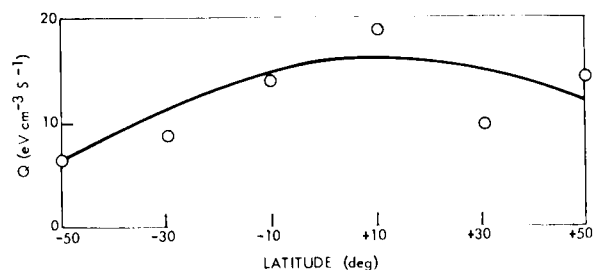


FIGURE 3-23. Variation of heat input near noon with latitude, at 500 km altitude.

electrons which initially are moving upwards will have a large range in this direction and so will go spiralling along the magnetic field lines.

It is then natural to suggest that it is these photo-electrons which, by Coulomb collisions with the ambient electrons, are responsible for the energy input above 600 km. An approximate calculation shows that they will in fact deposit the correct amount of energy at high altitudes in this way. Thus, we can account for all the major features of the daytime electron temperature distribution in terms of the photo-ionization process, and we may note the following points.

1. Since positive ion collisions become increasingly less efficient at removing the photo-ionization energy at great heights, we may expect thermal conduction of energy in a downward direction in the electron gas to become important. In fact, it appears to be significant at least by 600 km, and probably determines the temperature increase with altitude above this level.

2. The temperature increase with latitude is not due to an increase in heat input (figure 3-23) but to the fall in electron density which reduces the rate of energy loss by positive ion collisions; the geomagnetic control of temperature is similarly due to the variation of electron density.

Heat Input at Night. The lack of thermal equilibrium at night shows that an additional heat source, amounting to 0.1 eV/cc sec at 800 km must also be operative. Presumably its diurnal variation is small enough to leave photo-ionization as the main daytime source. The source of the night time heat is not yet known; it is supposed that it arises either from electric fields or from particles and so is of magnetospheric origin in either case. If particles are responsible they must be of low energy, and some similarities of the geographical distribution of the heat source with that of low energy electrons observed in Sputnik III by Savenko, Shavrin and Pisavenko (1963) (26) suggest that electrons of 1-2 keV energy might be involved.

Detailed Geographical Variation of Electron Density and Temperature

One powerful method of studying the longitudinal variations of the ionosphere is to compare measurements made at a given latitude on successive orbits, since to a good approximation the longitude is the only parameter to change. Figure 3-24 shows results obtained in this way for electron density in two magnetically very quiet periods. It will be seen that even at these times strong density irregularities exist, and that these irregularities are different in the two periods. It is possible that some of the change is due to the variation of local time between the two sets of measurements, but likely that changes of magnetospheric structure are also effective.

Similar variations of temperature with position are shown in figure 3-25. In this case, the effect of local time can be studied by the statistical method used. It is found that in addition to the patterns characteristic of noon and midnight, another occurs near dawn which will be further discussed below. In every case, the variations of temperature are closely correlated with those of density shown in figure 3-24 in such a way that the regions of high density are also those of low temperature. Thus, these variations are indicative of the powerful control of the ion-electron collision rate over the electron temperature, since in the regions of high density the cooling rate of the electron gas is also high.

The behavior of electron temperature near dawn is of particular interest. It was first shown by Bordeau and Donley (1964) (27) that the temperature is a maximum at dawn, though it can also be seen from figure 3-26 that this is true only at relatively low altitudes and at near-equatorial latitudes. This confirms the explanation of the effect given by Dalgarno et al, that it arises from a time lag in the vertical re-distribution of ionization at dawn (which is inhibited by the geomagnetic field) relative to that of atomic oxygen, so that the cooling rate temporarily lags the photo-ionization heating rate. It will be noted that the local variations of temperature in the dawn period are centered on the geomagnetic equator, which is consistent with the explanation given.

ARIEL I: THE FIRST INTERNATIONAL SATELLITE

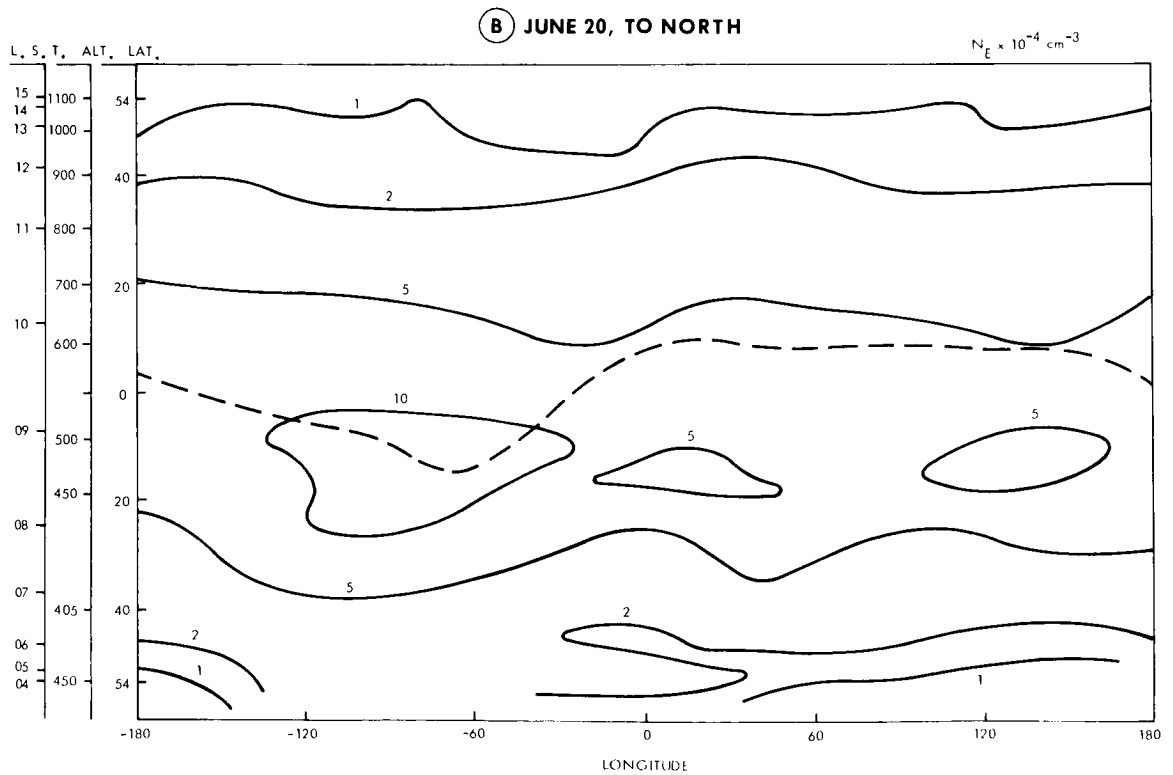
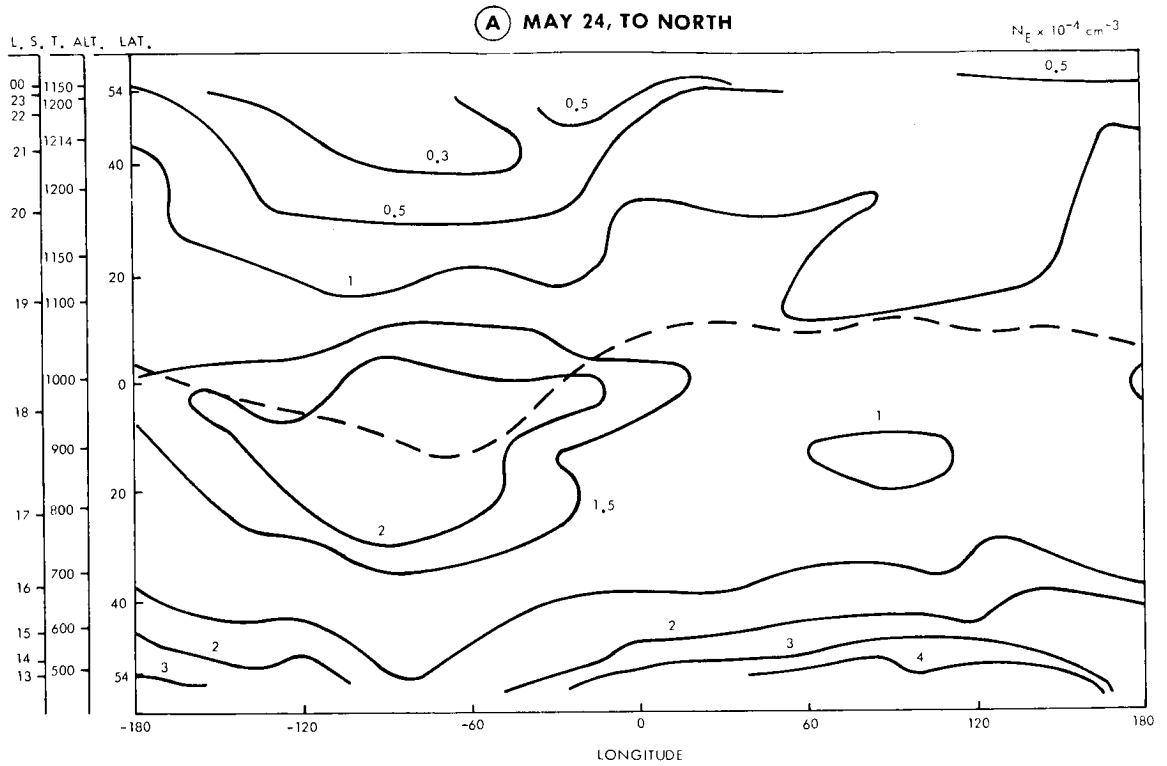
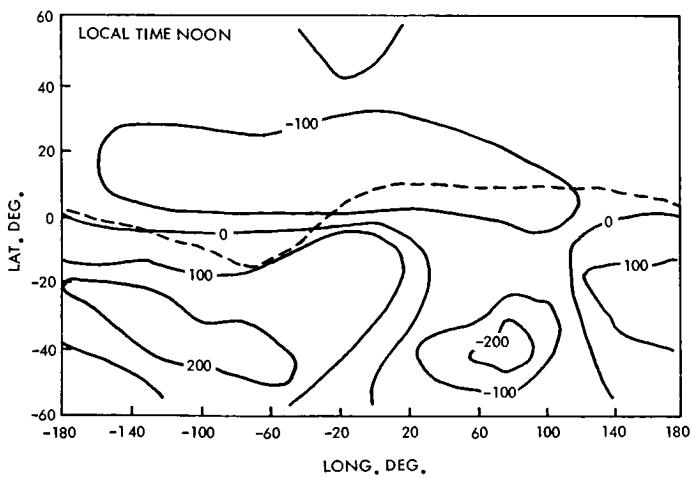
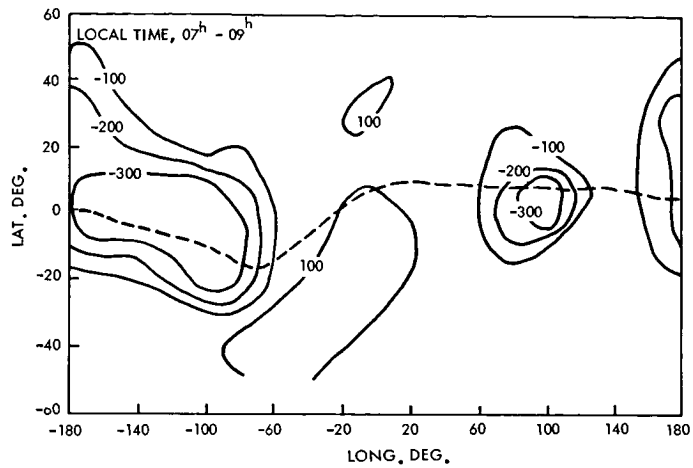


FIGURE 3-24. Contours of electron density for northbound passes.

UNITED KINGDOM EXPERIMENTS

**(A) LOCAL TIME
07-09 HOURS**



**(B) LOCAL TIME
NOON**

**(C) LOCAL TIME
MIDNIGHT**

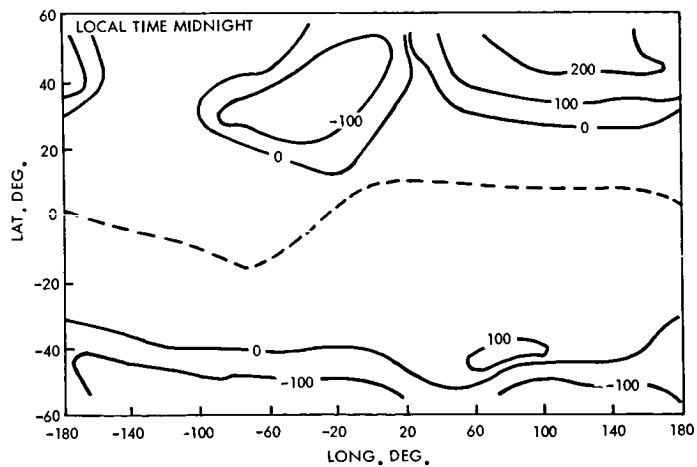


FIGURE 3-25. Variations of temperature with position.

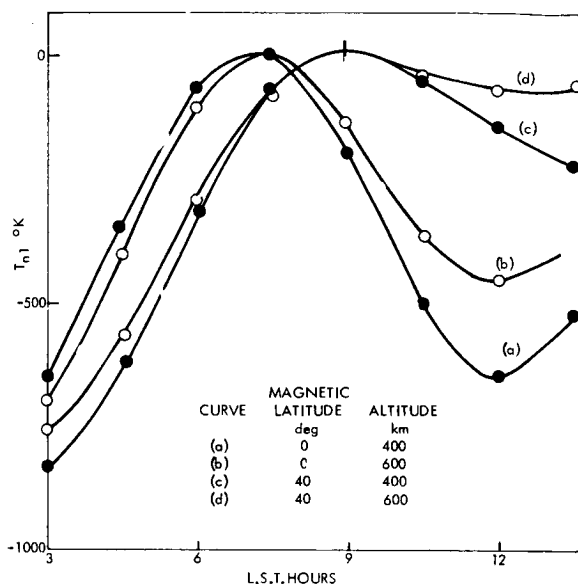


FIGURE 3-26. The variation of electron temperature near dawn, showing the dawn maximum at equatorial latitudes. The temperature variations have all been normalized to the same maximum value for comparison.

Temperature and Density Variations in Magnetic Storms

The effect of magnetic activity has been studied by comparing the temperature and density near a particular location before, during and after several magnetic storms. Typical results are shown in figure 3-27 for the storm of May 27-28, 1962. Points on the satellite track where the density increased during the storm are marked; no significant decreases having been encountered. Points where the temperature fell are also marked; it will be seen that these correlate well with the density changes, although significant temperature changes are sometimes apparently not accompanied by density changes. This is only an effect of instrumental sensitivity, which is higher for the temperature changes. Thus, the storm changes illustrate the importance of collisional cooling (both by day and by night) just as do the geographical variations. In this storm only, temperature increases were observed in an area south of the Brazilian anomaly in the geomagnetic field.

A striking feature of all the storm-time changes is their structure which closely fol-

lows that of the geomagnetic shells which are marked on figure 3-27 particularly the $L=1.2$ shell, which Sayers (1964) (28) showed to be generally enhanced in density during this period. It is evident that the principal change is one of electron density, which then produced a change of electron temperature, since the electron temperature changes in the wrong sense to produce the density change by an alteration in scale height. The density change must occur below the level at which diffusive equilibrium sets in.

Part II Wake-Effects

U. Samir

Electron and ion temperature and densities obtained by Langmuir probes installed on Ariel I have been used to study the disturbances in the plasma due to the motion of a supersonic spacecraft moving through the ionosphere.

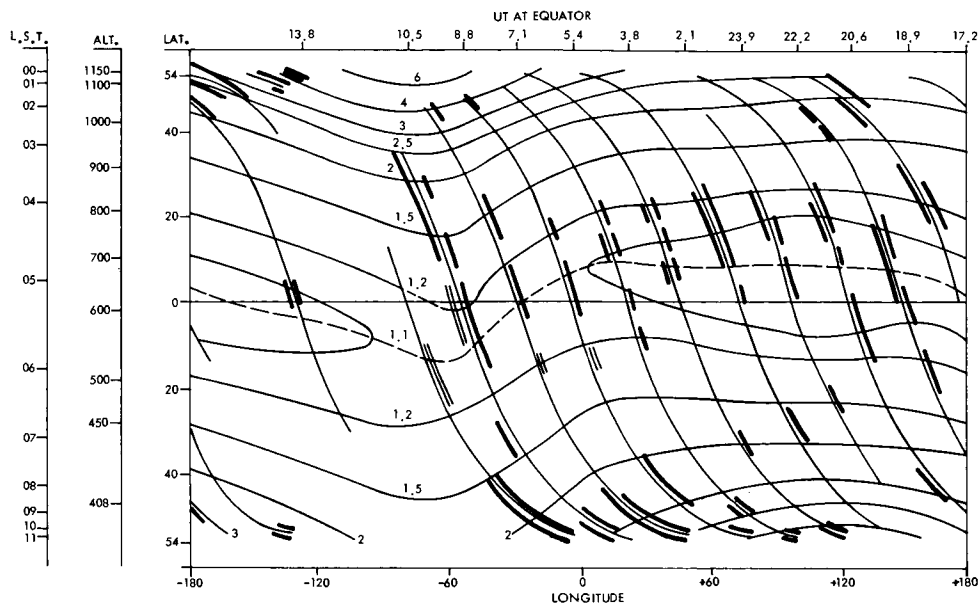
A wake depleted of ions and electrons was observed. Evidence is given for the existence of a kind of "turbulence" in the wake in which strong rapid oscillations occur.

When a body is moving supersonically through the ionosphere, various phenomena occur which are caused by the interaction of the body with the plasma. These phenomena are due to effects on the moving body itself as it acquires an electric charge by the accretion of ions and electrons, and also to effects of the body on the plasma. The motion of the body produces a disturbance in the plasma in the form of a wake whose nature depends on the specific characteristics of the plasma and the excitation of waves around the body and in the wake. Such effects can be detected by direct measurement devices or by indirect radio-propagation studies.

The phenomena involved in the interaction are of interest both for pure science and for engineering. The local disturbances can affect the usefulness of satellite measurements on the ambient plasma by affecting the operation of various types of plasma probes including Langmuir and impedance probes. It is clear, therefore, that the knowledge and understanding of these effects and the phe-

UNITED KINGDOM EXPERIMENTS

(A) ENHANCEMENTS MAY 27



(B) ENHANCEMENTS MAY 27-28

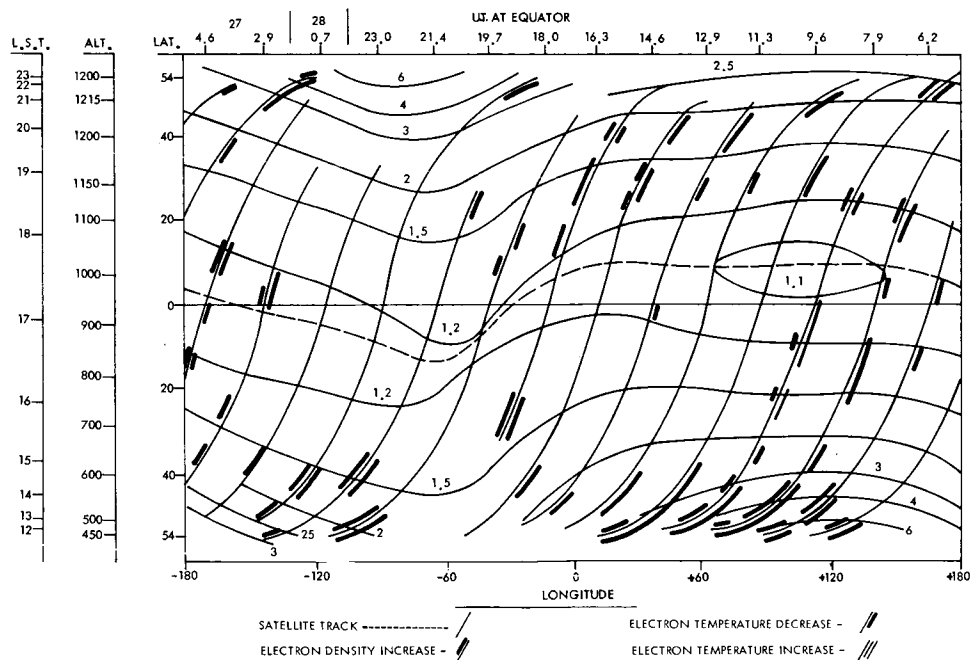


FIGURE 3-27. Variation of electron temperature and density during the magnetic storm of May 27-28th, 1962. The light lines represent the track of the satellite on successive orbits. Whenever a significant increase of electron density was encountered in the storm, a heavy line has been drawn on the left of the track. Where a significant decrease of electron temperature was observed, a heavy line has been drawn on the right of the track. Where a significant increase in temperature occurred, a double line has been drawn on the right of the track. (The electron density data has been taken from Willmore and Henderson, 1965.)

nomena involved are of importance if the results from direct measurement plasma probes are to be interpreted correctly. Moreover, the moving satellite is a kind of model experiment which may contribute to the understanding of the interaction of the planets and their satellites with the solar wind. An attempt was, therefore, made to use the measured ion and electron distribution near the Ariel I satellite in order to examine the effects caused by the body on the plasma (i.e., wake-effects and plasma oscillations).

The Experiment

No special apparatus was provided for the study of wake effects. The study was made from data taken from the electron temperature and density boom and base probes and from the spherical ion mass spectrometer probe. Locations of these probes are shown in figure 1-2. These data correlated with aspect and orbital data made possible the analysis of the effect of the spacecraft on its surrounding plasma. The electron probes (boom and base) were circular discs 2 cm. in diameter. The ion probe was a sphere 9 cm. in diameter surrounded by a concentric spherical grid 10 cm. in diameter whose po-

tential was adjusted to prevent electrons reaching the probe. More detailed descriptions of the experimental technique and the theory are given earlier in this section for the electron probes, and in the succeeding section for the ion probe. [For further details see Bowen et al (29) and G.S.F.C. (17).]

The method of analysis of the probe characteristics was based on that of Druyvesteyn (30) and Boyd and Twiddy (31). Briefly, for the electron probes the method is to deduce electron temperature from the current-voltage characteristics by using the ratio of the second to first derivative ($d^2i/dv^2/di/dv$). Knowing the temperature and current, the electron number density can be obtained. For the ion-probe the method is basically similar.

Results

The disturbance of the electron density was studied by the variation of the ratio of current collected by the base probe to that of the boom probe with angle of attack (angle between the spin axis and the velocity vector). The disturbance of the ion density was deduced in a similar way by using the ion probe and the electron boom probe, assuming that

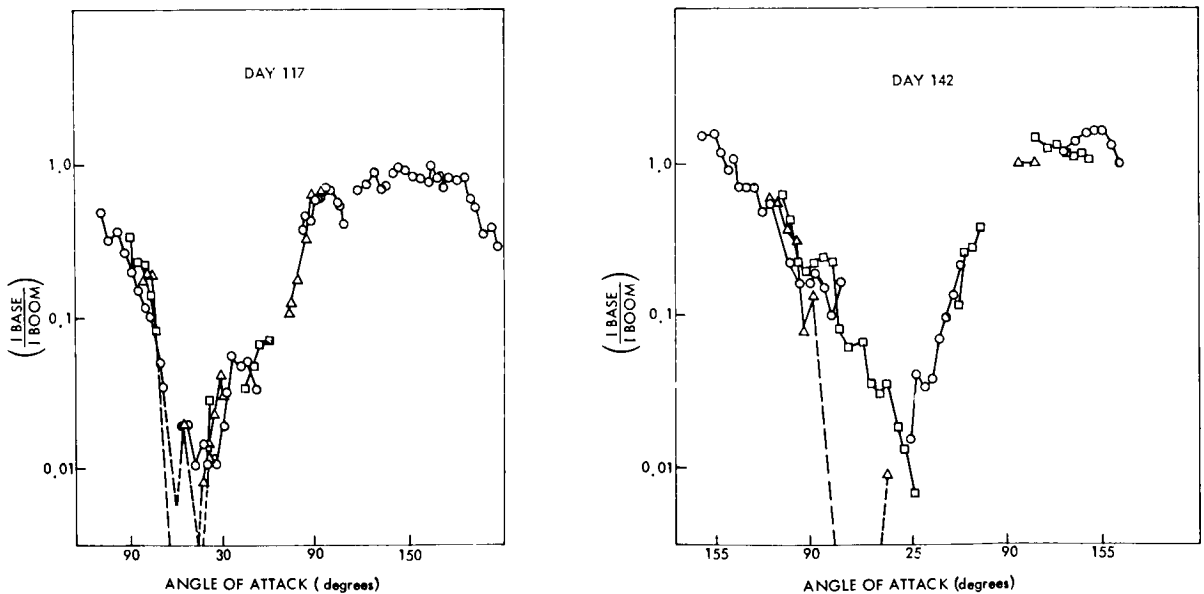


FIGURE 3-28. Electron density vs. angle of attack.

the boom probe, when not in the wake of the satellite, records the undisturbed plasma behavior.

Studying the variations of the current collected by the two electron probes with angle of attack, we found the wake to be depleted of electrons; whereas in front of the body there was no build-up of electrons, at least not within 20% (density changes of more than 20% would certainly have been detected). The data used for this analysis were selected so that the effect could not be accounted to photoemission. Quantitatively it was found that the decrease in electron density in the wake is probably to less than 1% of the ambient density. (See figure 3-28).

Studying the variations of the ratio of ion density to the ambient electron density (as

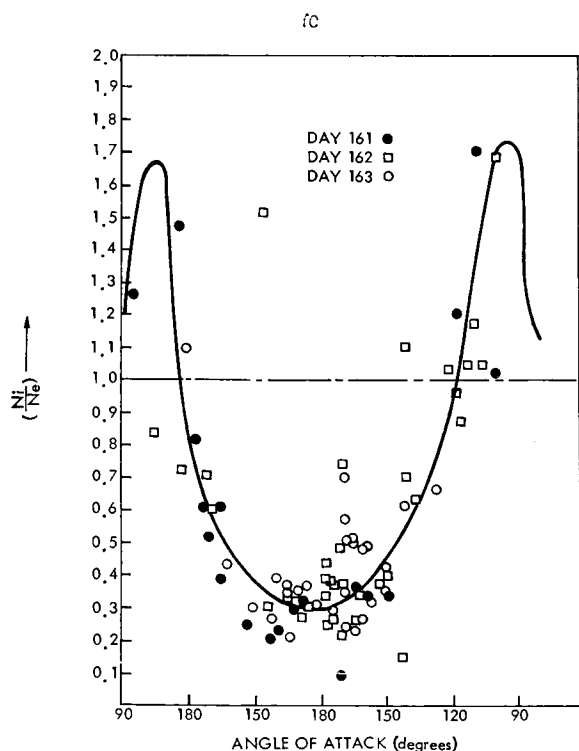


FIGURE 3-29. Plot of $\left(\frac{N_i}{N_e}\right)$ versus angle of attack.

measured by the boom probe), we found that the wake is depleted of ions as well as of electrons, but not to the same extent. (See

figure 3-29). It should be mentioned that while the electron base probe was on the skin of the satellite, the ion probe was a distance from the surface, so that this does not indicate a significant departure from quasi-neutrality in the wake.

An investigation was made of the electron probe characteristics, both boom and base, near the edge of the wake and elsewhere. Special attention was given to the modulation depth of the probe current. From an examination of the boom probe characteristics under a wide variety of conditions, it was found that the energy distribution is Maxwellian within the accuracy of measurement. This result is confirmed by the base probe whenever it is in the forward direction. However, when the base probe is near the edge of the wake, the variation of the modulation depth is quite different. This difference cannot be a result of an instrumental failure, because it was not observed at any other orientation. Examination of this behavior led to the conclusion that strong plasma oscillations at a frequency of about 3 kc/sec occur near the wake.

The applicability of Boltzmann's equation $N = N_0 \exp\left(\frac{-eV}{KT}\right)$ was tested using the difference in space potential at the probes (S_0) and the electron temperature (from the boom probe). It was found that the slope of the straight line disagrees by a factor of about 2.5 with the theoretical one. This could indicate the presence of very high frequency disturbance so that Boltzmann's equation is invalid, or the presence of lower frequency disturbances of large amplitude; so that although the instantaneous values of density and potential satisfy the relation, their time averaged values (which were measured) do not. The observations of the preceding paragraph suggest the latter conclusion.

Discussion

Present State of Theoretical Work. The majority of theoretical papers published on this subject have used methods of linearization as well as particle treatment (32, 33, 34) that were applied to both continuous and

rarefied plasmas. Some authors used the numerical approach which is not restricted to small objects and takes account of the influence of the electric field of the body on the motion of the ions. However, various simplifying assumptions which are made cast doubt on their direct applicability to the motion of a spacecraft in the ionosphere. It seems to us that the most applicable treatment is that by Al'pert et al (35). In that work the density distribution for both charged and neutral particles ahead and in the rear, as well as the potential distribution around spheres with reflecting and absorbing surfaces were calculated. A rarefied plasma (where the condition $\Lambda \gg R_0 \gg \lambda_D$ is satisfied, Λ being the m.f.p., R_0 —the radius of the sphere and λ_D —the Debye length) was assumed and the velocity of the sphere (V_s) satisfies the condition $V_T^{(e)} \gg V_s \gg V_T^{(i)}$ ($V_T^{(e)}$ and $V_T^{(i)}$ being the thermal velocities of the electrons and ions respectively). The effect of the earth's magnetic field was considered, although the effect of the electric field of the body on the ions was neglected. A wake depleted of both ions and electrons was found to exist in the rear hemisphere of the body and quantitative expressions were given for the charged particle density to be expected in the wake. The magnetic field was found to be insignificant in the close vicinity of the body, but significant at further distances. The very important problem of the excitation of waves was not considered, although its importance was emphasized. Several other theoretical papers discussed this problem, but no adequate theory is yet available nor has the effect of this process on the wake been generally considered.

Comparison With Our Measurements. Our results show that a wake depleted of ions and electrons exists behind the satellite, while the density in front of the satellite is within 20% of the ambient value. These results agree quantitatively with the theoretical predictions of 35 and 6.

We found that the minimum electron current to the probe when in the wake to be about 10^{-2} its ambient value. Al'pert et al (35) obtains an expression which under the

conditions of our experiment was about 8×10^{-4} . In this respect we find a discrepancy with the calculation. It is worth noting that in a Black-Knight rocket flight (37) we obtained results similar to those obtained by Ariel I.

Combining our result about the inapplicability of the Boltzmann equation in the wake with the fluctuations in the wake as obtained by the probe characteristic investigation, it is clear that the potential in the plasma is fluctuating, and the mean potential and density are no longer related by the Boltzmann equation. It is also possible that the fact that the wake density does not fall to the low values anticipated theoretically arises from the same cause. For even if the steady components of the electric field are insufficient to deflect the ions into the wake, it is possible that the fluctuating fields might be considerably stronger. Taking in account the satellite velocity and the length scale, frequencies of about 3 kc/sec. are low enough for the field to be effective.

Since we have been concerned with a plasma whose charged particles density is $(10^4-10^5)/\text{cm}^3$ the ion plasma frequency will be in the range (5–15 kc/sec). We therefore conclude that our observations show the existence of strong ion plasma oscillations in the wake.

SPHERICAL PROBE FOR MEASUREMENT OF ION MASS COMPOSITION AND TEMPERATURE

Project Scientists

Dr. R. L. F. Boyd, University College London
Dr. A. P. Willmore, University College London

Data Analysis

Dr. R. L. F. Boyd, University College London
Dr. W. J. Raitt, University College London
Miss Susan Laflin, University College London

Project Engineers

Dr. P. J. Bowen, University College London
Mr. J. Blades, Pye Ltd., Cambridge
Mr. R. Nettalship, Pye Ltd., Cambridge

Data Processing Programs

Dr. W. J. Raitt, University College London
Miss Susan Laflin, University College London
Mrs. Cleone P. Abbs, University

The Experiment

Ariel I carried a gridded spherical Langmuir probe biased such that the measurements referred only to the positive ions. The probe was swept in potential, the voltage range, sweep rate and telemetry data rate being such that Druyvesteyn analysis of the current-voltage curve would yield ion energy spectra capable of resolving the concentrations of hydrogen, helium and oxygen ions and yielding data on ion temperatures. The first and second derivatives of the current-voltage relation were obtained by onboard instrumentation, and these together with the

Experimental Results

As soon after launch as the first digitized data became available, it was found that peaks in the second derivative channel were being obtained whose positions on the energy scale and widths indicated the presence chiefly of He^+ and O^+ ions during the daytime and He^+ and H^+ ions at night. An early result (40) obtained by simply dividing the data into those obtained with (a) the satellite in sunlight representing daytime conditions and (b) the satellite in darkness representing night-time conditions, revealed that the transition altitude from predominantly O^+ ions to predominantly He^+ ions occurred around 950 km. during the day, and the transition from He^+ to H^+ ions occurred at about 1200 km. at night. These results applied to a fairly small sample of data taken at low latitudes over the American continent. Further results obtained when the orbit had precessed sufficiently for low altitudes to occur in darkness indicated that at night the O^+ to He^+ transition occurred at about 450 km. (41). The detection of He^+ ions confirmed the theoretical predictions of Nicolet (42) and greatly extended the earlier experimental detection by Bourdeau et al. (43).

When sufficient data had been reduced on a digital computer to give ion densities from the raw telemetered data of the first derivative channel, a study was made of the variation of transition altitudes with solar zenith angle (40) (figure 3-31). Solar zenith angle was used rather than local time so as to make some allowance for seasonal variations over the period investigated. The transition altitudes were obtained from the measured ion compositions at some other altitude by extrapolation using the hydrostatic equation and a sinusoidal variation of exospheric temperature with time, the maxima and minima being obtained from the COSPAR International Reference Atmosphere corrected for change in solar activity. The results were grouped into two latitude bands centered on 40°N and on the equator, the former being 10° wide, the latter 20° wide; longitude was limited to about $75^\circ\text{W} \pm 20^\circ$ by using data from only two recording stations. The

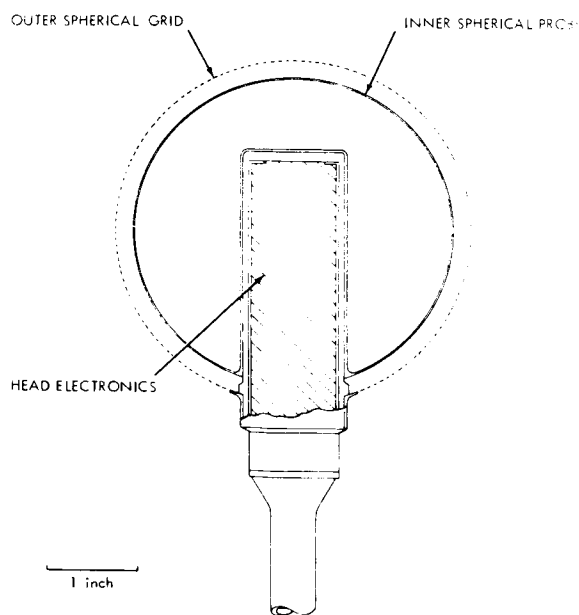


FIGURE 3-30. Sectional view of mass spectrometer probe.

probe voltage were telemetered back to the ground. A cross sectional diagram of the probe is shown in figure 3-30. The details of construction and operation of the probe are described elsewhere. (17, 38 and 39)

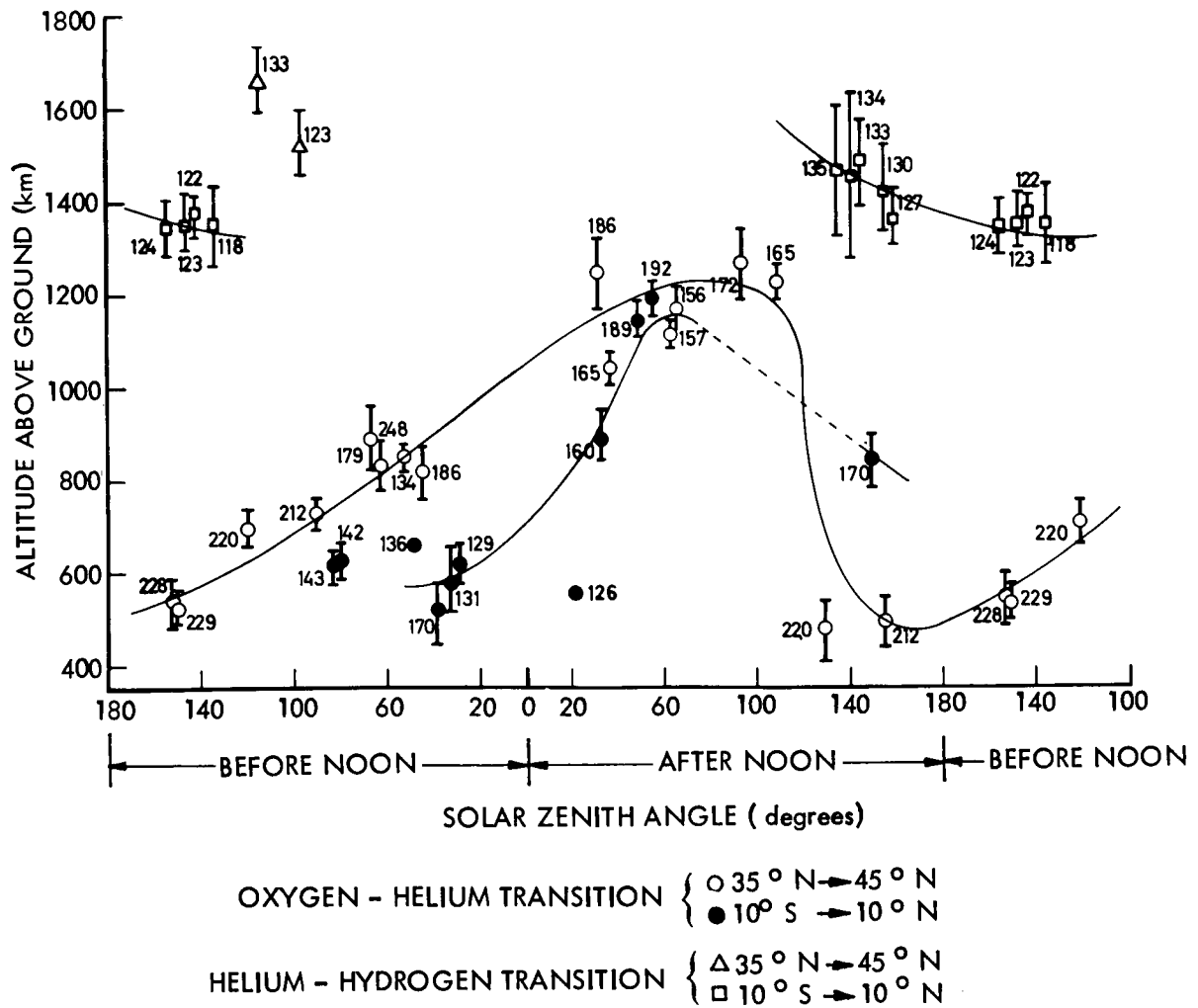


FIGURE 3-31. Variation of ion transition altitude with solar zenith angle.

results showed a twofold change in transition altitude for O^+ and He^+ during the day, the maximum altitude occurring at zenith angles corresponding to about 1700h. As expected from the earlier work the He^+-H^+ transition was only observed for zenith angles approximately corresponding to the period midnight to 0600h. During the rest of the day the hydrogen concentration was too small below apogee to be observed. The asymmetry about noon, and the fact that there was some difference in the maximum transition altitude for the different latitude regions, showed that the effect is not solely controlled by the solar zenith angle.

In an attempt to isolate the other factors controlling the ion composition, a synoptic study (44) was made for two periods, one when the orbit was such that apogee occurred over the equator, with local time varying from 930 at the north point to 2130 at the south point, and the other when there was a variation from perigee at the south point at 1000h. to apogee at the north point at 2200h. In each case the data from a number of passes spread over a period of 4 to 5 days were used to obtain ion composition contours uncorrected for change in local time and altitude. Both periods showed marked geomagnetic control in the N. hemisphere, and the latter

UNITED KINGDOM EXPERIMENTS

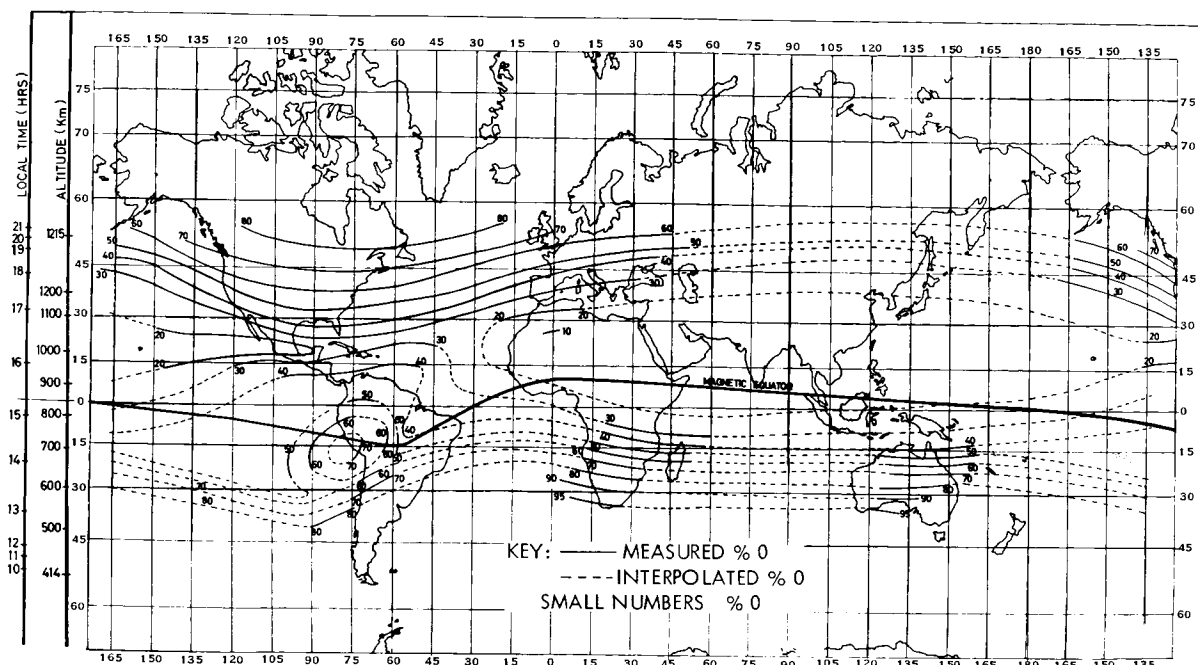


FIGURE 3-32. Smoothed ion composition contours days 151-155, 1962 (% O^+ in O^+ and He^+ mixture).

period contained more results for the southern hemisphere where similar geomagnetic control appeared to be occurring. Over South America a rather confused situation appeared, and it is not possible to be precise in assigning the contours. However, it appears that a peak or possibly a ridge in the percent O^+ occurred at about $75^\circ W$ $15^\circ S$ of fairly limited geographic extent. (figure 3-32)

The most striking feature in the northern hemisphere for the second period was the increase in percent O^+ with latitude in spite of the fact that the altitude was also increasing. A similar increase in percent O^+ occurred in the southern hemisphere, but this must be due in part at least to the decrease in altitude. The percent O^+ increase in northern latitudes strongly suggests a rising ion temperature with latitude, an effect also supported by the ion temperature measurements, but the possibility of a change in the neutral gas composition cannot be excluded.

The study of ion temperatures from the width of the second derivative of the probe curve was hampered by interference from the dielectric constant experiment probe to meas-

ure electron concentration which caused a loss of data at voltages corresponding to the occurrence of H^+ and He^+ peaks. As a result, the only temperature results analysed in any detail (45) were those obtained from O^+ ions for ion density greater than about 10^5 cm^{-3} . These data came from altitudes below 600 km. and from local times within two hours of noon for the period of operation of the second derivative channel. The variation of ion temperature with latitude for the local time period 1000h to 1200h in the longitude range $50^\circ W$ to $150^\circ W$ over a period of about 20 days was investigated. It was found that in spite of a large scatter the results showed a marked trend of increasing temperature with latitude. At low latitudes the mean ion temperature was close to the gas temperature calculated by Harris and Priester (46), that is about $800^\circ K$; whereas at latitudes of about 40° the mean ion temperature was about $1600^\circ K$ (figure 3-33).

The availability of real-time data only has restricted the analysis of the mass spectrometer data to broad general features. Nevertheless work is continuing on the computer analysis of variations of ion composition with

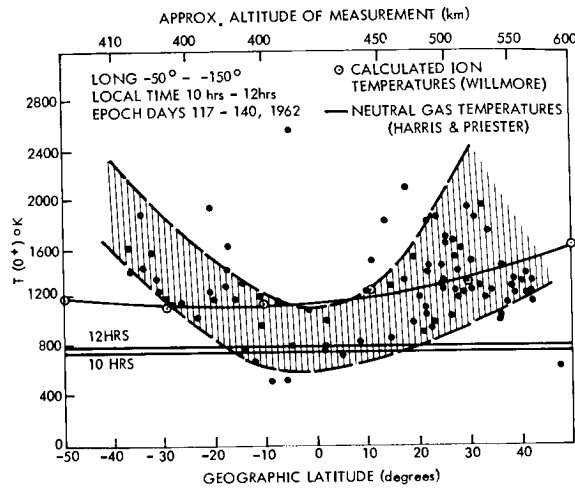


FIGURE 3-33. Ariel I oxygen ion temperature as a function of geographic latitude.

latitude and altitude using all the useful data. Some allowance for longitude variation is made by working in geomagnetic co-ordinates. In an initial analysis, compensation for the altitude variation has been made by dividing the data into two height ranges and correcting the percent O^+ to two mean levels (600 km and 1000 km) using the hydrostatic equation and the neutral gas temperature. The feature of increase in percent O^+ with latitude is again apparent from this increased quantity of data, and a detailed study of the diurnal variation of percent O^+ at a given altitude has been made for a range of latitudes. Data for the northern hemisphere corrected to 100 km shows for all latitudes a minimum O^+ at 0500h and a maximum at 1500h. However the maximum in the south-

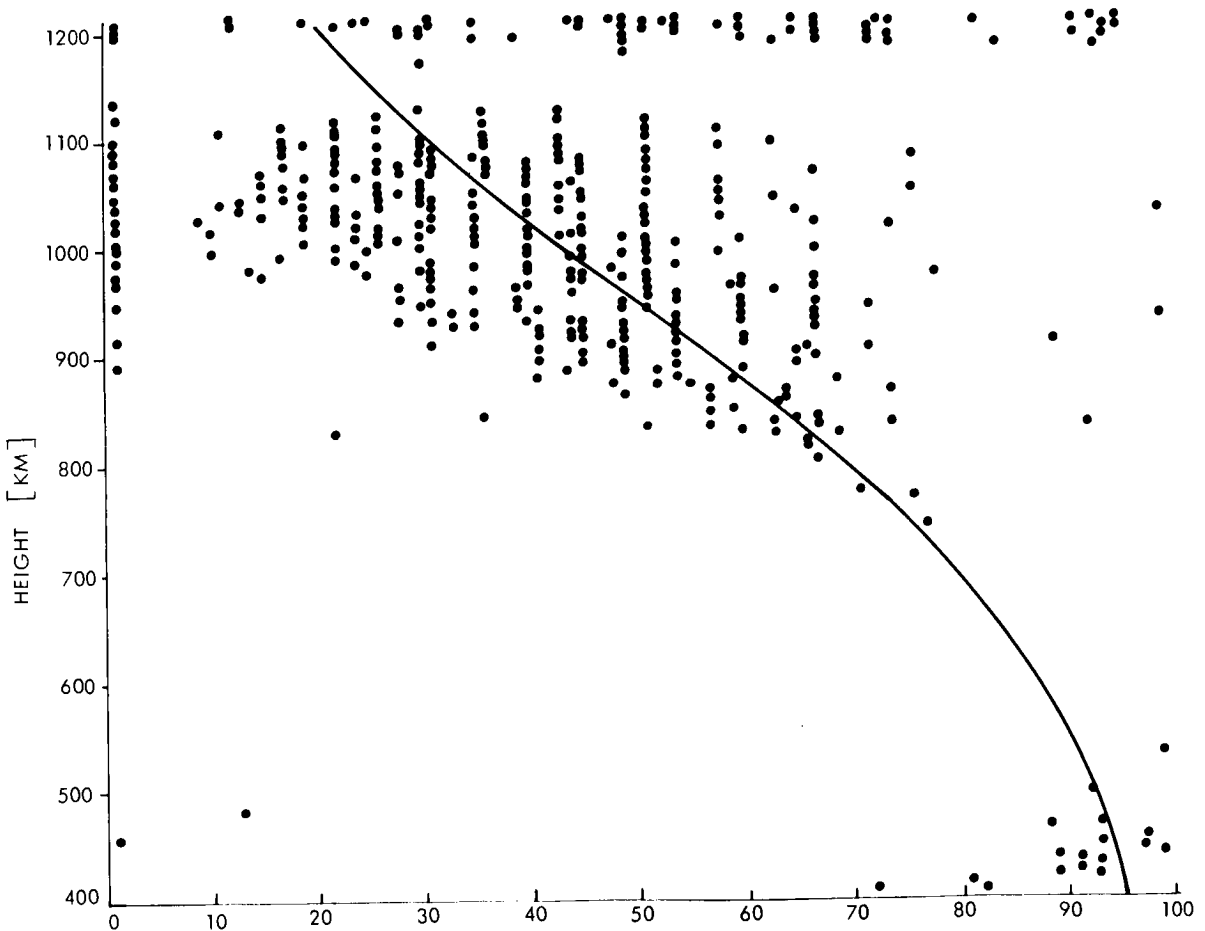


FIGURE 3-34. Theoretical variations under conditions of diffusive equilibrium.

ern hemisphere is not so well delineated as that in the northern because of lack of data after about 1630h. Part of the explanation of these differences may be attributed to the fact that the data applied to the period between the vernal equinox and the summer solstice in the northern hemisphere.

A further phenomenon of significance is revealed by a plot of values of %O⁺ obtained over the period from day 117 to day 181 between the hours 1200 and 1700 L.S.T. and latitudes 10°–40° N. The full line in figure 3–34 shows the theoretical variation to be expected under conditions of diffusive equilibrium (taking $T_+ = 2000\text{ K}$ *g (constant)* = 750 Km/sec and 50%O⁺ at 950 Km). The large scatter of the points is an indication of the variability of the composition from day to day but the trend of the %O⁺ to greatly exceed the diffusive separation ratio is also clear. It seems, therefore, that while total ion pressure is given by the hydrostatic equation the partial pressures of the individual components at this time are not in hydrostatic equilibrium. A high altitude source of O⁺ leading to a downward flux of about $10^7\text{ cm}^{-2}\text{ sec}^{-1}$ at 950 Km is indicated, inter-diffusion velocity of the O⁺ and He⁺ streams being around 0.1 Km sec^{-1} at this altitude. The occurrence of this effect in the afternoon is presumably due to the great increase in relative concentration of neutral oxygen at great heights at this time.

The results on ion composition and temperature from Ariel I may be summarized as follows. Measurements have shown that in the altitude range from 400 to 1200 km for latitudes from 54°N to 54°S there are three predominant ions, oxygen, helium and hydrogen. The presence of He⁺ ions had been predicted as a theoretical possibility and some earlier measurements of ion mass spectra were in general agreement with the prediction. The Ariel I results confirmed the broad picture and greatly extended knowledge of the dependence of the ionic composition on latitude, longitude, altitude and local solar time. The study of diurnal variations showed that the O to He transition altitude varied by a factor of two and synoptic studies

showed strong geomagnetic control of this parameter. Both the synoptic variation of ion composition and direct ion temperature measurements indicate a marked increase in ion temperature with latitude.

The partial pressures of O⁺ and He⁺ are not in hydrostatic equilibrium in the afternoon but appear to be seriously disturbed by a downward flux of O⁺ and an upward flux of He⁺.

MEASUREMENTS OF THE SPATIAL ELECTRON DENSITY DISTRIBUTION BY MEANS OF AN R. F. ELECTRON DENSITY PROBE

Project Scientist

Professor J. Sayers, University of Birmingham

Data Analysis

Miss P. Rothwell, University of Birmingham

Miss B. T. Loftus, University of Birmingham

Project Engineer

Mr. J. H. Wager, University of Birmingham

The Experiment

The ambient electron density along the path of the satellite was determined by measuring the electric permittivity of the medium using a radio-frequency probing signal of 10 Mc/sec and an electrode system which produced only slight radiation at this frequency. The electrodes consisted of a pair of flat circular grids of fairly high transparency—approximately 80%. The diameter of the grids was 4 inches and they were supported 3 inches apart on the ends of two short tubes containing inner co-axial rods connected to the grids. These tubes were mounted on a small junction box which, in turn, was fixed on the end of a boom approximately 3 feet in length.

The permittivity was measured in terms of the current flowing between the two electrodes in response to a constant applied signal of 3 volts rms. This signal was provided by a 10 Mc/sec crystal controlled oscillator, the amplitude being electronically stabilized at the above value.

The electric permittivity of a medium containing free electrons in the presence of a magnetic field and subject to collisions between the electrons and a neutral gas has been derived by Appleton (47). The general Appleton expression for the permittivity is complex, involving terms arising from the electron collision frequency in addition to non-isotropic terms depending on the magnetic field. If, however, the probing frequency is chosen so as to be high compared with the electron collision frequency and also high compared with the gyro-frequency, the Appleton expression reduces approximately to the following simple form:

$$\epsilon = \epsilon_0 \left\{ 1 - \frac{4 N e^2}{m \omega^2} \right\}$$

where

ϵ_0 is the permittivity of free space,

ω is the probing frequency, and

N, e, m (in CGS units) are the electron density, charge and mass respectively.

The permittivity of the medium determines the impedance presented by the disc electrodes to the 10 Mc/sec signal and in the absence of electron collisions this impedance is purely reactive.

The r. f. current between the electrodes consists of two parts:

1. The constant vacuum displacement current;
2. The electron current, which is proportional to the electron density.

This second component was selected electronically and amplified to give a measure of the electron density. Before considering how this was carried out, it is necessary to discuss the effects of space charge sheaths on the electrodes.

Space Charge Sheaths and Electron Depletion

In a classic paper on plasma probes Langmuir and Mott-Smith (48) showed that when a probing electrode in an ionized gas has a potential which is more negative than the local plasma potential, the resulting current to the electrode is carried by positive ions and

the effect of the applied negative potential is to displace the plasma electrons from the immediate vicinity of the electrode. The positive ions are accelerated towards the electrode in this region: but, because of their inertia, they move comparatively slowly and form a substantial positive space charge which has a screening effect on the applied probe potential. At a certain distance, which is calculable when the geometry and other factors are known, the screening is complete. The applied probe potential does not penetrate beyond this point which is, in fact, never quite sharp: the diffuseness of the boundary being determined by the temperature conditions in the plasma. In the geometry which was adopted for the rf electron probe, the application of a few volts negative potential to the electrodes with respect to space potential was sufficient to establish an ion sheath which excluded all electrons from the space between the grids and from the fringe area around the grids in which the rf probing field was appreciable. Under these conditions the effective permittivity was equal to that of free space. The small changes in permittivity produced by the plasma electrons were thus measured by a circuit which subtracted the value of the rf current between the grids when the latter were at space potential from the current with the electrodes at some suitably large negative potential.

This presented one remaining problem in that space potential relative to the vehicle was not known. Space potential could, however, be located and the ability to do so depended on the fact that if the potential on the grid electrodes was made more positive than the plasma space potential, electrons were accelerated in passing close to or between the grids, and provided they did not lose an appreciable fraction of their added energy in collisions with the gas—a few tens of collisions are admissible—the average population density of electrons in the vicinity of the grids would be less than in the undisturbed plasma. A maximum electron density between grids thus occurred at space potential and this was representative of the true

plasma population density. The determination of the electron density when the grids were at space potential was accordingly carried out by applying a dc sweep voltage to the measuring head relative to the satellite hull and recording the maximum response in the electron signal.

Electronic Circuit Functions

Figure 3-35 is a schematic diagram of the electronic functions of the equipment. The

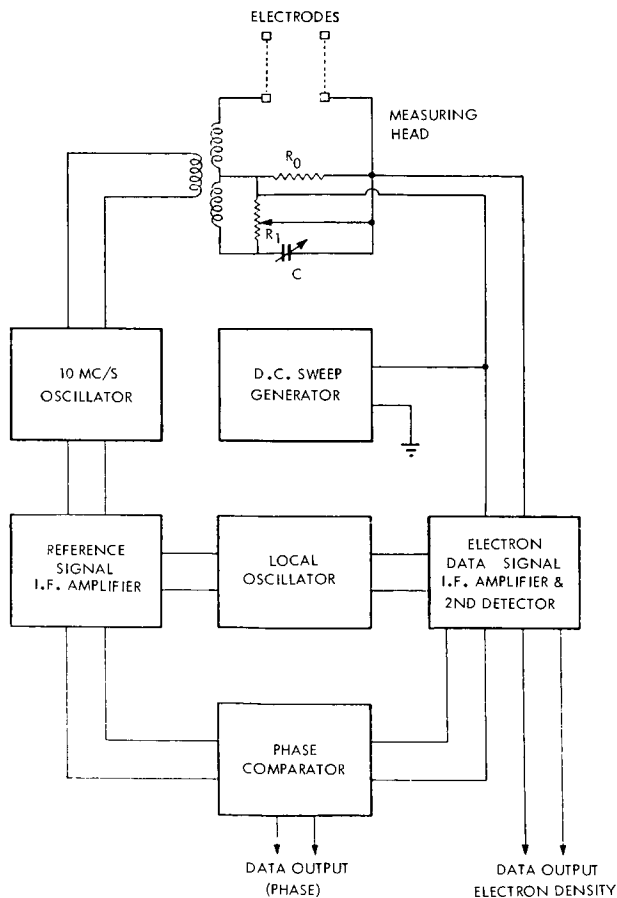


FIGURE 3-35. Schematic diagram of the electronic circuit for electron density measurement.

current between the grids in response to the 10 Mc/sec signal flows through the viewing resistance R_0 . The part of this current corresponding to the capacitive displacement current in the absence of ionization is re-

moved by a balancing current of opposite phase which is adjusted by the variable condenser C . The variable resistance R_1 provides a small phase adjustment to achieve a true null balance. The voltage developed across the viewing resistance R_0 is thus, at space potential, proportional to the electron density and the constant of proportionality is directly calculable from the circuit constants. A sawtooth waveform, which provides the scan for space potential, is superimposed on the measuring head from the dc sweep generator.

A crystal controlled local oscillator enables the electron data signals to be converted to a frequency of 20 Kc/sec before amplification. The phase of the electron data signals is compared with a reference signal obtained directly from the 10 Mc/sec oscillator in order to establish that the data signals are in the correct phase for free electrons between the grids.

Data Recovery

Data Stored on Magnetic Tape. From the point of view of this experiment, a vital part of the data handling system which NASA provided on board the satellite was a magnetic tape recorder. This was capable of storing data from a number of experiments for one complete orbit of the satellite and a ground command link enabled the stored data to be transmitted by rapid playback when the satellite was over a suitable receiving station. By this means the electron density was measured at one minute intervals throughout almost every orbit of the satellite from the time of launch until 16 July. Before the data were presented to the tape recorder the peak on the electron signal corresponding to space potential was determined by an additional electronic unit and stored for a short time in readiness for recording. In this way the need for further computing on the recovered data from the tape was eliminated. The data from 27 April until 8 July, 1962, were printed by automatic means and made available in World Data Centers.

Table 3-1 is a reproduction of a page from

TABLE 3-1.

Electron Density Data Points

Day	BIRMINGHAM		99995162117 1		10102832		Geographic Location
	Time sec. U.T.	Long.	Lat.	Alt. Km.	Time, local	Electron density	
117.	31699.016	-54.2	36.3	1023.	18825.579	0.756E	04 -6.1
117.	31760.500	-51.2	38.6	1002.	19597.992	0.101E	05 -6.1
117.	31821.875	-48.1	40.8	979.	20424.262	0.126E	05 -6.1
117.	31883.078	-44.6	42.9	956.	21309.510	0.126E	05 -6.1
117.	31944.641	-40.9	45.0	932.	22268.143	0.202E	05 -6.1
117.	32005.984	-36.8	46.8	908.	23297.217	0.202E	05 -6.1 N. Atlantic
117.	32067.172	-32.5	48.6	883.	24401.903	0.227E	05 -6.1
117.	32128.750	-27.8	50.1	858.	25595.468	0.227E	05 -6.1
117.	32190.141	-22.7	51.4	832.	26866.979	0.252E	05 -6.1
117.	32251.281	-17.4	52.5	806.	28210.219	0.302E	05 -6.1
117.	32312.750	-11.7	53.3	780.	29629.013	0.302E	05 -6.1 S.W. Ireland
117.	32374.281	-5.9	53.8	754.	31103.439	0.378E	05 -6.2
117.	32435.437	0.1	54.0	728.	32603.550	0.479E	05 -6.1 York, England
117.	32497.000	6.2	53.8	702.	34125.859	0.554E	05 -6.1
117.	32558.328	12.2	53.3	676.	35630.818	0.630E	05 -6.1 Berlin
117.	32619.516	18.1	52.5	651.	37098.543	0.731E	05 -6.1
117.	32681.019	23.8	51.4	626.	38523.049	0.882E	05 -6.1
117.	32742.484	29.2	50.0	602.	39875.631	0.983E	05 -6.2 Kivev
117.	32803.672	34.2	48.3	579.	41149.039	0.116E	06 -6.1
117.	32865.219	39.0	46.4	556.	42350.765	0.134E	06 -6.1 Rostov
117.	32926.594	43.4	44.2	535.	43470.251	0.164E	06 -6.1
117.	32987.781	47.5	41.9	514.	44511.054	0.189E	06 -6.1 Caspian Sea
117.	33049.156	51.3	39.4	495.	45484.739	0.214E	06 -6.0
117.	33110.750	54.8	36.7	477.	46397.300	0.251E	06 -6.1
117.	33171.891	58.1	33.9	461.	47245.491	0.344E	06 -6.0
117.	33233.359	61.2	31.0	446.	48047.198	0.456E	06 -6.1
117.	33294.859	64.1	28.1	432.	48804.422	0.604E	06 -6.1
117.	33376.234	66.8	25.0	421.	49521.333	0.790E	06 -6.1 Pakistan
117.	33417.422	69.4	21.9	411.	50203.099	0.809E	06 -6.1
117.	33479.016	71.9	18.7	403.	50861.509	0.790E	06 -6.0 Bombay
117.	33540.391	74.2	15.4	397.	51494.293	0.800E	06 -6.1
117.	33601.578	76.5	12.2	393.	52106.484	0.800E	06 -6.1 S. India
117.	33663.141	78.8	8.8	390.	52708.063	0.790E	06 -6.1
117.	33724.547	81.0	5.5	390.	53297.763	0.809E	06 -6.1 Ceylon
117.	33785.734	83.2	2.2	392.	53878.756	0.800E	06 -6.1
117.	33847.203	85.3	-1.1	396.	54459.410	0.800E	06 -6.1
117.	33908.687	87.5	-4.5	402.	55040.790	0.809E	06 -6.0
117.	33970.062	89.7	-7.8	409.	55625.272	0.800E	06 -6.1
117.	34031.266	91.9	-11.0	419.	56215.808	0.716E	06 -6.1
117.	34092.844	94.1	-14.3	431.	56821.515	0.511E	06 -6.1 Indian Ocean
117.	34154.172	96.5	-17.5	444.	57440.107	0.409E	06 -6.1
117.	34215.359	98.9	-20.7	459.	58076.639	0.288E	06 -6.0
117.	34276.844	101.4	-23.8	475.	58740.159	0.214E	06 -6.1
117.	34338.328	104.0	-26.8	493.	59432.305	0.181E	06 -6.1
117.	34399.516	106.8	-29.8	512.	60154.491	0.139E	06 -6.1

one of the five volumes of these data and represents data from about half of one orbit over the geographical locations indicated on the right-hand margin. Each line represents one data point. There were some 50,000 observations in all.

Direct Transmission Data. In addition to the tape recorder data system, a direct data link was also used. This provided access to the complete electron signal throughout each dc scan for space potential, so that the correct operation of the experiment might be verified and the peak electron signal at space potential observed on the recovered data. The amount of data available by direct transmission was much more limited than that by the tape recorder, since direct data could only be acquired while the satellite was within telemetry range of a tracking station.

Some Observational Results and their Interpretation

It has long been recognized that the F_2 region above its maximum density shows a decay of ionization with increasing altitude which does not resemble a Chapman profile. For example, Storey (49) showed that observations on the propagation of whistler atmospherics required for their interpretation a much higher ionization density above the F_2 layer than would be expected for a simple Chapman layer. Storey recognized the significance of the observation that there was a positive correlation between the occurrence of whistlers and magnetic storms and concluded that there must exist above the F_2 layer some source of ionization (additional to ultraviolet radiation) associated with magnetic effects. A further significant step in the study of the upper ionosphere by considerations based on radio wave propagation was made by Obayachi (50). In his paper he suggested that high frequency radio propagation might take place in the outer ionosphere along ducts formed by field aligned ionization strata. Convincing experimental evidence for the existence of field aligned patches of ionization extending to hundreds of kilometers was soon found as follows:

1. From radar soundings by Matthew and Dearden (51).

2. From a study of the scintillation in radio reception of satellite signals by Singleton and Lynch (52).
3. From whistler observations by Crouchley and Duff (53).
4. From studies of ionograms from the satellite Alouette 1 by King et al (54).

A further unusual feature of the F_2 region was discovered by Appleton (55). This is the Appleton equatorial anomaly and in its simplest form can be recognized as a depression of the F_2 ionization maximum over the magnetic equator accompanied by peak densities on each side of the equator. The effect is very marked during the day and usually is difficult to observe or is absent during the latter half of the night. The association with the magnetic equator and, in some cases, symmetry about the magnetic equator indicates close geomagnetic control of the anomaly.

Mitra (56) sought to explain the Appleton anomaly in terms of ionization formed at high levels in the F_2 region over the magnetic equator diffusing north and south along field lines leading to enhancement of ionization at lower levels on either side of the equator. Martyn (57) was the first to appreciate the significance of vertical movements in determining the morphology of the F_2 region and in particular of the Appleton anomaly. The idea was further developed by Lyon and Thomas (58) who observed that the afternoon enhancement of the anomaly crests north and south of the magnetic equator occurs first on the side nearest to the geographic equator and the greater height of the F_2 maximum also occurs on the side nearest to the geographic equator. It is suggested that these two observations support the theory that the anomaly results from diffusion of ionization along lines of magnetic force from the magnetic equator. Goldberg and Schmerling (59) have also advanced the theory of diffusion to explain the magnetic anomaly, but Risbeth et al (60) conclude that diffusion processes alone will not account for the observed magnitude of the effect and that bulk vertical movements must be an important mechanism as was pointed out by Martyn

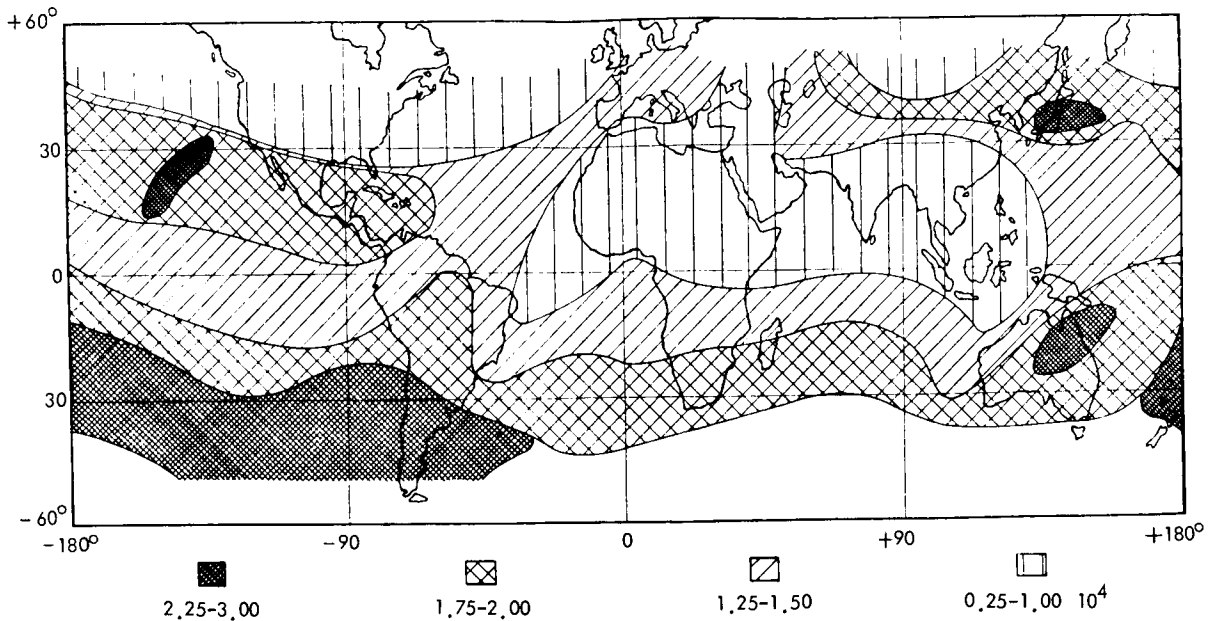


FIGURE 3-36. World contour map of the electron density at an altitude in the region of 1100 km near local midnight in the period 27 April to 6 May 1962 (In the unhatched region at the bottom of the map the density probably lies between 0.75 and 1.50 ($\times 10^4$) but there are very few data).

(57) many years earlier. Mariani (61) has sought to account for the effect by including a consideration of geomagnetic control in terms of the pitch angles of photo-electrons produced in F_2 .

The use of satellites to carry direct measuring instruments to explore the upper ionosphere and to carry radio propagation experimental equipment such as the topside sounder of Alouette opened a new chapter in the investigations of the F_2 region and above.

The results now available from the Ariel satellite indicate the existence of regions of enhanced ionization, in the topside ionosphere, of a much more extensive and systematic character than has been previously supposed. The significance of the new results can be best appreciated by considering the distribution of electron density in sections of constant altitude and by confining our attention to periods near midday or near midnight in order to avoid the added complexity of dawn or sunset conditions. Figure 3-36 illustrates such a section at an altitude in the

region of 1100 km for conditions near local midnight in the period 27 April to 6 May 1962. This diagram shows contour lines of equal electron density on a world map. These results show the existence of two bands of enhanced electron density at mid-latitudes north and south of the equator. An important feature of these bands is that they do not follow lines of equal geographic latitude, but the two bands show corresponding departures from the parallels of longitude in such a way that their distance apart in latitude is approximately constant. Furthermore, a line drawn midway between the maxima of the two bands coincides closely with the magnetic equator. The bands of electron density enhancement are, therefore, bands of approximately constant magnetic latitude suggesting that the geomagnetic field plays an important role in the mechanism of production of these enhancements. The bands on figure 3-36 are, in fact, consistent with enhancement of ionization density on a magnetic shell which crosses the magnetic equa-

torial plane at an altitude of 1.8 earth radii from the center of the dipole approximation to the earth's field. This altitude at the magnetic equator is called the L value of the magnetic shell following the notation of McIlwain (62).

Constant altitude sections near perigee (400 to 500 km altitude) at approximately local midnight have also shown corresponding bands of enhancement of electron density. The centers of these bands are observed at higher latitudes north and south than in the case of the apogee section, showing that the enhancement exists in a layer whose altitude

varies with latitude and longitude so that its peak follows a particular magnetic shell. The L value of this shell usually lies in the range 1.6 to 1.9.

A further important feature of the enhancement on the above magnetic shell is the suppression of the effect in the longitude range 60°W to 65°E of the northern hemisphere and a sharp reduction of the intensity of ionization east of the South Atlantic anomaly. The result of this is that over the Atlantic ocean both north and south of the equator regular enhancement on the 1.8 magnetic shell is not marked. There are, how-

(A) 8 JULY,
11.23-11.49
 $88^\circ\text{W}-154^\circ\text{W}$

(B) 8 JULY,
18.10-18.37
 $171^\circ\text{W}-115^\circ\text{W}$

(C) 9 JULY,
05.49-06.14

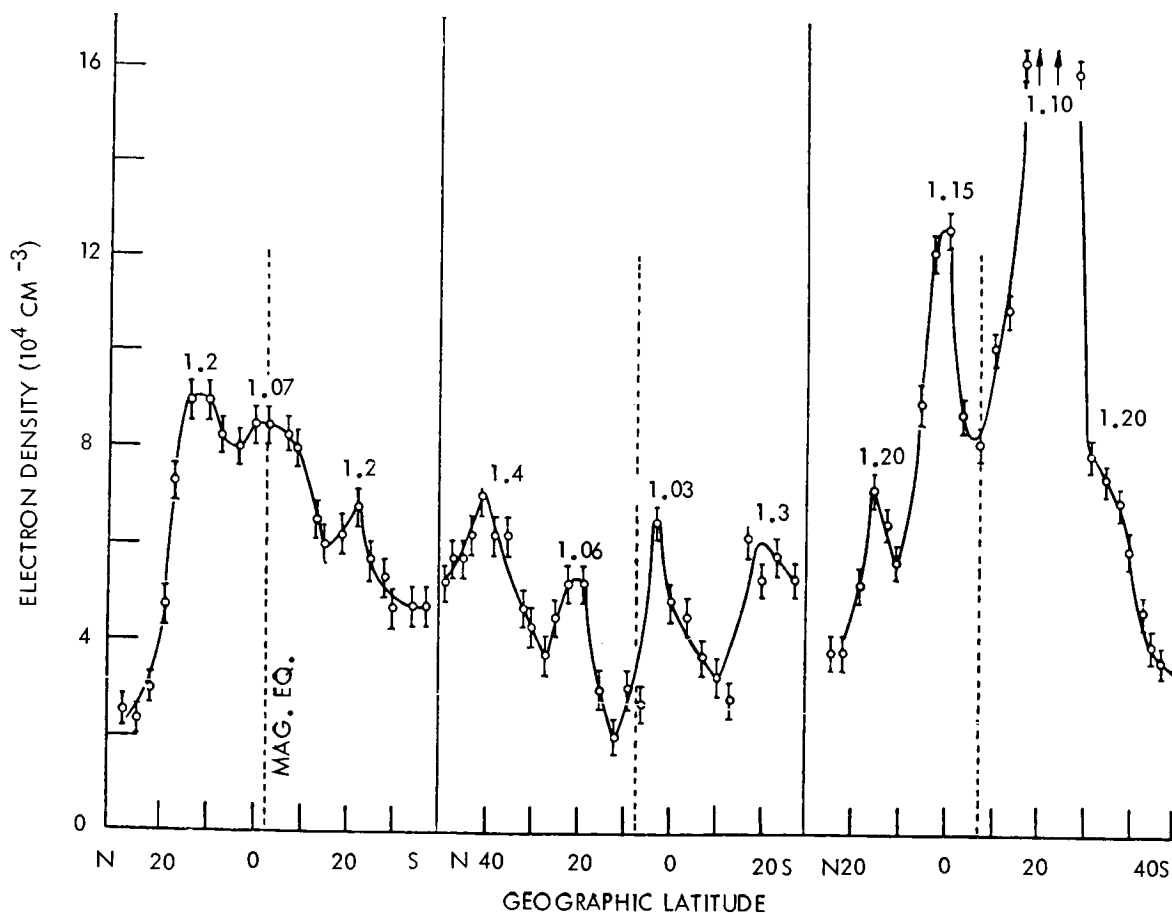


FIGURE 3-37. Approximately horizontal profiles of electron density at an altitude in the region of 400 km (perigee) and near midnight local time.

ever, fairly intense day-to-day fluctuations and these are greatest in the region of the South Atlantic.

The enhancement described above is the main regular feature of the topside ionosphere at low- and mid-latitudes near midnight in the period of these observations. Examination of individual passes reveals additional structure in the form of enhancement on other magnetic shells. During the day these additional enhanced regions become relatively more pronounced and this is also the case during the night at lower altitudes than those of figure 3-36. Examples of the additional enhanced regions in lower L shells are given in the results from a few sections of the Ariel orbits shown in figure 3-37. These are for passes near perigee and near local midnight for three different longitudes. The L values, defining the magnetic shells in which the peaks are located, are noted in the diagram. By examination of a large number of such records it has been found that in addition to the $L=1.8$ shell, enhancement of electron density generally occurs on two lower magnetic shells, namely, $L=1.09 \pm 0.05$ and $L=1.25 \pm 0.05$. Referring again to figure 3-37 the evidence for the magnetic field alignment of the enhanced regions will be clear from the way in which the latitude and separation of the peaks varies with longitude so as to follow constant L values. This is shown in more detail in figure 3-38 for the $L=1.25$

shell. In this diagram the latitudes of the maxima of the enhanced regions as intersected at an altitude of approximately 1100 km (apogee) during the day is shown as a function of longitude. Contour lines of the intersections of the L shells 1.22, 1.25 and 1.27 at the same altitude are indicated on the diagram, together with the magnetic dip equator. It will be noted that enhancement is fairly clearly defined on an L shell between 1.22 and 1.27 and this, of course, results in symmetry about the magnetic equator. Figure 3-39 shows the shape of the various magnetic shells in which enhancement of ionization has been found. The asymmetry between the western and eastern sections is due to the fact that the first-order approximation to the actual geomagnetic field is a magnetic dipole whose center is displaced from the geographic center in the direction of India.

The fact of magnetic shell alinement of the enhanced regions is strong evidence that the enhancement is due to additional ionization by energetic particles. The occurrence of this ionization preferentially in particular shells must be due to irregularities in the pattern and intensity of the geomagnetic field. Although the detailed mechanism underlying this correlation with particular magnetic shells and not with others is not understood, the overall pattern is fairly consistent. For example, the suppression of the enhancement on the $L=1.8$ shell east of the Atlantic with a gradual recovery in the eastern hemisphere suggests that trapped electrons which drift eastwards are an important source of this enhancement. If these electrons are lost out of the 1.8 shell over the South Atlantic anomaly only weak enhancement would be expected over an extended eastern range of longitude until the shell becomes replenished.

The lowest shell at $L=1.0$ to 1.14 appears to be more complex than the other two and is possibly due to some process quite different from those responsible for the higher shells.

In view of the evidence that the shell enhancements in the topside ionosphere are due to energetic particle ionization, it is of particular interest to consider the direct observational evidence for the existence of such

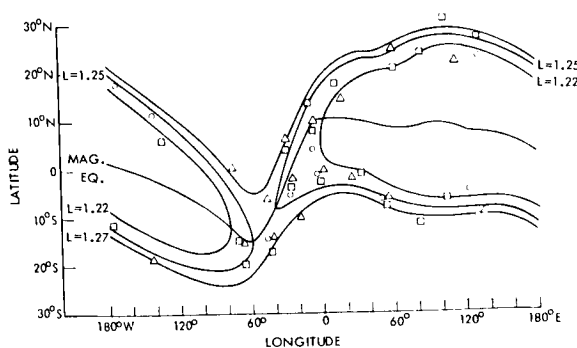


FIGURE 3-38. World map of the peaks of the enhanced regions encountered at an altitude of approximately 1100 km during the day with contour lines of the L values at the same altitude. O, 8 July; \square , 9 July; \triangle , 10 July, 1962.

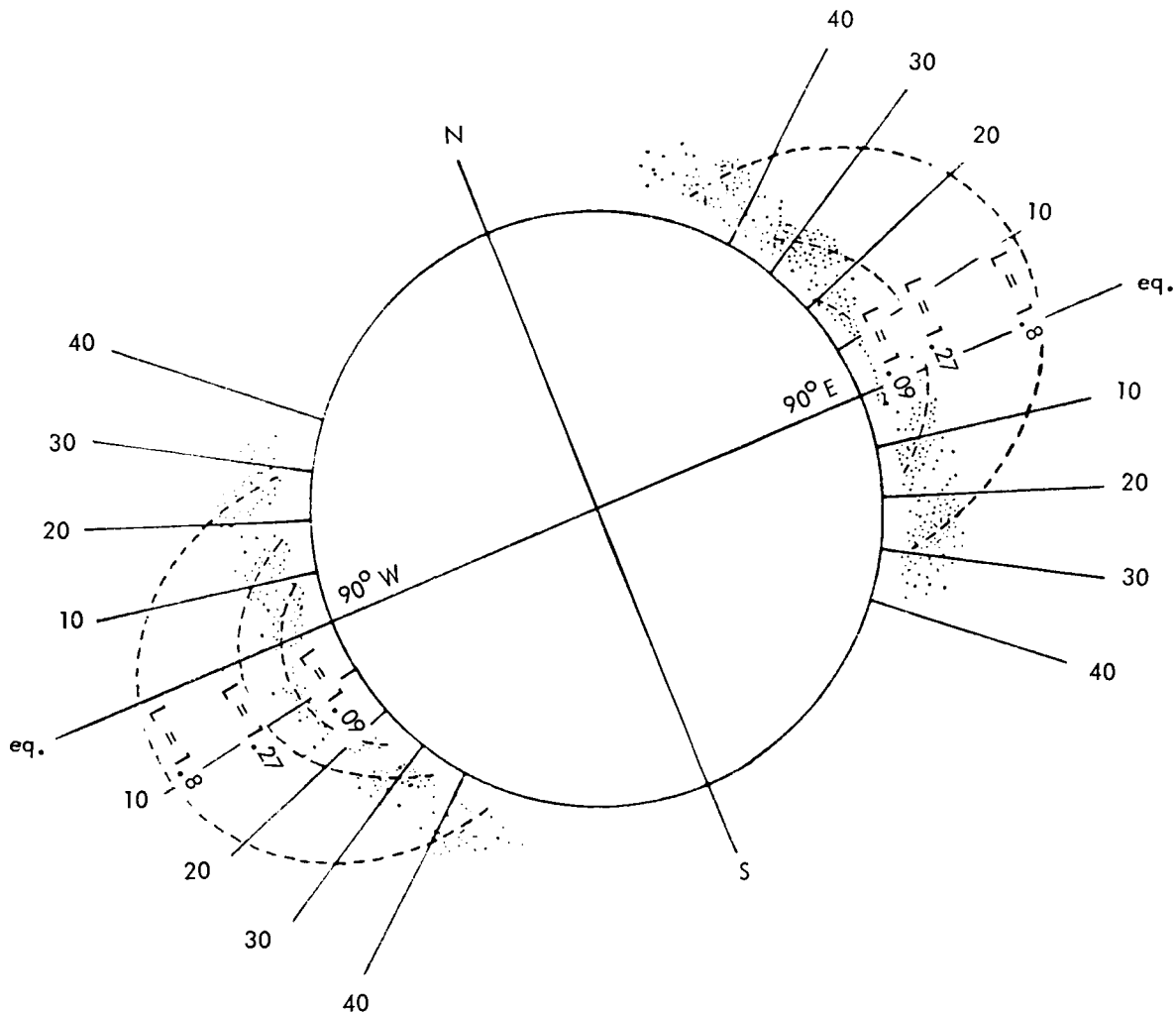


FIGURE 3-39. Representation to scale of the three regions of enhancement. The shading represents the altitude range over which electron density has been obtained by Ariel.

particles. It has been reported by Hess (63) that as a result of the 'Starfish' high-altitude nuclear explosion on 9 July, 1962, energetic electrons appeared in the magnetic shell $L=1.25$. However, the results now presented indicate that some enhancement of ionization was present in the 1.25 shell before the Starfish event. Paulikas and Freden (64) have also recorded energetic particles from Starfish in L shells near 1.2 and 2, but they have pointed out that pre-Starfish observations by Schrader et al (65) with the satellite OSO I also recorded energetic particles near $L=1.2$

and near $L=2$. We must therefore regard enhancement of ionization in a belt aligned in the magnetic shell $L=1.25$ as a natural structure, and it is evident that some preferential mechanism exists for the accumulation of ionizing particles in this shell. The ionization by such particles must be assumed to take place at altitudes not far from the F_2 layer maximum, and enhancement in the magnetic shell in depth is the result of upward diffusion of the ionization substantially within the magnetic shell in which it is produced.

IONIZATION PRODUCED BY A HIGH ALTITUDE NUCLEAR EXPLOSION

The Starfish high-altitude nuclear explosion over Johnston Island (latitude 16°N , longitude 169°W) which took place at 0900 hours U. T. on 9 July, 1962, produced very intense and short-lived ionization both locally and at the magnetic conjugate point to the site of the explosion. This ionization density amounted to an order of magnitude increase over the normal level, but on the next pass of the satellite over each of the two regions on the following day the ionization had decayed to practically the level of the day before the explosion. Figure 3-40 shows the electron

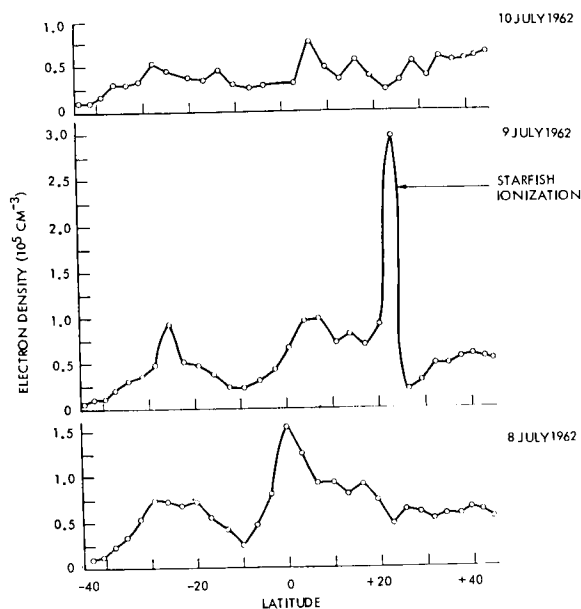


FIGURE 3-40. Comparison of the ionization density recorded over Johnston Island a few hours after the explosion with the ionization density on the previous and following days.

density record from the satellite on the first occasion of a pass just west of Johnston Island, which occurred about $6\frac{1}{2}$ hours after the Starfish event. For comparison the corresponding passes are shown on the preceding day and on the following day. The width of this cloud of ionization was a few thousand kilometers along the path of the satellite and the peak density was $3 \times 10^5 \text{ cm}^{-3}$, which is

about six times the normal level. The point magnetically conjugate to the site of the explosion is at approximately 15°S , 170°W , and the orbit of Ariel passed close to this point, being slightly to the west, approximately five hours after the 'Starfish' event. The record of the electron density for this pass is shown in figure 3-41 with the passes

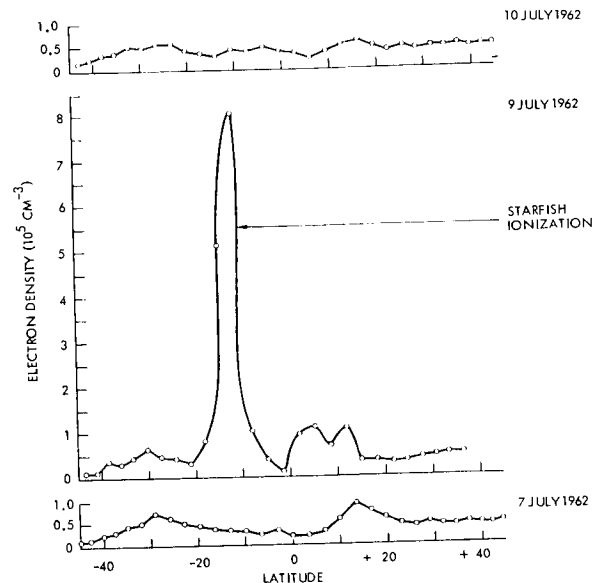


FIGURE 3-41. Comparison of the ionization density at a point magnetically conjugate to the site of the explosion with the ionization at the same place 2 days earlier and on the day following the event.

of the two adjacent days for comparison. The enhancements shown in figures 3-40 and 3-41 are on approximately the same longitude and at L values of 1.18 and 1.10. Further clouds of ionization were encountered a few hours after the explosion near southern apex of the satellite orbit, again on a similar longitude a few degrees to the east and at an L value of 6.0. It thus appears that the explosion produced an ionization cloud extending over some thousands of kilometers in altitude, from 25°N to at least 54°S latitude, but very much flattened in longitude. This is not unlike the form which it might be anticipated the actual fireball of the explosion would take as it expands and then diffuses

under the constraint of the geomagnetic field. Further details of the Ariel data relevant to the Starfish event have been reported by Rothwell, Wager and Sayers (66).

IONIZATION BY CORPUSCULAR RADIATION AT HIGH MAGNETIC LATITUDES

The inclination of the orbit of Ariel to the equator is 54° , but because of the asymmetries of the geomagnetic field the satellite intersects sections of magnetic shells of high L value south of Australia and over northern Canada. In these regions large variations of ionization density have been recorded and there is a close correlation between these variations and changes in the K_p index of

magnetic disturbance. This correlation is illustrated in figure 3-42, which shows the observed electron density for a series of sections of southern apex passes of the satellite. These passes were chosen from the data for 26, 27, and 28 May, 1962, because on these three days the K_p index showed a rapid rise from 1 on the 26th to 2^+ on the 27th and this was followed by a rapid decrease to the former value on 28 May.

It will be noted on figure 3-42 that on 26 May and 28 May the electron density was fairly constant for all the southern apex sections of the orbit, but on 27 May there was a two-fold rise in electron density. While it is possible to find many individual examples

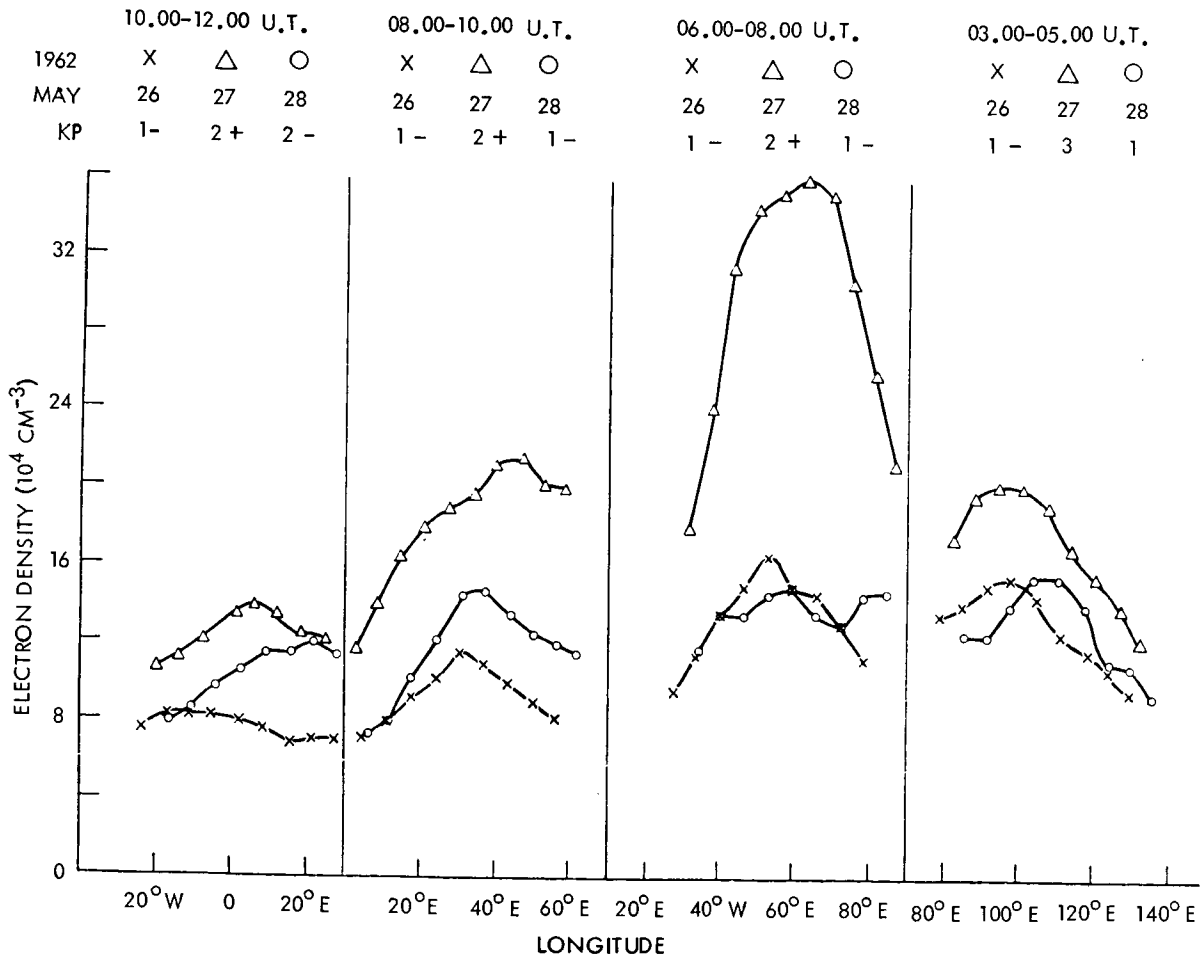


FIGURE 3-42. Individual profiles of electron density near southern apex, midday, showing the correlation between the electron density recorded and the K_p index.

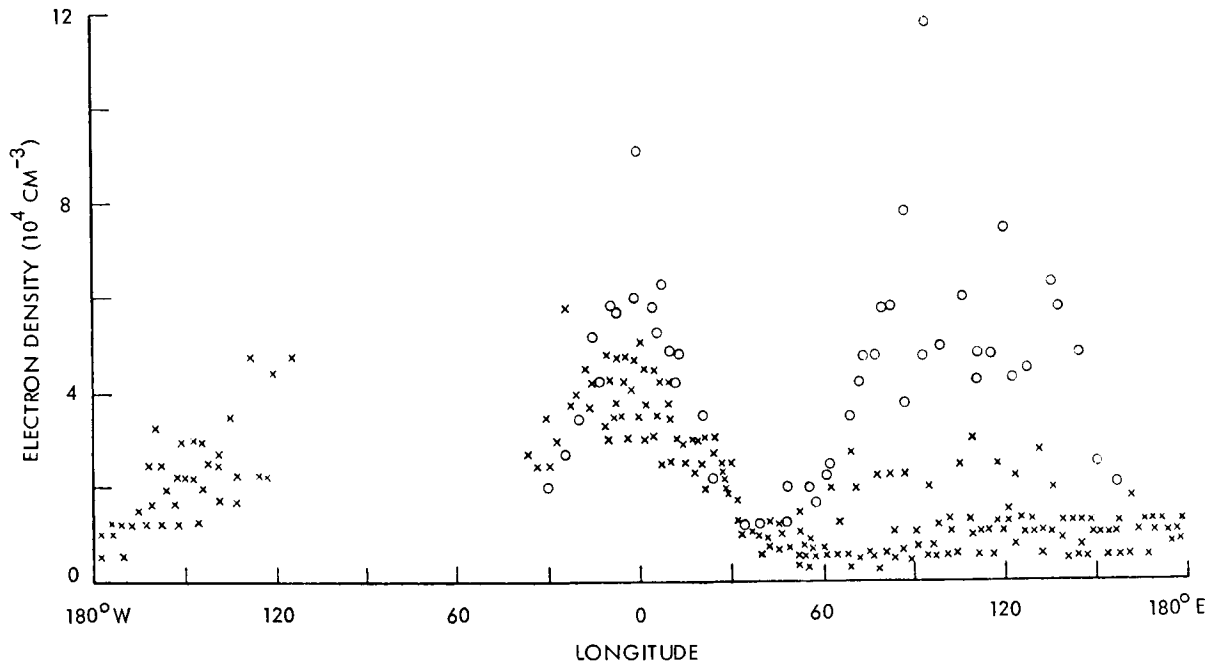


FIGURE 3-43. Collected data from a large number of records showing the correlation of ionization density at southern apex with the K_p index figure (9-15 June, X, Very calm period, $K_p < 3$; O, disturbed period, $K_p > 3$).

similar to the above, the correlation between the electron density and the K_p index is best investigated on a statistical basis. The collected data covering a complete band round the globe at 54°S for a period of about one week at the end of May, 1962, are shown in figure 3-43. It will be seen that there is a close correlation between the electron density and the K_p index and that the largest increases in electron density for high K_p index are observed in high magnetic shells of L value 3 to 6. Observations of the electron density in the high L shell regions over northern Canada for magnetically quiet and magnetically disturbed periods show only a comparatively slight correlation of electron density with K_p index. It is not clear why the correlation should be so weak in the N. hemisphere, but it may be associated with the intensity of the magnetic field which will determine the altitude of mirror points for trapped radiation. Alternatively, there may be a seasonal effect connected with the distortion of the magnetosphere by solar wind

pressure, but in any case these two effects will probably be related.

OBSERVATIONS DURING A 'SUDDEN COMMENCEMENT'

One well-defined sudden commencement occurred during the period 27 April to 9 July and this took place at 4.14 hours U. T. on 27 May. At this time Ariel was passing near the southern apex at 110°E longitude where high L value magnetic shells are encountered. Conditions were, therefore, favorable for observing corpuscular ionization and the results are shown in figure 3-44, for the day of the sudden commencement (27 May) and for the two previous days and one following day for comparison. It will be observed that on 25 and 26 May very steady conditions of ionization were observed in a band encircling the earth at 54°S and at 440 Km. altitude: the second of these days showing a distribution of ionization practically identical with the first. Where the band intersects high L shells (in the range L 3 to 7) south of Aus-

MAY 1962

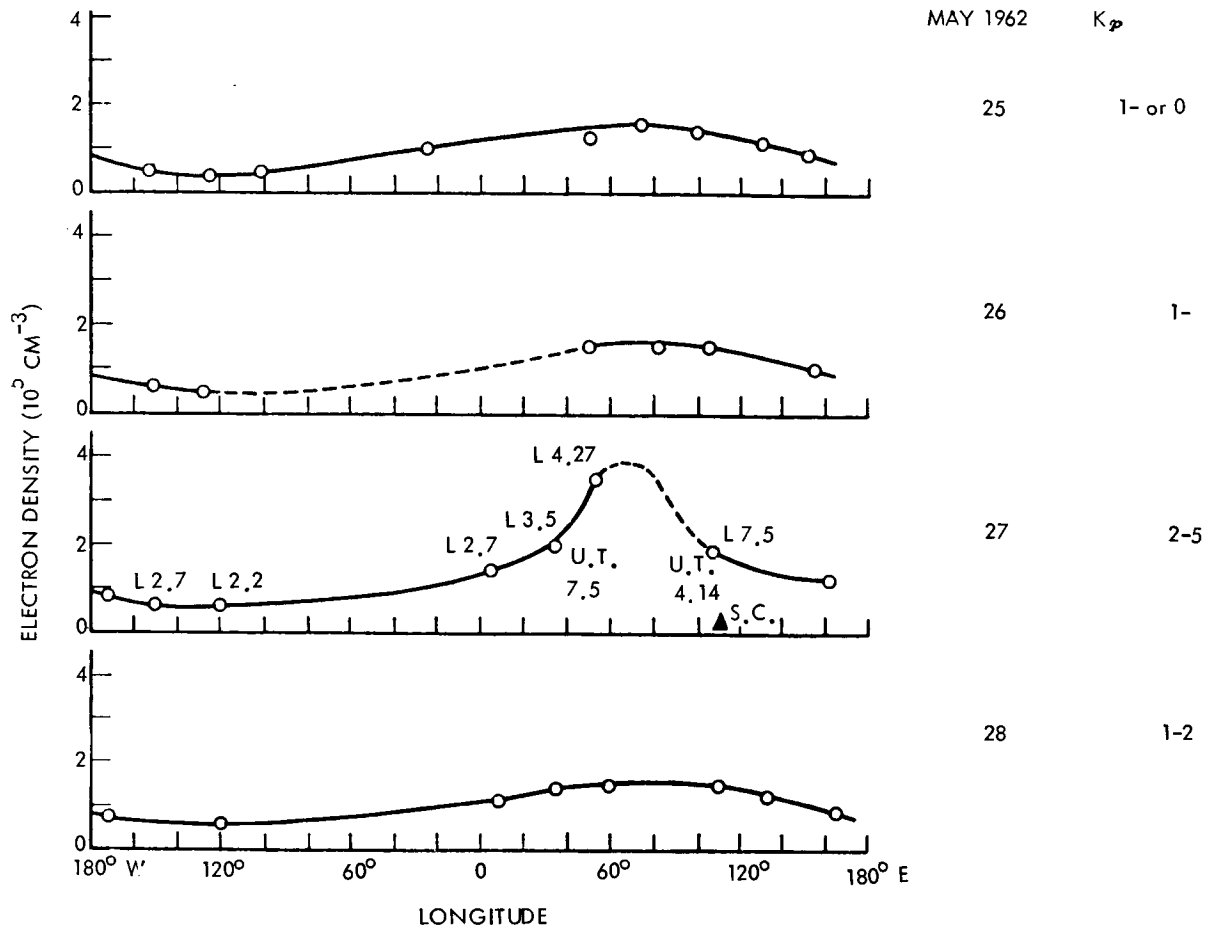
K_p

FIGURE 3-44. The electron density near southern apex about 2 hours after a sudden commencement with the corresponding records for the 2 previous days and the day following the s.c.

tralia, the ionization is two to three times higher than in the magnetically lower latitude sections of the band (L 2 to 3). The satellite passed through the high L region about two hours after the sudden commencement event and recorded a two to three-fold increase in the local ionization density: but a few orbits later when the S-apex was at low L values no increase of ionization density was recorded. On the next occasion (24 hours later) when the satellite scanned the high L region the whole pattern was indistinguishable from that two days preceding the S.C. event.

ASPECT HISTORY AND SPIN RATE ANALYSIS

Design Engineers

Dr. J. H. Alexander
Dr. P. J. Bowen

Data Analysis

Mr. C. L. Henderson
Dr. A. P. Willmore

The aspect sensor was designed and constructed at University College, London. It has been fully described by J. H. Alexander (1963) (67), and more briefly in NASA-SP-43 (1963) (17) and by R. C. Baumann (1964) (68). Its purpose was to provide information on the solar aspect and the spin rate of Ariel I, these quantities being essential to the interpretation of data from the radiation experiments. Spin rate data have also proved essential in the interpretation of electron temperature and density observed by the U.C.L. boom probe (Willmore et al, 1962) (40). The orientation of the spin axis in space has been estimated largely from solar

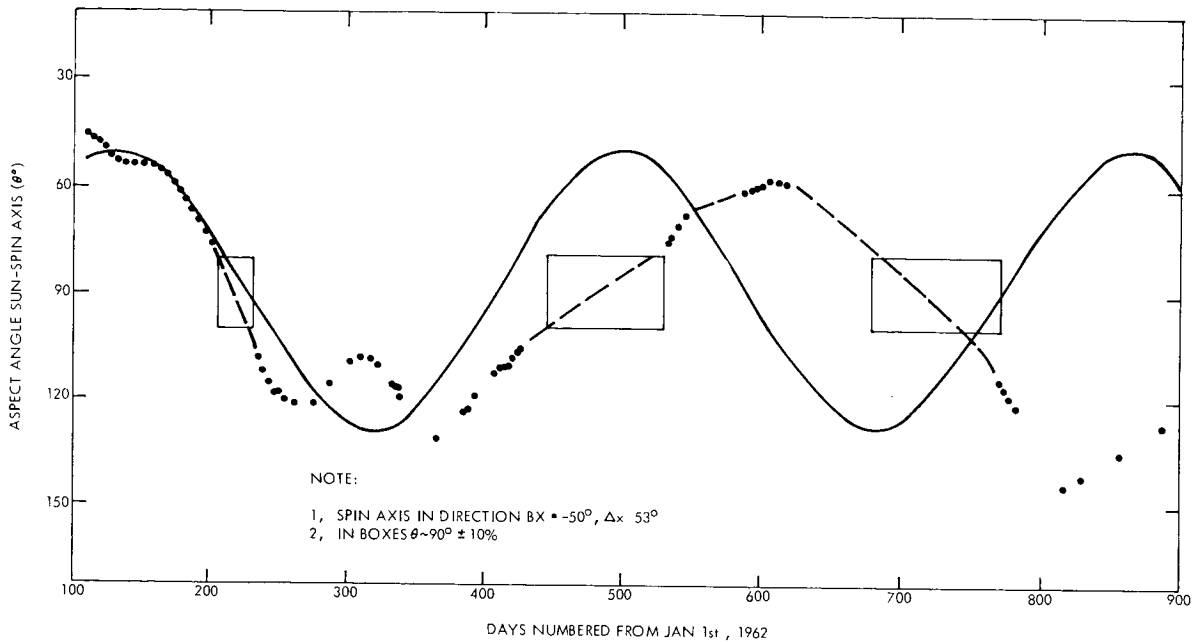


FIGURE 3-46. Variations of aspect angle with time.

Launch Period

A second aspect sensor was fitted to the third stage rocket. Data from this and the satellite sensor gave a graphic history of the sequence of operations involved in placing Ariel I in orbit. From the observed sudden decreases in spin rate and shocks recorded by accelerometers in the rocket, it was evident that the sequence of erection of booms and paddles did not take place according to plan. The solar paddles were not erected simultaneously, and their erection took place 14 minutes earlier than expected. The Birmingham electron density boom was also erected prematurely. The effect of this was to produce a steadily increasing nutation or coning angle at a rate of about $4^\circ/\text{minute}$. This nutation angle reached a value of about 57° at the time of separation of the satellite from the third stage. Fortunately, despite this series of mishaps, the spin rate in orbit was very close to the designed rate, and the nutation damped out within a few days.

Aspect History

The variations of aspect angle with time

are shown in figure 3-46. Note that the aspect angle in the figure and in the text from this point is the complement of the measured angle and defines the displacement of the solar vector from the spin axis.

If the direction of the spin axis in space, looking from the center of the satellite up through the mass spectrometer probe, is stated in terms of spherical coordinates referred to the ecliptic plane, then the aspect angle is given by

$$\cos \theta = \cos \beta_x \cos (\Lambda - \Lambda_x) \dots (1)$$

where $\theta = \text{aspect angle}$

$\beta_x = \text{celestial latitude of spin axis}$

$\Lambda_x = \text{celestial longitude of spin axis}$

$\Lambda = \text{celestial longitude of sun}$

If the direction of the spin axis were fixed in space, β_x and Λ_x would be constant, and θ would vary in approximately sinusoidal fashion between the limits of β_x and $180^\circ - \beta_x$ with a period of a year. This was approximately the case for about the first hundred days from launch.

Two ambiguities in equation (1) have to be resolved.

1. The aspect sensor is inherently incapable of distinguishing between aspect angles above and below the satellite equator, i.e. between θ° and $180^\circ - \theta$.
2. The signs of β_x and of $(\Lambda - \Lambda_x)$ are unknown.

The ambiguities were resolved simultaneously by making an independent estimate of the direction of the spin axis from the time of the maximum wake effect on the base electron temperature probe, using the data shown in Bowen et al (1964) (29) for days 117 and 142. This gave a mean value for β_x and Λ_x which was sufficiently accurate to eliminate the uncertainties.

The direction of the spin axis, using the assumption of a constant direction up to day 190, is $\beta_x = -50^\circ$, $\Lambda_x = 53^\circ$. This corresponds to declination -30° and right ascension 63° . The corresponding "theoretical" variation of θ is shown in figure 3-46. There is some indication of a precession of the spin axis about this mean direction, with a cone angle of the order of 10 degrees.

The aspect data for the period after day 190, when the Starfish nuclear explosion occurred, show some evidence of radiation damage to the sensor, but also evidence of a long-term drift in the direction of the spin axis. If the assumption of a constant direction of the spin axis is relaxed, equation (1) remains valid for any instant of time, but now θ is the half-angle of a cone around the earth-sun line, and the spin axis lies somewhere on this cone. The variation of θ with time can be transformed into a surface in the "space" coordinates of celestial latitude, celestial longitude and time. In principle, any line drawn on this surface in the direction of increasing time would define a possible variation of the spin axis coordinates. The value of θ defines an upper limit to the possible absolute value of celestial latitude, and when $\theta = 90^\circ$, the celestial longitude is $\Lambda_x = \Lambda \pm 90^\circ$.

These conditions, plus the expectation that the precessional motion will not be much more than one degree/day allow us to estimate the

time variations. A plot of the surface mentioned above shows that there is a net drift in the direction of increasing celestial longitude (or right ascension) of the order of 0.25 degree/day over the period of observations.

A preliminary examination of possible torques, based on the treatment by E. C. Semple (1964) (69), shows that the mean magnetic dipole moment of Ariel, estimated (17) at 200 dyne dm/gauss, is sufficient to produce a spiral precession with a period of 92 days and an initial half-cone angle of the order of 10 degrees. This angle will increase as the spin rate of the satellite decreases. The spiral will drift in the direction of increasing right ascension. Torques due to solar radiation and aerodynamic pressures are expected to be smaller but still significant, attributed mainly to contributions from the solar paddles.

Spin Rate Analysis

Figure 3-47 shows the variation of spin rate with time. The rate generally decreased, with a superimposed wave producing periods of increasing spin. This has been observed on very few spacecraft. The forces expected to have significant effects on the spin rate were:

- magnetic damping
- aerodynamic pressure
- radiation pressure

Magnetic damping was minimized by the use of non-magnetic materials as far as possible, and it was estimated (17) that the half-life of the spin rate due to this effect be one year. From the curve, the half-life appears to be 1.5 years.

A number of valuable papers on the effects of various torques on satellites has been published under the editorship of S. F. Singer (1964) (70). Among these, one by W. J. Evans gives a clear analysis of the forces due to aerodynamic and solar radiation pressure on a plane surface. The following analysis is based on that of Evans, with slight changes in symbols for convenience.

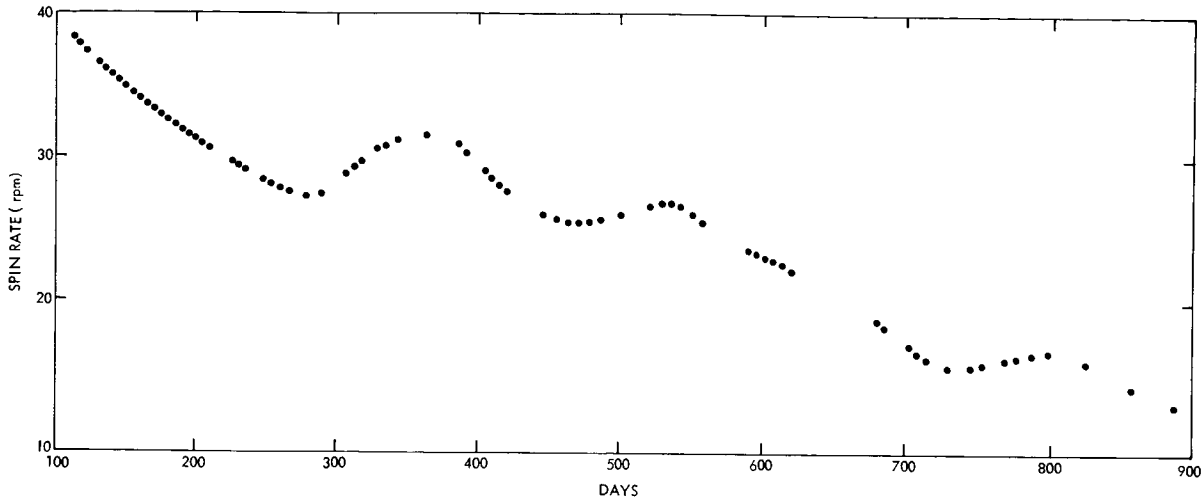


FIGURE 3-47. Variation of spin rate with time.

Aerodynamic Effect

We assume that the aerodynamic contribution to the spin rate is due solely to pressure on the solar paddles, which are so tilted as to act like a propeller. Evans develops a complicated formula for the total pressure or incident plus re-emitted normal momentum flux on an elementary surface.

He assumes the incident stream is in free molecular flow and in Maxwellian equilibrium. His expression does not reduce to zero when the incident stream is parallel to the surface, because of the thermal velocity of the particles within the stream, and because he is considering a single surface.

In the case of a solar paddle, which can be taken for simplicity as a flat plate, an incident stream parallel to the surface would flow over both sides, and the net effect would be a zero force. Under these conditions Evans' formula can be considerably simplified and can be shown to become, with slight approximations,

$$P = pU^2 \left\{ (2 - \sigma^1) \left(1 + \frac{1}{2S^2} \right) + \frac{\sigma^1}{2S} \left(\frac{\pi T_w}{T} \right)^{1/2} \right\} \cos^2 \eta \dots (2)$$

where P = pressure

p = air density

U = relative velocity of stream

σ^1 = reflection coefficient (0 for specular reflection, 1 for completely diffuse reflection)

$S = U/W_0$

W_0 = most probable thermal velocity of stream

T_w = surface temperature of paddle

T = stream temperature

η = angle of incidence of stream, measured from the normal to the paddle surface.

By inserting values appropriate to Ariel's orbit into the formula, we find that easily the most significant terms are p and η . The expression in the curly brackets is a pure number, and is of the order 1.1 for purely diffuse and 2.0 for purely specular reflection. We have assumed that the reflection is diffuse.

In applying the formula to determine the torque about the spin axis, we have to consider the paddles in pairs, since paddles I and III are on axes inclined at 45° and II and IV at 67.5° to the spin axis. The pressure and the resulting torque, which is a constant times the pressure for a given paddle, are averaged for a rotation of the satellite as a function of θ , the angle of attack, or angle between the inward stream vector and the spin axis. In calculating this average, the

effect of shielding due to the intervention of the body of the satellite or another paddle was taken into account. This amounted to about 5% of the average.

The variation of torque with θ was approximately symmetrical about $\theta=90^\circ$. There was a large retarding torque, almost constant for $0 \leq \theta \leq 60^\circ$, then a linear change through zero to a similar accelerating torque for $120^\circ \leq \theta \leq 180^\circ$. The mean torque over a rotation is finally averaged around an orbit. The major effect is clearly near perigee, where the density and stream velocity are a maximum. Averaging over a third of an orbit centered on perigee is sufficient to give the torque to two orders of magnitude.

For Ariel's geometry, a good approximation to the resultant acceleration effect is:

$$\frac{d}{dt}(\text{spin rate}) = KP_p f(\theta_p) \text{ rpm}/100 \text{ days.}$$

where $K=5.8 \times 10^{14}$

P_p = density at perigee (gm/cc)

θ_p = angle of attack at perigee

$f(\theta) \approx -1$ for $0^\circ \leq \theta \leq 60^\circ$

$\approx +1$ for $120^\circ \leq \theta \leq 180^\circ$

with a linear change for $60^\circ = \theta \leq 120^\circ$

The long term variation of this acceleration is shown in figure 3-48, together with that

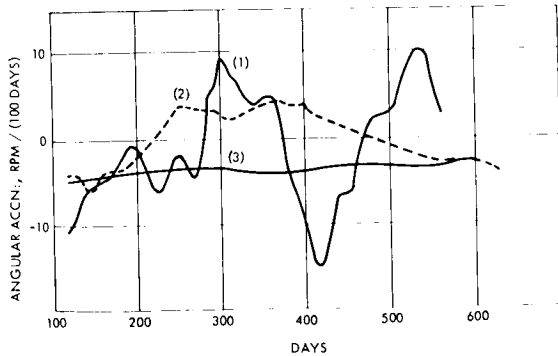


FIGURE 3-48. Long term acceleration variations. Due to (1) aerodynamic pressure, (2) direct solar radiation, and (3) magnetic damping.

due to direct solar radiation discussed in the next section.

Radiation Pressure Effect

Evans develops a formula for a surface in which there is no loss by conversion of radiation to electric power. It must therefore be modified when applied to a surface of solar cells. The incident radiation pressure, or normal momentum flux, is

$$P_i = \frac{S_i}{c} \cos \eta = \frac{S}{c} \cos^2 \eta$$

where S = solar constant,

$$= 1.395 \times 10^6 \text{ erg cm}^{-2} \text{ sec}^{-1}$$

c = velocity of light

η = angle of incident energy to the paddle normal, as before,

For contribution by reflection and re-emission, we have

$$P + \tau^1 + \alpha = 1$$

where P = reflectivity

τ^1 = transmissivity

α = absorptivity

In our case τ^1 can be regarded as equivalent to loss by conversion into power, and so is not zero. We cannot therefore eliminate α from the equations.

For diffuse reflection,

$$(Pr)_d = \frac{2}{3} P^s / c \cos \eta$$

For specular reflection

$$(Pr)_s = P^s / c \cos \eta$$

For re-emission of absorbed radiation

$$P_e = \frac{2}{3} x^s / c \cos \eta$$

So the total pressure is $P = P_i + P_r + P_e$

diffuse: $P_d = S/c [\cos^2 \eta + \frac{2}{3} (P + \alpha) \cos \eta]$

specular: $P_s = S/c [(1 + P) \cos^2 \eta + \frac{2}{3} x \cos \eta]$

According to J. H. Huth (1959) (71) the maximum efficiency of silicon solar cells is 14% in full sunlight, and loss by reflection is from 10 to 50%. Applying these figures we have:

$$P + \alpha = 0.86$$

$$P = 0.32 \pm 0.2$$

$$\therefore \alpha = 0.56 \pm 0.2$$

Inserting these values, we find that the type of reflection affects the total pressure by less than 10%. For convenience we assume the reflection is diffuse.

As for the case of aerodynamic pressure, the torque is averaged over a rotation of the satellite, and expressed as a function of θ , the aspect angle between the spin axis and the direction of the sun. The same expression of course applies to the case of earth-emitted and earth-reflected radiation, with appropriate definitions of θ .

For direct solar radiation torque, we then deduce the average per orbit by multiplying by the fraction of the orbit that is sunlit.

For earth-emitted radiation, the torque averaged round an orbit is very small. For a circular orbit the average would be exactly zero. To a first approximation we therefore neglect it.

Earth-reflected radiation, where it is a maximum, acts in the opposite direction to the solar radiation. Elsewhere its effective source is a point somewhere along the arc between the sub-satellite point and the sub-solar point. We have made a rough approximation to the average effect of this radiation by reducing the value of the solar radiation torque by one eighth.

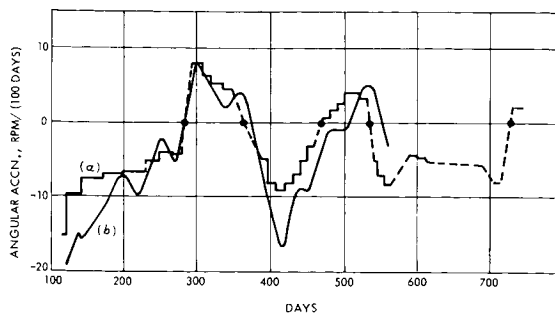


FIGURE 3-49. Resultant total acceleration; (a) observed and (b) calculated.

Total Acceleration

We have converted torques due to aerodynamic pressure and radiation pressure to resultant spin rate accelerations. We now adopt an estimate of about 1.5 years for the half-life for deceleration due to magnetic damping. The accelerations due to these three forces have been summed, and are shown in figure 3-49 together with the observed acceleration.

The aerodynamic effects were computed assuming that the spin axis was in the constant direction deduced for the first hundred days, and the agreement of the calculated and observed accelerations is a confirmation of the essential correctness of this orientation, while the departure in phase for the later period is probably due to a significant drift of the axis.

CHAPTER 4

Satellite Structure and Subsystems

The United States' responsibility for the satellite structure and subsystems was discharged by the Goddard Space Flight Center, and included the spacecraft structure, its separation and release system, and all spacecraft electronics not specifically associated with an experiment. The remainder of this section describes these components and systems and summarizes their performance during the life of the satellite. The fact that useful information was received from the satellite over a period of more than two and one-half years attests to the generally successful performance of the spacecraft.

STRUCTURE AND MECHANICAL DESIGN

C. L. Wagner

The Ariel I structure and mechanisms design encompassed two separate major areas of endeavor: (1) the satellite itself and (2) the development of a separation and release system interface structure and associated mechanisms.

The satellite itself relied heavily on the use of epoxy-bonded filaments of Fiberglas, used in combination with machined wrought aluminum alloys for much of its structure. The ancillary interface system (Dutchman and separation structures) was largely composed of magnesium thin-wall castings.

The overall spacecraft configuration is shown in figures 4-1 and 4-2. Figure 4-1 shows the satellite as it was stored in the vehicle prior to deployment. Figure 4-2 shows two views of the deployed satellite.

Satellite Structure

The spacecraft structure was divided into two main groups: the basic structure and the appendages. The basic structure was further divided into the following subcomponents:

1. Upper dome,
2. Mid-skin,
3. Shelf and base assembly,
4. Lower dome

The appendages were as follows:

1. Four solar paddles,
2. Two inertia booms,
3. Electron density experiment boom,
4. Electron temperature experiment boom.
5. Telemetry antennas.

Design Parameters

Several design considerations were paramount in the development of the structure:

The Scout 25.7-inch-diameter heat shield limited the payload size to 23 inches in diameter by 2 feet in length, not including certain experiments.

The aft appendages were folded into the space described by a hollow cylinder 23 inches O. D. x 18 inches I. D. x 4 feet, 8 inches long.

The structure had to be manufactured of non-metals and/or nonmagnetic materials, so that the effects of magnetic spin damping would be reduced to a degree that the half-life of the satellite's spin rate be one year.

The total satellite weight could not exceed 135 pounds.

ARIEL I: THE FIRST INTERNATIONAL SATELLITE

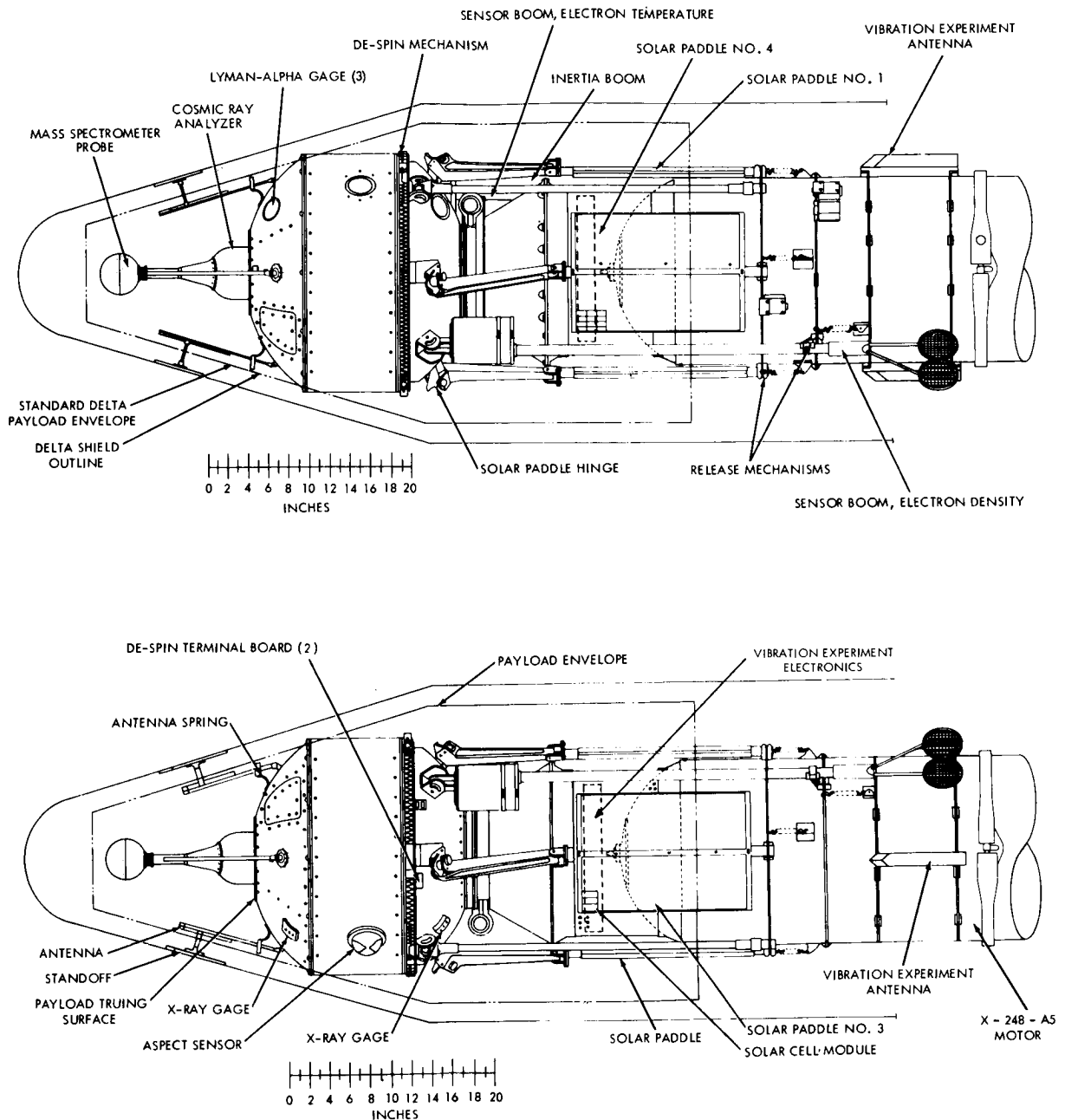


FIGURE 4-1. Ariel I before deployment; (Top) view along the Y axis, and (Bottom) view along the X axis.

The structure had to withstand accelerations and vibrations of the launch vehicle. In this case the ABL-X248-A5 motor (last stage) governed.

Outer Structure

As a result of the above considerations the

material chosen for the skin of the Ariel I was epoxy-bonded Fiberglas. The domes were constructed from monofilament glass fibers cross-woven into cloth laminations that were molded into a spherical shell of $13\frac{1}{2}$ -inch radius by $5\frac{5}{8}$ inches high. Shell Epon 828 with a CL hardener was used as the bond-

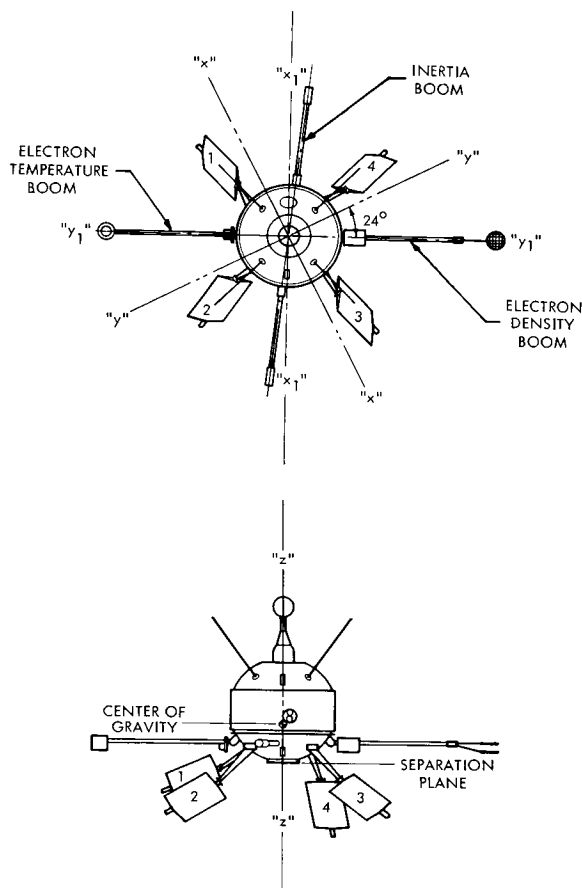


FIGURE 4-2. Ariel I deployed configuration.

ing agent. The top dome was $\frac{1}{16}$ inch thick, and the bottom dome—basically used only as a thermal shield—was $\frac{1}{32}$ inch thick. The midskin was made from a cylinder of epon-bonded, monofilament-wound Fiberglas $\frac{1}{16}$ inch thick x 23 inches in diameter x 10.7 inches long.

Upper Dome. Into the top of the upper dome skin was bonded and riveted an aluminum disk $8\frac{1}{2}$ inches in diameter x 0.2 inch thick. Machined integrally with, and centrally located on, the disk is a 7-inch-I.D. thin-walled cylinder extending internally 3.7 inches. This hat-shaped structure supported the cosmic ray-ion mass sphere experiments and the eight radial Fiberglas ribs, which were also attached to the dome skin—thus giving stiffness and strength to the dome. A machined aluminum ring was bonded and

riveted to the base of the dome to allow the assembly to be bolted to the top of the 23-inch-diameter mid-skin. Holes were cut in the dome to allow attachment of experiments and antenna mounts.

Mid-Skin. The mid-skin Fiberglas was bonded and riveted to two end flanges, machined from AISI 6061-T6 aluminum, which were shaped to provide nonshifting attachment to the upper structure and the shelf-base assembly. In detail, shear lips prevented radial movement, pins prevented rotational displacement, and machine screws tied the components together.

Lower Dome. The lower dome was segmented and fitted with doublers for installation of sensors and the segments themselves. Gold-plated aluminum machine screws held these components in position.

Shelf and Base Assembly

The instrument shelf and base assembly was made from AISI 6061-T6 aluminum plates, bars, and billets machined into shape and semipermanently affixed into the assembly condition. Two views of the shelf and base assembly are shown in figure 4-3. The separate parts are as follows.

Shelf. The shelf was a 21-inch-diameter plate 0.08 inch thick with eight integral stiffening ribs leading radially from a $7\frac{1}{2}$ -inch-diameter integral cylinder to the outer periphery. This undercarriage of ribbing tapered from 0.7 inch at the cylinder to 0.3 inch at the 21-inch diameter periphery. The top of the shelf at the 21-inch diameter was dished upward one inch and then extended radially to the 23-inch diameter. This step was machined to provide (1) a mounting sur-system and to provide a mating surface for the mid-skin.

Base. The base was a cylinder of seven inches I. D. and fitted into the $7\frac{1}{2}$ -inch-outer diameter short-shelf cylinder, extending aft $6\frac{1}{2}$ inches. The aft two inches were machined to an $8\frac{1}{2}$ -inch I. D. to provide proper view angles for the spin-axis-mounted electron temperature sensor. The forward seven inch-diameter x $4\frac{1}{2}$ -inch-long space was provided to contain the above sensor,

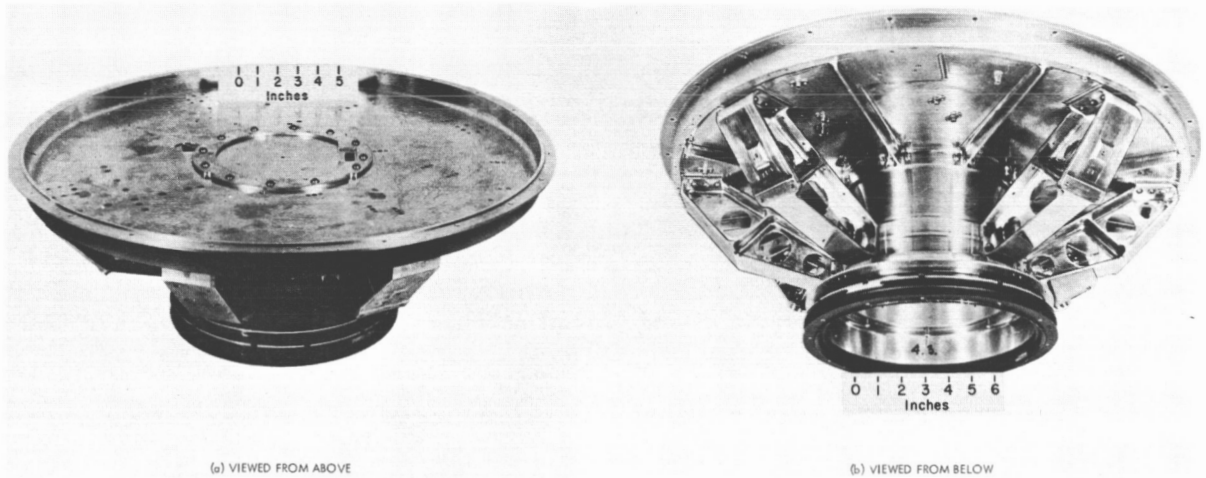


FIGURE 4-3. Shelf and base assembly.

the satellite's tape recorder, and the boom escapement mechanism. The outer diameter was machined to provide (1) a mounting surface for the separation adapter ring, (2) a mounting surface for the bottom dome segments, and (3) a key for six support struts.

Struts. The six struts were each machined from solid stock in the shape of a modified "I" beam. Each strut served to support the shelf and to supply the mount for a paddle arm or experiment boom hinge. The struts were keyed to the base and, after being fastened into position with machine screws, were keyed to the shelf by shrink-fit shear pins.

Appendages

The eight appendages should be considered in three separate groupings: paddle arms; inertia arms; and sensor, or experiment, booms.

Paddle Arms. The paddle arm and hinge design was suggested by that used on Explorer XII; however, space considerations dictated by the Scout heat shield and paddle location restrictions required by the experiments complicated the design considerably. The arms themselves were long slender channels machined from AISI 7075 aluminum. One pair of arms lead directly from their hinges to the paddle interface; but space and positional requirements for the other pair of

solar paddles required a secondary folding hinge at the outboard end of each arm. From this secondary hinge extended the paddle interface of these two arms.

Inertia Booms. The inertia booms, when extended, provided a proper moment of inertia ratio so that the longitudinal axis remained the spin axis of the spacecraft. These booms were made of thin-walled tubes of epon-bonded Fiberglas cloth rolled into cylindrical shape. Each boom was attached to the shelf by a detent-locking, spring-loaded hinge, and the outboard end of its 30 inches terminated in a four-inch long, 0.7-pound stainless steel weight. Both the inertia booms and the paddles were designed to be erected at 52.4 rpm, thus reducing spin to 36.6 rpm.

Experiment Booms. The sensor booms were supplied by the experimenters, but the method of erection was a structural responsibility. The hinge halves were machined from solid stock and used a double detent lock and a torsion-spring positive force to assure opening in the event of no payload spin-up. (This consideration was true in all appendage extension.)

Escapement

Normal erection rotation speed of the experiment booms was 76.5 rpm, which would

have produced large shocks to the experiments if these booms had been allowed to open without restraint. As a result, an escapement device was designed to reduce these forces by controlling erection speed.

The clock escapement principle was employed in the design of the timing mechanism. Since the primary interest in the application was shock reduction rather than accuracy or timing, the less sophisticated mechanism called a "run-away-escapement" was used. It consisted of a gear train coupled to an escape wheel, and a pallet fitted over the escape wheel to control its rotation rate. Since two booms are required to be simultaneously controlled, a double pulley mounted on a shaft was coupled to the free end of the gear train. A doubled nylon cord, with one end attached to the boom and the other end to the pulley, served as the control link. The rotation rate of the escapement was a function of the satellite acting torque and the moment of inertia of the part. The pallet's moment of inertia was adjusted to allow the booms to erect in 2 or 3 seconds. This escapement was designed to control the boom erection at a satellite spin rate between 60 and 90 rpm.

By virtue of being tied together, the booms erected simultaneously, avoiding any unbalance that would cause coning of the payload. (The other appendages opened too quickly to create this problem.)

De-Spin Device

The de-spin system was built in a self-contained ring fitting in the space provided at the periphery of the shelf. It was of the "stretch yo-yo" design, which will de-spin a system having a 20 percent nominal spin rate error to 2 percent of the required final value. The basic components used a pair of equal weights attached to a matched pair of long tension springs wound one-half turn about the payload. The weights were released by pyrotechnique guillotine cutters, and the weight-spring combinations released themselves from the s/c when in a radial attitude from the spacecraft. By this system the payload was de-spun from 160 to 76.5 rpm.

Antennas

The four turnstile-type antennas were of the double-fold design, so that they would fit into the heat shield. These antennas were located on the top dome equispaced 90 degrees apart, and in their erected position made an angle of 40 degrees with the spin axis. Upon ejection of the heat shield, the antennas were erected to their length of $21\frac{3}{4}$ inches.

Battery Containers

The two containers for the spacecraft battery power supply were designed to withstand the force of expanding gas generated internally in the sealed batteries, which could result from a partial power system malfunction. The container could withstand loadings of 50 pounds from each of two stacks of batteries without significant expansion—thus preventing rupture of the batteries and subsequent contamination of the payload. These containers were mounted on the instrument shelf and provided structural rigidity in the area of the inertia boom hinge.

Structure Weight

The above mentioned structural components and mechanisms, plus miscellaneous supports, brackets, and adapters accounted for 51.6 pounds of the total spacecraft weight.

Separation and Release Systems

Although not a part of the spacecraft, the separation and release system was responsible for programming proper de-spin of the system, erection of the appendages, and separation of the payload. The system was designed to adapt the spacecraft directly to the fourth stage of the Scout vehicle. A thin-walled, machined magnesium casting in the shape of a hollow, truncated cone formed the basic transition unit from the satellite to the last stage. At the satellite interface were the separation spring, segmented Marman clamp, separation bolts, and the two 3-pin feed-through connectors that carry into the satellite the de-spin signal, battery charge, and turn-on, turn-off circuit. The wide base

of the cone fit over the forward shoulder of the vehicle interface and was bolted to studs protruding from that surface. Fastened to the cone itself were two 12-volt battery supplies and an electronic release sequencer. Bonded to the cylinder of the X-248 motor were brackets and supports holding the release cords and pin pullers—which, when retracted, were to release the cords and allow erection of the appendages. Total balanced weight of this system was 18.3 pounds.

Delta Dutchman

When the Ariel I was transferred to the Thor-Delta vehicle, an adapter ring was required to move the folded payload forward some 12 inches so that the petal-leaf second-to-third-stage separation skirt would not damage the sensor booms during stage separation. This Dutchman (Figure 4-4) was a

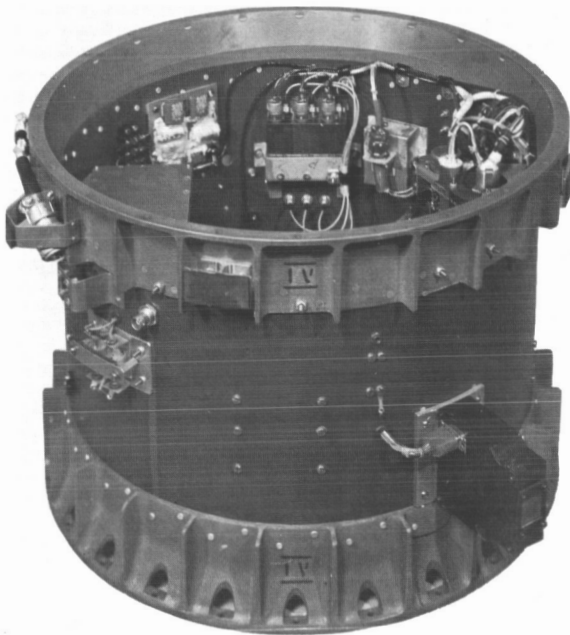


FIGURE 4-4. Dutchman adaptor cylinder.

fabrication of cast magnesium end rings separated by a 16-inch-diameter cylinder of rolled and welded 0.09-inch-thick magnesium sheet. The riveted fabrication was 13.0 inches long.

Since the Thor-Delta can carry a heavier payload than the Scout, the available space in the Dutchman cylinder was utilized to contain the electronics and sensors of a vibration and contamination experiment. The total weight of this composite was 17.0 pounds; the Dutchman accounted for 7.3 pounds of this total.

Structural and Mechanical Performance

Within the limits of information available, it may be stated that the structural and mechanical integrity of the spacecraft was maintained throughout the useful life of the satellite. The structure withstood launch and powered flight without discernible damage, and all appendages deployed, under the extra rigors of premature sudden de-spin, without damage. Valuable data on Delta vehicle vibration profile were obtained through the vibration experiment placed in the Delta Dutchman.

Premature De-Spin

The premature de-spin was the one failure that marred the structural and mechanical performance of the spacecraft. Four de-spin events occurred starting 100 seconds after ignition of the third stage X-248 rocket motor. Observed spin rate measurements and anticipated spin rate curve are shown in figure 4-5 for comparison of these events with those planned and predicted.

The measurements can be separated into five phases. From the completion of spin-up at 18^h 10^m 56^s, the spin rate increased to the end of third-stage burning. It then remained constant until 18^h 12^m 53.4^s, after which it decreased in four well-defined steps to 78 rpm at 18^h 14^m 15^s. This was the second phase. The third lasted until 18^h 25^m 30^s. From 18^h 18^m 20^s to 18^h 21^m 9^s, the spin rate diminished continuously, not in steps, and this is presumably true throughout the third phase. From 18^h 25^m 30^s to 18^h 28^m 30^s, the rate once again diminished in steps, and finally at 18^h 28^m 31^s it reached the value of 38.2 rpm, which was measured also at the end of the first orbit.

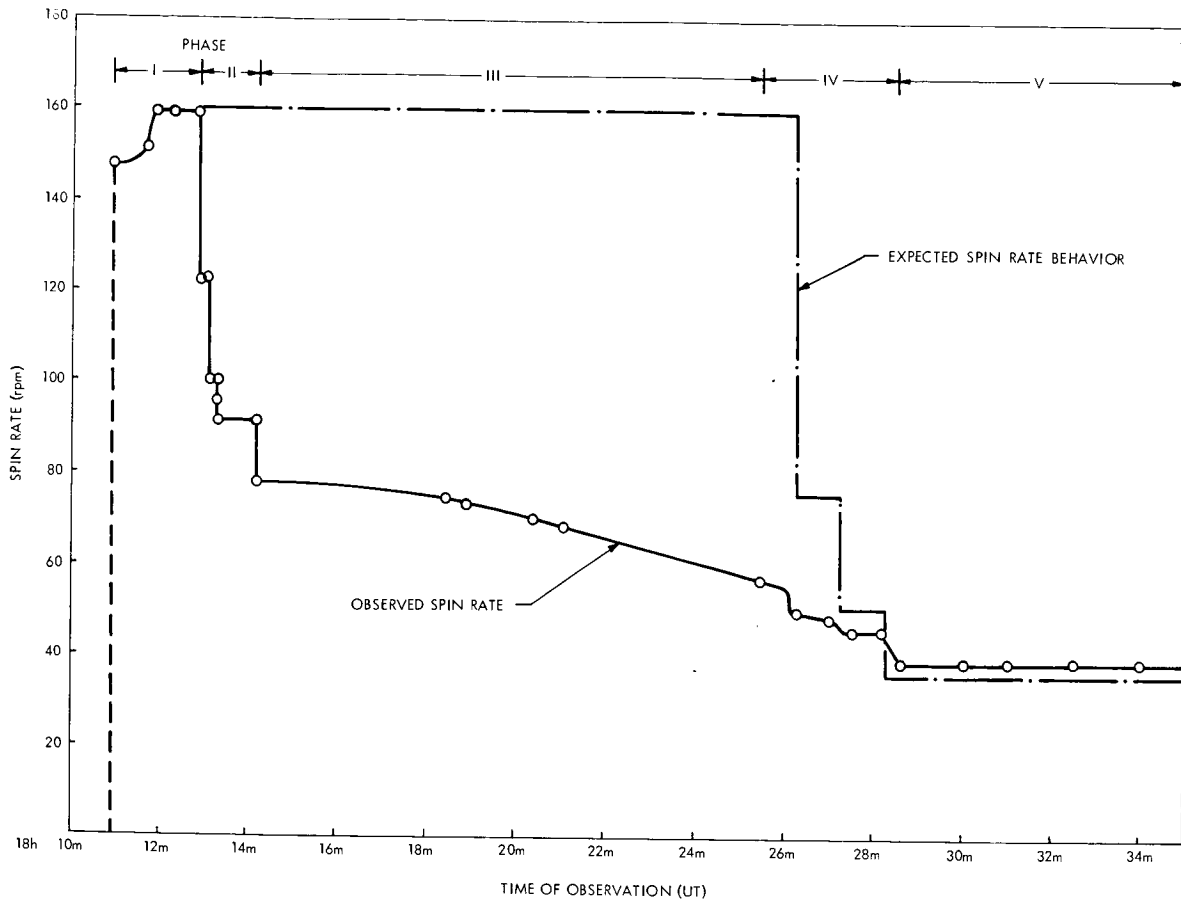


FIGURE 4-5. Expected and anticipated spin rate curves.

The anticipated spin rate variation with time is also marked on the graph. Apart from the agreement of the initial and final values, there is very little correspondence.

The four premature events which occurred in Phase II are shown in the graph of figure 4-5. The spacecraft rotational velocity changed from 158 to 122 rpm; then to 100 rpm; then to 90 rpm, and finally to 78 rpm in periods of less than 0.5 second each. A careful correlation of moment of inertia changes versus spin rate changes indicated premature erection of appendages in the following order:

1. Two adjacent solar paddles and one inertia boom
2. An experiment boom
3. A second experiment boom

4. The final two solar paddles and inertia boom

The spacecraft again saw rotational velocity changes in Phase IV: three de-spin sequences occurred at the prescribed time schedules. The first of these was undoubtedly due to yo-yo release, and the other two de-spins may have been due to pin puller release action. The point to be emphasized is that, if the premature erection sequences listed above did occur, the structure received far more serious stresses than normal erection would impart. Had not the design test series been as stringent as it was—and action taken to increase margins of safety where deemed necessary—Ariel I surely would have lost at least part of her appendages during the premature de-spins.

As a result of post launch tests and anal-

yses, the best explanation of the premature deployment, and resulting de-spin, is that the nylon tie-downs and/or RTV bonded tie-down fittings failed because of third stage skin temperatures in excess of those on which the tie-down system design was based. Typical X-248 temperature curves, on which the design was based, are shown in figure 4-6. From these curves it was determined that materials in the tie-down system would be subjected to heat only slightly in excess of 300°F. This was well within the tested limits of the nylon tie-down cords and the RTV bonding materials. Unfortunately this design did not take into account the effect of placing a foil shroud around the third stage motor to vent outgassing material away from the spacecraft. Prior to flight, test data were unavailable, and temperatures could not be accurately predicted. Subsequent tests on an X-258 motor with and without the foil wrapping indicated a marked increase in surface temperature for the foil wrapped motor. Figure 4-7 shows the mean curve for eight temperature sensors, located as shown in the illustration, on the surface of an X-258 motor.

Laboratory tests of the nylon cord under temperature and tension indicated a separation temperature in the range of 413°F to 459°F with initial tension of 80 pounds. Comparing this range with the curve of figure 4-7, it seems quite probable that the premature de-spin at approximately 100 seconds was caused by the failure of tie-downs under unanticipated temperature extremes.

Vibration Experiment

The Delta Dutchman was used to house the GSFC vibration experiment. This experiment was added after the change in vehicles necessitating the Dutchman provided room for additional instrumentation. Its purpose was to monitor flight vibration data for the ultimate purpose of establishing environmental test specifications for spacecraft launched on Delta vehicles.

The experiment telemetered three channels of data from liftoff to beyond premature de-spin of the Delta 9 vehicle. The three channels measured the vibrations along three orthogonal axes of the vehicle (longitudinal, lateral, and lateral + 90°).

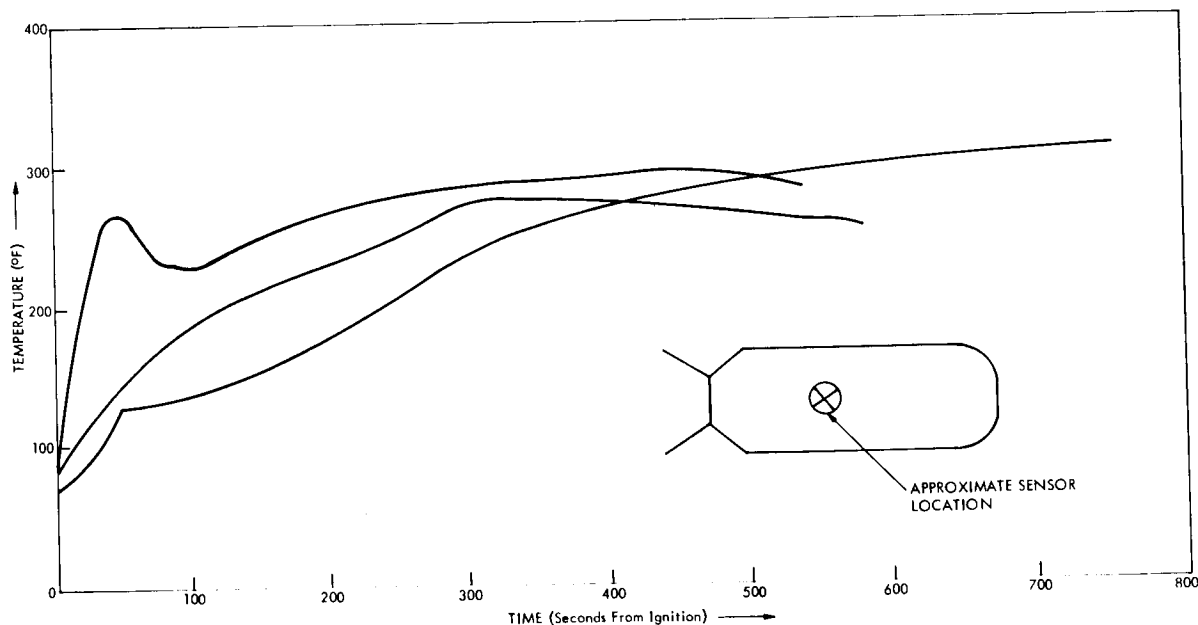


FIGURE 4-6. Typical temperature curves for X-248 rocket motor.

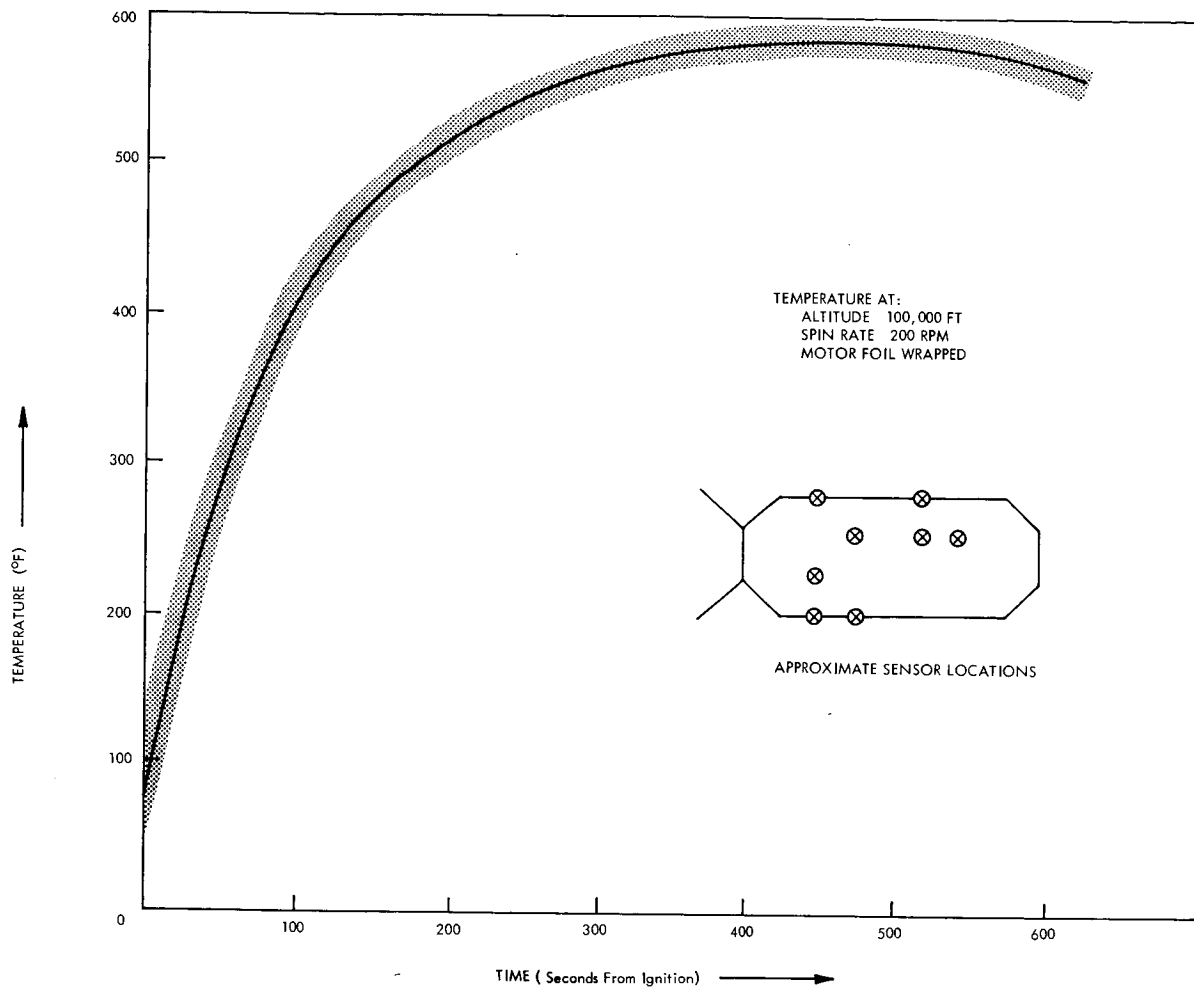


FIGURE 4-7. Mean temperature for eight sensors, foil wrapped X-258 motor.

Maximum vibration levels during first and second stage burning occurred at liftoff, staging, and fairing jettison with low levels between events. The third stage motor exhibited the normal resonant burning characteristics for this type of motor; that is, the tangential and longitudinal modes caused by acoustical cavity resonances.

A vibration summary from first stage ignition through second stage separation is given in table 4-1. Vibratory acceleration along thrust axis of the third stage is tabulated in table 4-2. With reference to table 4-2, it should be noted that the validity of values from 12 to 17 seconds is questionable because charge amplifiers were overloaded. A full discussion of the vibration experiment

results is given in NASA Technical Note, TN D-1683.

Detailed Data on Structure and Mechanical Design

Physical measurements of the structures and mechanisms of the Ariel I payload are presented as Appendix A.

THERMAL DESIGN AND COATINGS

M. Schach
 and
 R. E. Kidwell

The thermal design was based on an analysis of temperatures at 22 points in the main structure (figure 4-8) for the following parameters:

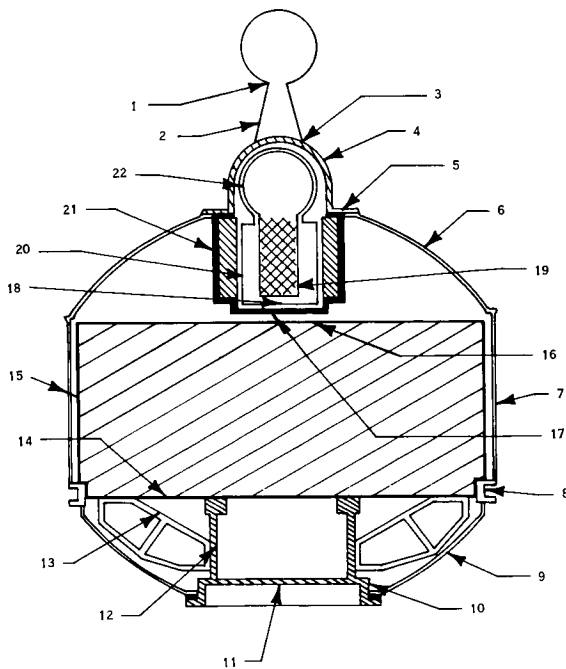


FIGURE 4-8. Temperature sensor location.

1. 63% and 100% sunlight;
2. Solar Aspect: 0 (Broadside), $\pm 30^\circ$, $\pm 45^\circ$, $\pm 60^\circ$, and $\pm 90^\circ$, allowing for shading by solar paddles and booms;

3. Internal power dissipation: 0.75, and 15 watts; and
4. Nominal or average values of the solar constant and the properties of the thermal coatings, and overall tolerances of $\pm 10\%$ to allow for seasonal variation of the solar constant, for uncertainties in the α/ϵ of the thermal coatings, and for approximations in the analysis.

Similar design calculations were made for the solar paddles and for the experiments mounted on booms.

There were a number of problems in the thermal design. First and foremost was the conflict between the experimenters' requirement for a stable and highly conductive surface, with a preference for gold or rhodium, and a thermal requirement for surface coatings with the proper and reliable values of α/ϵ , and a preference for a high percentage of black paint. The solution was a compromise where 75% of the surface area was coated with evaporated gold and the remaining 25% of the surface was coated with stripes of black and white paints.

Another problem was the development of a process for applying the thermal coatings to

TABLE 4-1.

Vibration Data Summary of Delta 9 Vehicle

Event	Composite Acceleration (peak g)		
	Thrust Axis	Lateral Axis	Lateral plus 90-Degree Axis
First-Stage Ignition	---	---	---
T-1	0.5	0.5	0.3
Liftoff, T+0	2.50	1.9	0.9
Liftoff +1 second	0.75	0.6	0.6
Main Engine Cutoff	2.0	0.3	0.4
Second-Stage Ignition	*	*	*
Jettison Fairing	0.25	1.0	1.0
Second-Engine Cutoff	2.25	0.3	0.3
Spinup	---	0.47	0.4
Blow Third-Second Stage Separation Bolts	---	1.57	0.4
Third-Stage Ignition	†	†	†

* RF signal dropout.

† See table 4 2.

TABLE 4-2.
Delta 9 Third-Stage Vibratory Acceleration Measured Along the Thrust Axis During Third-Stage Burning
One-Third-Octave Band Analysis. (All entries corrected for frequency response; paper speed 10 mm/sec;
pen writing speed 160 mm/sec; low-pass output filter (4200 cps)).

Center Freq. (cps)	Ign t=0	MAXIMUM ACCELERATION (g rms) AT TIME t (sec)																																													
		t=1	2	3	4	5	6	7	8	9	10	11	12	13	14	15	16	17	18	19	20	21	22	23	24	25	26	27	28	29	30	31	32	33	34	35	36	37									
40							.4			.13			.14					.2																													
50					.16	.22			.2																																						
63	.18								.18																																						
80	.16								.18																																						
100	.16				.14	.13			.16																																						
125	.18			.16	.12			.16	.18																																						
160	.16		.16	.16	.16	.16	.16	.14	.22		.22							.13																									.14				
200	.14	.13	.16	.2		.25	.2	.18	.2	.2	.16						.16		.16	.23	.16	.16	.18	.16	.18	.16	.16	.16	.16	.17	.13	.14	.16	.16	.16	.13											
250	.16	.16	.16	.19	.26	.27	.2	.2	.30	.16	.16	.16	.16	.14	.14	.16	.19	.19	.23	.43	.38	.38	.43	.38	.45	.43	.43	.45	.43	.32	.34	.34	.34	.34	.34	.32	.30	.38	.34								
320	.30	.32	.40	.30	.30	.61	.54	.37	.34	.38	.25	.28	.28	.28	.30	.28	.29	.32	.43	.38	.38	.43	.38	.45	.43	.43	.45	.43	.32	.34	.34	.34	.34	.34	.32	.30	.38	.34									
400	.16	.20	.22	.20	.25	.28	.22	.25	.25	.22	.20	.19	.16	.15	.16	2.08	2.08	.25	.20	.22	.25	.25	.25	.25	.25	.22	.20	.23	.16	.23	.20	.22	.25	.22	.20	.22	.20	.22	.20								
500	.22	.17	.22	.22				.22	.27			.19					.68	.68	.22		3.9	3.9	3.9	3.9	3.9	3.7	3.0	2.5	1.3	.49	.49		.24	.43													
630	.30	.30	.19	.25		.25	.30	.26	.28	.22								.25		13.4	13.4	13.4	12.0	10.7	9.6	7.6	5.9	2.5	1.1	.54	.27	.27	.43														
800	.35			.30	.24			.31	.33			.60						.31		.54	.54	.54	.52	.48	.39	.31	.26																				
1K	.32			.32	.57			.32	.33			.85					.24		.32	.24																											
1250	.44			.40	.55			.40	.40	.38							.28	.40	.56	.28	.71	.79	.63	.50	.44	.35	.32	.32																			
1600	.79			.50	.40	.40		.56	.56	.44																																					
2K	.71	.44	.44	.71	.50	.56	.56	.71	.71	.79	.50	1.58	2.24	3.96	7.06	9.95	11.2	4.0	.50	.56	.56	.50	.44	.56	.56	.56	.56	.56	.50				.56														
2.5K	2.5	.79	.79	.89	1.25	1.41	1.58	3.15	4.6	3.54	1.41	35.4	39.7	56.1	56.1	56.1	46.5	7.9	.89	1.41	.89	.79	.79	.79	.79	.79	.79	.79	.79	.79	.79	.79	.79	.79	.79	.79	.79	.79	.79	.79	.79	.79	.79	.79			
3.2K	2.5	3.5	5.0	7.9	17.7	21.3	21.8	12.5	12.5	12.5	11.0	11.0	8.8	7.9	5.6	5.6	4.4	3.5	3.5	2.0	3.2	1.8	1.7	1.6	1.4	1.4	1.6	1.4	1.4	1.4	1.4	1.4	1.4	1.4	1.4	1.4	1.4	1.4	1.4	1.4	1.4	1.4	1.4	1.2			
4K	28.8	26.5	25.0	25.0	15.8	8.3	6.0	4.0	4.8	5.6	5.6	4.0	16.0	4.4	4.4	3.5	4.4	6.3	7.0	4.0	4.0	3.5																									
5K																																															

← OVERLOAD →

the Fiberglas skins of the satellite that provided mirror-like gold surfaces with good adhesion and maintained the ability to withstand aerodynamic heating to 250°F. In addition, 1.5 mils of copper was required on the cylindrical section and forward dome to provide a ground plane for the antennas. This problem was solved by developing the following process. First, the substrate was sanded, cleaned, and baked at 310°F for one hour. Then layers of varnish, lacquer, paint, and metals were applied in the following sequence and baked at the temperatures and for the time intervals indicated (See figure 4-9.):

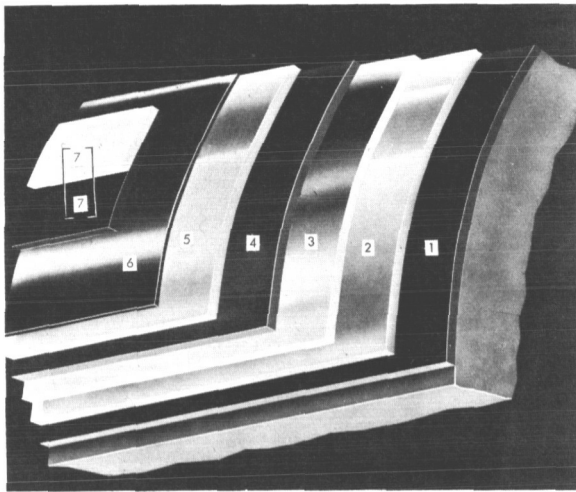


FIGURE 4-9. Thermal coatings.

1. Sealing varnish, 300°F for 20 minutes
2. Metallizing lacquer, 290°F for 30 minutes
3. Silver paint, 280°F for 18 hours
4. Electroplated copper, 1.5 mils
5. Lacquer, 275°F for 30 minutes
6. Evaporated gold, opaque coating
7. Four spray coats of black silicone paint in longitudinal stripes, 250°F for 30 minutes.

The lacquer was a special type developed for providing a smooth, mirrorlike finish as a base for the evaporated gold. Sealing varnish plus repeated baking at successively decreasing temperatures was used to prevent damage to the gold surface by outgassing of

the substrate when heated to 250°F. Final adjustment of the α/ϵ was made by applying white paint (ZnS, Silicone) over part of the black paint areas.

A third problem was to provide adequate temperature control for those experiments which were not located centrally in the spacecraft, and whose temperatures could be expected to vary widely with changes in solar aspect. The solution of the problem was to adjust the coating patterns to minimize the temperature extremes thereby avoiding temperatures that could cause failures. As an example, for the cosmic ray experiment it was necessary to keep the temperature of the perspex sphere (figure 4-8, node 22) well under 70°C, the sphere softening temperature, with sunlight incident on the forward surfaces of the satellite. On the other hand, when sunlight would be incident on the aft surfaces, the temperature of the photomultiplier (figure 4-8, node 19) could drop as low as -16°C. This would be below the desired minimum operating temperature but would not cause failure.

Finally, there were two thermal problems in conjunction with the launch phase. First, the heat radiated from the inner walls of the Delta nose fairing, followed by direct aerodynamic heating after fairing ejection, would cause overheating of the thermal coatings on the forward dome. Second, outgassing products from the heated inner walls of the nose fairing would condense on the spacecraft coatings causing a change in surface conductivity and an increase in the α/ϵ of the gold surfaces. Tests simulating the launch environment showed that the problem could be avoided if the inner wall temperatures did not exceed 125°F. This was accomplished by applying an ablative compound to the external surfaces of the conical section of the nose fairing to limit inner wall temperatures to 200°F and by attaching with standoffs to the inner wall an inner shield of Fiberglas impregnated with Teflon. The inner surface of the mylar shield which viewed the satellite was not expected to exceed 125°F when a 3 sigma low trajectory was used to predict the heating rates. The solution of the aerody-

dynamic heating problem was to delay the ejection of the nose fairing until the heating rate was sufficiently low to limit the maximum temperatures of the thermal coatings to 250°F.

Thermal Performance

Temperatures were monitored at three points in the satellite. However, temperature data have been made available for only one of these points, the temperature of the University College, London, Stack #2, located on the main shelf. These data can be used as a measure of the average temperature of the satellite and are plotted in Appendix B, along with data on percentage time in sunlight, solar aspect, etc.

The maximum predicted temperature for the observed range of orbital conditions was 40°C. Whenever the satellite went into 100% sunlight, the average temperatures ranged from 42°C to 47°C. This occurred for periods of from 4 to 10 days about four times a year. During these times the temperatures were 2°C to 7°C above maximum predicted values but remained within the 10°C safety margin between flight and proto-

type test levels. Most of the time the temperatures ranged between 22°C and 30°C.

To assess the accuracy of the thermal design the average internal power dissipation must be known. Since this was not telemetered it was estimated as a fixed load of 5 watts plus the percentage time in sunlight, times the product of the maximum charging current to the battery, and the voltage of the charge regulator. Both the current and the voltage were temperature dependent, and the values used correspond to the observed temperatures. The power estimates used were 11 watts at 64% sunlight and 25°C, and 13 watts at 100% sunlight and 45°C. A comparison of observed temperatures at 64% and 100% sunlight with corresponding predictions based on nominal design parameters and the above power estimate is shown in table 4-3. It is noted that the flight temperatures were from 9°C to 16°C higher than predicted. For the values shown in the table the average error is 12°C. This would correspond to a 17% error in the computed heat flow based on nominal values or 7% greater than the assumed $\pm 10\%$ tolerances. When the tabulated values are grouped according

TABLE 4-3.

Observed Temperatures With Corresponding Predictions

Date	Percentage Sunlight	Solar Aspect	Prediction °C	Observed °C	Error °C
May 3, 1962	64	40	13	24	11
May 25, 1962	100	34	32	42	10
June 16, 1962	64	30	13	23	10
Aug. 5, 1962	100	0	33	47	14
Aug. 21, 1962	64	0	14	23	9
Oct. 1, 1962	64	-32	10	24	14
Nov. 4, 1962	64	-25	10	26	16
Nov. 28, 1962	100	-15	31	42	11
Nov. 29, 1962	100	-15	31	45	14
Feb. 25, 1963	64	-15	12	28	16
Apr. 1, 1963	64	0	14	24	10
June 22, 1963	64	15	13	22	9
Aug. 27, 1963	64	30	13	26	13
Dec. 17, 1963	64	0	14	29	15
May 8, 1964	64	45	13	25	12
Aug. 26, 1964	64	0	14	25	11

to positive, zero, and negative solar aspects, the average errors are 11°C , 12°C , and 14°C , respectively. Since paddle shading occurred at negative aspects only, one can conclude that the basic error in the thermal design was 11°C or 12°C and that an additional 2°C or 3°C can be attributed to error in the analysis of paddle shading. The basic error can be attributed primarily to error in the measurements of the optical properties of the thermal coatings and to changes in these properties prior to or after launch. Because of improvements in measurement techniques since Ariel I, 6% of the 17% total error can be attributed to errors in measurement of the absorptance of the black paint and of the emittance of both the black and white paints. The remaining 11% error can be attributed to increased absorptance due to degradation of the white paint and the evaporated gold. Increased absorptances either from 0.25 to 0.45 for white paint or from 0.25 to 0.30 for gold would account for the 11% error.

A gradual degradation of the coatings is not apparent in the temperature data. Even

the radiation from the high altitude explosion of July 9, 1962, did not cause either a sudden or a gradual increase in satellite temperature. Most of the degradation that might have occurred must have happened during the first few days. This is consistent with data from ground tests with UV radiation. With samples of white paint and of evaporated metals, for which there is some evidence of surface contamination, the degradation is very rapid for the first few days and then tends to level off. The causes of surface contamination have not yet been evaluated. Possible suspects are contaminants in the application process, diffusion pump oil from thermal-vacuum tests, and the use of protective coatings.

ELECTRONIC SYSTEM

J. Turkiewicz

The major functions of the electronics supplied by the Goddard Space Flight Center were to provide power to all spacecraft systems, process and store data from the U.K.

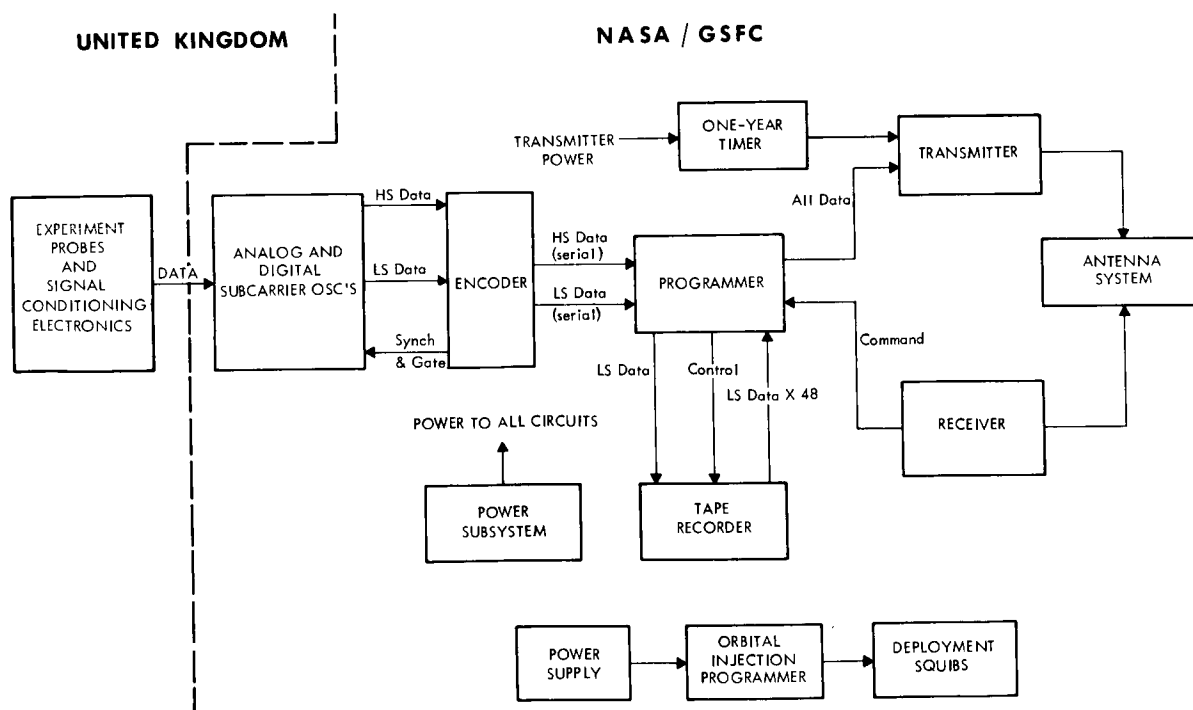


FIGURE 4-10. Electronic subsystems, functional block diagram.

supplied experiments, and transmit these data, both real time and stored, to ground tracking stations. Additional and independent electronic modules were provided by GSFC to program deployment events associated with orbital injection. This section describes those portions of spacecraft electronics provided by GSFC. (Experiment electronics, supplied by the U.K., are described in Chapter 3.) However, the interface between the experiments and GSFC electronics is discussed briefly where appropriate.

The functional block diagram of figure 4-10 illustrates the manner in which GSFC electronics accomplished their purpose. Data from experiment probes were converted by the U.K. experiment signal conditioning packages, to signals suitable for use by "analog and digital oscillator cards" furnished by the GSFC as a part of the encoder. Conversion of high-speed data to an FM analog in the range of 5kc to 15kc is illustrated in the graphs of figure 4-11. Low speed data were converted in a similar manner, but the frequency range was divided by 48.

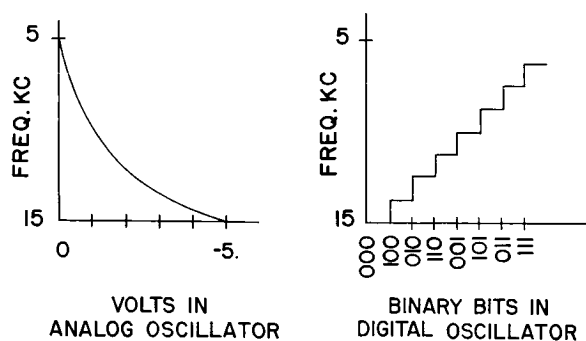


FIGURE 4-11. Probe data conversion.

Both low-speed and high-speed data were read out of their respective conditioning and oscillator circuits serially under control of synchronizing and gating signals from the encoder. These signals were generated by two electronic commutators in the encoder, one high-speed and one low-speed, operating simultaneously. (Low-speed data were stored on the tape recorder while high-speed data were being transmitted.) Figure 4-12 shows

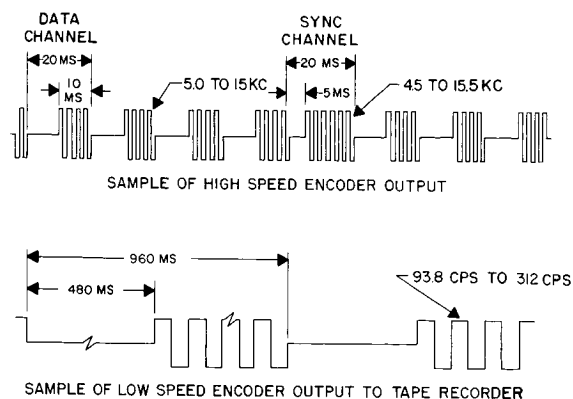


FIGURE 4-12. Idealized encoder output waveforms.

idealized waveforms of these outputs to the programmer. The high-speed output consists of 10-millisecond information bursts separated by 10-millisecond spaces, except for the synch channel which consists of a 15-millisecond burst and a 5-millisecond space. The low-speed output consists of 960-millisecond channels, each of which is divided into a 480-millisecond space and a 480-millisecond burst of low-speed information.

The programmer accepts the serial outputs from the encoder and acts as the control element in routing them to the tape recorder and transmitter as required. In normal operation, the high-speed data were routed to the transmitter for real-time transmission, and the low-speed data were routed to the tape recorder for storage. Once every orbit, when the satellite was over a ground station, a command to read out the stored data was transmitted. On receipt of this command from the receiver, the programmer switched the recorder to playback mode; the recorder played back stored low-speed data at 48 times the recording speed so that the recorder output to the transmitter looks the same as the high-speed encoder output; the programmer switched transmitter input from high-speed to low-speed data; and the stored data were transmitted to the ground station. After recorded data were transmitted the programmer switched the recorder back to record mode and restored the real-time input to the transmitter.

Power to the transmitter was provided through a timer designed to cut off the transmitter after one year of operation. (Fortunately, this timer failed to operate allowing more data to be collected.) The transmitter relayed all data to ground stations via the antenna system. Transmitter output format is shown in figure 4-13.

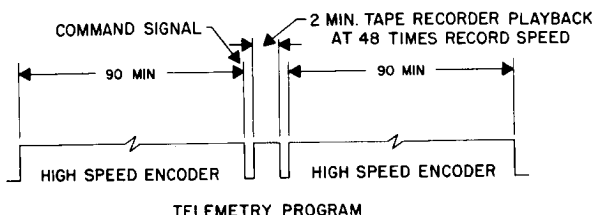


FIGURE 4-13. Transmitter output format.

The antenna system consisted of a four element array and a power divider which allows the system to be utilized for both transmitting and receiving. The receiver was used exclusively for the data readout command.

A separate electronic system was provided for orbital injection programming. Operating from an independent power supply, this electronic clock provided the signal to actuate separation and appendage deployment squibs at the right time and in the proper sequence.

ENCODER

H. White

The overall function of the encoder was to re-arrange the data from the experiments into channels and frames for transmission via the telemetry transmitter. The encoder is a two-speed device providing high-speed encoding (50 cps) for real time data and low-speed encoding (50/48 cps) for stored data. Table 4-4 identifies all inputs to the encoder identifying each as to whether it is high-speed (HS) or low-speed (LS) data. Encoder output format is shown in figure 4-14. A high-speed encoder sequence consisted of 16 frames each containing 16 information channels.

The low-speed encoder sequence consisted of two 15-channel frames.

The block diagram of figure 4-15 shows the major functional elements of the encoder and their relationship to the experiments and other spacecraft system elements. The primary encoder element is a crystal-controlled clock, the crystal frequency of which is divided to produce a 50-cps signal for the high speed (HS) encoder data rate. The 50 cps is divided by 48 to produce the low speed (LS) encoder data rate of 50/48 cps.

Operation of the HS encoder was made independent of the operation of the LS encoder for increased reliability. However, a loose type of synchronization between the two encoders was provided, synchronization being achieved when both encoders start their

FRAME	CHANNEL															
	0	1	2	3	4	5	6	7	8	9	10	11	12	13	14	15
0	S	C	C ₂	C ₃	E ₃	E ₄	E ₁	E ₂	T ₁	T ₂	U ₁	U ₂	I ₁	I ₂	E ₁	E ₂
1		C ₄	C ₅	C ₆												
2		T ₃	L	E _{m1}												
3		T _m	A ₁	E _{m2}												
4		U ₃	A ₂	E _{m3}												
5		U _m	P ₁	P												
6		I ₃	X _{m1}	X _{m2}												
7		I _{m1}	I _{m2}	P ₂												
8		C ₁	C ₂	C ₃												
9		C ₄	C ₅	C ₆												
10		T ₃	L	E _{m1}												
11		T _m	A ₁	E _{m2}												
12		U ₃	A ₂	E _{m3}												
13		P	P ₁	P												
14		I ₃	X ₁	X ₂												
15		X ₃	X ₄	X ₅												

HIGH-SPEED FORMAT

FRAME	CHANNEL															
	0	1	2	3	4	5	6	7	8	9	10	11	12	13	14	15
0	S	X ₁	X _{m1}	E ₄	E ₁	E ₂	E ₃	X ₁	C ₁	C ₂	C ₃	C ₄	X ₁	A ₃	C ₅	C ₆
1	S	X ₁	X	E _{m4}	E _{m1}	E _{m2}	E _{m3}	X ₁	T ₁	T ₂	T ₃	L	X ₁	U ₁	U ₂	U ₃

LOW-SPEED FORMAT

FIGURE 4-14. Encoder output formats.

TABLE 4-4.
Encoder Input Data

Experiment	Nomenclature of Each Output	Experiment	Nomenclature of Each Output
Electron temperature no. 1	U_1 —HS U_2 —HS U_3 —HS U_m —HS U_1 —LS U_2 —LS U_3 —LS	X-ray counter—Con.	X_4 —HS X_5 —HS X_{m1} —HS X_{m2} —HS X_1 —LS X_{m1} —LS
Electron temperature no. 2	T_1 —HS T_2 —HS T_3 —HS T_m —HS T_1 —LS T_2 —LS T_3 —LS	Cosmic ray	C_1 —HS C_2 —HS C_3 —HS C_4 —HS C_5 —GS C_6 —HS C_1 —LS C_2 —LS C_3 —LS C_4 —LS C_5 —LS C_4 —LS
Mass spectrometer	I_1 —HS I_2 —HS I_3 —HS I_{m1} —HS I_m —HS	Electron density	E_1 —HS E_2 —HS E_3 —HS E_4 —HS E_{m1} —HS E_{m2} —HS E_{m3} —HS E_{m4} —HS E_1 —LS E_2 —LS E_3 —LS E_4 —LS E_{m1} —LS E_{m2} —LS E_{m3} —LS E_{m4} —LS
Lyman-alpha	L —HS L —HS		
Aspect	A_1 —HS A_2 —HS A_3 —HS A_3 —LS		
Performance parameters	P —HS PV_1 —HS PV_2 —HS Pt_1 —HS		
X-ray counter	X_1 —HS X_2 —HS X_3 —HS		

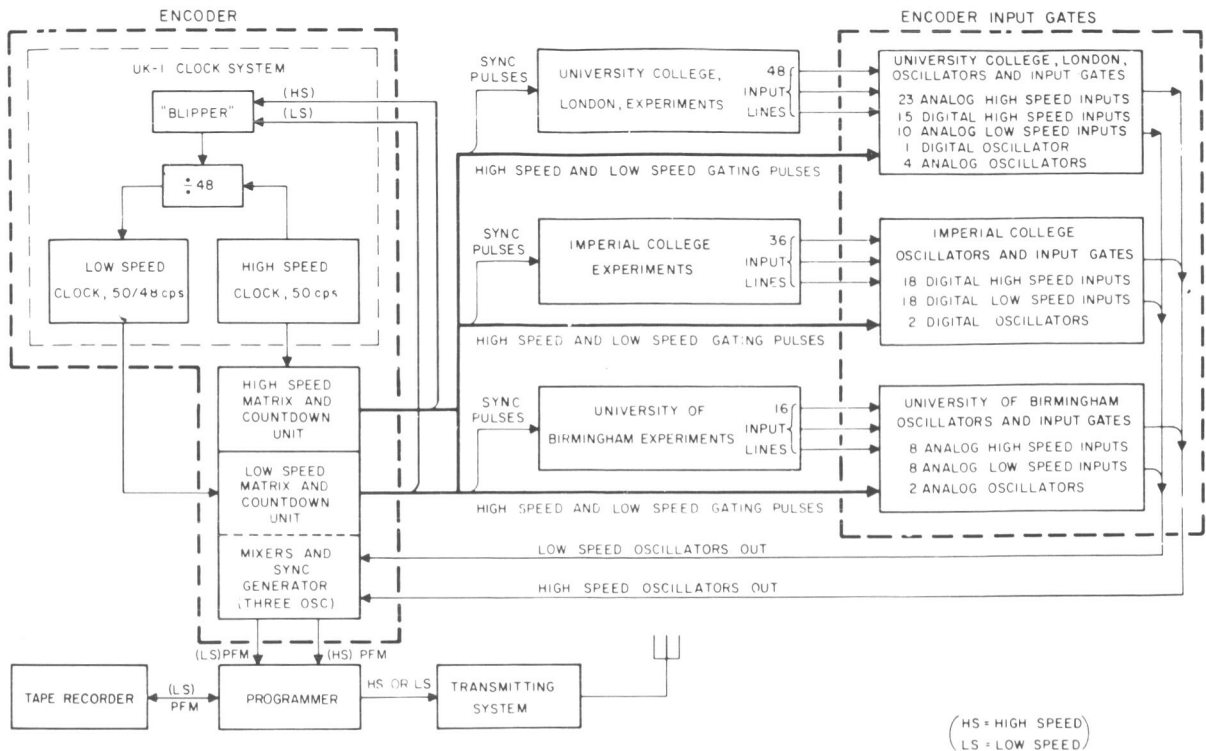


FIGURE 4-15. Encoder functional block diagram.

respective sequences within 20 milliseconds of each other. Where the time difference was greater than 20 milliseconds, a "blipper" circuit shortened the LS sequence by 20 milliseconds, causing the next LS encoder sequence to begin 20 milliseconds earlier. This "blipper" operated once for each LS encoder sequence until synchronization was achieved between the two encoders.

The encoder circuits were solid state circuits packaged on printed circuit cards. The encoder shown in figure 4-16 is a duplicate of the Ariel I flight encoder.

As far as can be determined from available data, all encoder circuits operated reliably and in accordance with design characteristics throughout the useful life of the satellite.

PROGRAMMER
J. Schaffert

The main function of the programmer was to control the transmission of LS and HS encoder data to the ground station. A block

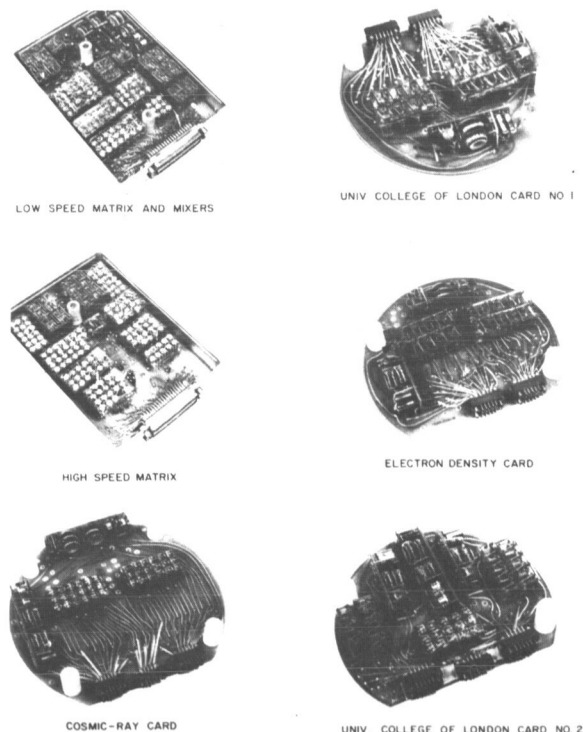


FIGURE 4-16. Encoder circuit cards (not to scale).

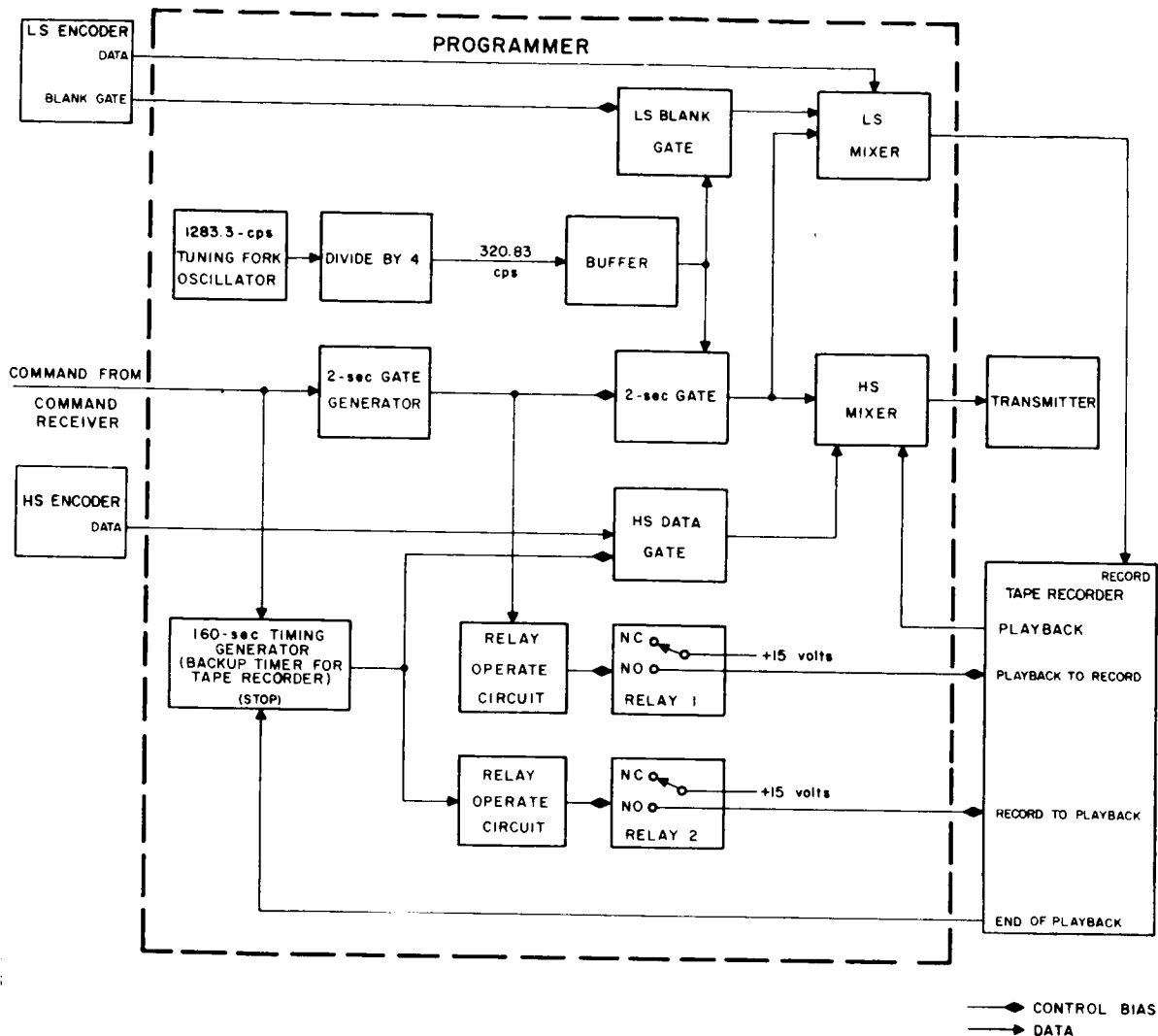


FIGURE 4-17. Programmer functional block diagram.

diagram of the programmer is shown in figure 4-17. With reference to this diagram the programmer sequence of events was as follows:

1. Before command from Command Receiver:
 - a. HS data applied through HS data gate and mixer to transmitter.
 - b. LS data applied through LS mixer to record input of tape recorder.
 - c. Blank gate from LS encoder causes a burst of 320.83 cps signal to be recorded.
2. Command from Command Receiver:
 - a. Triggers two-second gate generator and 160-second timing generator.
 - b. Two-second gate generator enables the 320.83 cps signal to be recorded on tape recorder; inhibits the high-speed data to the transmitter, and enables the 320.83 cps signal to be applied to the transmitter as identification of successful command.
 - c. The end of the two-second gate generator output signal energized relay 1, causing the tape recorder to switch from record to playback.
 - d. Playback output of the tape record-

er is played back at 48 times record speed and is applied through HS mixer to transmitter.

- e. Output of 160-second timer inhibits the HS data gate, preventing the transmission of HS data while LS data are transmitted. The 160-second timer is also used as a back-up device to the playback timer in the tape recorder.
 - f. The end of the 160-second timer signal opens the HS data gate and energizes relay 2.
 - g. Output of relay 2 switches tape recorder from playback to record.
 - h. The end-of-playback signal from tape recorder inhibits the 160-second timer for the tape recorder only if the recorder switches automatically from playback to record.
3. End of playback cycle:
 - a. Programmer is returned to the condition outlined in 1 above.

At the end of the two seconds of 320.83 cps the programmer (1) switched the tape recorder from record to playback simultaneously shifting the tape speed to 48 times its record speed, and (2) connected the transmitter to the tape recorder.

Transmission of tape recorder playback for a period of 125 to 134 seconds was controlled by a timer in the tape recorder. This period of time was sufficient to play back all stored data. This included a 15.4-kc pulse, approximately 42 milliseconds long, which is the playback of the two seconds of the 320.83 cps signal recorded immediately prior to tape recorder playback. This pulse indicated the end of LS encoder data and also served as a time reference for correcting data from both encoders.

The programmer circuits were packaged on two printed circuit cards. Card No. 1 contained the high- and low-speed encoder signal chains. Card No. 2 contained those circuits associated with the command signal and recorder control. All circuits were solid state to meet space, weight, and reliability constraints.

No clear-cut analysis of programmer per-

formance can be made. There are logical arguments that the periodic appearance of 320 cps modulation on the received telemetry signal for relatively long periods of time could have been caused by intermittent failure of one or more of the programmer circuits. However, attempts to reproduce this failure in the laboratory by varying environmental parameters were inconclusive. It can only be stated that all programmer circuits operated satisfactorily prior to the Starfish event, after which there may have been an intermittent circuit failure.

TAPE RECORDER

P. T. Cole

The magnetic tape recorder was designed with the following characteristics:

Tape Speed

Record Mode—0.25 ips

Playback Mode—12 ips

Power Consumption (Over temp. range of -20°C to $+30^{\circ}\text{C}$)

Record Mode—0.5W

Playback Mode—0.75W

Flutter—1% p-p from dc to 200 cps

Dynamic Signal-to-Noise Ratio—30 db (min.)

A functional block diagram of the recorder is shown in figure 4-18. The recorder uti-

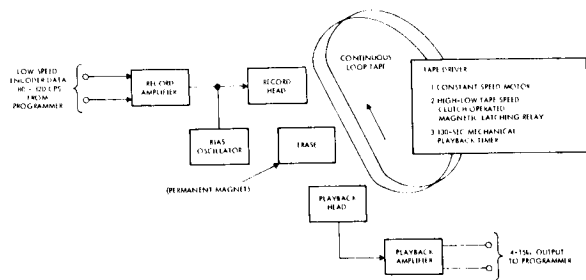


FIGURE 4-18. Tape recorder functional block diagram.

lized a continuous loop tape to record and playback low-speed encoder data. It operated under control of programmer circuits which, in turn, were responsive to commands received via the command receiver. Low-speed encoder data were recorded at 0.25 ips and

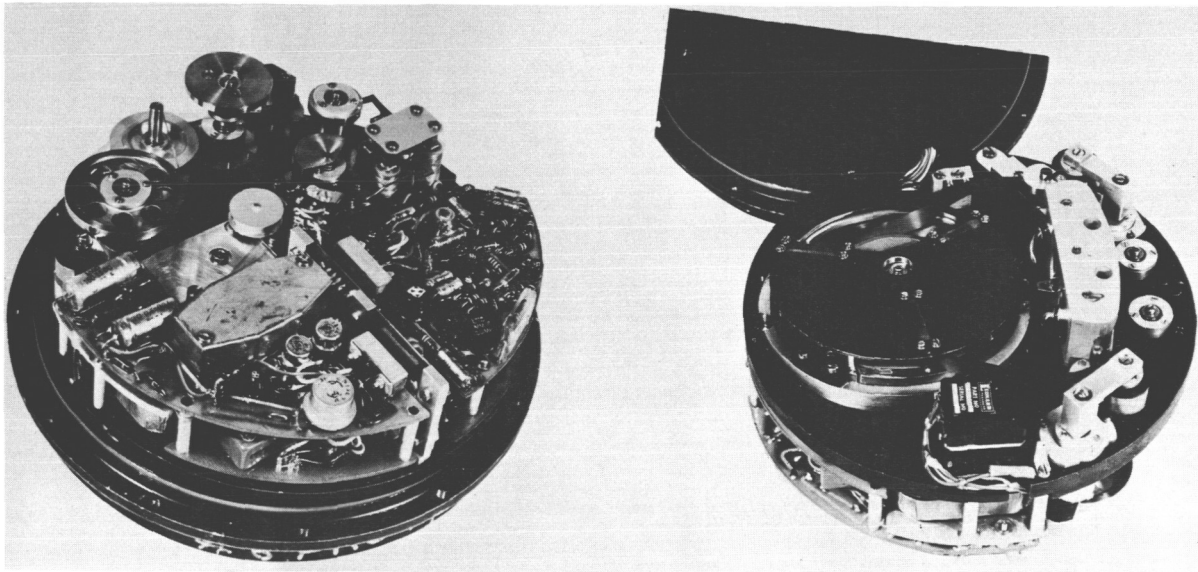


FIGURE 4-19. Tape recorder with cover removed.

played back at 12 ips, making the modulation frequency range of the low-speed data the same as that of high-speed data.

The physical configuration of the recorder is shown in figure 4-19. It is packaged in a cylindrical configuration with a mounting plate approximately midway across the cylindrical envelope. On one side of the mounting plate are the drive motor and drive mechanism along with recorder electronics. On the other side the tape reel tension arms and heads are mounted. The d-c control circuit

is separately packaged on a printed circuit card as shown in figure 4-20.

The tape recorder performed reliably from launch to the end of July 1962, at which time it failed. The exact nature and cause of its failure cannot be determined. Although this failure occurred shortly after the Starfish event, there is no clear-cut evidence relating failure to irradiation of any of its components. The failure became manifest when command trial produced no playback, however, the background noise of the recorder motor was evident, indicating that the motor was still operative. Further analysis indicates that the motor, playback amplifier, and "back-up" record mode timer remained operative throughout the useful life of the satellite.

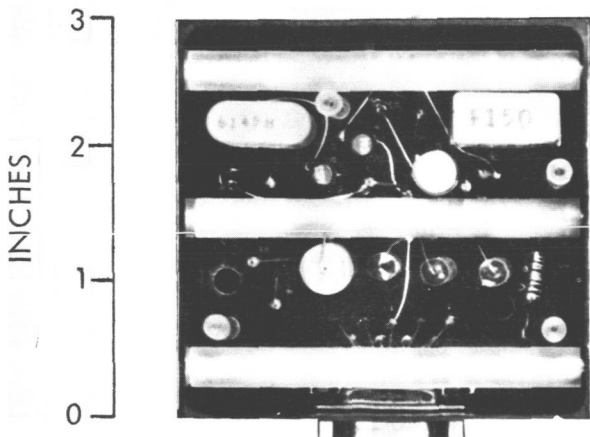


FIGURE 4-20. Direct current control circuit card.

Tape Recorder Stall Power Switch
and Timer—T. D. Clem

This device was designed to remove power from the tape recorder in case of motor stall. If the motor current drain exceeded 300 milliamperes for more than 70 seconds, the power to the tape recorder would be removed. This circuit was reset each time a playback command was received. This circuit was

separately packaged on a printed circuit card. It was designed to operate only in an emergency, and there is no evidence that it was ever required to operate.

TELEMETRY TRANSMITTER

D. S. Hepler

The telemetry transmitter was designed for a minimum of one year's continuous operation with the following operational characteristics:

Power Output—250 mw
Frequency—136.410 mc/s \pm 0.002 %
Modulation—Square Wave Phase \pm 1 rad.
Incidental Frequency Modulation—<2.5 cps
Incidental Frequency Modulation—<3 %
Input Voltage—18vdc
Power Drain—900mw
Harmonic Power—60db

The functional elements of the transmitter are a crystal-controlled oscillator operating at a frequency of 68.205 megacycles; a buffer

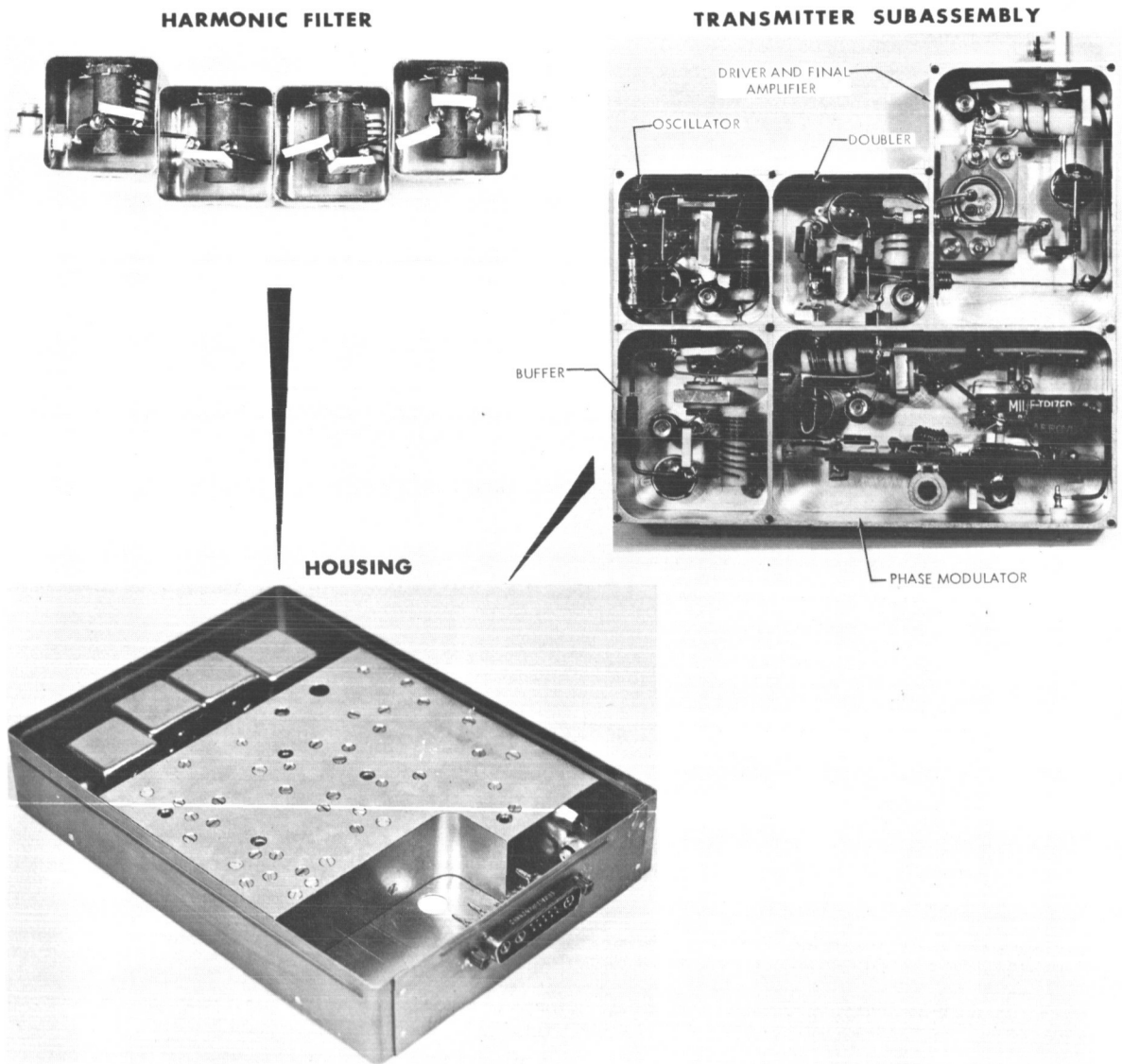


FIGURE 4-21. Transmitter packaging.

stage to isolate the oscillator from the phase modulator; a phase modulator that varies the phase of the carrier (the instant phase excursions are controlled by the LS and HS encoder output data); a doubler stage that multiplies the modulator output frequency to 136.410 mc/s; a driver stage to amplify the doubler output power to about 60 milliwatts; a final amplifier that delivers 250 milliwatts to an antenna load impedance of 50 ohms; and a harmonic filter to prevent radiation of unwanted harmonics of the carrier frequency.

The telemetry transmitter module is shown in figure 4-21. The transmitter module contains two major subassemblies: the transmitter rejection filter and the transmitter subassembly. The four-section transmitter rejection filter filters the signal from the antenna to the command receiver, and is located on the transmitter module due to space considerations. The transmitter subassembly consists of a machined, compartmented casting with functional elements housed as shown. This design provides RFI shielding for the transmitter as well as inter-stage shielding within the unit. The transmitter is transistorized to provide compactness, light weight and high reliability.

The telemetry transmitter performed throughout the useful life of the satellite with no measurable degradation in signal strength or modulation characteristics. The unit was evaluated in February 1965, at which time it was noted that the measured carrier frequency was 136.405 mc/s. Although this shift from the original frequency is in excess of the design tolerance of 0.002%, it is approximately what would be expected from radiation and aging of the frequency determining quartz crystal for the extended period of operation. The 0.002% tolerance was based on a life of one year, but the transmitter operated reliably for more than twice that period.

COMMAND RECEIVER

D. S. Hepler

The command receiver was designed with the following basic characteristics:

Circuit type—Superheterodyne

Modulation—Amplitude

Sensitivity— $> -100\text{dbm}$

Power Requirement— $+12\text{vdc @ } 4\text{ ma}$

The receiver is a double-superheterodyne unit with an amplitude-modulation detector. A decoder, which follows the detector, contains a tone filter, a signal integrating circuit, and an output trigger circuit to signal the programmer to switch the tape recorder from record to playback. The subcarrier tone that amplitude-modulates the received signal, must be present for 0.1 second minimum, and the carrier must be modulated at least 30 percent before the decoder will command.

The receiver physical configuration is shown in figure 4-22. All components are mounted on a printed circuit board which is installed in a single shielded container.

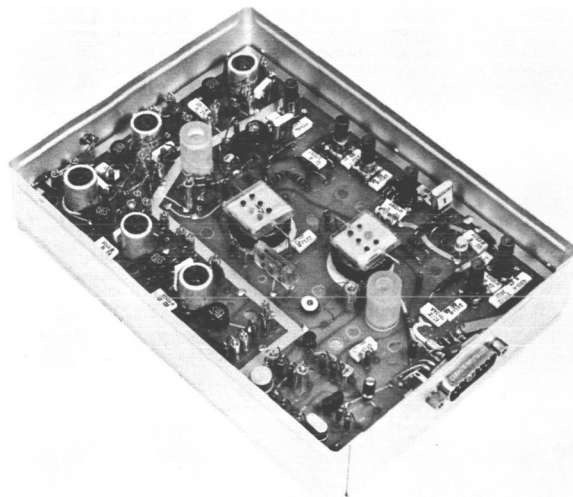


FIGURE 4-22. Command receiver packaging.

Receiver performance was satisfactory over the entire useful life of the satellite. The command receiver was interrogated on February 4, 1965, by the Blossom Point Tracking Station. The command was successful as evidenced by the presence of the "horn" and the change in modulation characteristics of the transmitter. No accurate information is available on the present receiver sensitivity or shift of frequency of the local oscillators as caused by aging and radia-

tion effects. The last interrogation, however, did indicate the sensitivity was sufficient for normal network operations.

ONE-YEAR TIMER

J. Schaffert

A one-year timer (figure 4-23) was incorporated in the spacecraft to remove power

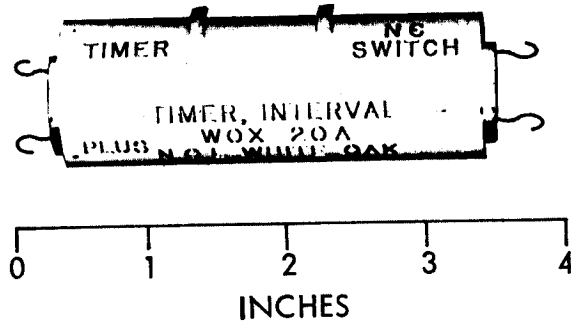


FIGURE 4-23. One-year timer.

from the transmitter at the end of one year. Two timers were used in a parallel redundant hookup. The timers employed an electrochemical de-plating process having a timing accuracy of ± 10 percent.

This type of timer appeared to be ideal for long term, low accuracy, timing applications because of its simplicity and small weight and space requirements. Fortuitously, the timer failed, and useful data were collected over a period of approximately two and one-half years.

There is no specific information from the spacecraft to indicate the reason for the failure. However, subsequent tests indicate that timing action probably ceased because of electrolyte leakage, which effectively shunted the polarizing current. As a result of its performance on the spacecraft and the subsequent tests, this timer is not considered adequate for long-term applications.

RF ANTENNAS

J. K. Steckel

The Ariel I spacecraft antenna system in-

cludes a coaxial hybrid power divider, coaxial phasing lines, and a canted turnstile antenna. The hybrid power divider and filter provide about 20-decibel isolation between the command receiver and the transmitter. The antennas are driven from the base, each pair acting as a dipole, with the dipole pairs in phase quadrature. Radiation in the plane of the turnstile is essentially linear, while circular polarization is obtained along the spin axis. The total power radiated varies with satellite aspect from +2 to -4 decibels relative to an isotropic radiator. Spacecraft commands are received through the same antenna system and have about the same pattern, but see an additional two decibel loss because of mismatch at the command frequency.

Antenna system performance was satisfactory and in accordance with design characteristics throughout the life of the satellite. The characteristic variations in radiated power with changing aspect proved very useful in obtaining a reasonably accurate estimate of spin rate after the spin rate sensor failed. This was accomplished by establishing a correlation between spin rate data before failure and recorded receiver age voltages. Having established such a correlation, spin rate could be estimated from age curves taken after spin rate failure.

POWER SYSTEM

F. C. Yagerhofer

Power to the spacecraft electronics was provided by a solar cell array and two battery packs. Power control and regulator circuits include a shunt voltage limiter, a battery charging current limiter, a battery switching network, an undervoltage detector, a hold-off relay and turn-on plug, and several dc-to-dc converters.

The functional relationships among the major elements are shown in the block diagram of figure 4-24. A brief description of each of the major components is given in the following paragraphs.

Solar Cell Array—L. Slifer

The solar cell array consists of four solar paddles (figure 4-25) arranged in a series-

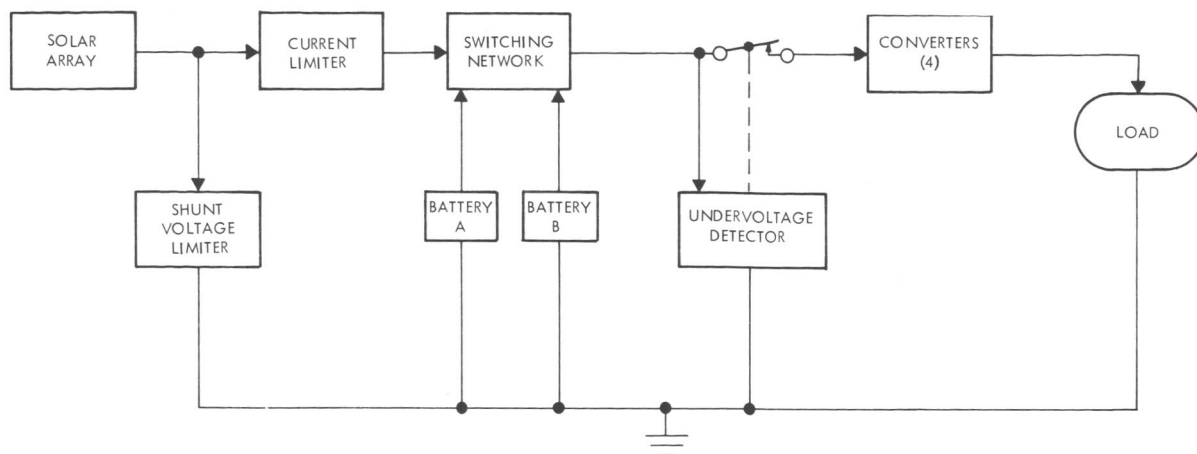


FIGURE 4-24. Power system functional diagram.

parallel matrix. It furnished 0.5 to 2 amperes at 15 volts, depending on the spacecraft

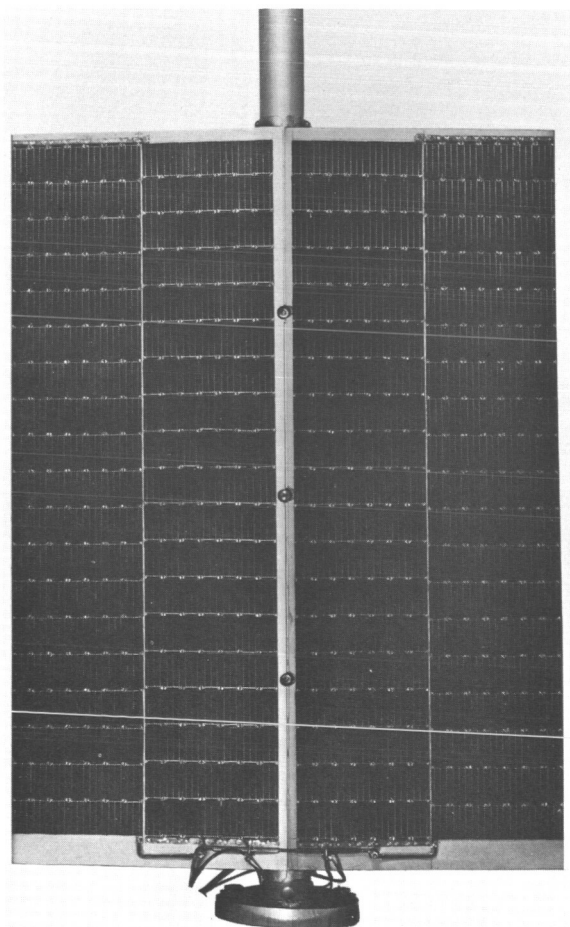


FIGURE 4-25. Solar cell array.

aspect to the sun and radiation degradation. The solar cells are p-on-n type silicon cells that perform as photoelectric converters. The cells are flat mounted, of gridded construction, and exhibit a high efficiency. While the spacecraft is orbiting in sunlight, the solar cells power all electronic subsystems on board the spacecraft and supply a charging current to the two battery packs.

Shunt Voltage Limiter—J. Paulkovich

The shunt voltage limiter regulates the solar paddle output voltage to 14.5 volts. Excess power from the solar paddles is dumped through a pair of power resistors located on the arms that extend the solar paddles; the dumping is controlled by a pair of power control transistors.

Battery Charger Current Limiter—L. Veillette

The battery charging current limiter (figure 4-26) regulates the battery charging current to a value not in excess of 0.5 ampere. This current prevents the generation of hydrogen in the batteries due to excessive charging currents.

Battery Packs—E. R. Stroup

Each battery pack consists of ten individual cells connected in series. The cells are nickel-cadmium, sintered-plate type, hermetically sealed in a stainless-steel case. Each

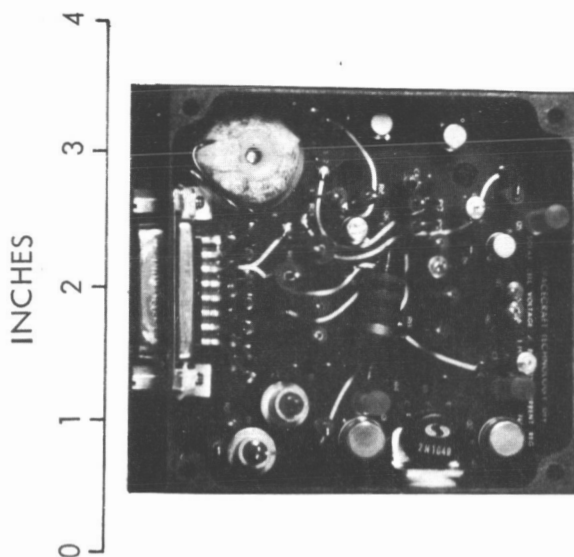


FIGURE 4-26. Battery current regulator.

cell has a nominal potential of 1.3 volts. All ten cells have a nominal output of 13 volts.

Battery Switching Network—L. Veillette

The battery switching network (figure 4-27) connects the battery with the higher voltage to operate the spacecraft. The other

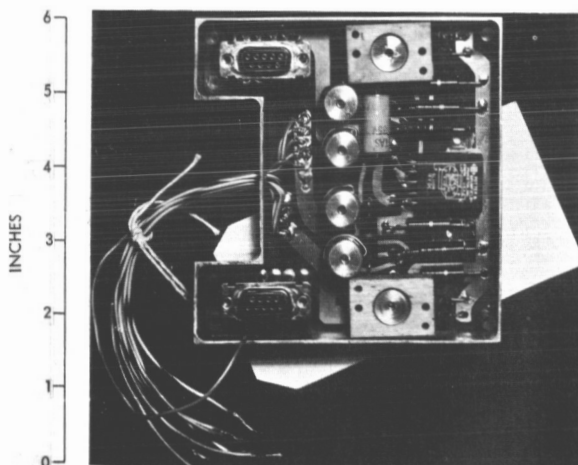


FIGURE 4-27. Battery selector.

battery is connected to the solar cell array and receives a trickle charge from the array. When the voltage difference between the two

batteries exceeds 1.2 volts, the standby battery is connected to operate the spacecraft.

Undervoltage Detector—J. Schaffert

The undervoltage detector (figure 4-28) disconnects both battery packs from the spacecraft electronics when the output volt-

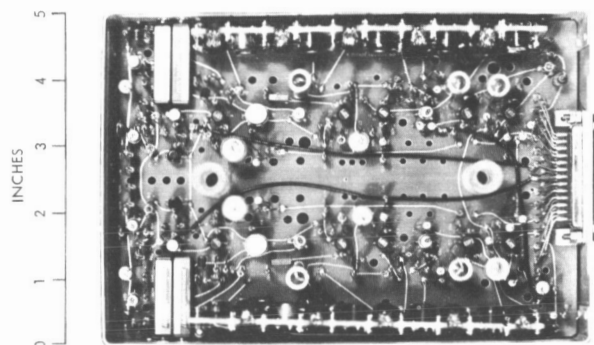


FIGURE 4-28. Undervoltage detector.

age of both batteries falls below the minimum acceptable level. The detector also activates a recycling timer which, after 18 hours, connects the battery output to the spacecraft electronics. During the 18 hours, the batteries are connected to the solar cell array and are charged. At the end of the 18-hour charging period, the batteries are connected to the spacecraft electronics. If, after this charging period, the batteries are still below the minimum acceptable level, the charging cycle is repeated.

Dc-to-Dc Converters—F. C. Yagerhofer

The dc-to-dc converters supply the different dc voltage levels required to operate the spacecraft electronics. There are four converters in the power system: the prime converter, encoder converter, U.K. converter, and undervoltage detector converter. Converter circuit cards are shown in figure 4-29.

The prime converter is connected to the main powerline at the output of the undervoltage relay. The outputs of this converter are +12 and -18 volts, regulated to 1 percent at 80-percent efficiency. This converter supplied power to the transmitter, command

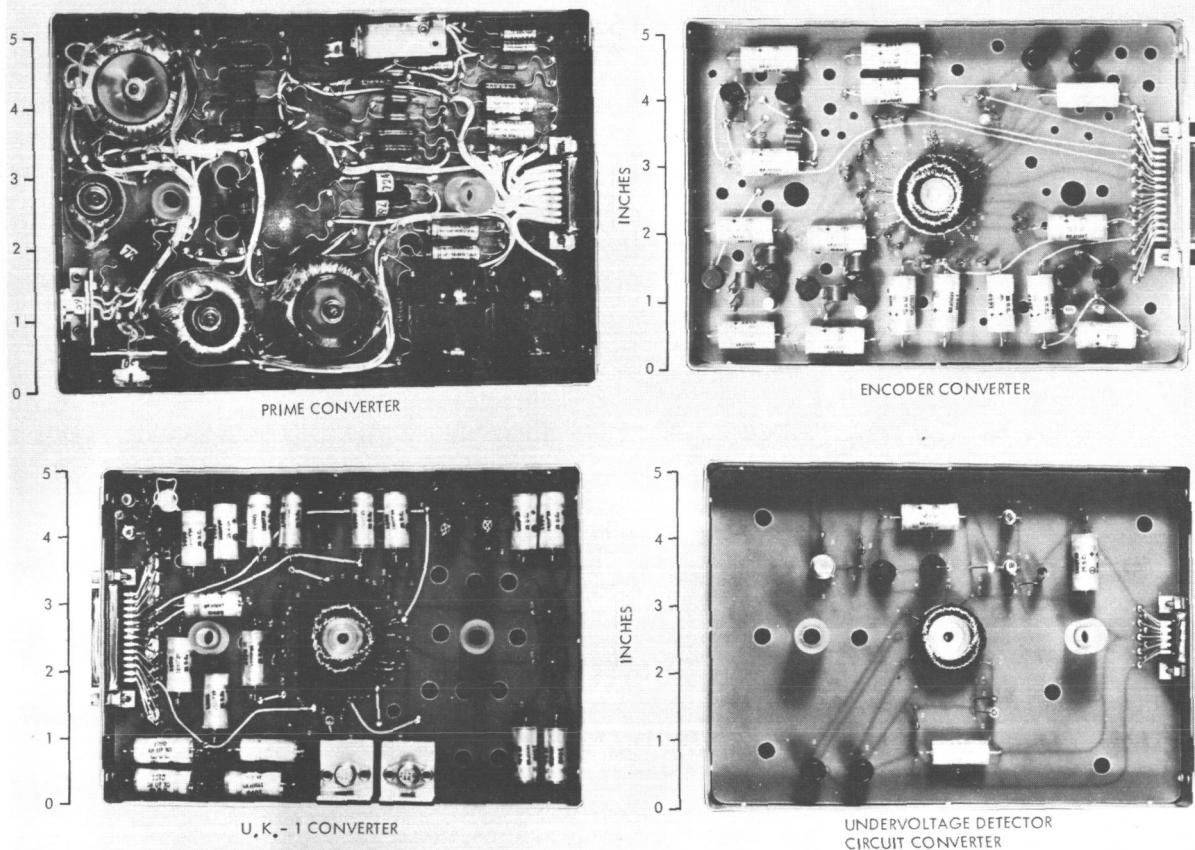


FIGURE 4-29. Dc to dc converter cards.

receiver, programmer, encoder converter, and U.K. converter.

The encoder power converter furnishes the $+1.9$, -4.0 , -6.2 , -2.7 , and $+6.7$ volts to the encoder. The -2.7 volts is regulated to 0.25 percent; all the remaining voltages are regulated to 5 percent. This converter has an efficiency of about 30 percent.

The U.K. converter supplies all power to the experiments. The output voltages are $+6.5$, $+15$, and -6.5 volts—all at ± 5 percent; -9.0 volts at ± 10 percent; 12 volts at ± 8 percent; -15 volts at ± 7 percent; and 24 volts at ± 8 percent. The overall efficiency is about 60 percent.

The undervoltage detector circuit converter is connected to the main power line; this converter furnished $+15$ and -18 volts, both at ± 5 percent and at an efficiency of approx-

imately 50 percent. This converter is disconnected from batteries only when the hold-off relay is actuated.

Pre-Launch Power Control

A turn-on plug and a hold-off relay were provided to control the application of power to spacecraft systems during ground operations. The turn-on plug is a bridging connector which opened battery circuits when removed. Blockhouse control for turning the spacecraft power system on and off with the turn-on plug installed in the spacecraft was effected by de-energizing and energizing the hold-off relay, respectively, from the blockhouse. When the spacecraft was launched, the hold-off relay was in its de-energized state, thereby connecting the battery system to operate the spacecraft.

Solar Array Performance—L. W. Slifer

The specific cause, or causes of undervoltages, which occurred much more frequently than anticipated, subsequent to the Starfish event, cannot be determined with any degree of certainty. It can only be assumed that these were caused by a combination of solar cell degeneration, caused by excessive radiation, and excessive current drain resulting from degeneration in circuit performance in the various subsystems. Irradiation certainly produced a significant degrading effect upon the solar array, since it had been designed for stability only in a low energy, low flux radiation environment. However, two unfortunate circumstances combined to lead to a conclusion, which perhaps was drawn too quickly, that the solar array had degraded to the point where it was inadequate to power the spacecraft. These circumstances were (1) because of design restrictions, no performance parameters for monitoring the power system were included in the satellite, and (2) although radiation effects on solar cells were well known, effects on other spacecraft components, particularly semiconductors, were relatively unknown. Since information on solar cells was available, it was easy to assume that solar cell degradation was the complete answer to the spacecraft malfunction.

The error of this assumption is evident in that the best calculable estimate of solar cell degradation is 50 percent which is not sufficient to account for more than a small portion of the periods of spacecraft malfunction. This is demonstrated in table 4-4 and the profile of spacecraft performance given in Appendix B.

In table 4-4, the undegraded power between the flight aspect limits of approximately 45° and 135° is presented along with the spacecraft and battery charge power requirements.

It can be seen that 65 to 80 percent degradation of the solar array would be required in order for it to be incapable of sustaining the normal spacecraft during full sunlight orbits where no battery charging is required, and, also, that this degradation is too large to permit any extended continuous operation during eclipse orbits where battery charging is required in addition to the spacecraft requirements.

Several features of the Ariel I solar array were novel in satellite application. This solar array was the first satellite power supply in which:

- a. Flat-mounted (as opposed to shingled) solar cells were used.
- b. Series-parallel redundance (complete

TABLE 4-4.
Solar Array Power, Loads, and Degradation

Aspect (Sun line to spin axis angle)	Undegraded Output	Spacecraft Battery Eclipse Orbit)		Spacecraft alone (100% sun- light)	
Angle (Degrees)	Power (Watts)	Power (Watts)	Allow- able Degrada- tion (%)	Power (Watts)	Allow- able Degrada- tion (%)
45	16.0	10.8	32.5	5.4	66.3
90	26.5	10.8	59.3	5.4	79.6
135	18.75	10.8	42.5	5.4	71.2

redundancy within each cell group) between solar cells were used.

c. Shallow-diffused ("blue," "blue-shifted") gridded solar cells were used.

d. Silicone base bonding materials for both solar cells and cover glasses were used.

Each of these features was a significant development in reliability and/or efficiency for solar arrays. Each has become standard practice and is used in the design of almost all solar arrays.

Power System Performance—F. C. Yagerhofer

The power system performed satisfactorily throughout the useful life of the satellite. Unfortunately, because of the limitations of spacecraft design, there were not enough power system housekeeping data, such as internal and external battery temperatures and voltage and current measurements, to make a detailed analysis of performance throughout the life of the satellite. However, the fact that the spacecraft transmitted intelligible scientific data intermittently over a period of approximately two and one-half years is reasonable proof of satisfactory operation.

In summary, it is felt that the power system operated satisfactorily, well in excess of

its original design characteristics. Its successful operation provided rigorous proof of some design techniques and material.

The undervoltage detector and its associated recycle timer were thoroughly proven by the frequent undervoltage conditions. These circuits, originally designed to operate only in an emergency, have operated reliably for more than 250 cycles at the time of this analysis.

ORBITAL INJECTION PROGRAMMER

J. Schaffert

The orbital injection programmer was a battery-operated electronic timing system. Its function was to program the events associated with the ignition and separation of the third stage. The functional block diagram of figure 4-30 illustrates the operation of the programmer with respect to these events. At the time of third-stage motor ignition (t_0), two pressure switches provided signals to start a 900-second timer. At the end of this timing period two pulses were applied to the silicon-controlled rectifier circuit, which in turn fired one pair of squibs. This time is designated t_1 . The t_1 output from

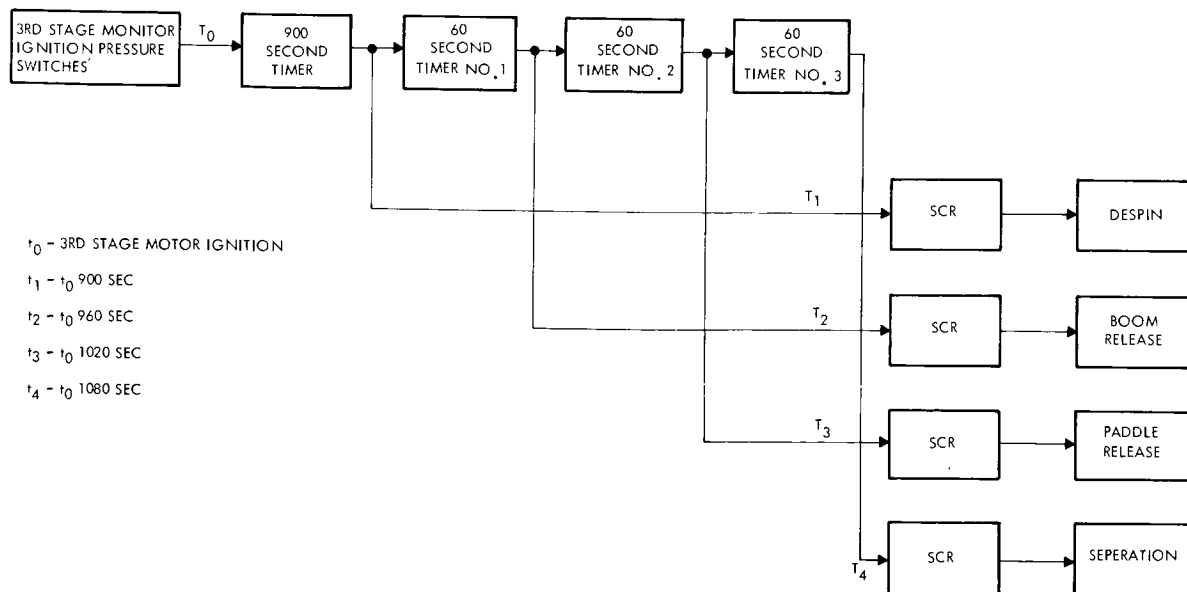


FIGURE 4-30. Orbital injection functional block diagram.

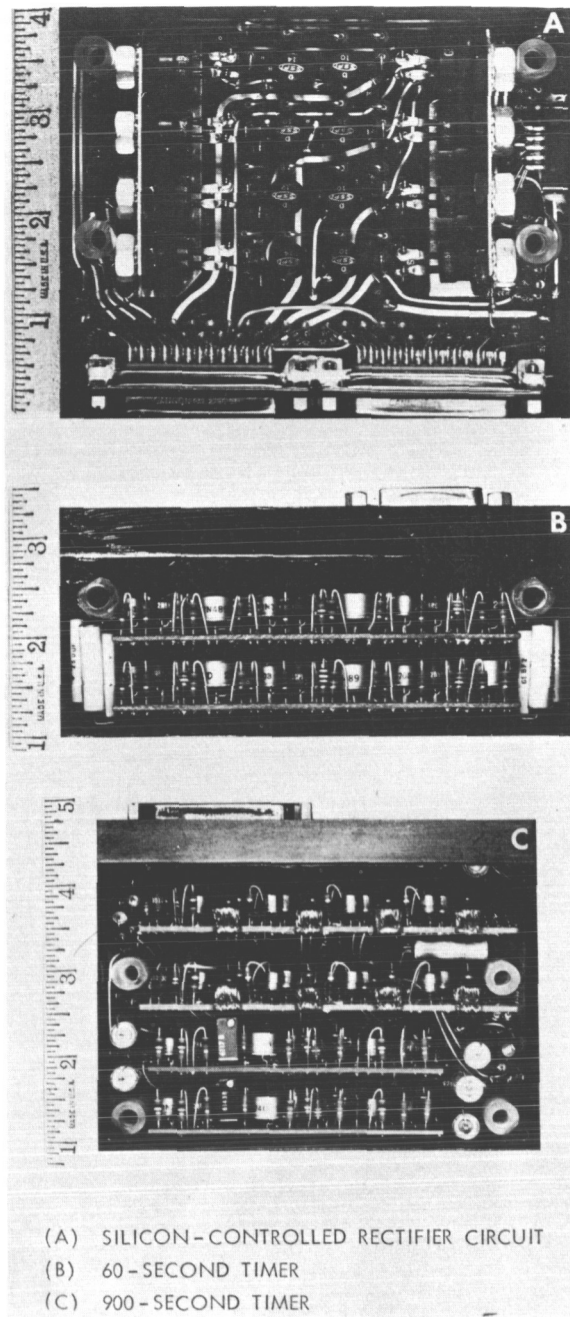


FIGURE 4-31. Orbital injection programmer.

the 900-second timer started a 60-second timer. At intervals of 60 seconds from time t_1 , pulses were provided to the silicon-controlled rectifier circuit to fire three additional pairs of squibs. The times of these firings are designated t_2 , t_3 and t_4 .

The orbital injection programmer was redundant throughout, including two separate batteries. Thus, failure of either programmer could not prevent the squib firing sequence from being completed. Accuracy of the timing cycles was five percent or better. The events at the squib firing times were: de-spin (t_1), boom release (t_2), paddle release (t_3), and separation (t_4).

The orbital injection programmer circuits were packaged on three separate printed circuit modules of medium density packaging. These modules are shown in figure 4-31.

Although the deployment events did not occur with proper timing, all available evidence indicates that this was caused by mechanical failure of tie-downs rather than the programmer. An analysis of the de-spin profiles indicates that the squibs did, in fact, fire at the proper times.

Despite the fact that this device was designed and fabricated on a crash basis as an electronic replacement for an inadequate mechanical timer, its performance proved the reliability of the design.

CHAPTER 5

Tracking and Data Acquisition

The Ariel International Ionosphere Satellite was launched from Cape Canaveral, Florida, by a Thor-Delta vehicle and was placed into a near-earth elliptical orbit having an apogee of 1214 kilometers (754 statute miles, 655 nautical miles), a perigee of 390 kilometers (242 statute miles, 210 nautical miles), an inclination of 55 degrees, and an anomalistic period of 99 minutes. (On board the satellite is a single PFM-PM telemeter with a power output of 250 milliwatts. This telemetry system was used by the STADAN network for tracking and data acquisition.)

THE LAUNCH WINDOW

The Theory and Analysis Office of the Data Systems Division was responsible for computing the Launch Window for the Ariel I satellite. The constraints governing the launch window were as follows:

1. The spin axis sun line angle vary from 40 degrees to 140 degrees.
2. The initial spin axis sun line angle to be less than 90 degrees and then increase with time.
3. Launch time be such that the time the satellite will be in the sunlight is a maximum during the early life-time of the satellite.
4. Lifetime of the satellite to be one year.

Based on a nominal trajectory supplied by the Douglas Aircraft Company extensive computer runs were made to determine the launch windows. The launch window calculations determined that for the actual

launch date of April 26, 1962, Ariel I should lift-off between 17 hours 48 minutes U.T. and 18 hours 57 minutes U.T.

Ariel I lifted off the pad at approximately 1800 hours U.T. on April 26, 1962.

The Orbit

The Data Systems Division, in addition, was responsible for determining the orbit, supplying the tracking stations with predictions, and furnishing the experimenters Refined World Maps. Graphs of some of the orbital elements of Ariel I are given in Appendix B. A comparison of nominal and actual orbit parameters follows:

	Nominal	Actual
Apogee	1027 Km. (638 S.M.)	1214 Km. (754 S.M.)
Perigee	370 Km. (230 S.M.)	390 Km. (242 S. M.)
Inclination	55 Deg.	55 Deg.
Period	99 Min.	99 Min.

Tracking

Tracking Ariel I was the sole responsibility of the Space Tracking and Data Acquisition Network (STADAN) during the active life-time of the satellite. During the launch and early orbit phase, additional tracking was obtained from the Cape Canaveral doppler tracking station, NORAD, U.S. Naval Space Surveillance System, and the SAO Baker-Nunn Network. Sufficient tracking data were obtained from the 136.410 Mc/s telemetry transmitted to accurately compute and con-

tinually update the orbit. A total of 3372 tracking messages were received during the active lifetime of the satellite. The following STADAN stations were responsible for tracking the Ariel I spacecraft.

Antofagasta, Chile, S.A.*
 Blossom Point, Md., U.S.A.
 Lima, Peru, S.A.
 Quito, Ecuador, S.A.
 Johannesburg, South Africa
 Woomera, Australia
 Fort Myers, Fla., U.S.A.
 St. Johns, Newfoundland
 East Grand Forks, Minnesota, U.S.A.
 Winkfield, England

These stations are shown on the map of Figure 5-1. The circles around each station indicate the approximate effective area covered by each station. Thus if a given orbit path is superimposed on the map as

*This station was relieved of operation in August, 1963.

shown, those periods during which the satellite was tracked and data acquired can be determined.

Data Acquisition

The Ariel I spacecraft utilized a PFM/PM telemetry system operating at 136.410 Mc/s and a power output of 250 milliwatts. In this system, the analog or digital measurement data from a given experiment frequency-modulated a subcarrier oscillator. This subcarrier oscillator phase-modulated the rf carrier ± 50 degrees. The subcarrier oscillators operated in the 5 to 15 Kc. range. Upon command from the ground, playback data from an on-board tape recorder were transmitted at a speed of 48 times the recording rate. These data were normally obtained near the point of closest approach to the receiving station. Signal levels obtained at the STADAN stations ranged roughly between -80 dbm and -145 dbm with the average

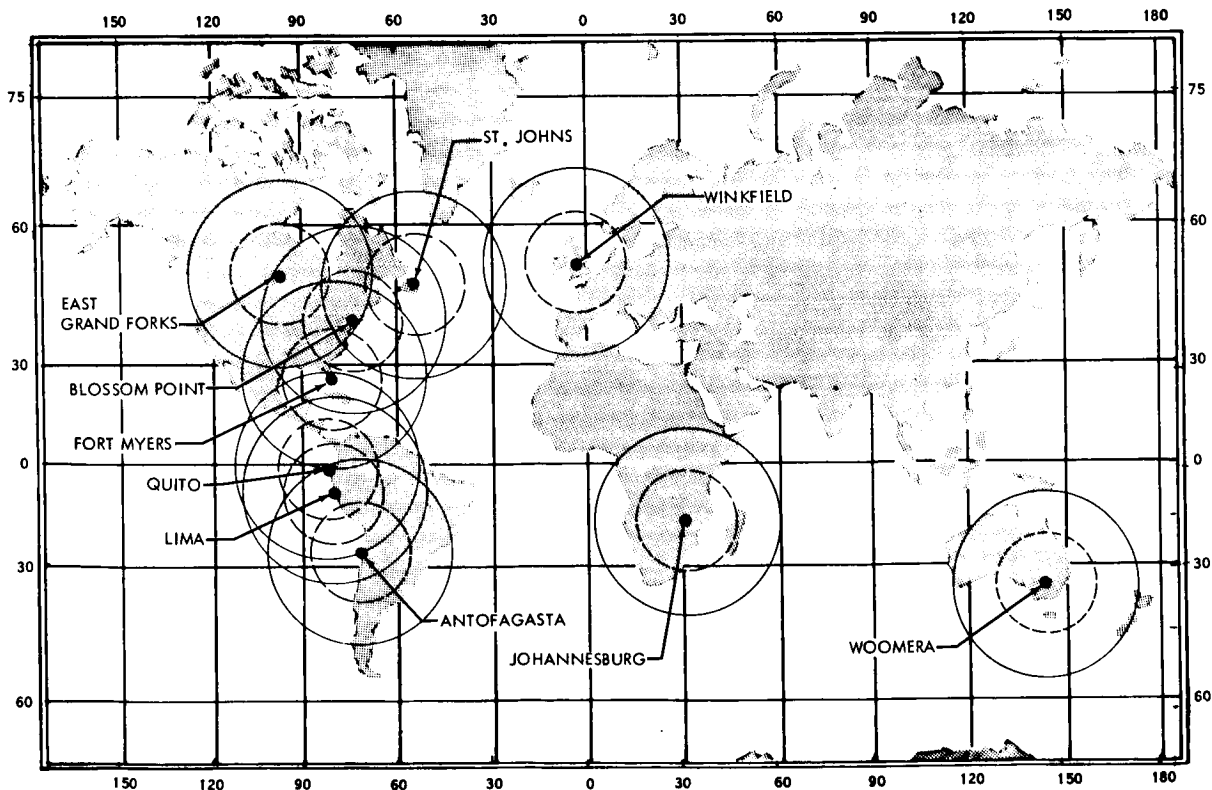


FIGURE 5-1. Tracking station locations and areas of effectiveness.

about -100 dbm. Very little difficulty was experienced in obtaining usable data at the stations. Those STADAN stations responsible for tracking were also responsible for the acquisition of telemetered data from the spacecraft. In addition, the two British operated DSIR stations, one located in the South Atlantic area and the other at Singapore, were also responsible for data acquisition from the Ariel I spacecraft. A block diagram of the telemetry acquisition system used at the STADAN stations is shown in figure 5-2. The following system parameters were utilized:

1. Antenna polarization—linear
2. Dual channel preamplifiers—136.500 Mc/s.
3. Mod. I telemetry receivers

Frequency:

Receiver A—136.410 Mc/s.

Receiver B—136.410 Mc/s.

Inputs:

Receiver A—output of vertically polarized antenna system

Receiver B—output of horizontally polarized antenna system

Operation—AGC mode

Bandwidth (2nd I.F.)—100 kc

Output Converter—62 kc center frequency

Output Converter—Oscillator— 3.312 Mc/s. ± 20 cps.

4. Tracking filter

Input—62 kc output of Mod. I receiver having highest signal level

AGC—slow (changed to slow to eliminate keystone effect with fast AGC)

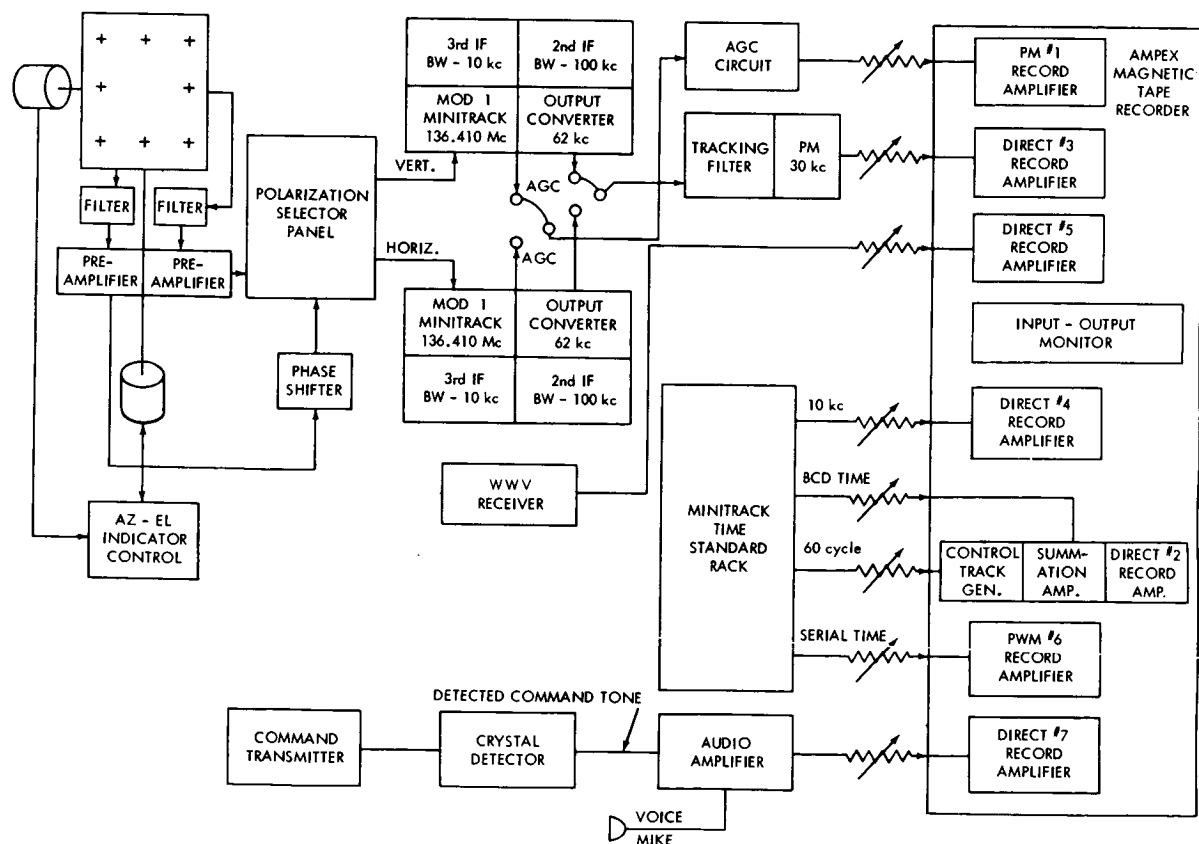


FIGURE 5-2. Data acquisition system functional block diagram.

- Phase modulation output—detected
5–15 kc
Tracking loop bandwidth—Not less
than 25 cps
5. Minitrack timing signals

- Standard frequency—10 kc
Time—Serial and binary coded time
Precision clock drive—60 cps
6. Magnetic tape recorder track assignments—see table below:

Track	Record Amplifier	Source	Signal
1	FM	AGC Circuit	AGC
2	Direct	Control Track Generator and Data Input (Minitrack)	60 cps, 70% AM on 18.24 kc carrier
3	Direct	PM Output of Tracking Filter	BCD Time
4	Direct	Minitrack	5–15 kc detected signal
5	Direct	WWV Receiver	10 kc standard
6	FM	Minitrack	WWV time
7	Direct	Audio Amplifier	Serial coded time
			Voice and command tone

7. Magnetic tape recorder tape speeds
FR-600—15 in/sec.
FR-100—7½ in/sec.

The spacecraft operated normally after launch for a period of about three months. As much real-time data as possible was being recorded according to station availability and the spacecraft priority schedule. With the exception of about one orbit per day, the requirement for playback data once/orbit was achieved. This represents roughly 93% success in obtaining playback data.

On July 12, 1962, the satellite turned off because of a malfunction in the spacecraft. This resulted from degradation of the solar cells and other semiconductors by high energy electrons in the artificial radiation belt produced prior to this date. Since that time, intermittent turn-offs were observed reducing the amount of data acquired per unit time to one-third of that expected. The tape recorder system ceased operation shortly there-

after and playback commands were stopped at all stations except Blossom Point and East Grand Forks on August 18, 1962. After it was determined that no playback data were being received, all stations were relieved of command responsibility on September 8, 1962. Throughout the duration of the satellite life, operation was intermittent until all tracking, command, and data acquisition support was temporarily dropped on July 1, 1964. Ariel I support was again resumed on August 26, 1964 after the launch of the IE-A (1964-51A) spacecraft on August 25, 1964. For two months, Ariel I and IE-A recorded similar data until all support was finally terminated on November 9, 1964 at the request of the Ariel I Project Office.

During the active life of the spacecraft, a total of 11,910 tapes were received from the STADAN, South Atlantic, and Singapore stations representing over 2000 hours of real-time telemetry data.

CHAPTER 6

Data Processing

Processing of Ariel I data consisted of six major steps, as shown in figure 6-1. Of these six, the first three were the responsibility of the Data Systems Division of the Goddard Space Flight Center, and the second three were performed by various groups within the United Kingdom.

The sharing of responsibility between GSFC, for digitizing, and the U.K. for digital computer reductions and analysis, imposed a new set of difficulties on an art not then well developed. Specifically, a close coordination between the digitizing and subsequent processes was sought. Since, in this case, the two stages would be separated by 4000 miles, exceptional care was exercised to insure that the digitized tapes shipped to England were correct. Although this was costly, in practice it worked very well and the data were reduced with very little reprocessing. The

design and writing of digitizing and quality control programs and the management of the GSFC data processing system were done by the Data Processing Branch.

In the U.K. the initial computer operations were centralized under the Space Research Management Unit (SRMU). The Space Department of the Royal Aircraft Establishment (RAE) undertook the preparation of the main computer programs.

NASA/GSFC PROCESSING

C. M. Stout
C. J. Creveling

Collection, Collation and Evaluation of Analog Tapes

Inputs to data processing consisted of magnetic tapes of the detected telemetry signal from STADAN, South Atlantic and Singa-

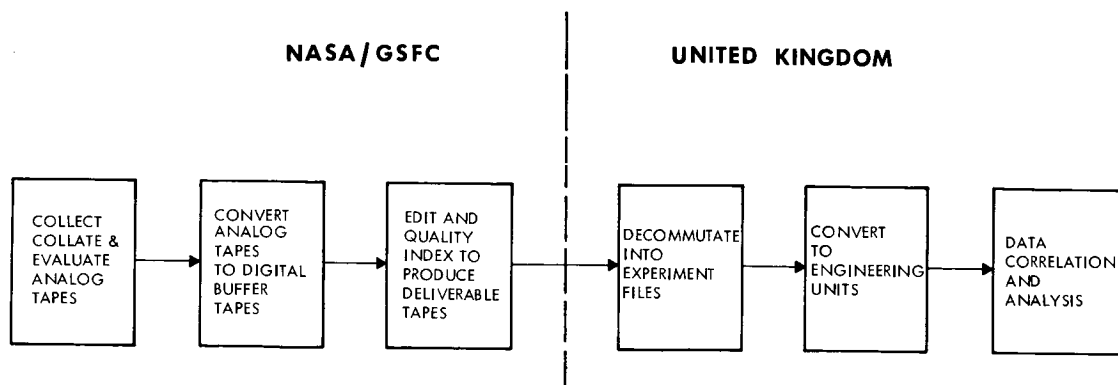


FIGURE 6-1. Major steps in the data processing procedure.

pore stations. These stations were at the following locations:

Antofogasta, Chile
 Blossom Point, Maryland
 Lima, Peru
 Quito, Ecuador
 Santiago, Chile
 Johannesburg, South Africa
 Woomera, Australia
 Fort Myers, Florida
 St. Johns, Newfoundland
 East Grand Forks, Minnesota

Winkfield, England

Singapore

South Atlantic

The format for telemetry tapes was set forth in Operations Manuals of Plan 2-62 for the Minitrack Stations. The tapes consisted of $\frac{1}{2}$ inch $1\frac{1}{2}$ mil thick analog (or instrumentation) tape 2400 feet long on which the recorded signals are multichannel recorded simultaneously on seven tracks in accordance with IRIG standards.

The track allocations were as follows:

Track	Type of Recording	Track Content
1	FM	Automatic gain control
2	Direct	Combined servocontrol and binary coded decimal time
3	Direct	Telemetry data signal demodulated from carrier
4	Direct	Reference 10kc standard frequency
5	Direct	Time from WWV radio signal
6	PWM	Serial Coded Time
7	Direct	Voice, command tones

Magnetic tape recorder speeds depended upon the type recorder available at the ground data acquisition station, being generally at $7\frac{1}{2}$ inches per second (Ampex FR 600; the Ampex FR-100 recording at 15 in/sec).

Upon arrival from tracking stations tapes were logged into a tape library and a punched card prepared for each file. (A file is defined as a satellite pass over a given station.)

From these cards a periodic listing (figure 6-2), which was updated to account for all tapes received, was generated. Most analog tapes contained multiple passes, resulting in multiple cards per tape. Separate cards were also prepared for the low-speed data (i.e. satellite tape recorded data) which were recorded on the same tape as the high speed data. As each file completed the various

SAT	STA	TAPE NO	DATE YR/MO/DA	PASS NO	CODE	INTERNATIONAL START TIME	STOP TIME	MIN DATA REC'D	DATE EVAL.	CARD NO.
S51	GFO	0001	620426	0001	62 15 1	193315	194915	011 20430	A1 20503	1
S51	MOJ	0001	620426	0001	62 15 1	193317	194646	010 20427	B1 20428	1
S51	BPO	0001	620426	0001	62 15 1	193914	195143	008 20427	C2 20427	2
S51	FTM	0001	620426	0001	62 15 1	194348	195530	012 20427	C2 20427	1
S51	LIM	0001	620426	0001	62 15 1	195304	200157	009 20509		1
S51	AGA	0001	620426	0001	62 15 1	200146	200740	006 20508	A1 20510	1
S51	JOB	0001	620426	0001	62 15 1	202155	203140	009 20430		1
S51	SNP	0001	620426	0001	62 15 1	203610	210010	024 20501		1
S51	MOJ	0001	620426	0002	62 15 1	211630	212229	015 20426		2
S51	LIM	0001	620426	0001	62 15 1	211630	212229	015 20509		1

FIGURE 6-2. Typical periodic listing of tapes received.

stages of the processing cycle, the dates of same were punched in the card, providing a consolidated input for accounting purposes.

A representative sample of the analog tapes was evaluated for quality of ground station data acquisition and recording technique, quality of signal, determination of low-speed and high-speed encoded telemetry recordings, and the presence of time and command tones. A total of 56 percent of the tapes received were evaluated. The tape evaluation process consisted of the following major steps:

1. A check as to whether or not each of the tape tracks contained the proper information and to see that the station logs accompanying each tape were properly prepared.

2. Paper recordings of the three time tracks (i.e. Binary Coded Time (BCD), Serial Decimal Time (SDR), and WWV) were compared for consistency and accuracy.

3. The PFM data as displayed on an oscilloscope were observed.

4. Paper recordings were made of the AGC level.

Where anomalies existed an attempt was made to determine the cause, or at least determine whether or not they were caused by improper operation of ground equipment.

Since the aim of the tape evaluation operation was to ensure proper station telemetry data acquisition and recording and to prevent repetitive or continuing errors, rapid response was desirable. On the other hand, since chronological processing of data was required by the experimenter, a time lag to permit the incoming tapes from various stations to be assembled in near chronological order was needed. The scheduling procedure, shown in block diagram form in figure 6-3, shows how this problem was resolved with tape evaluation being performed on a two-day cycle with digitization of the tapes awaiting three weeks' and one week's worth being processed on a sustained basis. "Quick look" tapes, on the other hand, were processed on an expressline basis.

Reports summarizing the results of the tape evaluation were submitted weekly to the

Network Operations and Engineering Division. However, if gross discrepancies were discovered, this information was relayed the same day to pertinent personnel within that division.

Analog-To-Digital Conversion

Conversion from analog to digital tapes was accomplished by means of the Satellite Telemetry Automatic Reduction System (STARS). This equipment and its development are described in detail in this chapter under "Data Processing Equipment Development." It utilized the following functional elements:

- analog tape unit,
- time decoder,
- tone-burst signal converter,
- comb filter,
- digitizer,
- computer format control buffer, and
- digital tape unit.

The analog tape unit played back the signal in the same form and without distortion as recorded. The time decoder decoded either the serial decimal (SD) or binary coded decimal (BCD) time and provided the correct time to the computer format control buffer coincident with frame synch recognition. The comb filter is a sharp, narrow-band frequency separator that resolves frequencies from 4.5 kc to 15.4 kc in about 100 cps steps. A later model operating at 4x speed covered 20 to 60 kc in 400 cps steps. The comb filter has 128 tuned crystal filters spaced across the used frequency band. Each filter element drives a threshold detector and trigger circuit. During the time interval when a tone burst is applied to the filter bank, one of the threshold detectors is activated and the information is presented to subsequent digitizing equipment. The digitizer transfers the digital value of each comb filter to the computer format control buffer where a sequence starting with digitized time and followed by digitized data are stored in the memory unit until unloaded, a record at a time, onto a digital tape in accordance with the buffer's controls. The relationship of the STARS

line to the total processing system is illustrated in figure 6-4.

The initial equipment for digitizing Ariel I data was eventually supplemented, and finally supplanted, by the introduction of high speed equipment using a comb filter capable of operation between 20 kc and 60 kc, thus

permitting a speedup of 4 to 1. Data recorded at 7½ inches per second could thus be played back at 30 inches per second, permitting an increased efficiency in the automated digitizing operation. Operation at the 4x rate was found to be equal to and, in some respects, superior to operation at 1x rate as

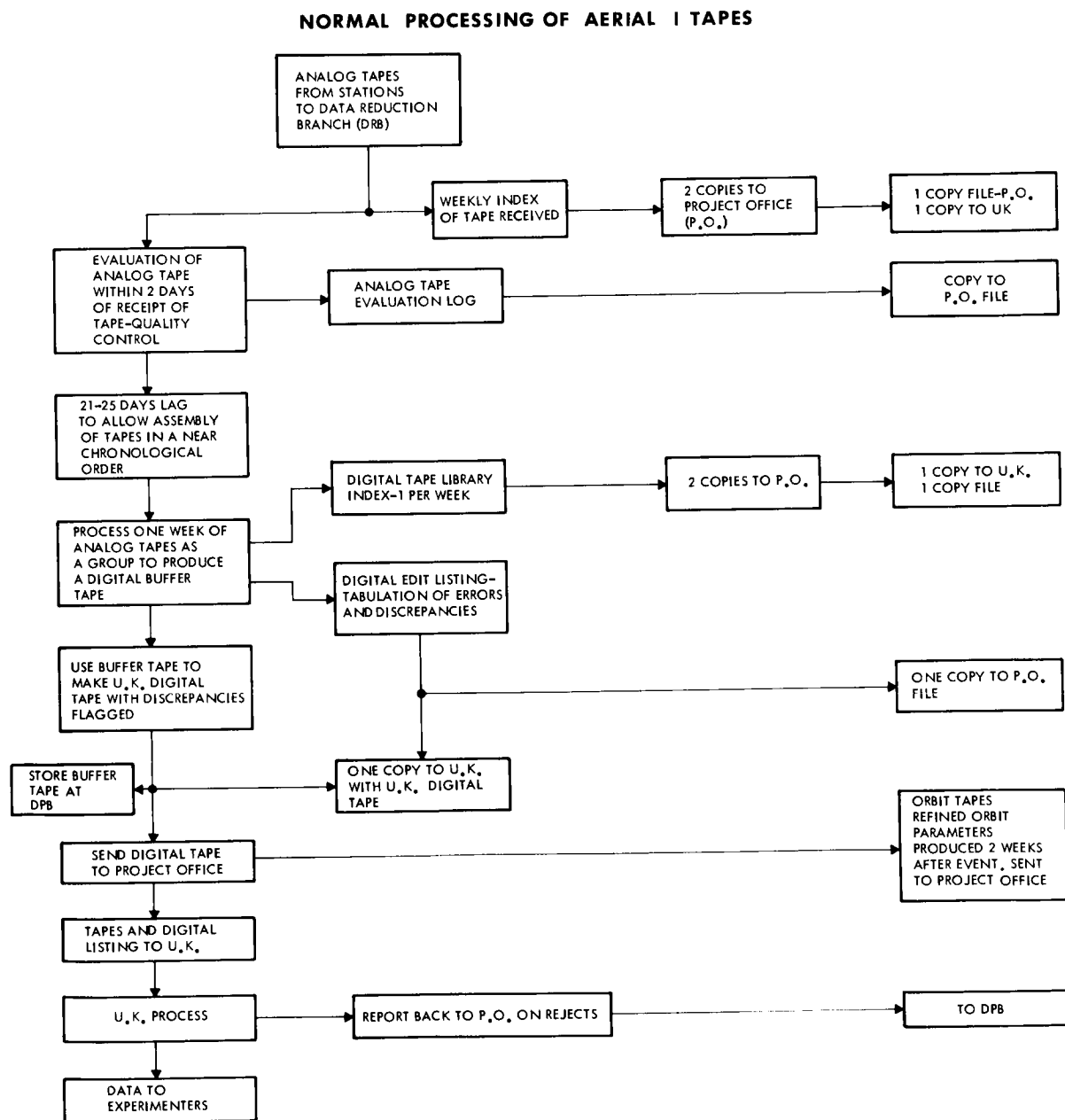


FIGURE 6-3. Data processing scheduling procedure.

DATA PROCESSING

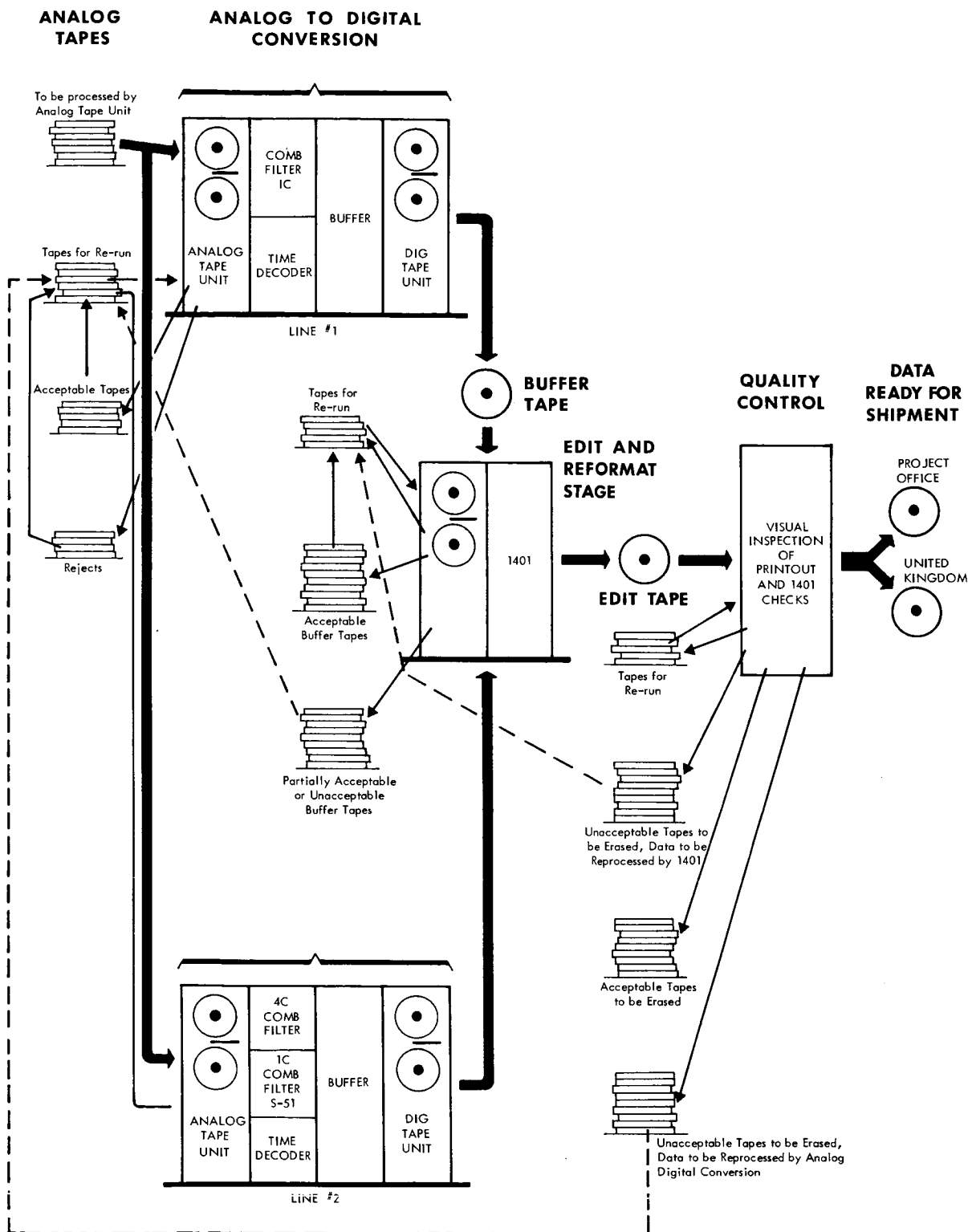


FIGURE 6-4. Ariel I GSFC data processing system, functional diagram.

evidenced by the amount of time inconsistencies and percentage of bad data points. The higher speed operation, initiated in January 1964, facilitated the rapid reduction of a large backlog of unprocessed tapes to a normal level.

Each pass or file on an analog tape was recorded as a separate entity on the digital tape, with each file being preceded by an identification record and terminated by an end of file record. Different formats were used for the high-speed and low-speed data. Moreover, the high-speed and low-speed data were recorded on separate digital tapes. This was done in a two step operation, wherein all high-speed data files were processed in

one pass of the analog tape and then the low-speed data processed in a second playback of the tape. A 10:1 ratio of data compression was effected during the analog to digital conversion process, i.e. approximately ten times as much PFM data were stored on a given area of digital tape as compared to analog tape. This does not take into account the supplementary information i.e. AGC, 10 kc linearizing frequency and voice, which is recorded on the analog tape but is not recorded on the digital tape. By virtue of the compression permitted by the digital recording process, multiple analog tapes were recorded on a single digital tape.

The output of the STARS line consisted of

A= I. D. NUMBER
B = ORBIT NUMBER
C= EDIT TAPE NUMBER
D= NUMBER OF FILES
E = PLAYBACK SPEED A=HI B=LO
F = DIGITAL START TIME
G= DIGITAL STOP TIME
H= BUFFER LINE (O-A-B)
I = BUFFER TAPE NUMBER
J = DATE DIGITIZED
K= OPERATOR CODE
L = TAPE RECORDER TIME CODE
M= EDIT DATE
N=P IF PRINTED BLANK IF NOT PRINTED
O = PRINT DATE
P = ERASE DATE
Q = CARD NUMBER

A	B	C	D	E	F	G	H	I	J	K	L	M	N
516211601001	0	2	48A180409			180653A		5	20516	BG		20602	
516211618001	0	2	48A185600			190519A		5	20516	BG		20602	
516211614001	1	2	48A193722			194809A		5	20516	BG		20602	
516211603001	1	2	48A194804			195435A		5	20517	BG		20602	
516211606001	1	2	48A195547			200024A		5	20517	BG		20602	
516211607001	1	2	48A200319			200703A		5	20517	BG		20602	
516211616001	1	2	48A202342			203107A		5	20517	BG		20602	
516211617001	2	2	48A212218			213122A		5	20517	BG		20602	
516211617001	2	2	48A214106			213122A		5	20517	BG		20602	
516211617001	2	2	48A214339			213122A		5	20517	BG		20602	
516211617001	2	2	48A220631			213122A		5	20517	BG		20602	

FIGURE 6-5. High-speed edit listing.

digital magnetic tapes in IBM binary coded decimal format suitable for further automatic data processing. The tapes were one-half inch wide by 1.5 mils thick by 2400 feet long and were stored on ten-inch reels. They were seven-track tapes in accordance with IBM standards for alpha-numeric code. Digitized sensor data (analog) were encoded in terms of numbers between zero and 128, and digital data as sequences of numbers using the digits zero through seven.

Digital Operations

The magnetic tape outputs from the STARS line were used as buffer tapes to produce final tapes for delivery to the United Kingdom with the following characteristics:

1. All digital tapes were divided into two categories: a) high-speed encoding and b) low-speed encoding.

2. All digital tapes were in standard IBM binary coded decimal (BCD) format, using even parity, and written at 200 bits/inch.

3. All tapes were checked for time consistency, the inconsistencies being appropriately flagged. A summary of the number of time inconsistencies and data word dropouts was prepared as an on-line listing and supplied with each tape.

4. The first record in each file constituted an identification record, and the number of files on a tape was counted. Figure 6-5 is an example of the high-speed edit showing the number of files on an edit tape listing. Figure 6-6 is an example of the low-speed encoder file listing.

The manner in which the data were regimented on the tapes is apparent in the following definitions.

File—A file constituted data received from

<p>A= I. D. NUMBER B= ORBIT NUMBER C= EDIT TAPE NUMBER D= NUMBER OF FILES E= PLAYBACK SPEED F= DIGITAL START TIME G= DIGITAL STOP TIME H= BUFFER LINE (O-A-B) I= BUFFER TAPE NUMBER J= DATE DIGITIZED K= OPERATOR CODE L= TAPE RECORDER TIME M= EDIT DATE N=P IF PRINTED BLANK IF NOT PRINTED O= PRINT DATE P= ERASE DATE Q= CARD NUMBER</p>													
A	B	C	D	E	F	G	H	I	J	K	L	M	N
516211701001	10	1	39B102833			103038A		7	20529	EG		20518	
516211712001	10	1	39B102838			103030A		6	20529	GG		20518	
516211803010	20	1	39B042503			042708A		8	20529	EG		20521	
516211803011	21	1	39B06090B			061117A		8	20529	EG		20521	
516211814005	28	1	39B170052			170252A		9	20529	GG		20521	
516211801005	20	1	39B185200			185405A		9	20529	GG		20521	
516211801013	20	1	39B205200			205242A		9	20529	GG		20521	

FIGURE 6-6. Low-speed edit listing.

a single pass over a telemetry station and corresponded therefore to the data from one analog tape recorded at that station. An *end-of-file* mark was used to separate successive files. These marks were an unwritten gap of $3\frac{1}{2}$ to 8 inches in length followed by a bit in the 8, 4, 2 and 1, tracks of the alphanumeric code (i.e. C B A 8 4 2 1). The tape mark was followed immediately by a longitudinal even parity check character.

Record—A record consisted of a number of characters separated by an unwritten interval (inter-record gap) of $\frac{3}{4}$ inch. A high-speed encoded record consisted of 976 characters. The low-speed encoder record consisted of 872 characters. *Identification records* constituted the first record of each file. The identification record consisted of a 12-character word (ID word) repeated as many times as was necessary to fill up the record. The format of the ID word was as follows:

Day Count			Tape	
Satellite	Year	of Year	Station	Number
xx	xx	xxx	xx	xxx

If an end-of-file mark occurred at the end of the ID record, this meant that the ID record was incorrect, the next succeeding record being the corrected ID record.

Frame—A frame consisted of a sequence of sensed data between synchronization pulses. A high-speed frame consisted of 16 data words corresponding to 16 bursts; the low-speed frame consisted of 16 bursts and sixteen blanks or 32 data words. In both types of frames a time word appeared immediately following the first burst (i.e. the synchronization burst) of that frame. This time word was used for computer check of time inconsistencies.

Word—Words were divided into two types: a) time words and b) data words. Time words consisted of 12 BCD characters, the first character containing a bit in at least the 8 and 4 track (i.e. CBA 8421=001100). Data words consisted of 3 BCD characters representing the burst frequency quantized by filters in the comb filter. Digital sensor data words appeared with numerals zero thru seven as the first character followed by two

zeros, analog sensor data by any number from 001 to 128.

The digital tapes obtained from the STARS line conversion were fed directly into an IBM 1401 computer. The purpose of the initial stage of computer processing was to edit and quality check the data to determine that the STARS line equipment was functioning properly and to flag time and data inconsistencies. Printouts of such discrepancies, together with summary information printed at the end of processing each file of data, provided the basis for either passing or rejecting the file. In the latter case the file was usually re-processed through the STARS line.

Some of the checks made by the computer were as follows:

a. Correct file identification—Each file identification was printed on the operator's console display for verification.

b. Correct frame time intervals—If the time per frame was not within a prescribed interval of time, the frame was denoted by an asterisk. This normally occurred as a result of data dropouts of one or more frames of data during the STARS line processing.

c. Incorrect time—An example would be backward time where the time for a following frame was less than the preceding frame. Each occurrence of incorrect time data resulted in a printout.

d. Illegal data characters—Numbers outside the acceptable range. For analog transducer data channels, the acceptable range was 000–119, whereas for digital transducer data channels only eight discrete values were acceptable. Also included in this check were data channels with a unique code indicating that none of the comb fingers reached its threshold. Information printed at the end of each file was as follows: the file identification, the station start and stop recording time, the amount of missing time as calculated from the time gaps, the number of bad or missing data points, the number of frames, and the percentage of data recovered from the file.

The output from the initial computer processing operation was an edited tape recorded in a prescribed format and containing

all the information that was contained on the digital tape obtained from the STARS line. In addition, the edit tape contained the flags indicating time drop outs, incorrect time, and incorrect or missing data. The edit tapes, together with the related punch cards, were sent to the U.K. for further processing. The edit tape was recorded in an IBM compatible tape format in order to permit direct input to the IBM 1401 computer used for the first stage computer processing in the U.K. Information contained on the Orbit tape consisted basically of sub-satellite latitude and longitude and height of satellite. This position information was given at constant time intervals throughout each orbit. A total of

80 tapes of orbital position were sent to the U.K.

Quality Control

Two types of quality control were instituted for Ariel I data. The first was performed automatically by the edit computer (IBM 1401) as outlined above. The second was performed by visual examination of sample printouts to assure the experimenters that electronic equipment was not malfunctioning.

The following special characters were employed to indicate either data, time, or low-speed anomalies:

Purpose	Character	Print	Bit Sequence
Data Dropout	Dash	-	0100000
Improper Time Advance	Asterisk	*	0101100
Proper Time Advance	Dot	.	0111011
Low-Speed Frame, Sync. Pulse	And	&	0110000

Inconsistent frame time was determined by comparing two successive frame times and determining the differences. For a burst blank duration of 20 milliseconds (the nominal burst blank period), the frequency would be 50 cps. During rf interference checkout of Ariel I it was found that this 50 cps signal interfered with a 100 cps signal used for time encoding. Therefore, the burst blank rate was changed to 55 cps. This change, in turn, shortened the burst blank duration to 18.2 milliseconds, and made the frame consisting of 16 burst blank sequences 291 milliseconds in duration instead of the nominal 320 milliseconds. Accordingly the quality control program was altered to compare the successive time frames to 291 ± 20 milliseconds. If the difference fell outside this range, an asterisk character was inserted at the end of the frame.

Dropout data were determined by noting the occasions when three dash characters appeared in a sequence of data. These occa-

sions were then counted and the sum accumulated for each file. The sum of data dropouts was printed, along with the sum of time intervals inconsistent, in an on-line hard copy printout.

The proper time advance was shown by the presence of a dot, and the recognition of low-speed frame, that is the presence of the command tone, was shown by the presence of an ampersand. Examples of printouts of magnetic tape representing both high-and-low speed encoded data are shown in figures 6-7 and 6-8 respectively.

Upon completion of the automated editing operation, the computer printed out the following:

1. Label or identification word
2. Start time
3. End time
4. Total time difference between start and end times
5. Time lost or dropped out
6. Percentage of time lost to total time

ARIEL I: THE FIRST INTERNATIONAL SATELLITE

Identification Label → 516217701238

FRAME NO.	Z TIME			CHANNEL NO.															
	Day	Hr.Min	Sec	1	2	3	4	5	6	7	8	9	10	11	12	13	14	15	16
13	-07	1918	37.399	031	042	032	105	105	103	105	075	075	071	084	051	105	105	105	700 •
14	-07	1918	37.719	030	200	500	105	105	102	105	074	076	071	084	051	105	103	105	005 •
15	-07	1918	38.039	700	700	700	105	105	103	105	074	076	072	085	051	105	103	105	000 •
0	-07	1918	38.359	500	700	300	105	105	103	104	075	075	070	084	051	105	103	105	005 •
1	-07	1918	38.679	100	500	400	105	104	103	105	074	076	072	084	051	105	103	105	100 •
2	-07	1918	38.999	081	044	105	105	105	103	105	075	075	071	084	050	106	103	105	005 •
3	-07	1918	39.318	071	026	103	105	105	102	104	074	077	071	083	051	105	103	105	200 •
4	-07	1918	39.639	083	087	105	105	103	103	105	075	076	071	084	050	105	103	105	005 •
5	-07	1918	39.958	073	079	032	105	105	103	105	073	076	071	084	051	105	103	105	300 •
6	-07	1918	40.278	030	046	085	105	104	103	105	075	076	071	083	051	105	103	105	005 •
7	-07	1918	40.598	048	047	032	105	105	103	105	075	075	071	085	051	105	103	105	400 •
8	-07	1918	40.918	500	700	300	105	105	103	105	073	076	074	084	051	105	103	105	005 •
9	-07	1918	41.239	100	500	400	105	103	103	105	074	077	072	085	051	105	103	105	500 •
10	-07	1918	41.558	083	044	105	105	105	103	105	074	076	071	085	050	105	103	105	005 •
11	-07	1918	41.878	071	054	103	105	104	103	105	074	077	071	084	051	105	103	105	600 •
12	-07	1918	42.198	085	072	105	105	105	103	105	076	075	071	085	051	105	103	105	005 •
13	-07	1918	42.518	032	043	032	105	105	103	105	075	075	072	083	050	105	103	105	700 •
14	-07	1918	42.838	031	500	300	105	105	103	105	074	076	071	083	050	105	103	105	005 •
15	-07	1918	43.158	700	700	700	105	105	103	105	073	076	071	084	050	105	103	105	000 •
0	-07	1918	43.478	700	700	300	105	104	078	105	074	077	071	084	050	105	081	105	005 •
1	-07	1918	43.798	100	600	400	105	105	083	105	074	077	071	085	051	105	087	105	100 •
2	-07	1918	44.118	086	045	050	094	092	065	101	075	077	071	085	051	105	068	103	005 •
3	-07	1918	44.438	072	081	074	041	093	071	103	075	077	071	085	050	105	075	102	200 •

Signifies playback of low speed recorded data as a result of a station command.

11	-07	1927	59.885	066	059	074	023	097	031	103	043	076	043	075	047	105	035	103	600 •
12	-07	1928	00.205	048	072	068	023	098	039	103	045	074	044	075	047	105	043	103	005 •
13	-07	1928	00.525	029	043	029	023	097	047	103	051	065	046	076	046	105	051	103	700 •
14	-07	1928	00.844	036	400	700	025	097	054	103	047	---	---	---	---	---	---	---	---
15	-07	1928	01.169	---	---	---	---	---	---	---	---	---	---	---	---	---	---	---	---
0	-07	1928	01.487	---	---	---	---	---	---	---	---	---	---	---	---	---	---	---	---
1	-07	1928	01.805	---	---	---	---	---	---	---	---	---	---	---	---	---	---	---	---
2	-07	1930	20.348	045	045	105	105	104	103	105	043	075	065	085	041	107	103	105	005 *

Indicates a time drop-out. (Frame 1 to 2)

FIGURE 6-7. Example of high-speed data printout.

7. Number of bad data points
8. Type of data (high- or low-speed)
9. Number of frames
10. Tolerance with which time frames are compared

The results of the human inspection of Ariel I processed data pointed out several interesting problems. Equipment malfunction was not uncommon, generally appearing in several forms. One was the apparent time

DATA PROCESSING

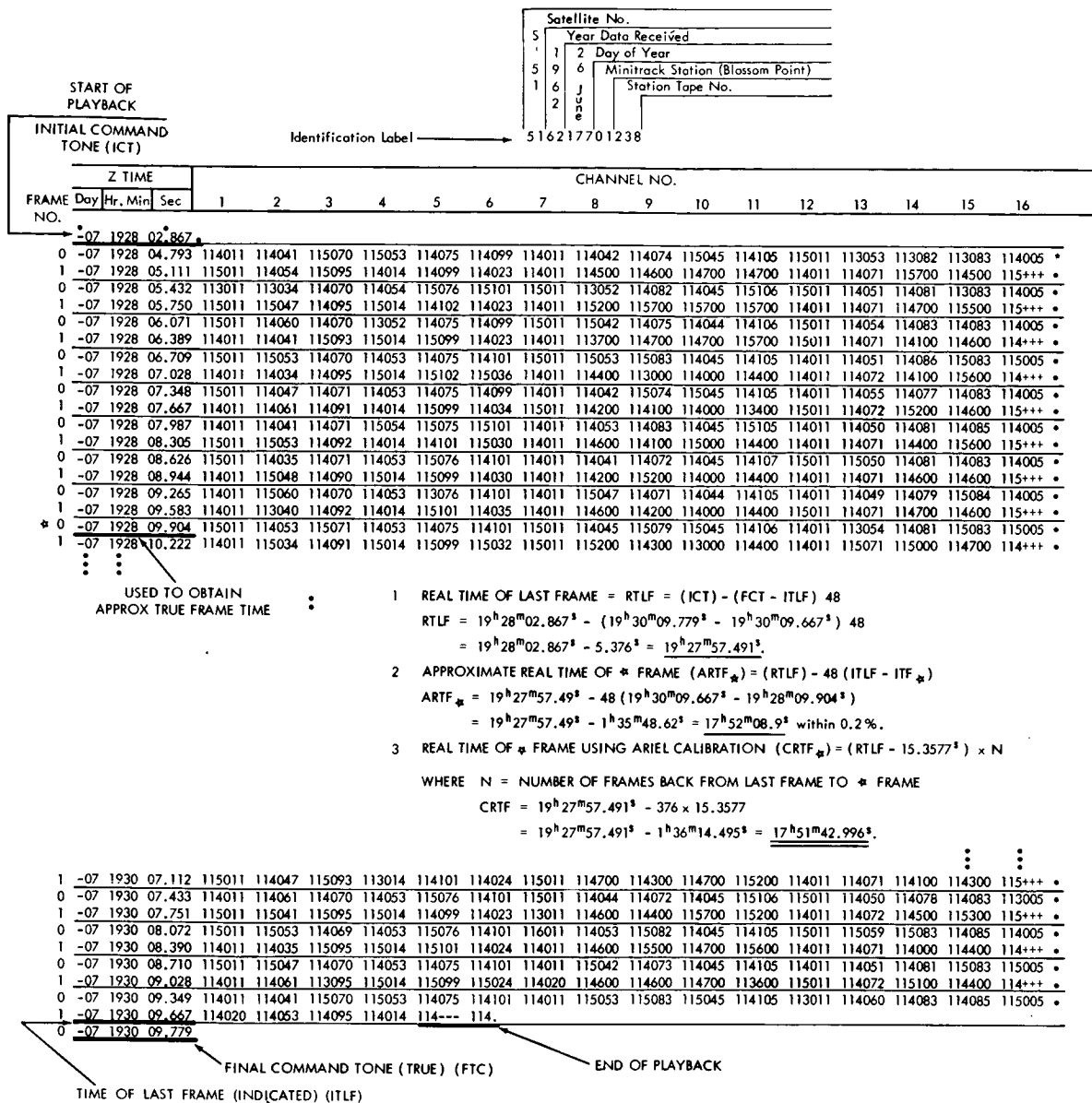


FIGURE 6-8. Example of low-speed data printout.

discontinuity. Time errors were generally traced to either encoding errors at the station, decoding errors at the digitizing station, or inability of a shift register to respond rapidly enough. Another frequent error discovered was the apparent absence of recognition of the command tone either at the beginning of a low-speed encoding sequence, at the end of the low-speed encoding, or, occasionally, at both beginning and end.

Data Processing Equipment Development

Two major types of equipment were developed for the processing of Ariel I Data: the STARS lines, previously mentioned, and the Ariel I test stands, which were used during integration and test of the satellite. The development and successful operation of these equipments were not only essential to the success of the Ariel I project, but also served

well in the data processing, test and integration of subsequent spacecraft.

Design of the Ariel I Stars Line—H. H. Levy

Until the advent of the Ariel I project, only one STARS (Satellite Telemetry Automatic Reduction System) system had been designed and put into operation (for the S-30, S-3, P-14, Vanguard 3 satellites). The Ariel I satellite introduced several new requirements for data processing and therefore the design of its data processor departed from that of the first STARS in a number of ways.

Format Description. The Ariel I format was made up of frequency bursts and blanks of data using PFM telemetry. The bursts

were 10 millisecs in duration. The frequency was constant during the burst but could be any frequency between 4.5 and 15 kc. A frame of data was comprised of 16 bursts and blanks with a frame sync pulse burst being 15 ms in duration with special frequencies in the burst. The telemetry was sent in two different formats. One (hi-speed) contained 16 frames per sequence, the other (low-speed) contained 2 frames per sequence. The hi-speed was real-time data while the low-speed was playback data from a tape recorder in the satellite. In both formats there were analog or octal channels in each frame of data. It was decided that the processor could more efficiently determine the octal or analog channels than the computer, so recognition of the frame sync, channel sync, frame sequence

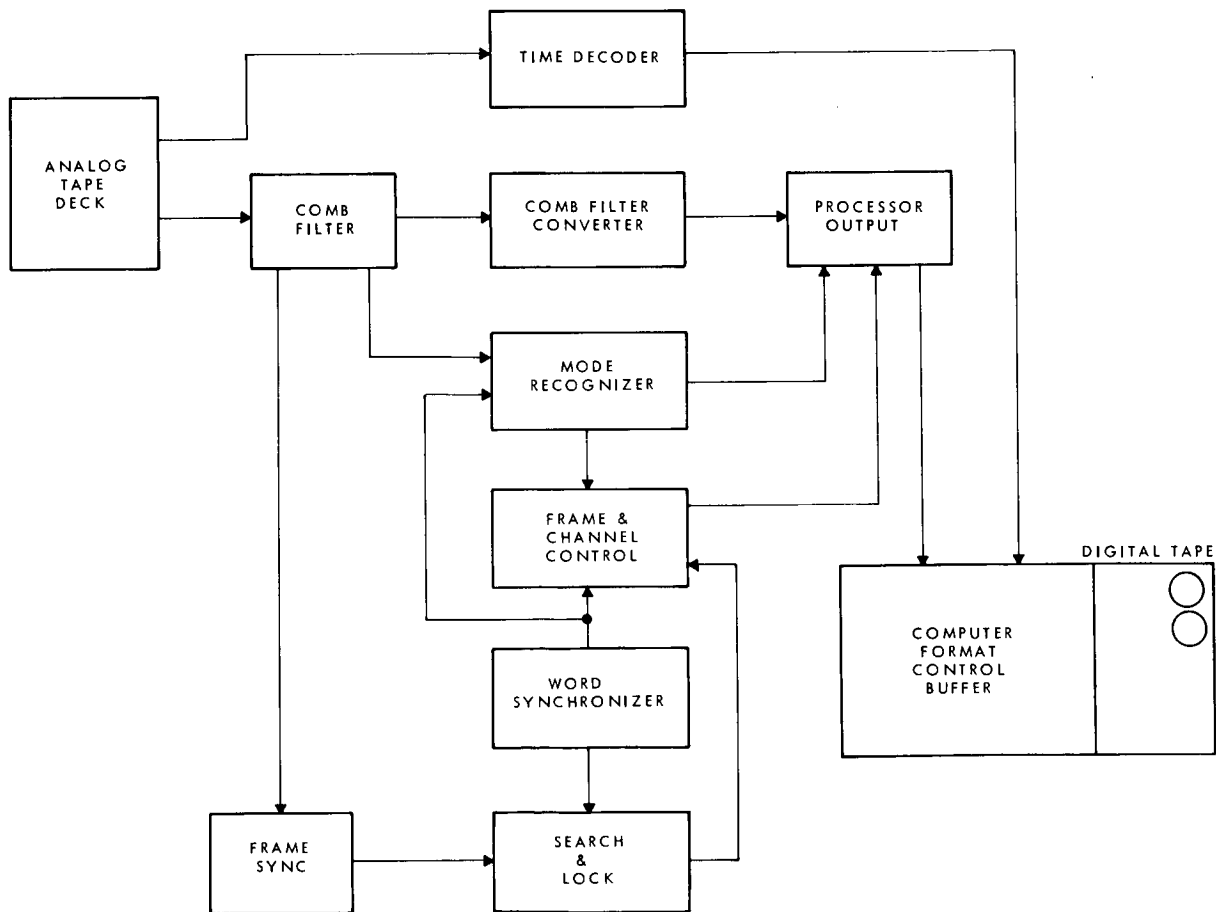


FIGURE 6-9. STARS line functional block diagram.

number, and hi-speed or low-speed were designed into the processor. The low-speed also had the blanks filled in with a reference frequency of 15.4 kc. This was digitized also as a check on the speed of the satellite tape recorder. The system used for processing the data is shown in figure 6-9.

General Equipment Description. An improvement in this system over previous systems was the addition of an automatic burst rate synchronizer and an automatic frame sync recognizer and verification system. This removed from the operator the control and decision previously needed by him to process a tape.

The sequence arrangement of Ariel I meant that, in order to correctly determine channels and frames, there must be an indicator of which frame was which. This was done by using the sync pulse position and encoding a specific frequency in the sync burst of a specific frame. Upon decoding the sync frequency the data processor could continuously monitor and check its frame decommutator position.

The beginning of a low-speed playback was recognized by a two-second burst of 320 cps. This required special filter and logic circuits. This signal was used to correlate the low-speed data with real time.

The system was designed to treat the data as follows: with a front panel switch in the hi-speed data position, the recognition circuits would detect the hi-speed format and when locked on correctly would then output data to the computer control buffer. When low-speed data were recognized while in the hi-speed mode, they were ignored and no data were sent to the buffer. As soon as the hi-speed resumed, the system output was resumed.

If the front panel switch was in the low-speed mode, the recognition circuits would detect the 320 cps tone and lock onto the low-speed data. At the end of the low-speed data the system would stop.

Subsystem Description. The system was comprised of several subsystems described as follows:

Comb Filter. A contiguous bank of 100-

cps bandwidth filters. One hundred and twenty-eight filters were used to cover the data band of 5-15 kc plus guard bands above and below the data band for special frequencies. This allowed 1% resolution of the data frequencies. The comb filter was redesigned to cope with the low-speed data which had the blanks filled in with the reference frequency. It was necessary to split off from the data channels the bank of filters from 15.1 kc to 16.3 kc and not have those teeth in the filter contribute to the AGC system in the bank since the AGC was designed for a 50-cps data word rate and the 100-cps rate would shift the AGC erroneously.

Comb Filter Converter. This was a logic system to convert one of the 128 pulses from the comb filter at any burst time into a BCD or octal number representing the frequency of the burst. If the data were analog, they were represented as a number from 1 to 123; if digital, a number from 000 to 700.

Word Synchronizer. A digital phase-locked loop acquired the phase and frequency of the telemetry burst rate and provided a clock to the remaining parts of the system. It also provided a flywheel for passing through missing data.

Frame and Channel Decommutation. This subsystem provided the logic to determine which frame and which channel were being recognized so that the data output could be indicated as either analog or octal.

Mode Recognizer. This circuit provided the necessary logic for determining whether hi-speed or low-speed data were being received.

Processor Output Control. This subsystem was a large multiplexer which gathered all data and commands and controlled the buffer operation.

Frame Sync, Search, and Lock. This unit detected frame sync, verified correct acquisition, and provided a flywheel over missing sync pulses. The system did not output data unless in the lock mode.

Computer Format Control Buffer. This was a commercial equipment which contained a time decoder, a memory, and a digital tape recorder. Its function is to receive data

from the processor or time from the time decoder, both upon command from the processor, and to put this information on a digital tape in IBM-binary coded decimal format. The digital tape then was suitable for further processing by a computer.

Ariel I Test Stand—A. Demmerle

The Ariel I (test stand) data reduction system was designed and three systems built to facilitate the integration and testing of the satellite. The system's input was the raw PFM signal, obtained from a receiver output or as recorded on an instrumentation tape deck. The outputs of the systems were decommutated and decoded data, which allowed the checkout of the entire satellite data collecting system, from the sensor, encoders, and modulator through the transmitters and RF equipment. These outputs were presented both as visual displays and on a paper-tape printout which served as a permanent record of the satellite's performance under the various tests for environmental conditions. The degree to which this system processed the data can be best seen by viewing at the PFM encoder format.

Each channel was a ten-millisecond blank followed by a sinusoidal ten-millisecond burst which conveyed information by virtue of the frequency of the burst. (There were two types of sequence, the high-speed sequence which consisted of 16 channels/frame and 16 frames/sequence which was used for real time data transmission, and a low-speed sequence with 16 channels/frame and two frames/sequence which was used for playing back, upon command, data which had been recorded on an on-board tape recorder.) During the low speed encoder data the blanks were filed by a 15.4 kc sinusoidal signal which was used as a reference signal to correct for on-board tape recorder speed fluctuations.

This data reduction system could:

1. Find and maintain synchronism between the data reduction system, and the telemeter format, i.e., be able to label any given channel and frame in the same way it had been labeled within the satellite encoder.

2. Display and print the frequency of any one channel in every frame.

3. Collect the data groupings C_1 , C_2 , C_3 , and C_4 , and C_5 , C_6 , and X_1 , X_2 , X_3 , X_4 , and X_5 , in which each channel was one of eight possible discrete frequencies, and thus three bits of the larger multibit number, and having compiled these three bit numbers, convert them to an easy-to-read decimal number for display and printout.

4. Keep track of how many high-speed and how many low-speed sequences had elapsed.

The principal differences between this system and the data reduction system for final in-flight data processing (STARS line) lie in two areas:

1. This system had a higher threshold signal-to-noise ratio; i.e., it could not process very noisy in-flight data, it did not use the sophisticated signal conditioning equipment of the final in-flight data processing lines.

2. It could not output all the data all the time, nor did it output data on a digital tape, ready for further data reduction by computer processing. Instead it visually displayed the output of only several channels of data at one time, which was all that was necessary for the integration testing and evaluation stage of a satellite design.

It was, however, capable of some processing of some in-flight data, and was in fact used for "quick look" immediately upon and after launch to see that the satellite was functioning properly. It was well suited to this purpose because of its ready output of readable, usable data.

Statistical Summary

Tabulated here are the totals of the data acquired, processed and shipped to the U.K. for the active life of Ariel I. This covers the period from launch up to the time data acquisition terminated in November, 1964.

1. *Telemetry Data Tapes Received from Network Stations*

a. No. Received From	
All Stations -----	11,910

DATA PROCESSING

b. Disposition:

- 1) Shipped to U.K. (Singapore and South Atlantic tapes) ----- 2,059
- 2) Stored at Federal Record Center, Alexandria, Va. 5,687
- 3) Stored in Building 16, GSFC ----- 4,164

2. Data Files

- a. No. Received From All Stations ----- 42,407
- b. Average No. Per Analog Tape ($42,407 \div 11,910$) ---- 3.5
- c. No. Processed and Sent to U.K. ----- 18,055
- d. No. Unprocessable ----- 24,352

3. Digital Tapes

- a. STARS Line Tapes (Stored in Building 16, GSFC) ----- 618
- b. Edit Tapes Sent to U.K. 597*
- c. Average No. of Files per Edit Tape ($18,055 \div 597$) --- 30

4. Hours of Data Sent to U.K. 3,307

a. Average Hours per Edit

Tape ($3307 \div 597$) ----- 5.50

b. Average Hours per File

($3307 \div 18,055$) ----- 0.18

As is apparent from the tabulation above, a large percent (57%) of the files received were unprocessable. The major cause of unprocessable tapes was the lack of modulation or unintelligible modulation. This was attributed to the degeneration of vehicle performance subsequent to the Starfish event in July 1962. The telemetry system operation became erratic. Days in which good quality data were acquired were followed by days in which poor quality or no data were acquired. These periods were as short as a few days and as long as three months.

Even though the percentage of unprocessable files was exceptionally high for Ariel I, the amount of data successfully processed was high as compared to most other satellites using PFM telemetry, as can be noted in the following table:

	Total Hours of Data Successfully Processed	Equivalent No. of Data Points Successfully Processed
Ariel I	3307	595,000,000
Explorer 12 (S-3)	1500	270,000,000
Explorer 14 (S-3a)	6232	1,120,000,000
Explorer 15 (S-3b)	1917	345,000,000
Explorer 18 (IMP-1)	5737	65,000,000

Conclusion

Processing of Ariel I data required a major support effort by GSFC entailing extensive use of tape evaluation equipment, signal processing equipment, and electronic computers; as well as persons competent in the use and application of this equipment. The erratic performance of the spacecraft telemetry after the Starfish event, presented the problem of salvaging the maximum amount of useable data from the telemetry tapes received. This problem was resolved by means of quality

control techniques, both machine and manual, at both the input and output ends of the data processing chain. The system, procedures and techniques that evolved from the processing of Ariel I data, have served as a valuable model in subsequent automatic telemetry data processing. All GSFC data processing support commitments were successfully met.

It would be grossly unfair to conclude without acknowledging the efforts and contributions of the members of the Data Processing Branch who were intimately involved in carrying out the operations described above. Mr. Thomas J. Lynch was responsible for the

* Twenty-six tapes were returned from the U.K., rerun, and sent back.

overall planning and the computer programming effort. Mr. Daniel Dembrow managed the production operations with the able assistance of Mr. Clyde Freeman. And finally, Mr. Bernie Narrow and Mr. Dembrow contributed greatly to the documentation presented herein.

UNITED KINGDOM PROCESSING

E. B. Dorling, U.K. Project Coordinator

The data from ARIEL I were received in the United Kingdom in digital form on a total of 623 magnetic tapes (including 26 which were redigitized on the NASA STARS line) with the individual experiments still intermixed. Satellite height-and-position data were also received on magnetic tape. The initial task in the U.K. was to separate the data on individual tapes, first analyzing and reducing them where possible and adding the orbital information and any other relevant geophysical data. Thus, each experimenter could be presented with his results in a form suitable for further independent analysis and interpretation.

The Computer Program

The computer operations in the U.K. were organized in the following way. The data, which were written in low density (200 ch./in.) binary coded decimal format were edited on an IBM 1401 computer. This operation checked the identification record on each data file (a file being the data acquired in one 10- to 20-minute pass of the satellite over a STADAN station), identified the synchronization pulses which began each encoder frame, checked that each data sample had its appropriate three-character word, and discarded any encoder sequence which was incomplete. The output was written on magnetic tape in high density (556 ch./in.) BCD in a standard format of one identification record and a series of long data records, one record per encoder sequence, each pass again being written as one file. If required, the edited data could at the same time be listed in columns on the 1401 printer for easy refer-

ence. Two 1401 edit programmes were prepared, one for the real-time (high-speed) data, the other for the stored (low-speed) data; these two types of data had been digitized in separate chronological sequences in the U.S. and were handled entirely separately from each other in the U.K.

One hour of high-speed data required 12 minutes to edit; the low-speed data took rather longer.

The edited data were next processed on an IBM 7090 computer. The inputs to the computer were a 1401 output tape, an orbital tape (a weekly data tape written at the GSFC in binary code, giving geodetic longitude, latitude and height against every minute of Universal Time), ten day cards and the program. The outputs were five high-density tapes, four in BCD carrying the results of the experiments contributed by each of the four groups of experiments, the fifth in binary, duplicating certain of U.C.L. data. Two 7090 programs were prepared, one for the high-speed data, the other for the low-speed data; both comprised a main program in FORTRAN with sub-routines and functions mainly in FORTRAN but with one or two (such as a sub-routine provided by the GSFC for reading the binary orbital tape) in FAP. The majority of the sub-routines contained complex logical arguments concerning the acceptance or rejection of data, followed by simple calibrations and the evaluation of functions. One sub-routine computed B/L values at given points and added these to the Imperial College and Birmingham low-speed data. Another sub-routine checked the timing of each frame and detected faulty values, correcting them where possible, printing them out where not. With the low-speed data the real times of each data frame were computed from the playback time accompanying each file, and were inserted. A necessary input with both programs was a batch of ten-punched cards or "day cards" which provided certain extra information necessary to the interpretation of some experiments. For instance, solar aspect measurements were carried on the high-speed encoder but were needed in the analysis of the stored data;

accordingly these measurements were reduced by hand in advance of the routine data processing and values were inserted on the low-speed day cards. Entries on these cards were also used to correct play-back command time errors which had been detected from records supplied by the GSFC. With the high-speed program the day cards were largely concerned with calculation of sunrise and sunset times.

In order to save future computer time the experimenters' outputs were written in special long records of several thousand characters each. The product of one computer run was written as a single file of these long records, a run being based usually on the contents of one U.S. digital tape, averaging 33 files or satellite passes. One file of high-speed data took about seven minutes to process on the 7090 (half this time on the 7094); the low-speed data took a little longer.

In general the low-speed data, which were of good quality, were processed fully well in advance of the high-speed data because of the great value of orbit-by-orbit coverage, coupled with the relative simplicity of the analysis procedures.

The product of a 7090 run was, as we have seen, five partially-filled experimenters' tapes. These tapes were collated from time to time to produce final master tapes. In some cases the masters have been or will be used on computers for a further stage of analysis; in others no further computer analysis is intended. In particular most of the stored Birmingham RF probe electron density data, to which were added Universal Time, local solar time, geodetic and geopotential height, geodetic and geomagnetic co-ordinates, have been printed in full and reproduced in four volumes for general scientific use; the remaining data may be published in a fifth volume in due course.

Program Modification

From time to time during the life of the satellite an experiment would cease to operate, and so at the appropriate stage in the data processing the 7090 computer program

was modified, usually by the removal of a sub-routine. With the failure of the Birmingham RF probe on 3rd March 1963 the U.C.L. electron density and temperature boom probe became the sole surviving sensor, and at this stage an important change in procedure was made. It was arranged that the responsibility for processing all data acquired should be taken over by U.C.L. from the S.R.M.U. To economize in machine time a new computer program was prepared by U.C.L. which, amongst other changes, dispensed with the preliminary 1401 editing routine. It also dispensed with the orbital tape and instead calculated each height and position from the appropriate orbital elements, a process which in this particular application saved computer time.

Errors in Data

The 1401 edit programs were written bearing in mind that the data would contain a variety of errors, or would fail to conform exactly with the specified format. Certain errors were not foreseen, however, and these either halted the 1401 (as, for example, with an asterisk) or they were carried through to the 7090, causing data to be rejected or to give faulty outputs or to cause the run to be terminated. Because of the large volume of other data awaiting attention, time was not spent on overcoming errors but, with certain exceptions, the tapes were put aside. Some ten per cent of the total data up to 3rd March 1963 were affected. The experimenters were informed of the position and were told that recovery would only be attempted by special request. The exceptions were the low-speed data and those data taken in the first three weeks after launch where the X-ray experiment was working correctly. Errors encountered here were first located and identified, then removed by selective copying. In order that as much solar X-radiation data as possible should be recovered some data were redigitized at the GSFC and in addition a few analog passes originally rejected as unusable were digitized. Where these data were then found to be too poor to be accepted by the 1401 edit program, they

were listed in their raw form and sent to the experimenter to be analyzed by hand; but it is of interest that little useful information could in fact be obtained from data rejected by the 1401.

Two difficulties encountered during the computer operations caused a disproportionate expenditure of time and money. One was the inability of the 1401 to deal with an asterisk, the result of encountering a crop of asterisks on data tape being a large number of extra 1401 operations and a proliferation of 7090 output tapes. The other difficulty was the action of the 7090 monitor in terminating a run when a fault was encountered, rather than permitting the fault to be skipped and the run continued. This again caused more 1401 copying operations and resulted in yet more 7090 output tapes. Unfortunately, it proved impossible to overcome these

difficulties by modifications to the programs in the time available.

Summary of Tape Operations

A total of 623 magnetic tapes (including 26 redigitized) were received in the U.K. from the Data Processing Branch of the GSFC. These carried 3307 hours of non-redundant data, including some 850 playbacks of low-speed data.

Of the total amount of digitized data received, about 37% (1200 hours) were processed by the S.R.M.U., using over 350 hours of IBM 1401 time and 140 hours of IBM 7090 time (not including time lost initially with program faults). About 31½% of the data were rejected because of errors. The remaining 60% (2000 hours) carried only electron temperature data and these were processed separately by U.C.L.

REFERENCES

1. BISWAS, S., FICHTEL, C. E., AND GUSS, D. E., "Study of the Hydrogen, Helium, and Heavy Nuclei in the November 12, 1960 Solar Cosmic-Ray Event," *Phys. Rev.* 128(6):2756-2771, December 15, 1962.
2. QUENBY, J. J., AND WENK, G. J., "Cosmic Ray Threshold Rigidities and the Earth's Magnetic Field, *Phil. Mag.* 7(81):1457-1471, September 1962.
3. WEBBER, W. R., "Time Variations of Low Rigidity Cosmic Rays During the Recent Sunspot Cycle—Section 9—The Differential Rigidity of the Primary Radiation at Sunspot Minimum," *Progress in Elementary Particle and Cosmic Ray Physics*, 1962 v. 6 (J. G. Wilson and S. A. Worthington, eds.): 192-206, Amsterdam: North Holland Pub. Co., 1962.
4. ELLIS, R. A., JR., GOTTLIEB, M. B., AND VAN ALLEN, J. A., "Low-Momentum End of the Spectra of Heavy Primary Cosmic Rays," *Phys. Rev.* 95(1):147-159, July 1, 1954.
5. POMERANTZ, M. A., "Solar Diurnal Variation of Cosmic Ray Intensity," *J. Phys. Soc. Japan* 17, Suppl. A-II: 1962.
6. KURNOSOVA, L. V., LOGACHEV, V. I., RAZORENEV, L. A., FRADKIN, M. I., "Energy Spectra of the Different Groups Issue of Cosmic Ray Nuclei Measured by Cherenkov Counters on Spaceships-Satellites," *Iskusstvennyye Sputniki Zemli* 12: 16-30, 1962.
7. ELLIOTT, H., "Cosmic Ray Work at the Imperial College of London in Relation to Solar Modulation and Geomagnetic Effects," *Proc. I.U.P.A.P. on International Conference on Cosmic Rays* 2:170, Jaipur, India: December 1963.
8. QUENBY, J. J., *Handbuch der Physik*, Band 46/2: Springer-Verlag, 1965.
9. DURNEY, A. C., ELLIOTT, H., HYND, R. J., AND QUENBY, J. J., "Satellite Observations of the Energetic Particle Flux Produced by the High-Altitude Nuclear Explosion of July 9, 1962," *Nature* 195(4848):1245-1247, September 29, 1962.
10. PIEPER, G. F., "A Second Radiation Belt from the July 9, 1962, Nuclear Detonation," *J. Geophys. Res.* 68(3):651-656, February 1, 1963.
11. CULHANE, J. L., WILLMORE, A. P., POUNDS, K. A., AND SANFORD, P. W., "Variability of the Solar X-Ray Spectrum Below 15A," *Space Research IV; Proceedings of the Fourth International Space Science Symposium, Warsaw, Poland, June 4-10, 1963* (P. Muller, ed.): 741-758, Amsterdam: North-Holland Publishing Co., 1964.
12. WHITE, W. A., "Solar X-Rays—Slow Variations and Transient Events," *Space Research IV; Proceedings of the Fourth International Space Science Symposium, Warsaw, Poland, June 4-10, 1963* (P. Muller, ed.): 771-779, Amsterdam: North-Holland Publishing Co.; New York: Interscience Publishers, 1964.
13. POUNDS, K. A., "Recent Solar X-Ray Studies in U. K.," *Annales d'Astrophys.* 28(1):132-145, 1965.
14. SHKLOVSKII, I. S., "Nature of Solar X-Ray Emission," *Soviet Astron.-AJ* 8:538, 1965.
15. DODSON, H. W., AND HEDEMAN, E. R., "McMath-Hulbert Observatory Working List of Flares and Daily Flare Index for 1962," Boulder, Colorado: *International Geophysical Year, World Data Center A, IGY Solar Activity Report Series*, No. 25 April 1, 1964.
16. BOWEN, P. J., BOYD, R. L. F., RAITT, W. J., AND WILLMORE, A. P., "Ion Composition of the Upper F-Region," *Proc. Roy. Soc.* 281A:504-514, October 6, 1964.
17. BAUMANN, R. C., "Ariel 1—The First International Satellite," NASA Special Publication 43, 1963.

18. BOURDEAU, R. E., AND DONLEY, J. L., "Explorer VIII Satellite Measurements in the Upper Ionosphere," *Proc. Roy. Soc.* 281A:487-504, October 6, 1964.
19. BOWLES, K. L., OCHS, E. R., AND GREEN, J. L., "On the Absolute Intensity of Incoherent Scatter Echoes from the Ionosphere," *J. Res. Nat. Bur. Stand.* 66D(4):395-407, July-August, 1962.
20. EVANS, J. V., "Diurnal Variation of the Temperature of the F-Region," *J. Geophys. Res.* 67(12):4914-4920, November 1962.
21. HANSON, W. B., "Electron Temperatures in the Upper Atmosphere," *Space Research III; Proceedings of the Third International Space Science Symposium, Washington, D. C.* (W Priestler, ed.):282-302, Amsterdam: North-Holland Publishing Company, 1963.
22. DALGARNO, A., MCELROY, M. B., AND MOFFETT, R. J., "Electron Temperatures in the Ionosphere," *Planet. Space Sci.* 11(5):463-484, May 1963.
23. BOURDEAU, R. E., "Ionospheric Research from Space Vehicles," *Space Sci. Rev.* 1(4):683-728, May 1963.
24. GROVES, G. V., "Latitude and Diurnal Variations of Air Density from 190 to 280 km as Derived from the Orbits of Discoverer Satellites," *Proc. Roy. Soc.* 263A:212-216, September 5, 1961.
25. HARRIS, I. AND PRIESTER, W., "Theoretical Models for the Solar-Cycle Variation of the Upper Atmosphere," NASA Technical Note D-1444, August 1962.
26. SAVENKO, I. A., "Soft Particle Radiation at an Altitude of 320 km in the Latitudes near the Equator," *Planet. Space Sci.* 11(4):431-436, April 1963 (translation).
27. BOURDEAU, R. E., AND DONLEY, J. L., "Explorer VIII Satellite Measurements in the Upper Ionosphere," *Proc. Roy. Soc.* 281A:487-504, October 6, 1964.
28. SAYERS, J., "The Electron Density Distribution in the Topside Ionosphere. I. Magnetic-Field-Alined Strata," *Proc. Roy. Soc.* 281A:450-458, 1964.
29. BOWEN, P. J., WILLMORE, A. P., AND BOYD, R. L. F., "Some Preliminary Results of the Plasma Probe Experiments in the Satellite Ariel," *International Conference on the Ionosphere Proceedings, 2nd, Imperial College London, July 1962* (A.C. Stickland, ed.): 517-522, London: Institute of Physics and the Physical Society, 1963.
30. DRUYVESTEYN, M. J., "Afterglow in Glow Lamps Filled with Neon, Argon, and Neon-Argon Mixtures," *Z. Physik* 57(5-6):292-304, 1929.
31. BOYD, R. L. F., AND TWIDDY, N. D., "Electron Energy Distributions in Plasmas I," *Proc. Roy. Soc.* 250A:53-69, February 24, 1959.
32. JASTROW, R., AND PEARSE, G. A., "Atmospheric Drag on the Satellite," *J. Geophys. Res.* 62(3):413-423, September 1957.
33. KRAUS, L., AND WATSON, K. M., "Plasma Motions Induced by Satellites in the Ionosphere," *Phys. Fluids* 1(6):480-488, November-December, 1958.
34. RAND, S., "Damping of the Satellite Wake in the Ionosphere," *Phys. Fluids* 3(4):588-599, July-August, 1960.
35. ALPERT, YA. L., GUREVICH, A. V., AND PITAEVSKIT, L. P., "Effects Produced by an Artificial Satellite Rapidly Moving in the Ionosphere or in an Interplanetary Medium," *Soviet Phys. Uspekhi* 6(1):13-16, July-August, 1963.
36. SAWACHUK, W., "Wake of a Charged Prolate Spheroid at Angle of Attack in a Rarefied Plasma," *Rarefied Gas Dynamics; Proceedings of the Third International Symposium on Rarefied Gas Dynamics held at the Palais de l'UNESCO, Paris in 1962 v. 2* (J. A. Laurmann, ed.): 33-44, New York: Academic Press, 1963 (also *Advances in Applied Mechanics Supplement 2*, v. 2, 1963).
37. NORMAN, K., AND WILLMORE, A. P., "A Measurement of Positive Ion Density in the Night Time F-Region," *Planet. Space Sci.* 13(1):1-8, January 1965.
38. BOYD, R. L. F., "Plasma Probes on Space Vehicles," *International Conference on Ionization Phenomena in Gases, Fifth Proceedings, Munich, August 82-September 1, 1961* (H. Maecker, ed.):1388-1396, Amsterdam: North-Holland Publishing Co., 1962.
39. BOYD, R. L. F., "The Use of Probing Electrodes in the Study of the Ionosphere," *J. Brit. I.R.E.* 22(5):405-408, November 1961.

REFERENCES

40. BOWEN, P. J., WILLMORE, A. P., AND BOYD, R. L. F., "Some Preliminary Results of the Plasma Probe Experiments on the Satellite Ariel," *International Conference on the Ionosphere Proceedings, 2nd, Imperial College, London, July 1962* (A. C. Stickland, ed.): 517-522, London: Institute of Physics and the Physical Society, 1963.
41. BOWEN, P. J., BOYD, R. F., HENDERSON, C. L., AND WILLMORE, A. P., "Measurement of Electron Temperature and Concentration from a Spacecraft," *Proc. Roy. Soc.* 281A:514-525, October 6, 1964.
42. NICOLET, M., "Helium, an Important Constituent in the Lower Exosphere," *J. Geophys. Res.* 66(7):2263-2264, July 1961.
43. BOURDEAU, E. C., WHIPPLE, E. C., JR., DONLEY, J. L., AND BAUER, S. J., "Experimental Evidence for the Presence of Helium Ions Based on Explorer VIII Satellite Data," *J. Geophys. Res.* 67(2):467-476, February 1962.
44. RAITT, W. J., BOYD, R. L. F., AND LAFLIN, S., "A Synoptic View of Ionic Constitution above the F-Layer Maximum," *Space Research V; Proceedings of the Fifth International Space Science Symposium, Florence, May 12-16, 1964* (D. G. King-Hele, P. Muller, and G. Righini, eds.): 629-634, Amsterdam: North-Holland Publishing Co., 1965.
45. BOYD, R. L. F., AND RAITT, W. J., "Positive Ion Temperatures Above the F-Layer Maximum," *Space Research V; Proceedings of the Fifth International Space Science Symposium, Florence, May 12-16, 1964* (D. G. King-Hele, P. Muller, and G. Righini, eds.): 207-211, Amsterdam, North-Holland Publishing Co., 1965.
46. HARRIS, I., AND PRIESTER, W., "Theoretical Models for the Solar-Cycle Variation of the Upper Atmosphere," NASA Technical Note D-1444, August 1962.
47. APPLETON, E. V., "Wireless Studies of the Ionosphere," *J. Inst. Brit. Eng.* 71(430): 624-650, October 1962.
48. LANGMUIR, I., AND MOTT-SMITH, H., "Studies of Electric Discharges in Gases at Low Pressures. Pt. I," *Gen. Elect. Rev.* 27(7): 449-458, July 1924.
 "Pt. II. Typical Experimental Data Illustrating the Use of Plane Collectors," *Gen. Elect. Rev.* 27(8): 538-548, August 1924.
 "Pt. III. Typical Experimental Data Illustrating the Use of Cylindrical Collectors," *Gen. Elect. Rev.* 27(9): 616-623, September 1924.
 "Pt. IV. Data on Discharges in Mercury Vapor Obtained with Cylindrical Collectors," *Gen. Elect. Rev.* 27(11): 762-771, November 1924.
 "Pt. V. The Use of Spherical Collectors and the Effects of Magnetic Fields," *Gen. Elect. Rev.* 27(12): 810-820, December 1924.
49. STOREY, L. R. O., "An Investigation of Whistling Atmospherics," *Roy. Soc. Phil. Trans.* A246(908):113-141, 1953.
50. OBAYASHI, T., "Geomagnetic Storms and Ionospheric Disturbances," *J. Rad. Res. Lab.* 6:375-514, June 1959.
51. MATTHEW, E. M., AND DEARDEN, E. W., *Science* 12:13.
52. SINGLETON, D. G., AND LYNCH, G. J. E., "Scintillation of the Radio Transmissions from Explorer VII. Pt. I. The Nature of the Scintillations," *J. Atmos. Terr. Phys.* 24: 353-374, May 1962.
53. CROUCHLEY, J., AND DUFF, K., "A Study of Whistling Atmospherics," *Aust. J. Phys.* 15(4):470-481, December 1962.
54. KING, J. W., *Space Research V; Proceedings of the Fifth International Space Science Symposium, Florence, May 12-16, 1964* (D. G. King-Hele, P. Muller, and G. Righini, eds.): 214, 250, 639, Amsterdam: North-Holland Publishing Co., 1965.
55. APPLETON, E. V., "Two Anomalies in the Ionosphere, May 25, 1946, November 9, 1946," *Nature* 157:691, 1946.
56. MITRA, S. K., "Geomagnetic Control of Region F₂ of the Ionosphere," *Nature* 158: 668-669, November 9, 1946.
57. MARTYN, D. F., "April 17, 1947 Atmospheric Tides in the Ionosphere I. Solar Tides in the F₂ Region," *Proc. Roy. Soc.* 189A:241-260, April 17, 1947.
58. LYON, A. J., AND THOMAS, L., "The F₂-Region Equatorial Anomaly in the African, American and East Asian Sectors during Sunspot Maximum," *J. Atmos. Terr. Phys.* 25(7):373-386, July 1963.

59. GOLDBERG, R. A., AND SCHMERLING, E. R., "The Effect of Diffusion on the Equilibrium Electron Density Distribution in the F Region near the Magnetic Equator," *J. Geophys. Res.* 68(7) : 1927-1936, April 1, 1963.
60. RISHBETH, H., LYON, A. J., AND PEART, M., "Diffusion in the Equatorial F Layer," *J. Geophys. Res.* 68(9) : 2559-2570, May 1, 1963.
61. MARIANI, F., "Pitch-Angle Distribution of the Photo-Electrons and Origin of the Geomagnetic Anomaly in the F₂ Layer," *J. Geophys. Res.* 69(3) : 556-560, February 1, 1964.
62. MCILWAIN, C. E., "Coordinates for Mapping the Distribution of Magnetically Trapped Particles," *J. Geophys. Res.* 66(11) : 3681-3691, November 1961.
63. HESS, W. N., "The Artificial Radiation Belt Made on July 9, 1962," *J. Geophys. Res.* 68(3) : 667-683, February 1, 1963.
64. PAULIKAS, G. A., AND FREDEN, D. C., "Precipitation of Energetic Electrons into the Atmosphere," *J. Geophys. Res.* 69(7) : 1239-1249, April 1, 1964.
65. SCHRADER, C. D., KEIFER, R. C., WAGGONER, J. A., ZENGER, J. H. AND BLOOM, S. D., "Proton, Electron Fluxes (> 75 kev) from OSO," *Paper no. 86 presented at the 44th Annual Meeting of the American Geophysical Union March 1963.*
66. ROTHWELL, P., WAGER, J. H., AND SAYERS, J., "Effect of the Johnston Island High-Altitude Nuclear Explosion on the Ionization Density in the Topside Ionosphere," *J. Geophys. Res.* 68(3) : 947-949, February 1, 1963.
67. ALEXANDER, J. H., "Electronic Instruments for Astronomical Measurements from Space Vehicles," Ph.D. Thesis, University College, London, 1963.
68. BAUMANN, R. C., "The Ariel 1 Satellite," *Proc. Roy. Soc.* 281A : 439-445, October 6, 1964.
69. SEMPLE, E. C., "A Study of the Spin-Axis Precession Characteristics to be Expected of the S53/UK3 Satellite," *R. A. E. Technical Memorandum No. Space 62*, Farnborough, England, 1964.
70. EVANS, W. J., "Aerodynamic and Radiation Disturbance Torques on Satellites Having Complex Geometry," *Torques and Attitude Sensing in Earth Satellites* (S. F. Singer, ed.) : 83-98, New York: Academic Press, 1964.
71. HUTH, J. H., "Power Supplies for Space Vehicles," *Advances in Space Science*, 1 (F. I. Ordway, III, ed.) : 111-157, New York: Academic Press, 1959.

ADDITIONAL BIBLIOGRAPHY

- BOURDEAU, R. E., "Ionospheric Results with Sounding Rockets and the Explorer VIII Satellite," *Space Research II; Proceedings of the Second International Space Science Symposium, Florence, Italy, April 10-14, 1961* (H. C. Van de Hulst, C. de Jager, and A. F. Moore, eds.): 554-573, Amsterdam: North-Holland Publishing Co., 1961.
- BOURDEAU, R. E., AND BAUER, S. J., "Structure of the Upper Atmosphere Deduced from Charged Particle Measurements on Rockets and the Explorer VIII Satellite," *Space Research III; Proceedings of the Third International Space Science Symposium, Washington, D. C. May 2-8, 1962* (W. Priester, ed.): 173-193, Amsterdam: North-Holland Publishing Co., 1963.
- BOURDEAU, R. E., DONLEY, J. L., SERBU, G. P., AND WHIPPLE, E. C., JR., "Measurements of Sheath Currents and Equilibrium Potential on the Explorer VIII Satellite," *J. Astronaut. Sci.* 8 (3) :65-73, 1961.
- CONN, J. H., SUTTON, J. F., *Report of Environmental Vibration Test—Structural Model No. 1, International Ionosphere Satellite, S-51, Goddard Space Flight Center 321.2 (JC) S-51-11, June 1961.*
- CORNILLE, H. J., JR., "A Method of Accurately Reducing the Spin Rate of a Rotating Spacecraft," NASA Technical Note D-1420, October 1962.
- DAVIES, A. H., HARRIS, I., *Rarefied-Gas Dynamics*, III, p. 661, 1963.
- ENG, T. L., "Energy Absorber for the Ariel I Instrument Booms," Washington, D. C.: NASA Technical Note D-1857, January 1964.
- FEDOR, J. V., "Analytical Theory of the Stretch Yo-Yo for De-Spin of Satellites," NASA Technical Note D-1676, April 1963.
- FORSYTHE, R. W., "A Method for Simulating Zero Gravity Erection of Satellite Appendages," NASA Technical Note D-1852, January 1964.
- FORSYTHE, R. W., "Analysis of Dissimilar Satellite Appendages During Erection," NASA Technical Note D-1688, January 1964.
- FRIEDMAN, H., "Solar Radiation," *Aeronautics* 7(8) :14-23, August 1962.
- FRIEDMAN, H., LIGHTMAN, S. W., BYRAM, E. T., "Photon Counter Measurements of Solar X-Rays and Extreme Ultra-Violet Light," *Phys. Rev.* 83(5) :1025-1030, September 1, 1951.
- FUECHSEL, C. J., KRUEGER, V. L., MARTIN, R. G., PIAZZA, F. D., TURKIEWICZ, J. M., "Electronic Integration of the S-51 Uk-1 International Ionosphere Satellite," NASA Technical Note D-3001, September 1965.
- HORD, W. H., *General Environmental Test Specification and Test Procedures for Design Qualification and Flight Acceptance Testing of Delta Launched Satellite.* NASA/GSFC/TE internal publication, September 1961.
- HORD, W. H., *Environmental Test Specifications for Design Qualification and Flight Acceptance Tests of the International Satellite.* NASA/GSFC/TE internal publication, December 1961.
- HORD, W. H., *Test Plan—Structural Test ETU #1 S-51 Satellite.* NASA/GSFC/TE internal publication, April 1961.
- HORD, W. H., *Environmental Exposures and Tests for Subassemblies of International Ionosphere Satellite S-51.* NASA/GSFC/TE internal publication, February 1961.
- HORD, W. J., "Environmental Test Program for Ariel I," NASA Technical Note D-2099, February 1964.
- KRASSOVSKY, V. I., "Exploration of the Upper Atmosphere with the Help of the Third Soviet Sputnik," *Proc. I.R.E.* 47(2) :289-296, February 1959.

- Kyoto, September 4-15, 1961. *Proceedings. v. 3, International Conference on Cosmic Rays* 33-44, Tokyo: Physical Society of Japan, 1962.
- LEDoux, F., Compilation, Design Tests Ariel Satellite (S-51). Goddard Space Flight Center internal publication X-634-62-157, Greenbelt, Md.: NASA 1962.
- O'BRIEN, B. J., LAUGHLIN, C. D., VAN ALLEN, J. A., Preliminary Study of the Geomagnetically-Trapped Radiation Produced by a High-Altitude Nuclear Explosion on July 9, 1962, *Nature* 195:939-943, September 8, 1962.
- POMERANTZ, M. A., AGARWAL, S. P., SCHWED, P., HANSON, H., "Satellite Determination of Heavy Primary Cosmic-Ray Spectrum," *Phys. Rev. Letts.* 6(7):362-364, April 1, 1961.
- POMERANTZ, M. A., AND WITTEN, L., "Satellite Investigation of Time Variations of Heavy Nuclei on the Primary Cosmic Radiation," *International Conference on Cosmic Rays and Earth Storm*,
- POUNDS, K. A., "Measurement of Solar X-Radiation," *J. Brit. I. R. E.* 22(2): 171-175, August 1961.
- POUNDS, K. A., WILLMORE, A. P., "Some Early Results from the X-Ray Spectrometer in Satellite U. K. 1," *International Conference on the Ionosphere Proceedings, 2nd, Imperial College London, July 1962* (A. C. Stickland, ed.): 517-522, London: Institute of Physics and the Physical Society, 1963.
- SAYERS, J., ROTHWELL, P., AND WAGER, J. H., "Evidence for a Further Ionospheric Ledge above the F₂ Region," *Nature* 195:1143-1145, September 22, 1962.
- SERBU, G. P., BOURDEAU, R. E., DONLEY, J. L., "Electron Temperature Measurements on the Explorer VIII Satellite," *J. Geophys. Res.* 66(12):4313-4315, December 1961.
- SCHWED, P., POMERANTZ, M. A., HANSON, H., BENJAMIN, H., Satellite Borne Instrumentation for Observing Flux of Heavy Primary Cosmic Radiation," *J. Franklin Inst.* 271(4):275-291, April 1, 1961.
- SHKLOVSKII, I. S., "Nature of Solar X-Ray Emission," *Soviet Astron.-AJ* 8:538, 1965.
- STROUP, E. R., "The Battery for the International Ionosphere Satellite Ariel I," *ARS Space Power Systems Conference, Santa Monica, California, Paper No. 2510-62*: 21 pp., September 25-28, 1962.
- WAGNER, C. L., JR., "Ariel I—Evolution of Its Structure," NASA Technical Note D-1903, September 1963.
- WILLMORE, A. P., "Ionospheric Heating in the F-Region," *Proc. Roy. Soc.* 281A:140-149, August 18, 1964.
- YAGERHOFER, F. C., "Design of the U. K. Scientific Satellite Solar Power System," *ARS Space Power Systems Conference, Santa Monica, California, Paper No. 2498-62*: 27 pp., September 25-28, 1962.

APPENDIX A

Physical Measurements of Ariel I

The weights, centers of gravity and moments of inertia are given in the following itemization:

SATELLITE ONLY*

Weight (lb)..... 135. 82

All components folded:

Center of gravity, forward of separation plane (in.)..... 5. 961

Moment of inertia (slug-ft²)

I_{xx} 5. 25

I_{zz} (Roll axis)..... 1. 99

I_{yy} 4. 75

All components extended:

Center of gravity, forward of separation plane (in.)..... 8. 125

Moment of inertia (slug-ft²)

x-x axis..... 5. 130

Roll axis..... 5. 484

y-y axis..... 4. 030

FOLDED ARIEL I PAYLOAD†

Weight (lb)

Orbiting satellite..... 133. 8

De-spin weights..... 2. 0

Separation and release system (with tiedowns)..... 21. 3

Dutchman and vibration experiment ‡..... 20. 6

TOTAL payload weight not furnished by Delta vehicle..... 177. 7

Center of gravity, forward of separation plane (in.)..... 1. 42

Moment of inertia (slug-ft²)

Pitch axis..... 9. 277

Roll axis..... 2. 610

SEPARATION UNIT AND DUTCHMAN†

Weight (lb)..... 35. 56

Center of gravity, aft of separation plane (in.)..... 8. 53

Moment of inertia (slug-ft²)

Pitch axis..... 0. 294

Roll axis..... 0. 451

ANTENNAS AND HARNESS (VIBRATION EXPERIMENT)†

Weight (lb)..... 3. 58

Center of gravity, aft of separation plane (in.)..... 44. 94

Moment of inertia (slug-ft²)

Pitch axis..... 0. 0705

Roll axis..... 0. 0831

TIE DOWNS†

Weight (lb)..... 2. 66

Center of gravity, aft of separation plane (in.)..... 32. 30

Moment of inertia (slug-ft²)

Pitch axis..... 0. 016

Roll axis..... 0. 080

* Refer to Figures A1 and A2.

† Refer to Figure A3.

‡ Includes U.K.-designed contamination experiment and solar aspect sensor, and telemetering antennas.

ARIEL I: THE FIRST INTERNATIONAL SATELLITE

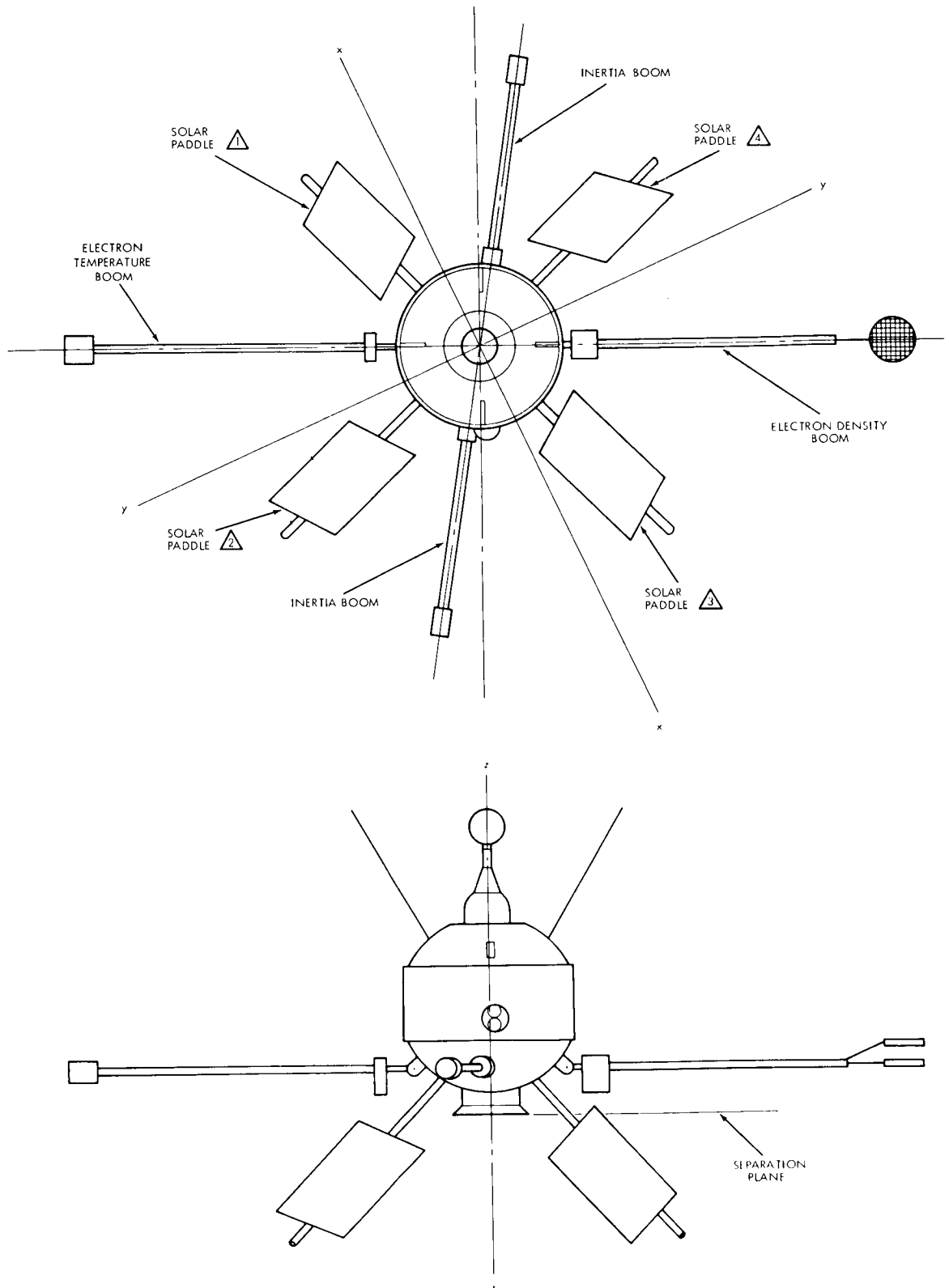


FIGURE A1. Payload axes.

APPENDIX A—PHYSICAL MEASUREMENTS OF ARIEL I

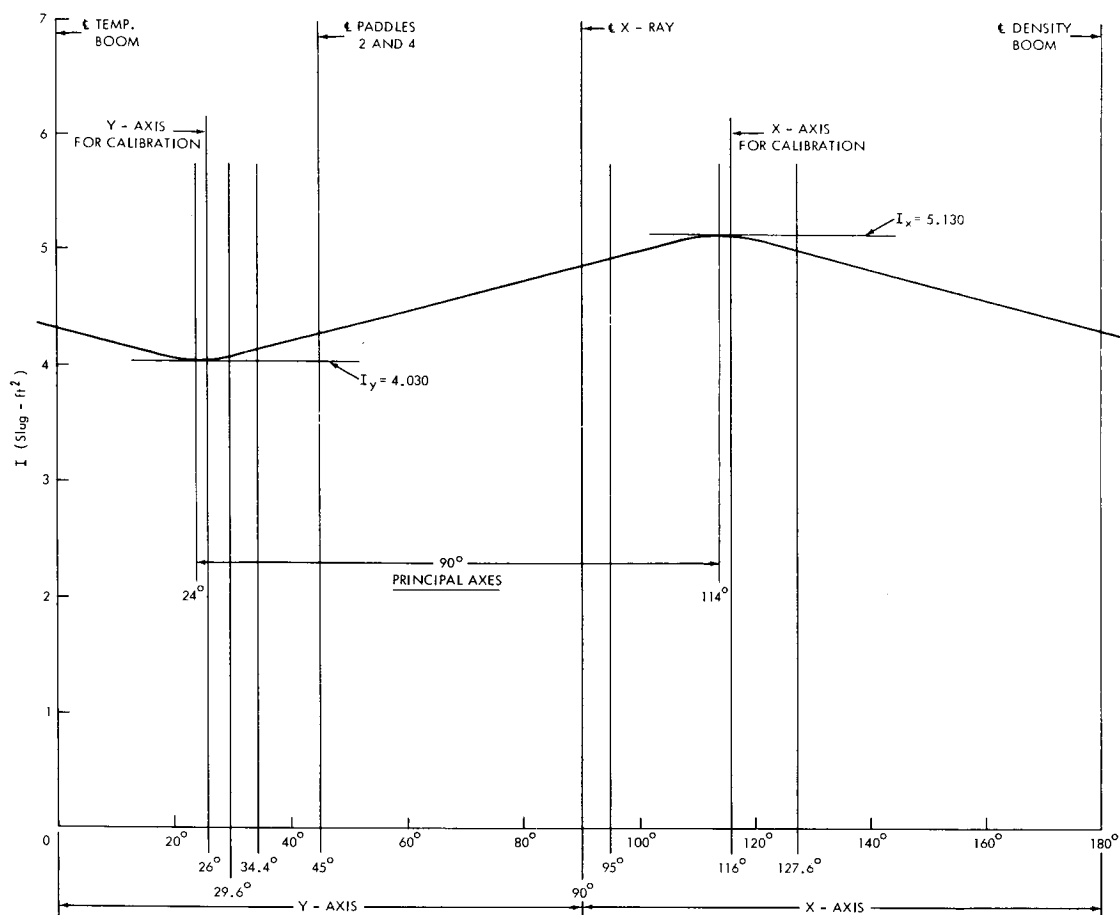


FIGURE A2. Principal moments of inertia vs. payload axes, all components extended.

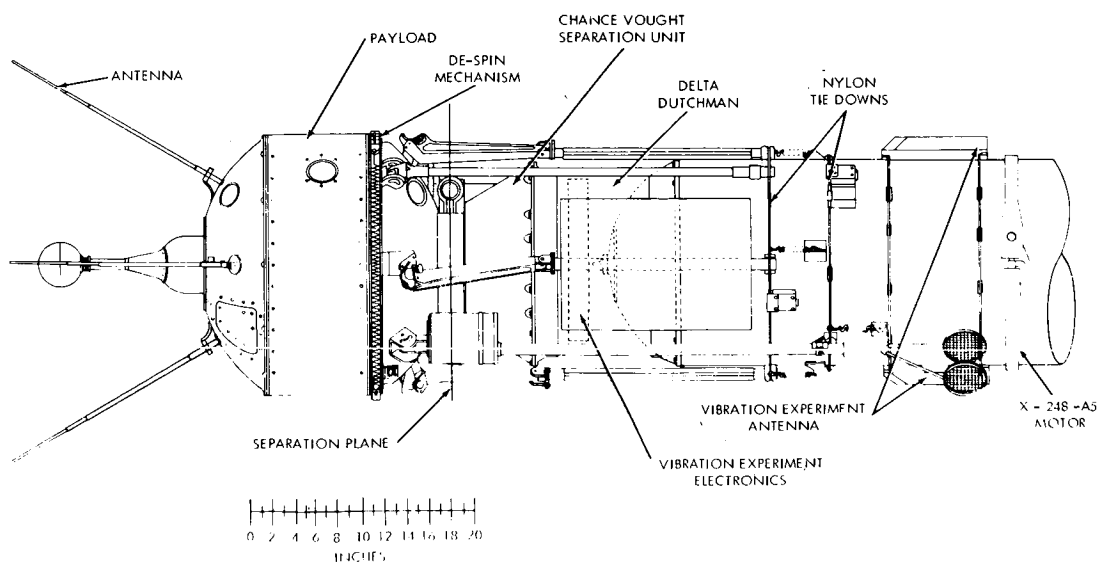


FIGURE A3. Ariel I nomenclature diagram.

ARIEL I: THE FIRST INTERNATIONAL SATELLITE

TABLE A1
Detailed Weight Breakdown of Ariel I

Item	Remarks	Weight (lb)	Item	Remarks	Weight (lb)
Upper dome	Includes thermal and RF coating	6.53	University College London Experiments—Continued		
Mid-skin	Includes thermal and RF coating	6.80	UCL electronics container 2	Includes 10 U.K. cards	6.76
Lower dome	Includes thermal grating only	1.52	Imperial College Experiment		
Shelf and base assembly	Shelf, struts, base, fasteners	12.63	Cosmic ray analyzer	Includes electronics	5.70
Paddle arms and hinges (4)	Includes interface fasteners	4.36	University of Birmingham Experiment		
Inertia booms and hinges (2)	Includes interface fasteners	3.85	Electron density boom	-----	5.50
Experiment boom hinges	Includes interface fasteners	0.87	Electronics container	-----	2.79
Escapement assembly	Includes nylon guides	1.54	GSFC Non-Structure Components		
De-spin housing	Includes guillotines	1.76	Tape recorder	-----	3.66
De-spin weights, Spring antennas (4)	Excluded from orbit weight	2.00	Tape recorder de control	-----	0.39
Separation ring adapter	Includes interface fasteners	0.51	Encoder card UCL no. 1	In UCL container 1	0.49
Battery containers	Includes spacers	3.05	Encoder card UCL no. 2	In UCL container 2	0.56
Dynamic balance	-----	1.93	Cosmic ray encoder card	Including container	0.96
Tape recorder and electron temperature supports	-----	1.07	Electronic pack A	2 encoder cards, encoder clock	5.87
Turn-on plug and housing	-----	0.14	Electronic pack B	2 converter cards, lid	6.93
Harness bracketry	Includes clamps fasteners	1.34	Battery selector	-----	0.50
Component bracketry	Non-structure components	0.91	1-Year timers (2)	-----	0.72
Internal thermal equalization	Coatings and heat sinks	0.97	Solar paddles (4)	Including spars	8.78
University College London Experiments			Battery packs (2)	Including potting	12.08
Lyman-alpha detectors (3)	-----	1.62	Solar shunt regulator	-----	0.24
X-ray counters (2)	-----	0.64	Harness network	Top dome, main assemble below shelf assembly	6.54
Solar aspect sensor	-----	0.43	TOTAL ARIEL I WEIGHT-----		
Ion mass spectrometer	Includes 4-inch extension tube	0.54	135.82		
Electron temperature sensor	-----	0.37			
Electron temperature boom	Includes balance weights	5.50			
UCL electronics container 1	Includes 4 U.K. cards	5.67			

TABLE A1. Detailed weight breakdown of Ariel I.

APPENDIX B

Operational Parameters of Ariel I

The following charts present a profile of all measured operational parameters throughout the useful life of the mission. In addition, a day-by-day profile of the quality of telemetry signal throughout the useful life of the satellite is shown.

1962 OMICRON (UK1-S51) ARIEL 1

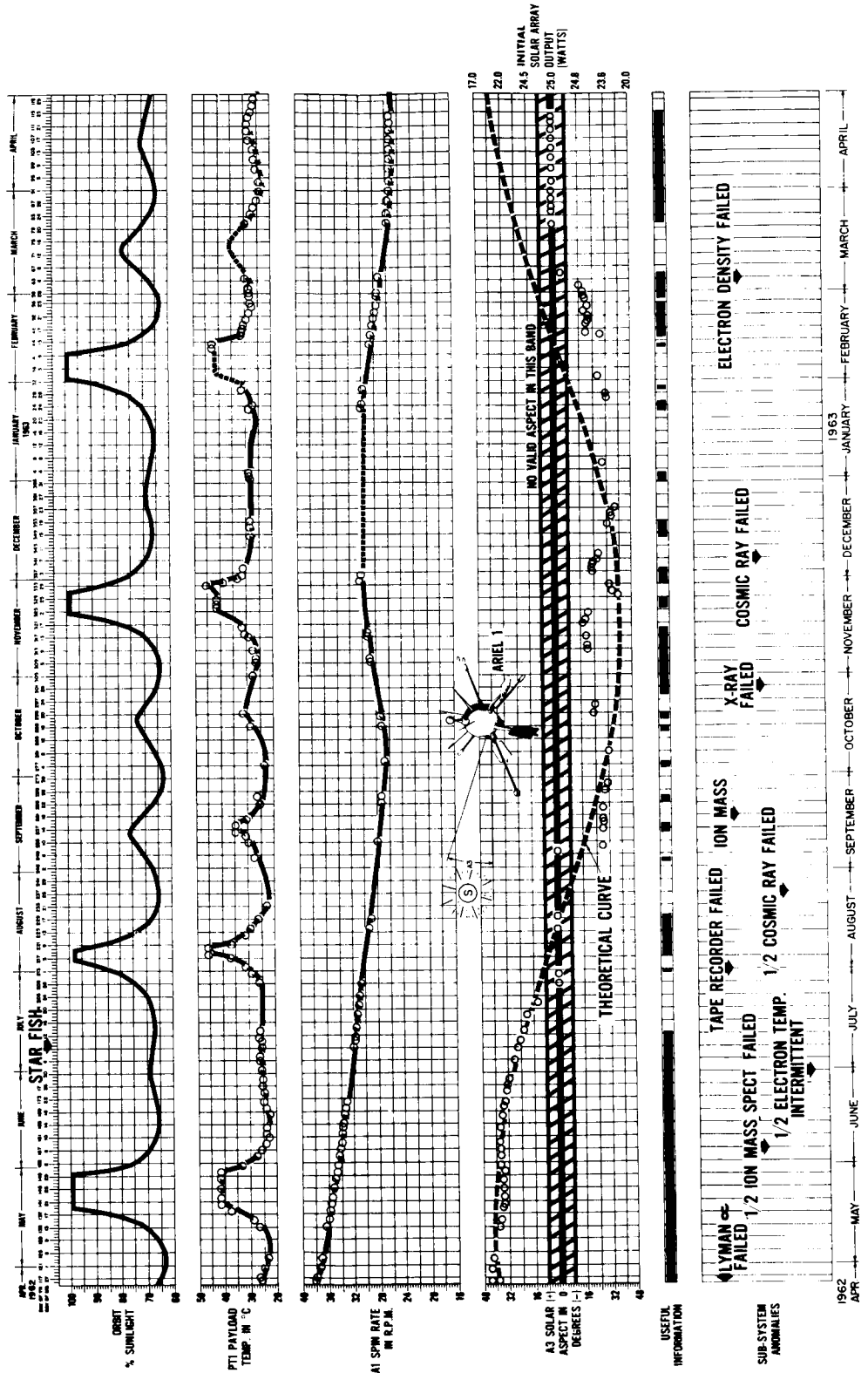


FIGURE B1. Ariel I profile, April 1962 through April 1963.

1962 OMICRON (UK1-S51) ARIEL 1

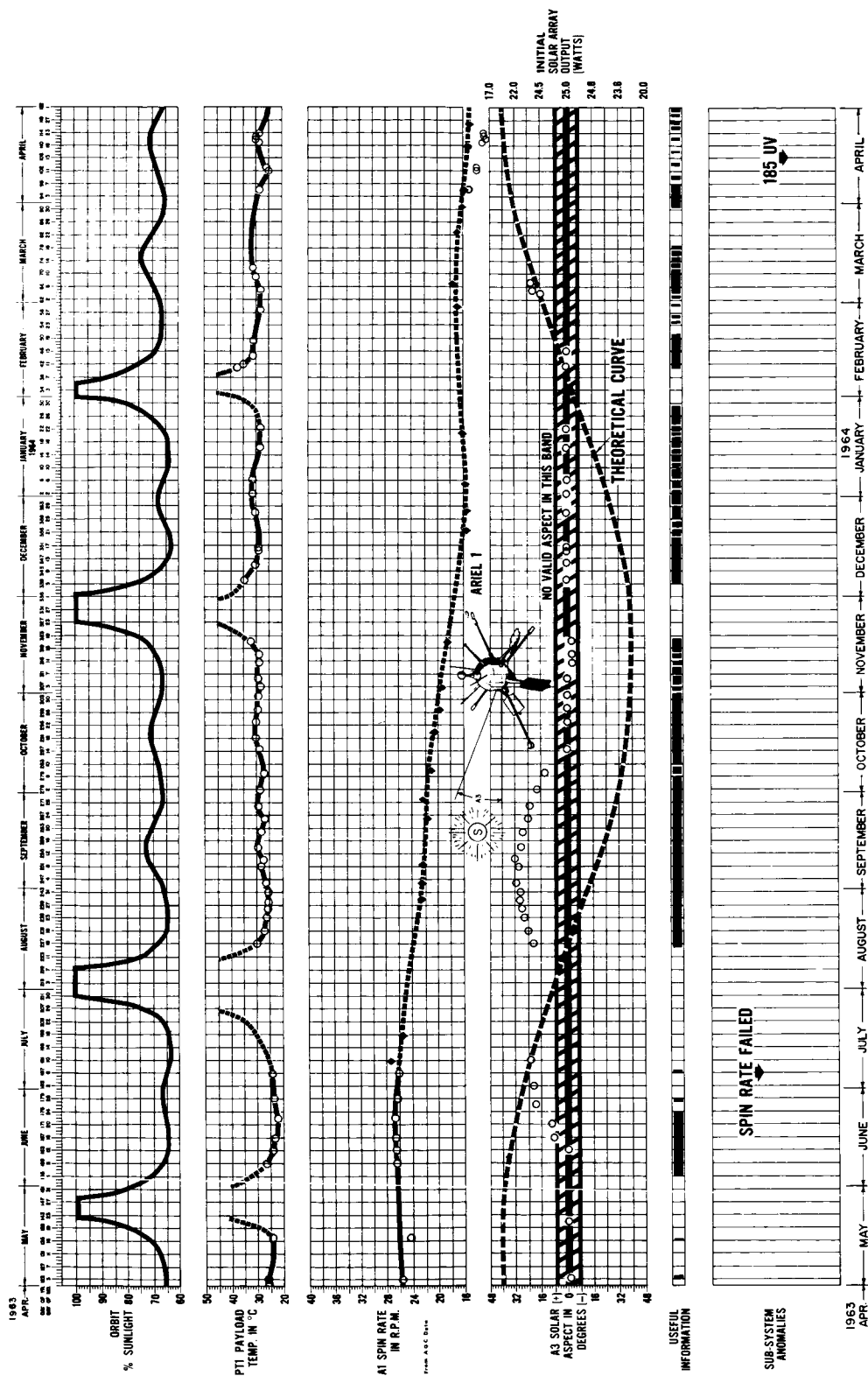
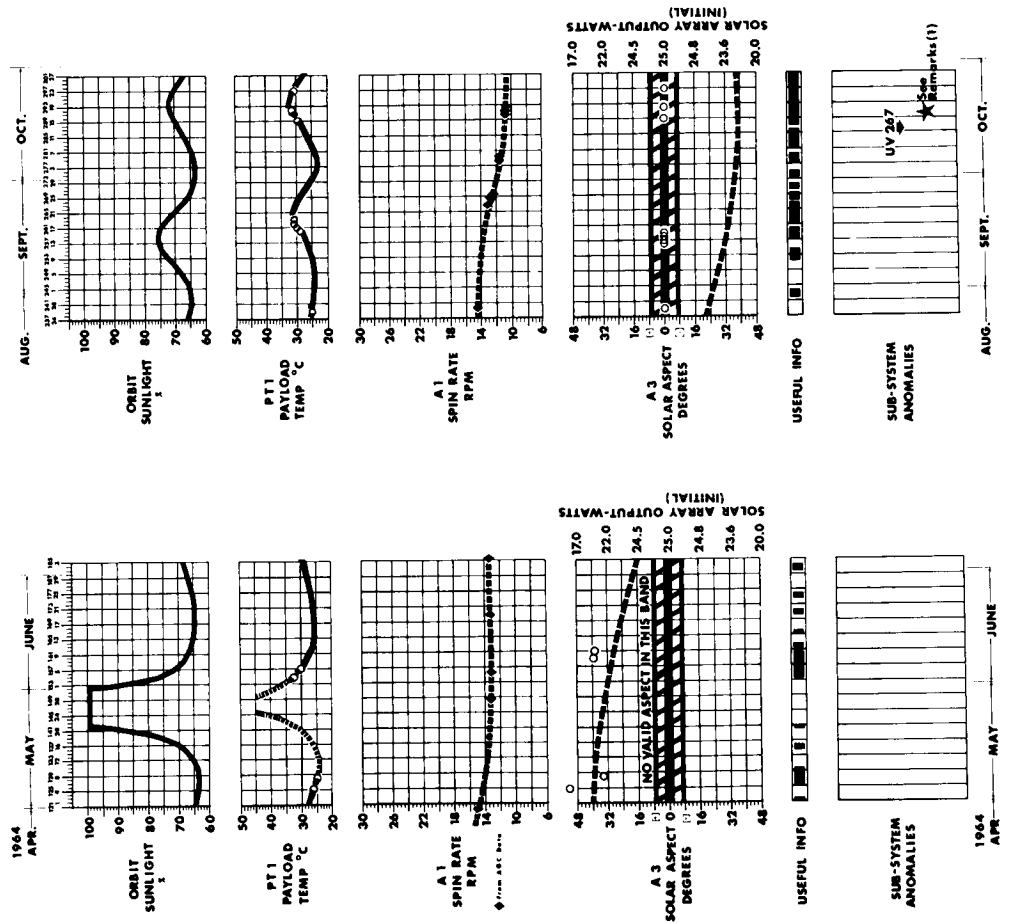


FIGURE B2. Ariel I profile, April 1963 through April 1964.



REMARKS

1. ★ EXTENSIVE ELECTRON TEMPERATURE EXPERIMENT/ENCODER ANOMALIES BEGAN OCTOBER 16, 1964.
2. CESSATION OF DATA ACQUISITION NOVEMBER 9, 1964. CAUSED BY THE INCREASED DIFFICULTY OF DATA REDUCTION.

FIGURE B3. Ariel I profile, May, June, Sept., and Oct. 1964.

APPENDIX B—SATELLITE PERFORMANCE PROFILE

GREENWICH MEAN TIME

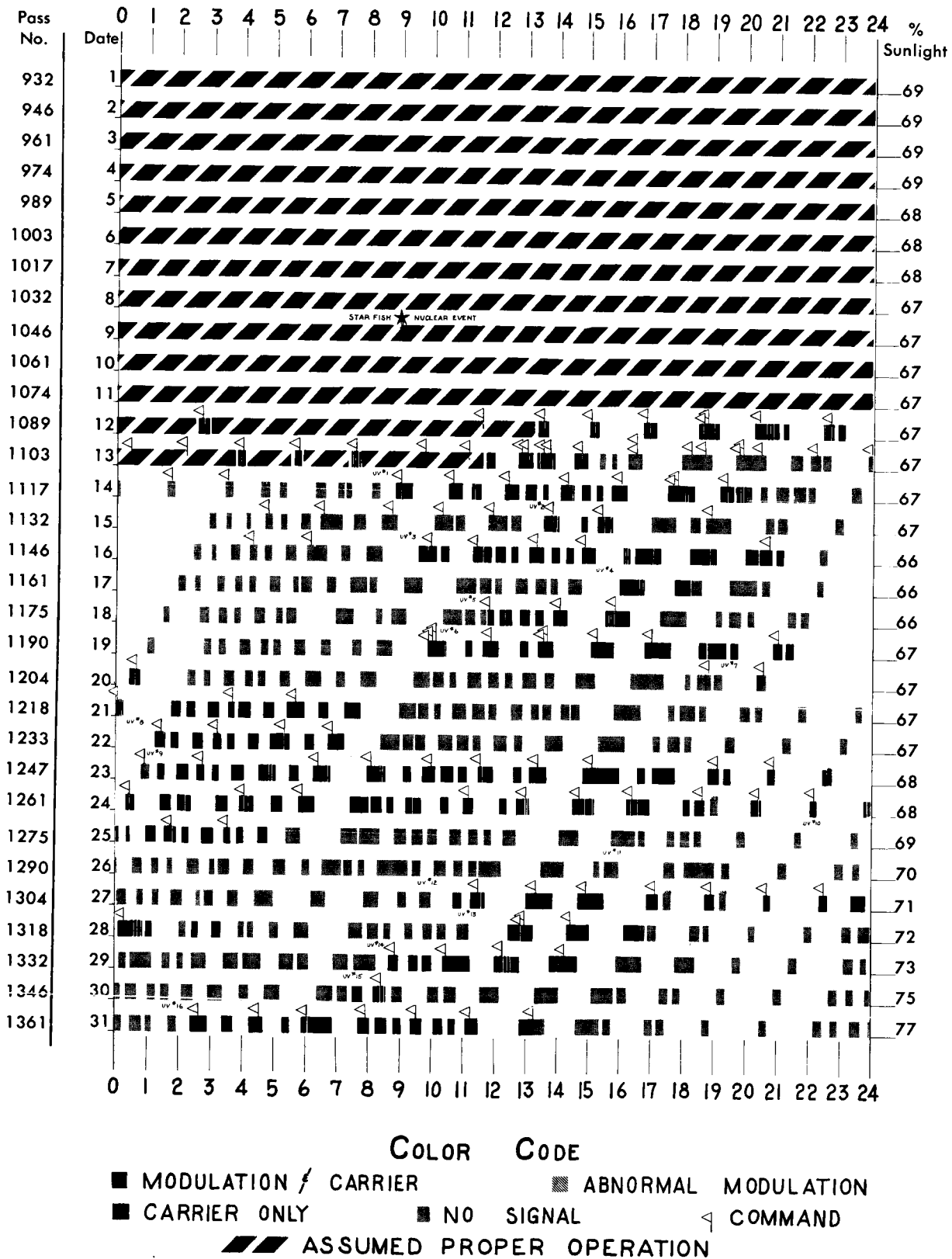


FIGURE B4. Ariel I profile, July 1962.

ARIEL I: THE FIRST INTERNATIONAL SATELLITE

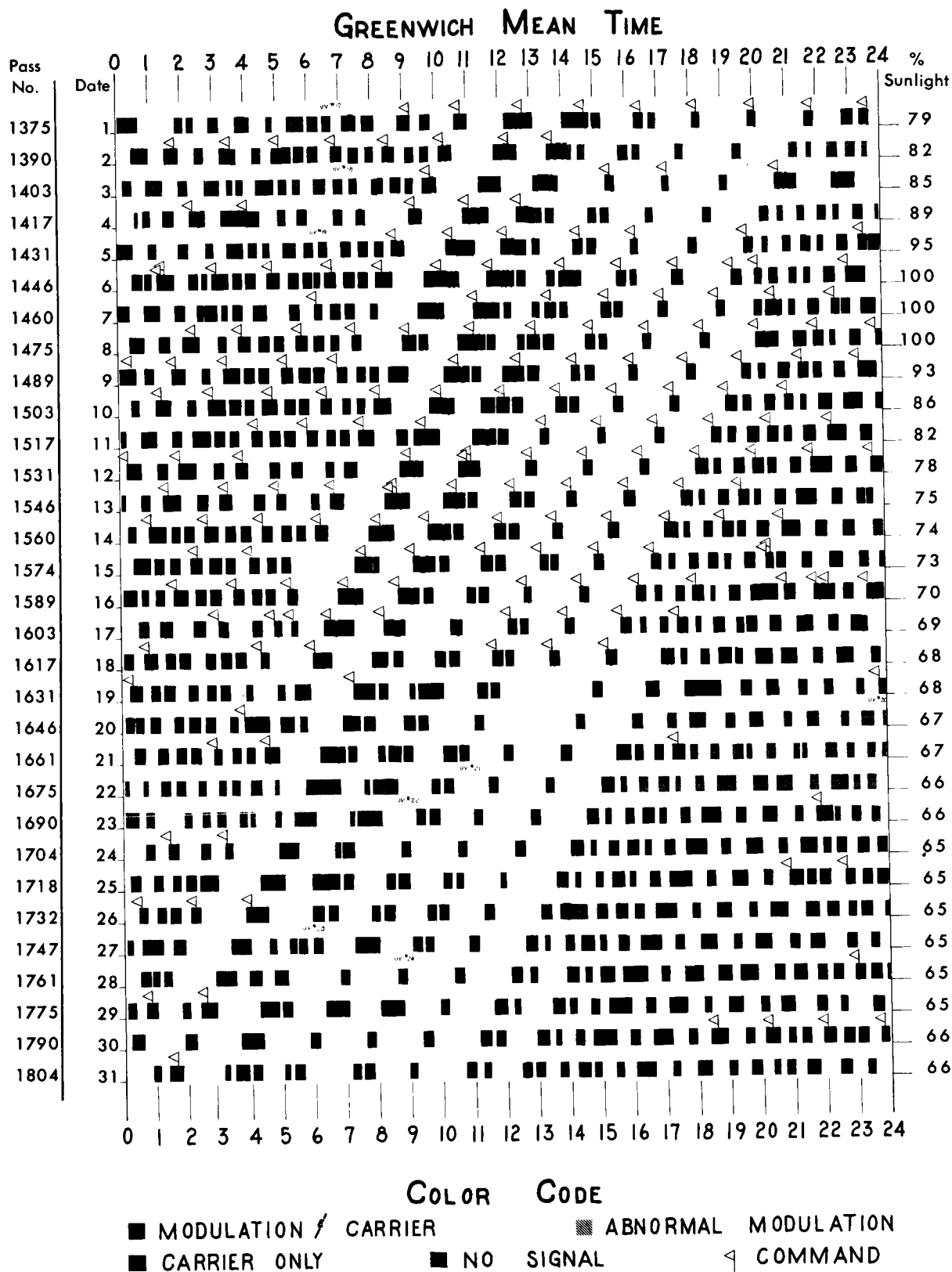


FIGURE B5. Ariel I profile, August 1962.

APPENDIX B—SATELLITE PERFORMANCE PROFILE

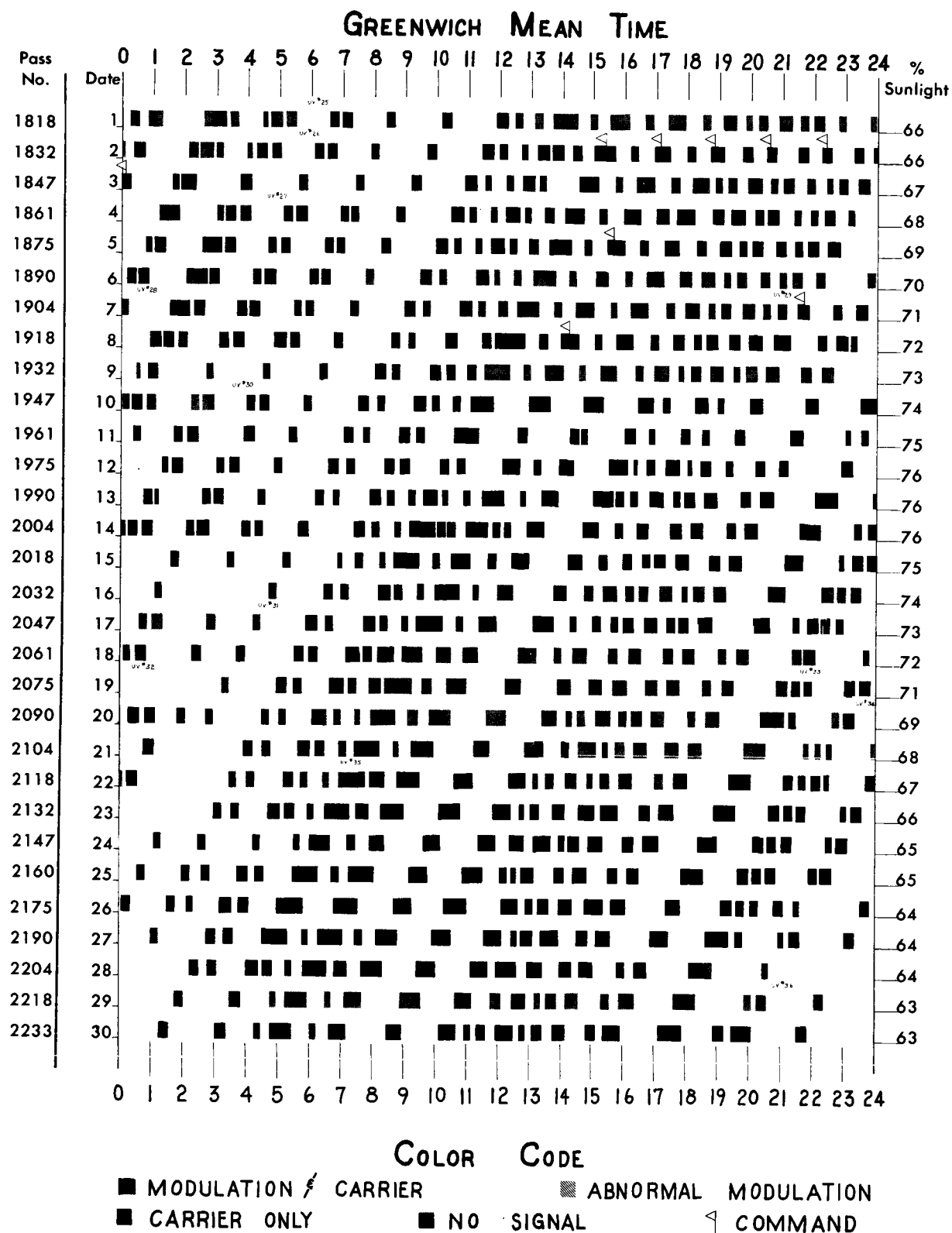


FIGURE B6. Ariel I profile, September 1962.

ARIEL I: THE FIRST INTERNATIONAL SATELLITE

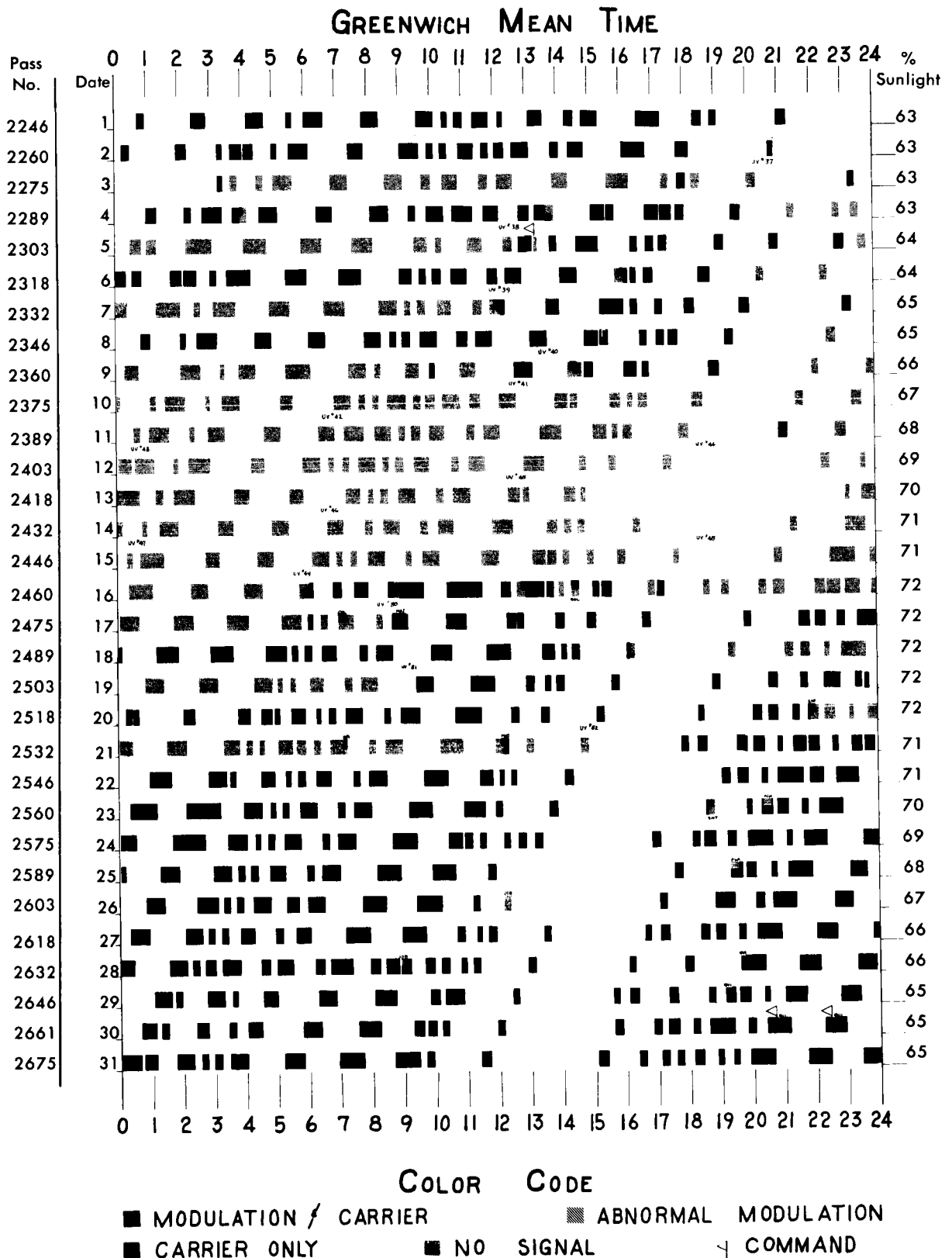
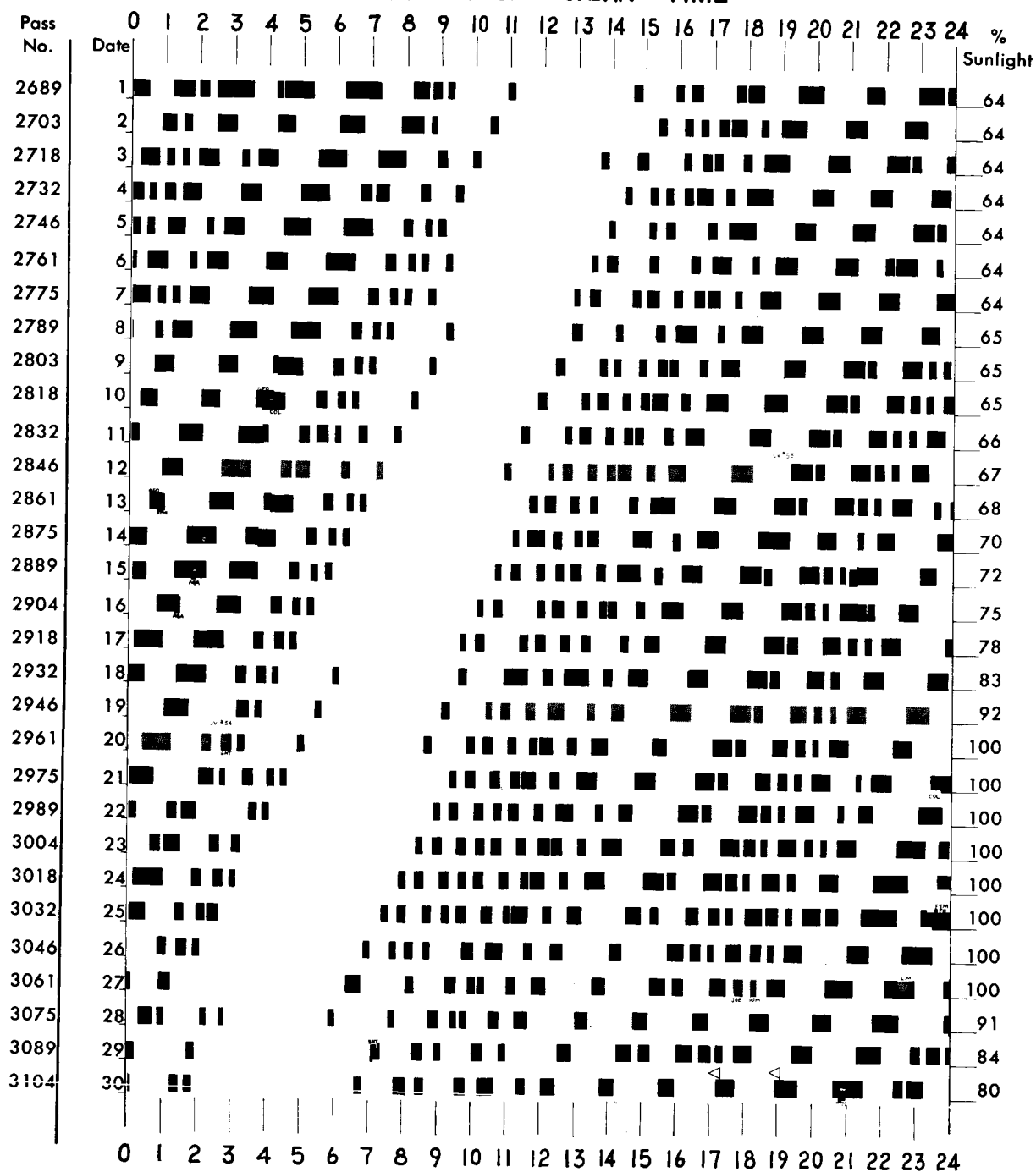


FIGURE B7. Ariel I profile, October 1962.

APPENDIX B—SATELLITE PERFORMANCE PROFILE

GREENWICH MEAN TIME



COLOR CODE

■ MODULATION / CARRIER ■ ABNORMAL MODULATION
 ■ CARRIER ONLY ■ NO SIGNAL ◁ COMMAND

FIGURE B8. Ariel I profile, November 1962.

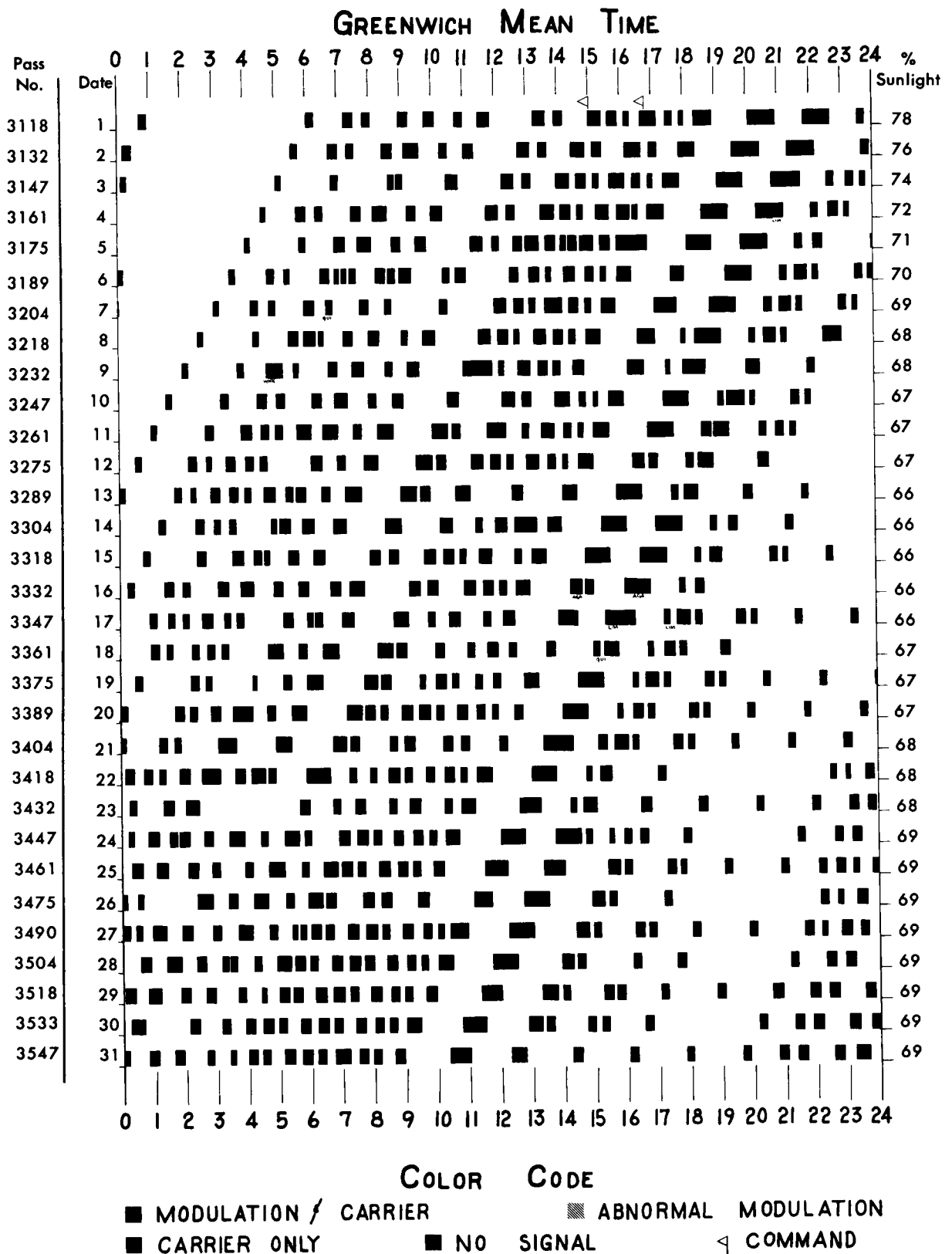
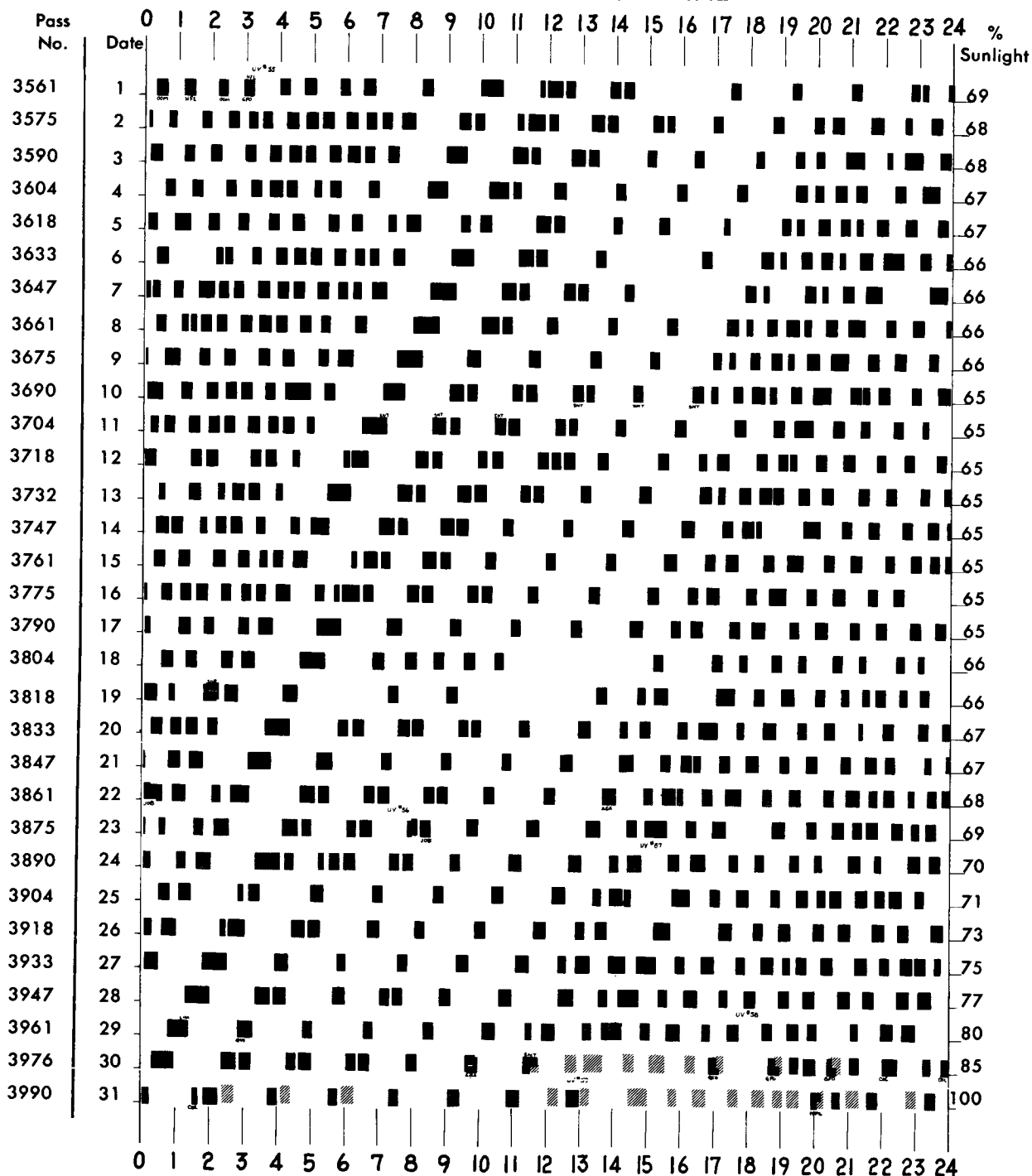


FIGURE B9. Ariel I profile, December 1962.

APPENDIX B—SATELLITE PERFORMANCE PROFILE

GREENWICH MEAN TIME



COLOR CODE

■ MODULATION / CARRIER ▨ ABNORMAL MODULATION
 ▨ CARRIER ONLY ■ NO SIGNAL ◁ COMMAND

ASSUMED PROPER OPERATION

FIGURE B10. Ariel I profile, January 1963.

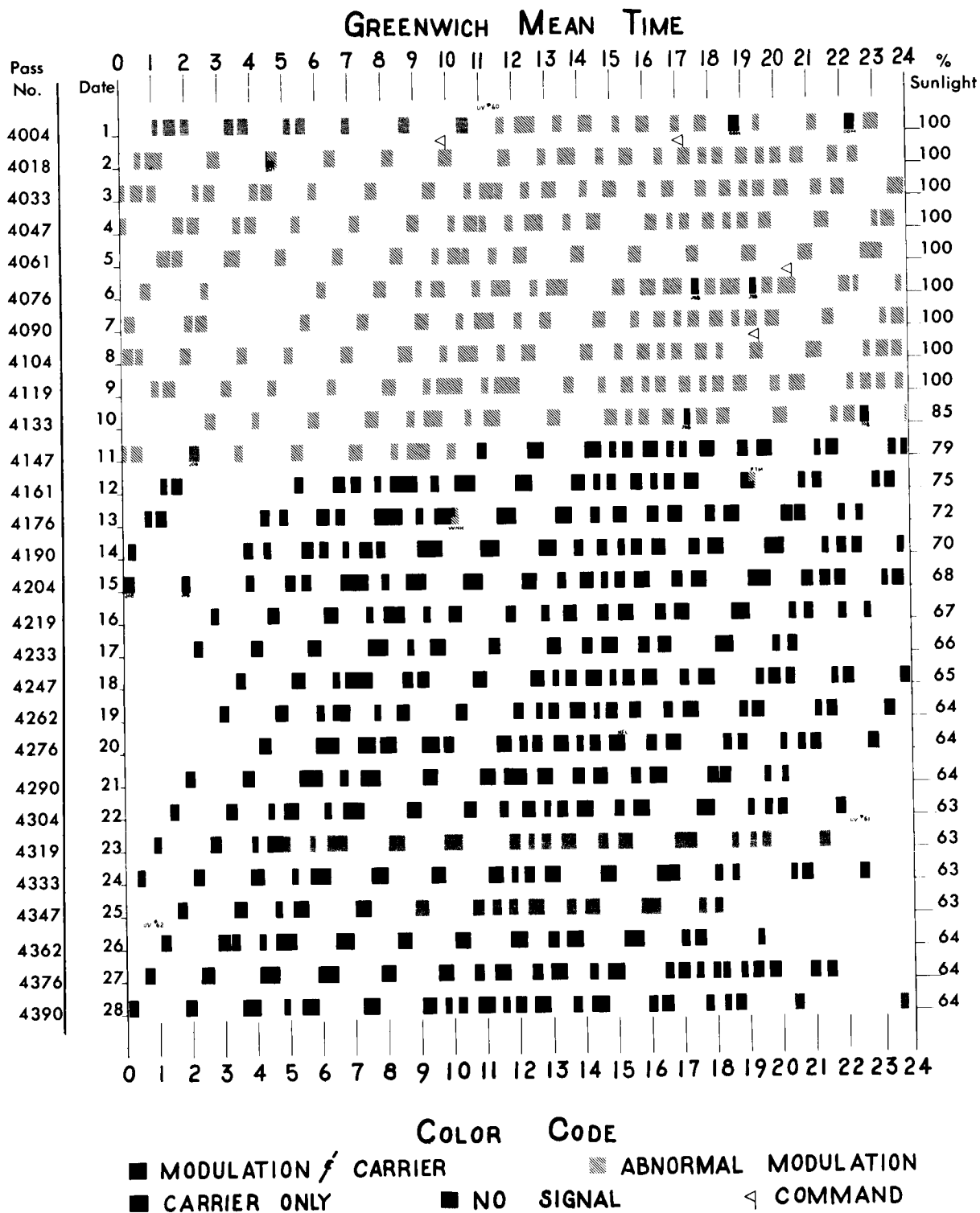
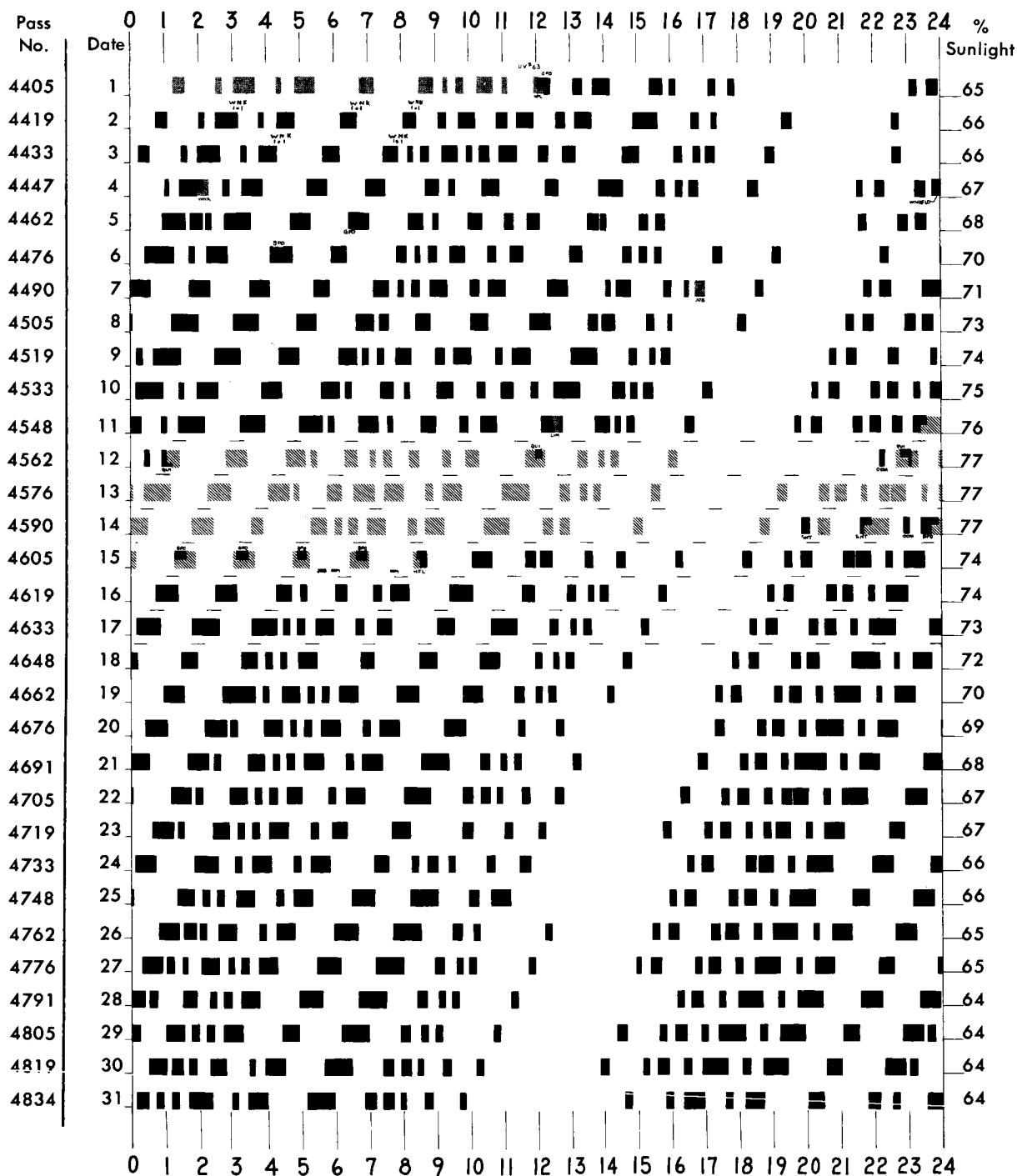


FIGURE B11. Ariel I profile, February 1963.

APPENDIX B—SATELLITE PERFORMANCE PROFILE

GREENWICH MEAN TIME



COLOR CODE

■ MODULATION / CARRIER ■ ABNORMAL MODULATION
 ■ CARRIER ONLY ■ NO SIGNAL ◁ COMMAND

FIGURE B12. Ariel I profile, March 1963.

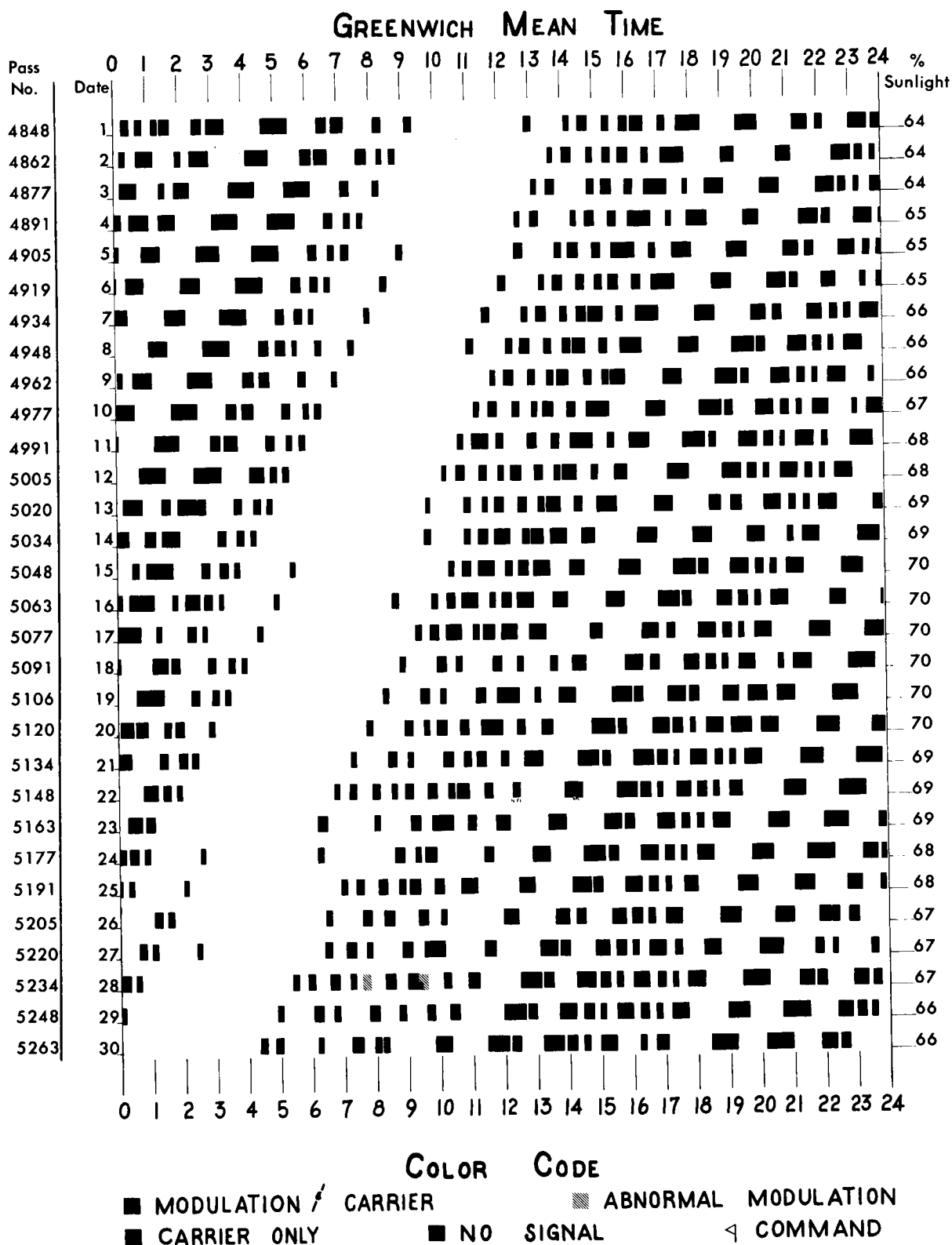
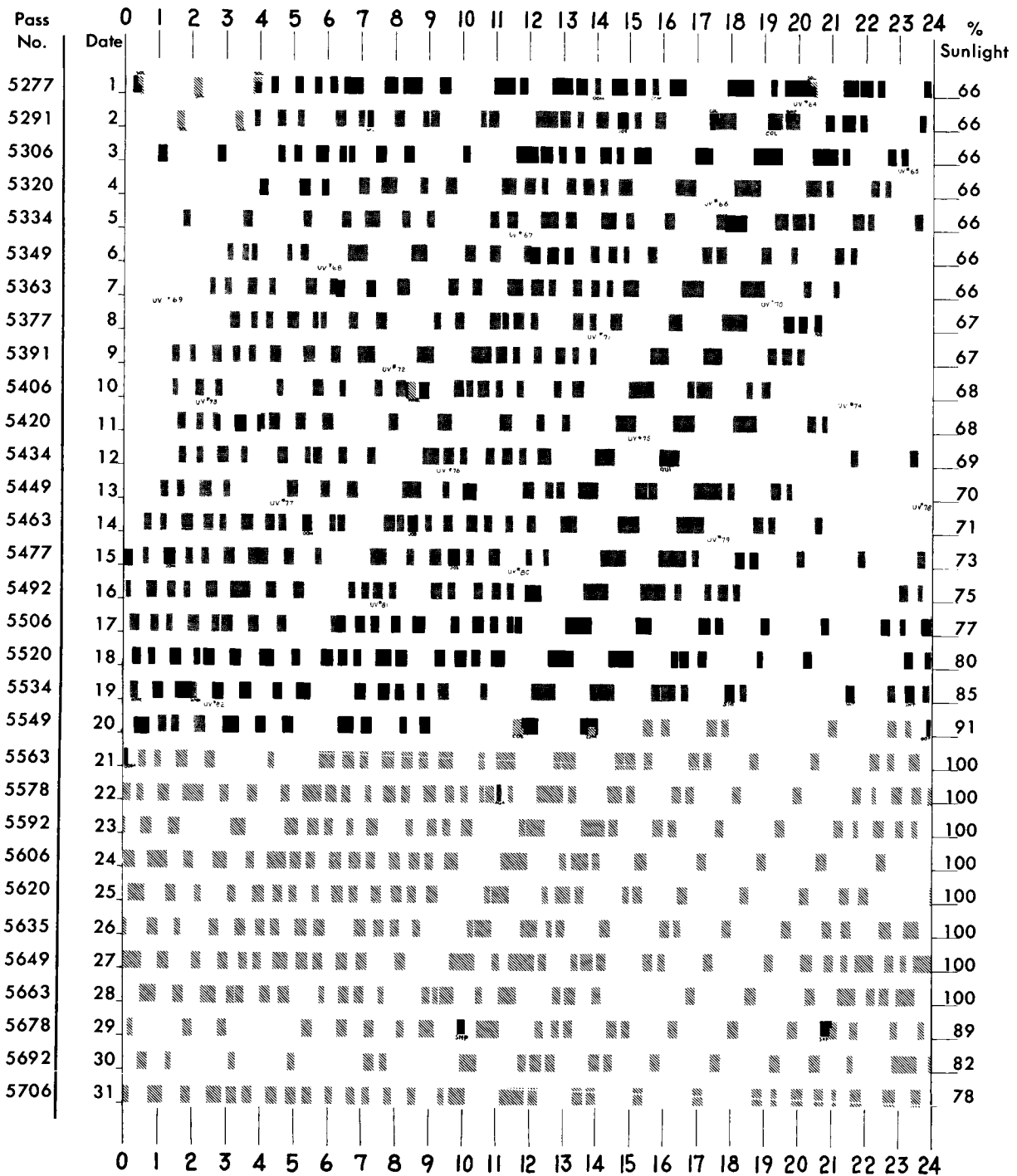


FIGURE B13. Ariel I profile, April 1963.

APPENDIX B—SATELLITE PERFORMANCE PROFILE

GREENWICH MEAN TIME



COLOR CODE

■ MODULATION / CARRIER ■ ABNORMAL MODULATION
 ■ CARRIER ONLY ■ NO SIGNAL ◁ COMMAND

FIGURE B14. Ariel I profile, May 1963.

ARIEL I: THE FIRST INTERNATIONAL SATELLITE

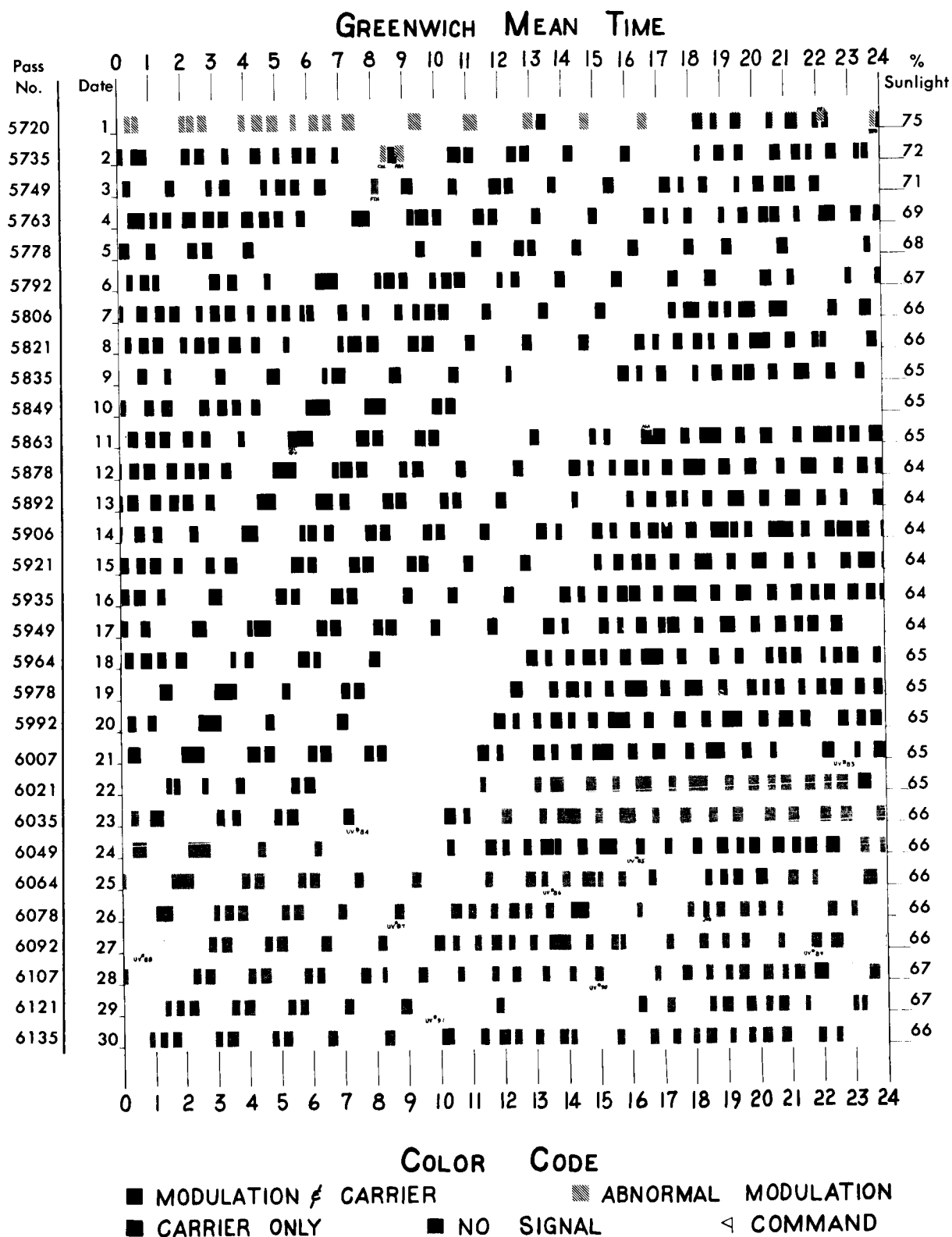
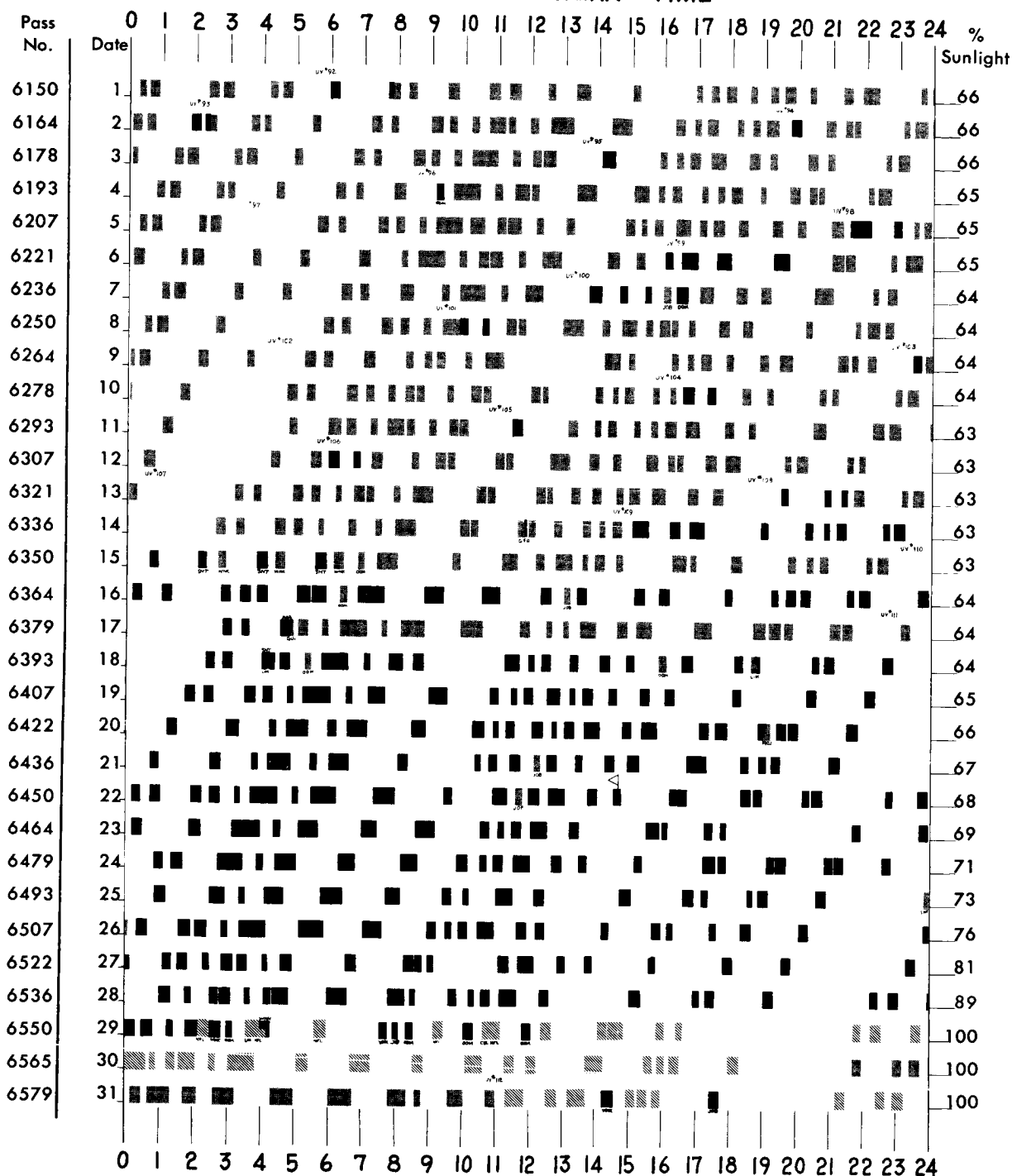


FIGURE B15. Ariel I profile, June 1963.

APPENDIX B—SATELLITE PERFORMANCE PROFILE

GREENWICH MEAN TIME



COLOR CODE

- MODULATION / CARRIER
- CARRIER ONLY
- ABNORMAL MODULATION
- NO SIGNAL
- ◁ COMMAND

FIGURE B16. Ariel I profile, July 1963.

ARIEL I: THE FIRST INTERNATIONAL SATELLITE

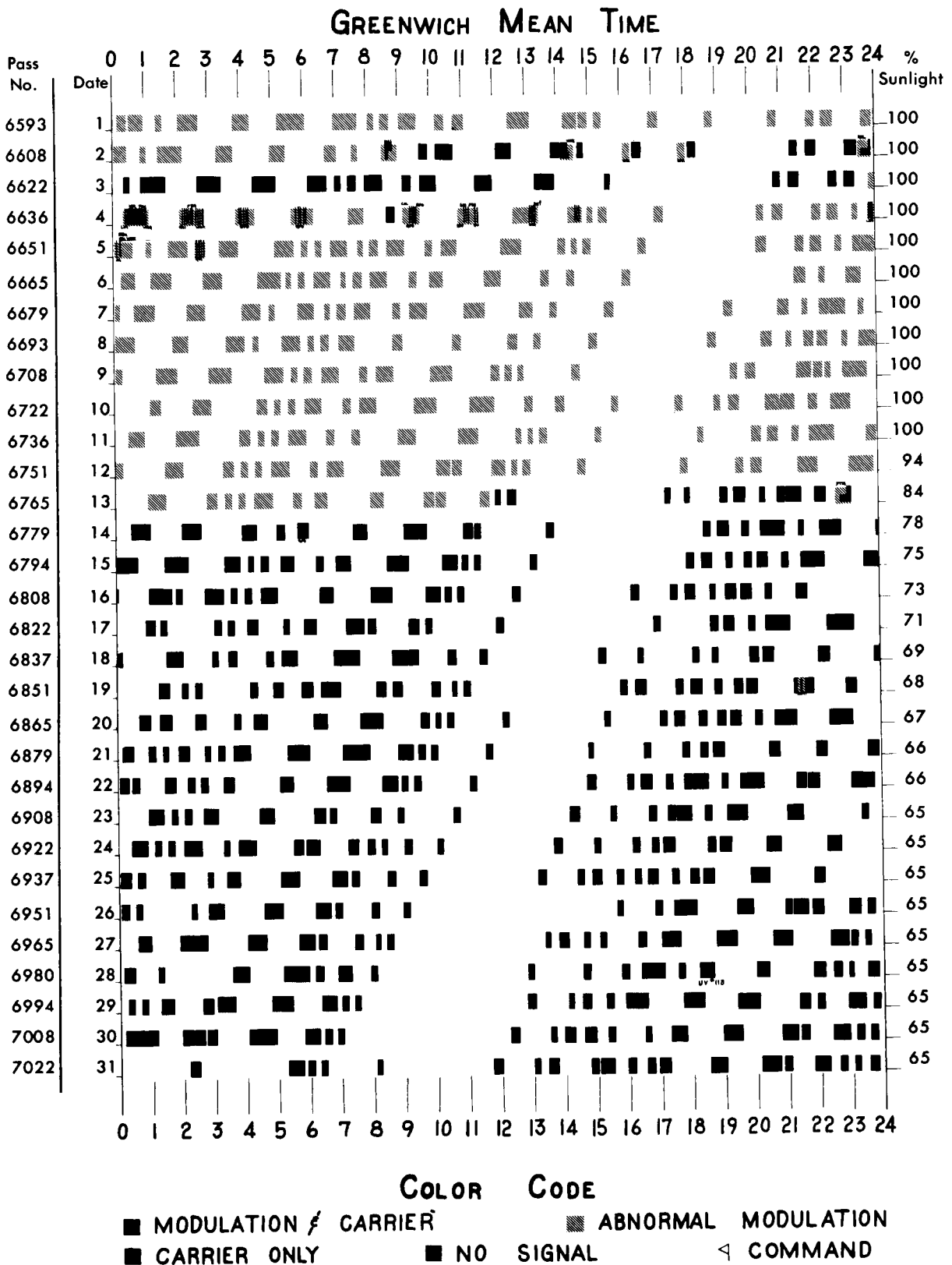
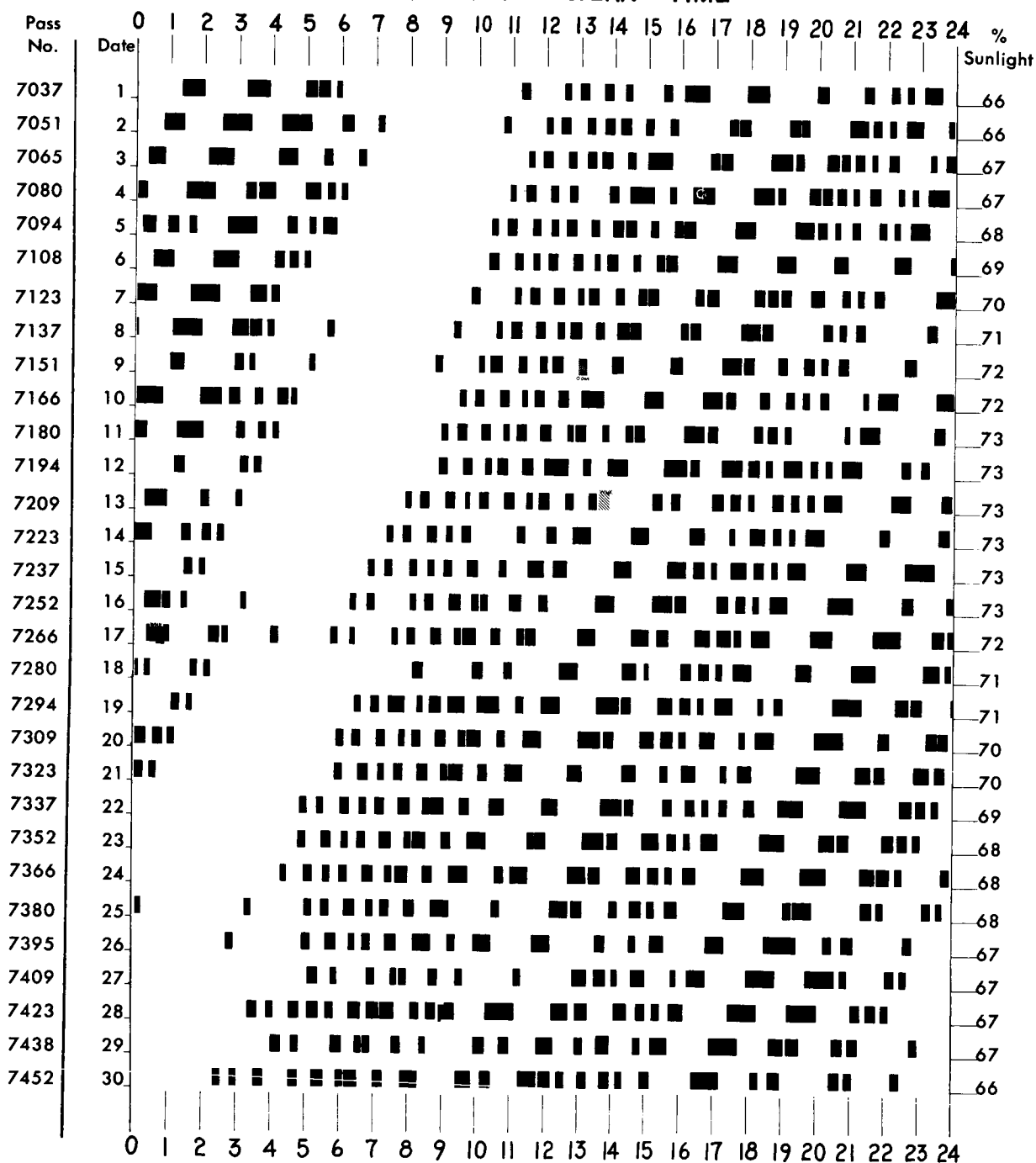


FIGURE B17. Ariel I profile, August 1963.

APPENDIX B—SATELLITE PERFORMANCE PROFILE

GREENWICH MEAN TIME



COLOR CODE

■ MODULATION / CARRIER ▨ ABNORMAL MODULATION
 ■ CARRIER ONLY ■ NO SIGNAL ◁ COMMAND

FIGURE B18. Ariel I profile, September 1963.

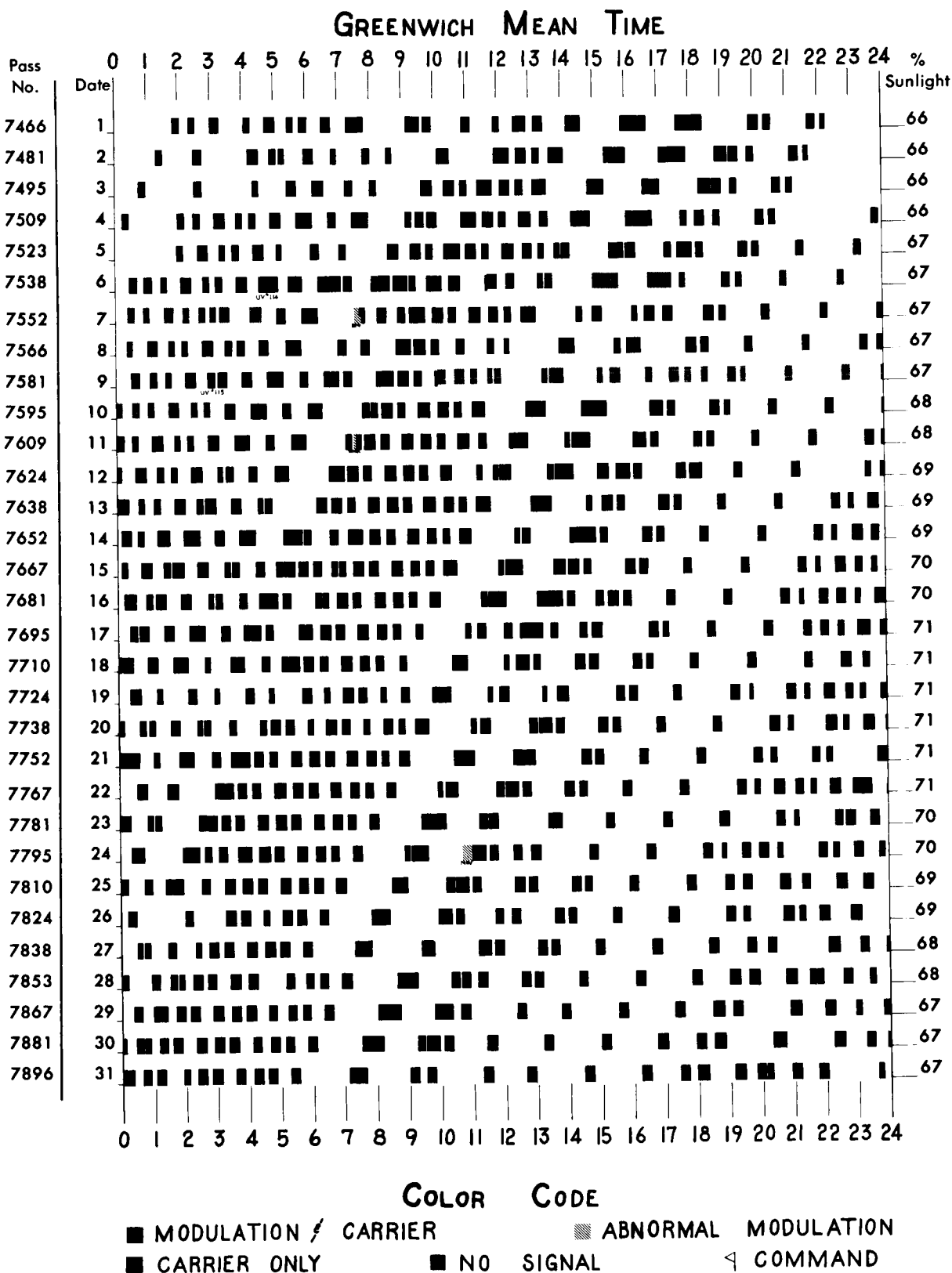
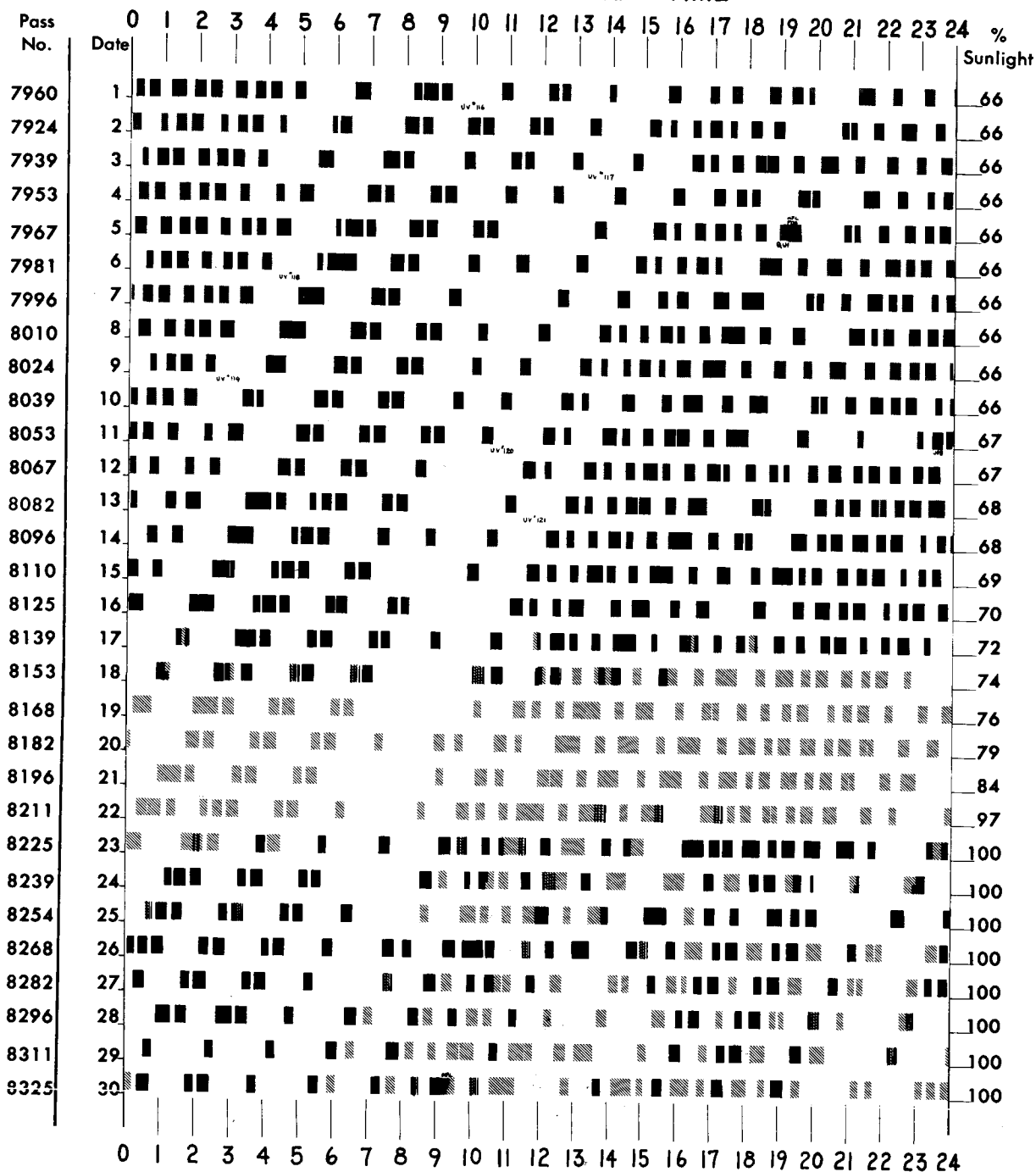


FIGURE B19. Ariel I profile, October 1963.

APPENDIX B—SATELLITE PERFORMANCE PROFILE

GREENWICH MEAN TIME



COLOR CODE

■ MODULATION / CARRIER ■ ABNORMAL MODULATION
 ■ CARRIER ONLY ■ NO SIGNAL ▽ COMMAND

FIGURE B20. Ariel I profile, November 1963.

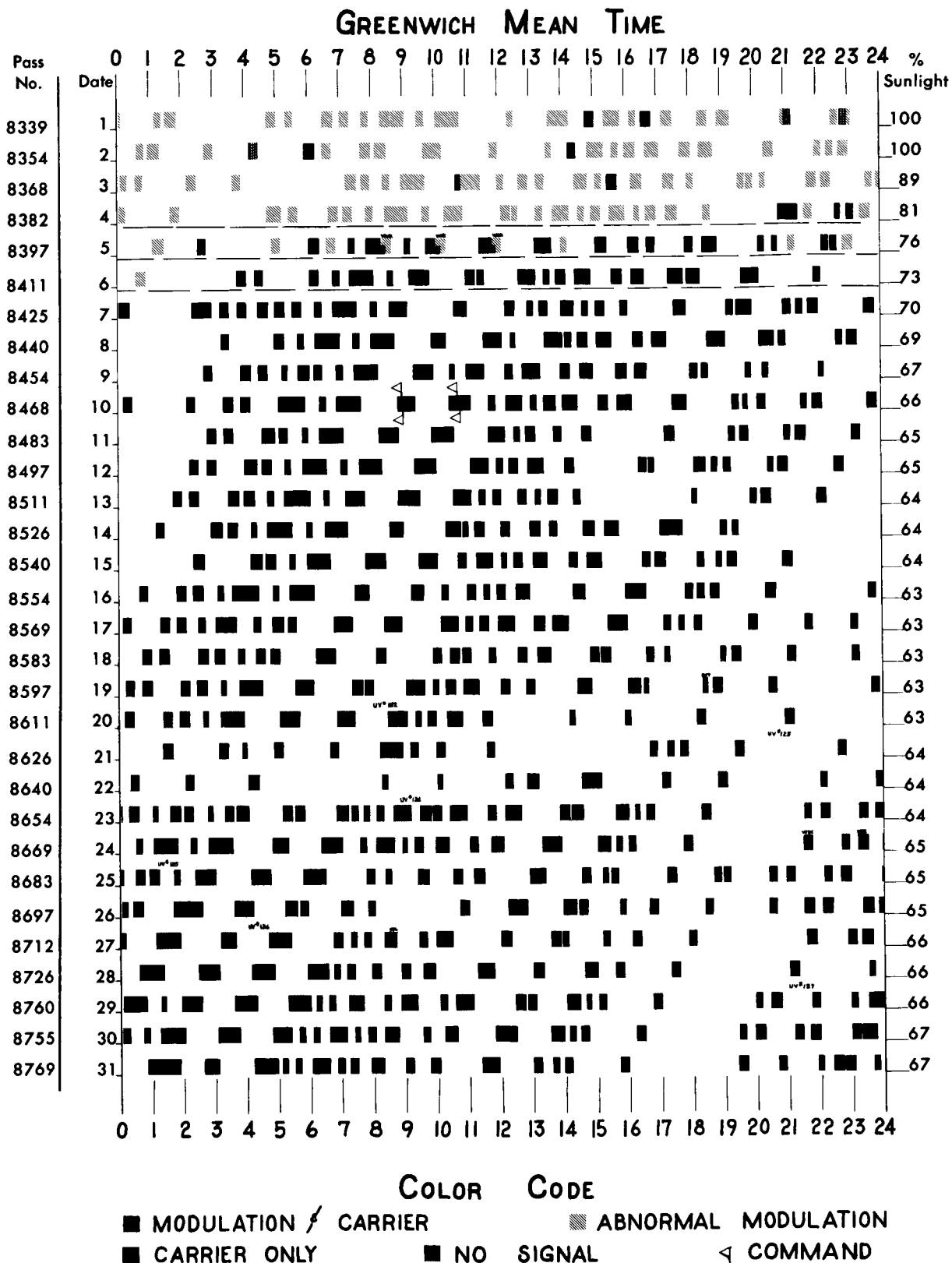
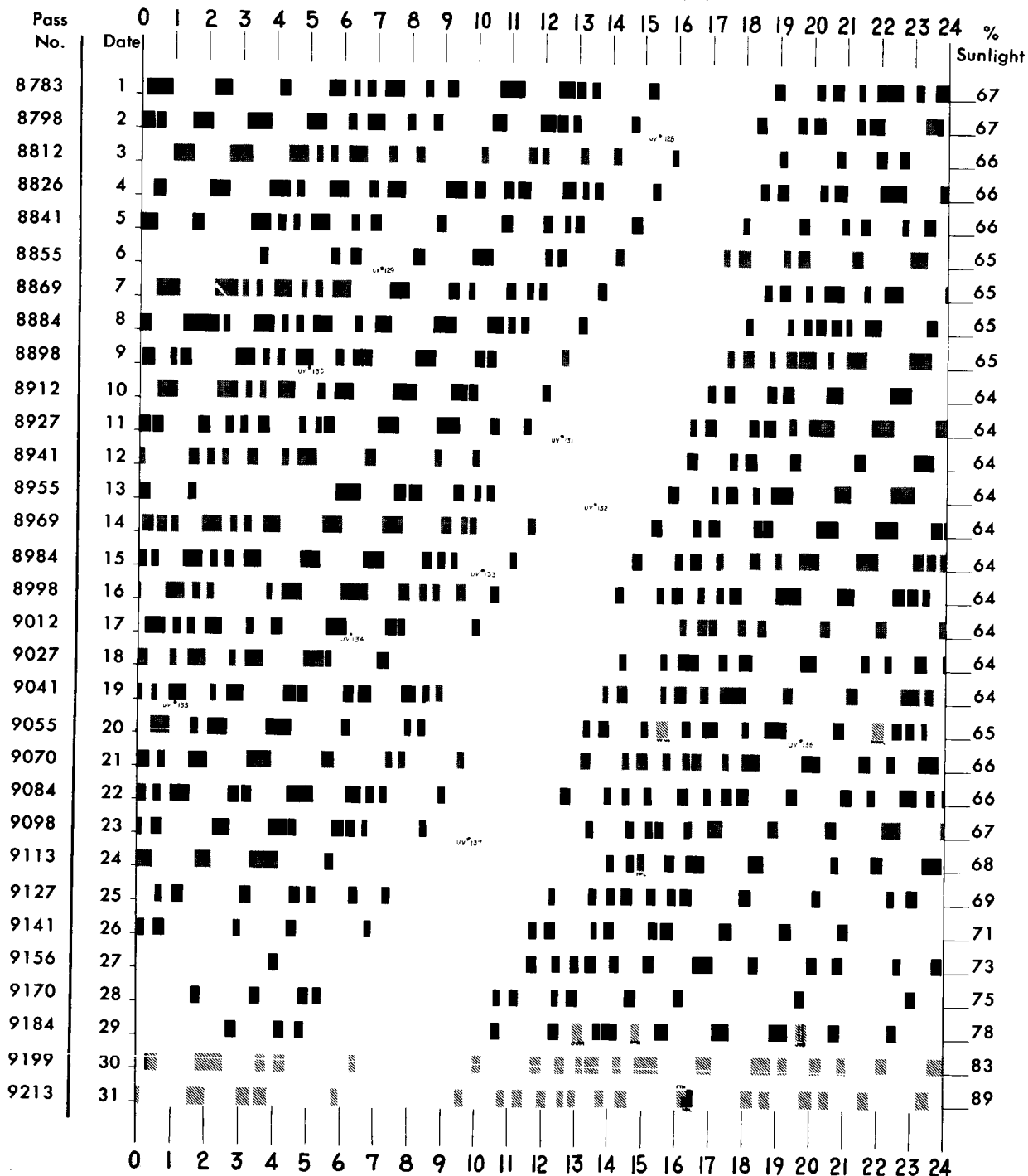


FIGURE B21. Ariel I profile, December 1963.

APPENDIX B—SATELLITE PERFORMANCE PROFILE

GREENWICH MEAN TIME



COLOR CODE

■ MODULATION / CARRIER ■ ABNORMAL MODULATION
 ■ CARRIER ONLY ■ NO SIGNAL ◁ COMMAND

FIGURE B22. Ariel I profile, January 1964.

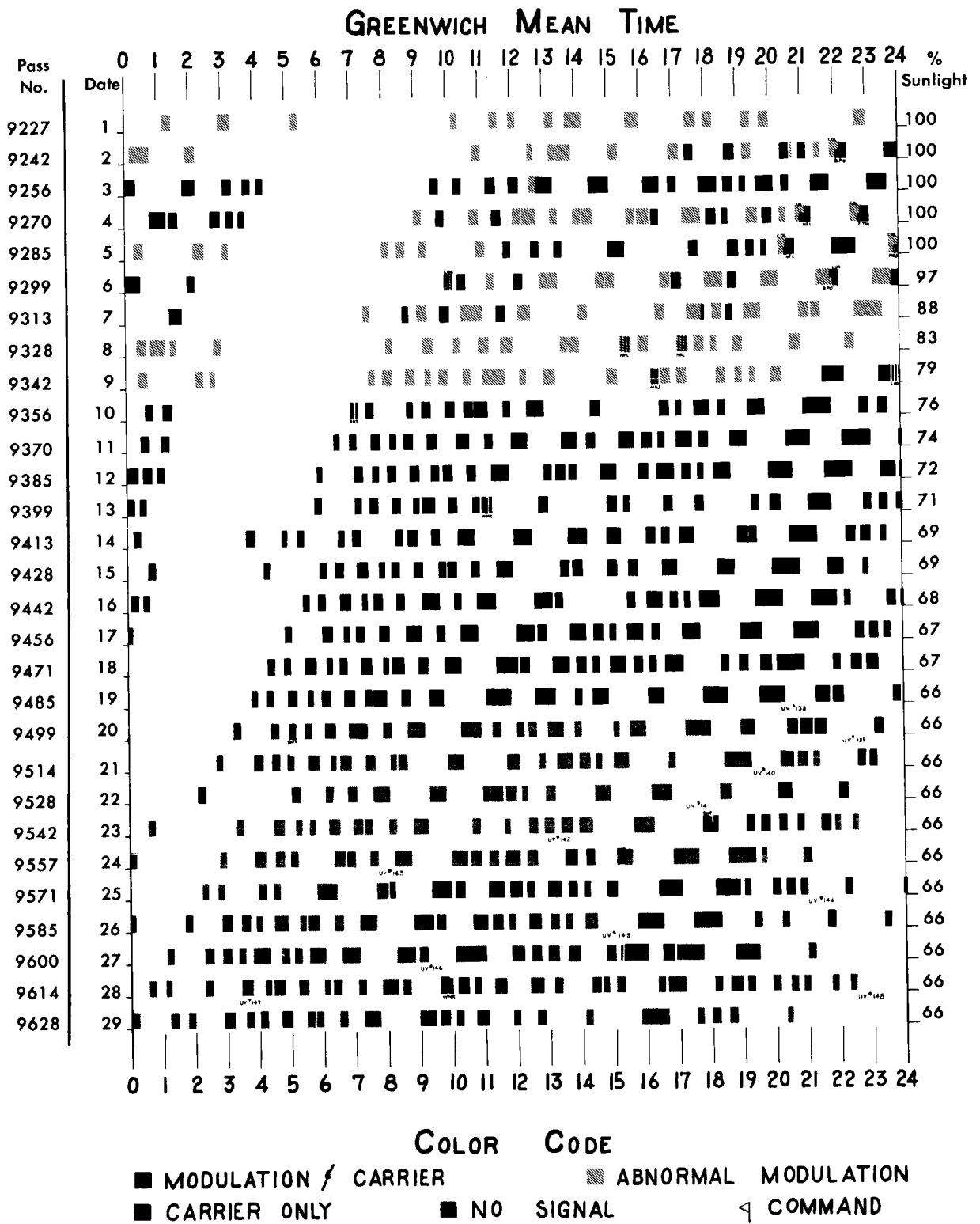
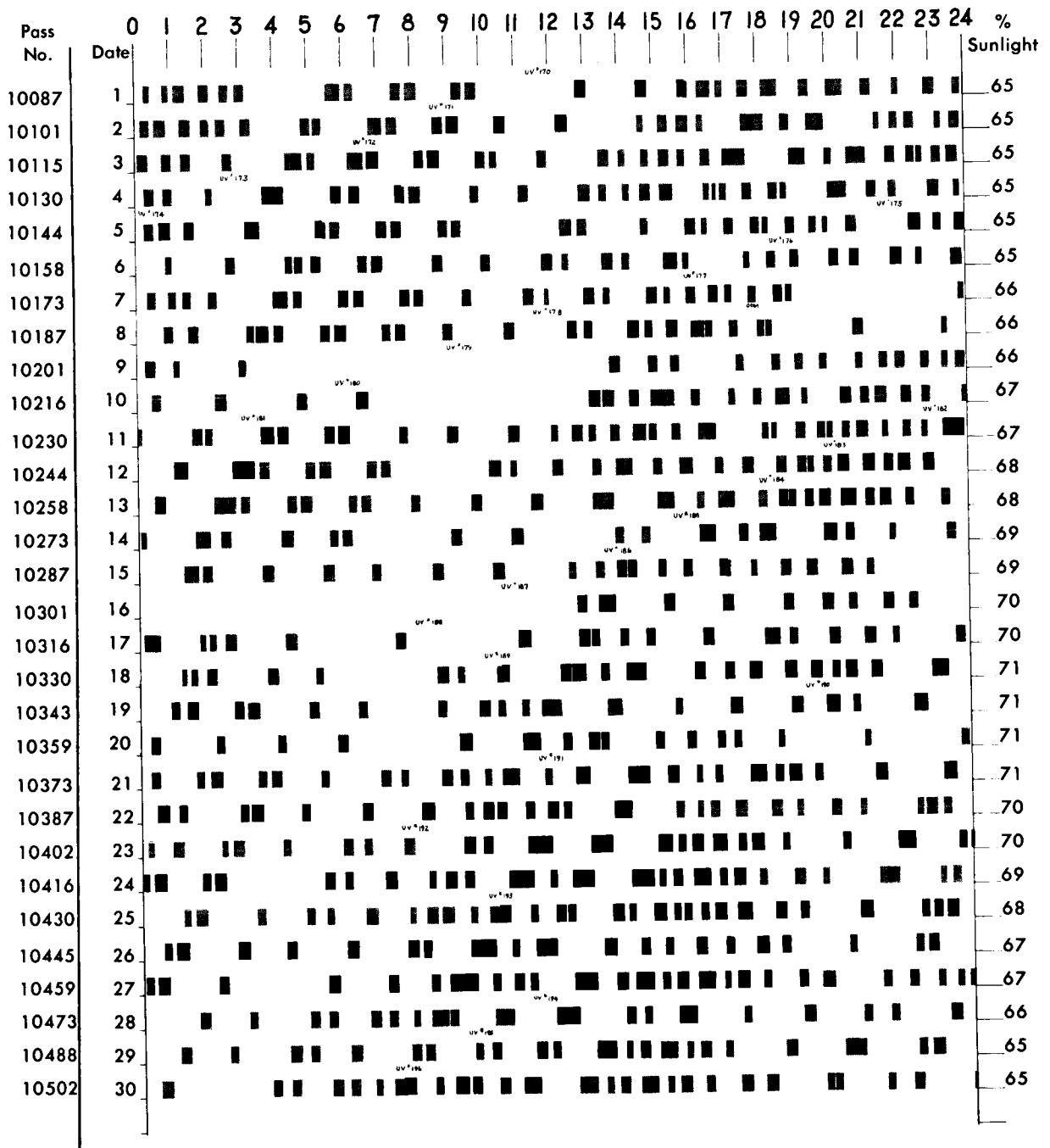


FIGURE B23. Ariel I profile, February 1964.

GREENWICH MEAN TIME



GREENWICH MEAN TIME



COLOR CODE

■ MODULATION / CARRIER ■ ABNORMAL MODULATION
 ■ CARRIER ONLY ■ NO SIGNAL ▽ COMMAND

FIGURE B25. Ariel I profile, April 1964.

GREENWICH MEAN TIME



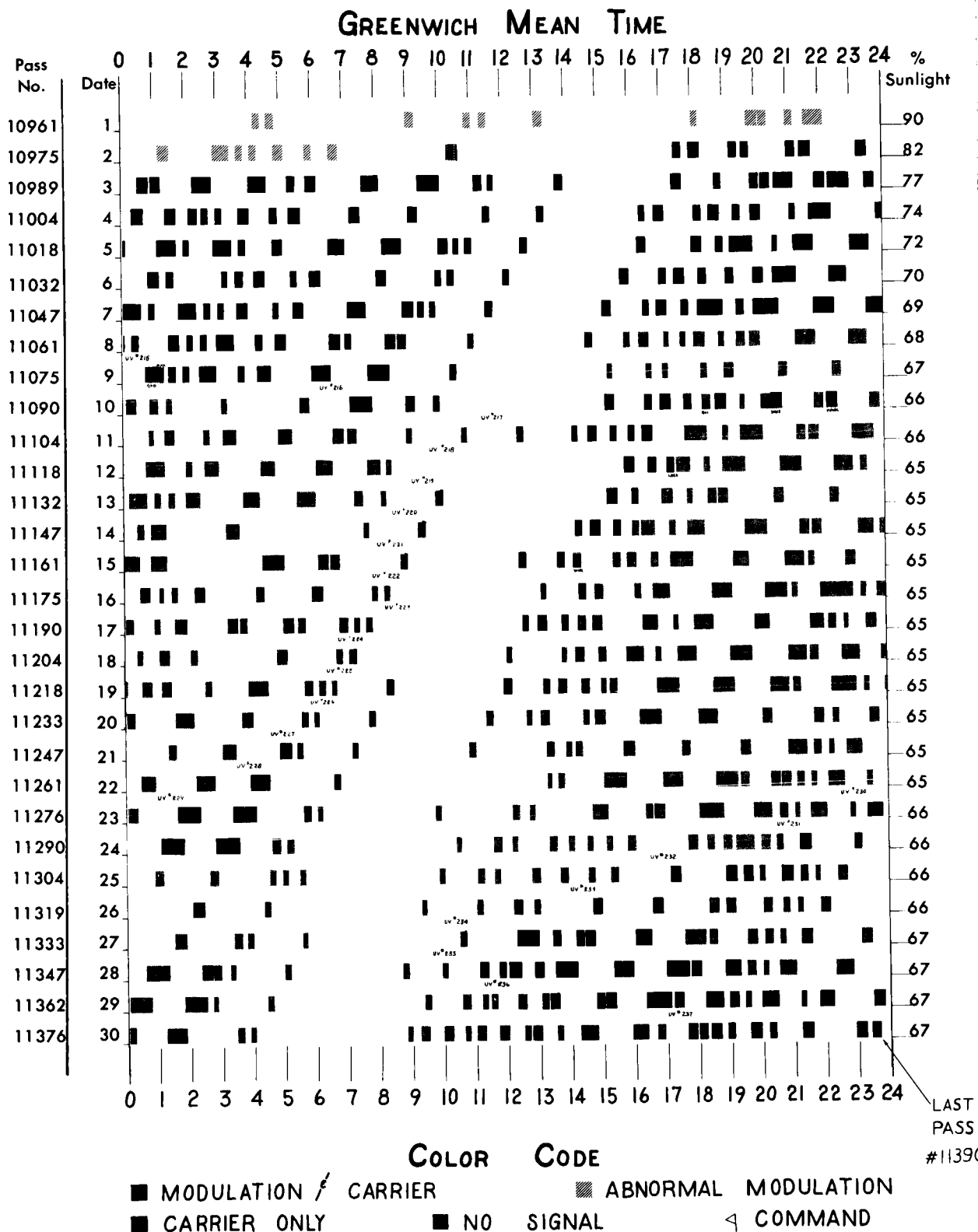
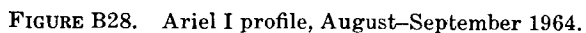
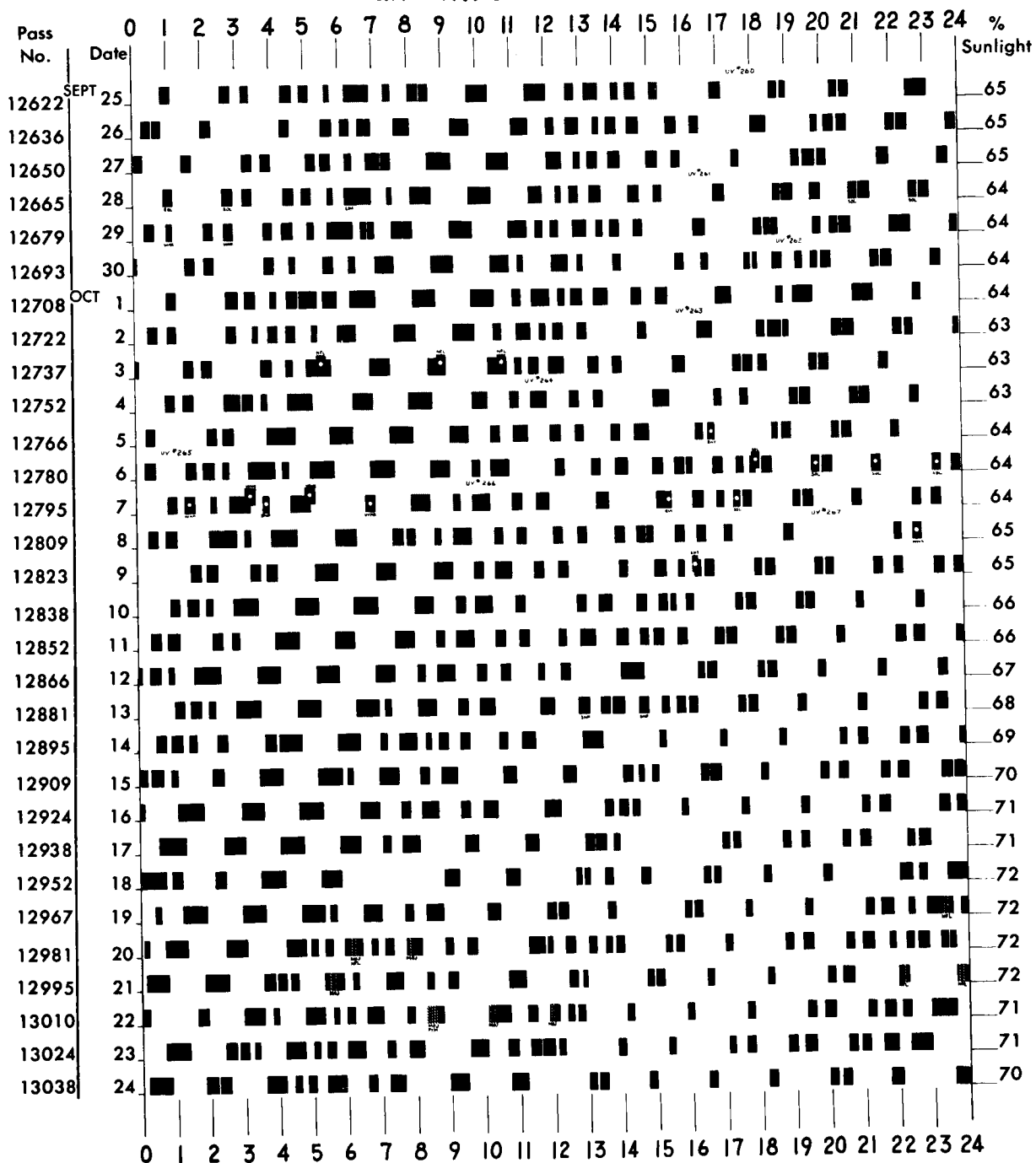


FIGURE B27. Ariel I profile, June 1964.

GREENWICH MEAN TIME



GREENWICH MEAN TIME



* TOTAL UNDERVOLTAGES
EXCLUDING 20 UV'S (ESTIMATED)
FOR NON-MONITORED PERIOD FROM
7/1/4 TO 8/24/4

COLOR CODE

- MODULATION / CARRIER
- CARRIER ONLY
- NO SIGNAL
- STADAN CONFLICTS (INCORRECT) LATE PASS PREDICTIONS
- ABNORMAL MODULATION
- ◁ COMMAND

FIGURE B29. Ariel I profile, September–October 1964.